

TECHNICAL DIGEST

1 9 9 6

BIOMEDICAL  
OPTICAL  
SPECTROSCOPY  
AND  
DIAGNOSTICS

MARCH 20-22, 1996  
ORLANDO, FLORIDA

SPONSORED BY  
OPTICAL SOCIETY OF AMERICA



19961122 147

**REPORT DOCUMENTATION PAGE**Form Approved  
OMB No. 0704-0188

Public reporting burden for this collection of information is estimated to average 1 hour per response, including the time for reviewing instructions, searching existing data sources, gathering and maintaining the data needed, and completing and reviewing the collection of information. Send comments regarding this burden estimate or any other aspect of this collection of information, including suggestions for reducing this burden, to Washington Headquarters Services, Directorate for Information Operations and Reports, 1215 Jefferson Davis Highway, Suite 1204, Arlington, VA 22202-4302, and to the Office of Management and Budget, Paperwork Reduction Project (0704-0188), Washington, DC 20503.

<b>1. AGENCY USE ONLY (Leave blank)</b>		<b>2. REPORT DATE</b>	<b>3. REPORT TYPE AND DATES COVERED</b> FINAL REPORT 01 Mar 96 - 28 Feb 97	
<b>4. TITLE AND SUBTITLE</b> Organization of the 1996 Biomedical Topical Meetings			<b>5. FUNDING NUMBERS</b>  61102F 2301/CS	
<b>6. AUTHOR(S)</b>  Dr Hennage				
<b>7. PERFORMING ORGANIZATION NAME(S) AND ADDRESS(ES)</b>  Optical Society of America 2010 Massachusetts Ave NW Washington, DC 20036			AFOSR-TR-96  0566	
<b>9. SPONSORING/MONITORING AGENCY NAME(S) AND ADDRESS(ES)</b>  AFOSR/NE 110 Duncan Avenue Suite B115 Bolling AFB DC 20332-0001			<b>10. SPONSORING/MONITORING AGENCY REPORT NUMBER</b>  F49620-96-1-0046	
<b>11. SUPPLEMENTARY NOTES</b>				
<b>12a. DISTRIBUTION / AVAILABILITY STATEMENT</b>  APPROVED FOR PUBLIC RELEASE: DISTRIBUTION UNLIMITED			<b>12b. DISTRIBUTION CODE</b>	
<b>13. ABSTRACT (Maximum 200 words)</b>  The Biomedical Topical Meeting was held in Orlando Florida on 18-22 March 1996.				
<i>DTIC QUALITY INSPECTED 3</i>				
<b>14. SUBJECT TERMS</b>			<b>15. NUMBER OF PAGES</b>	
			<b>16. PRICE CODE</b>	
<b>17. SECURITY CLASSIFICATION OF REPORT</b> UNCLASSIFIED	<b>18. SECURITY CLASSIFICATION OF THIS PAGE</b> UNCLASSIFIED	<b>19. SECURITY CLASSIFICATION OF ABSTRACT</b> UNCLASSIFIED	<b>20. LIMITATION OF ABSTRACT</b>	

TECHNICAL DIGEST

1 9 9 6

*Summaries of the papers  
presented at the topical meeting*

# BIOMEDICAL OPTICAL SPECTROSCOPY AND DIAGNOSTICS

MARCH 20-22, 1996  
ORLANDO, FLORIDA

SPONSORED BY  
OPTICAL SOCIETY OF AMERICA



Optical Society of America  
2010 Massachusetts Avenue NW  
Washington DC 20036-1023

AIR FORCE OF SCIENTIFIC RESEARCH (AFSC)  
NOTICE OF  
THIS TECH  
APPROVED  
DISTRIBUT  
JAN 96  
STIMULATED  
used and  
190-12

Approved for  
distribution

Articles in this publication may be cited in other publications. To facilitate access to the original publication source, the following form for the citation is suggested:

Name of Author(s), "Title of Paper," in *Biomedical Optical Spectroscopy and Diagnostics*, 1996  
Technical Digest (Optical Society of America, Washington DC, 1996), pp. xx-xx.

Optical Society of America

ISBN

Conference Edition 1-55752-426-2

1996 Technical Digest Series 1-55752-417-3

Library of Congress Catalog Card Number

Conference Edition 95-72746

Copyright © 1996, Optical Society of America

Individual readers of this digest and libraries acting for them are permitted to make fair use of the material in it, such as to copy an article for use in teaching or research, without payment of fee, provided that such copies are not sold. Copying for sale is subject to payment of copying fees. The code 1-55752-417-3/96/\$6.00 gives the per-article copying fee for each copy of the article made beyond the free copying permitted under Sections 107 and 108 of the U.S. Copyright Law. The fee should be paid through the Copyright Clearance Center, Inc., 21 Congress Street, Salem, MA 01970.

Permission is granted to quote excerpts from articles in this digest in scientific works with the customary acknowledgment of the source, including the author's name and the name of the digest, page, year, and name of the Society. Reproduction of figures and tables is likewise permitted in other articles and books provided that the same information is printed with them and notification is given to the Optical Society of America. In addition, the Optical Society may require that permission also be obtained from one of the authors. Address inquiries and notices to Director of Publications, Optical Society of America, 2010 Massachusetts Avenue, NW, Washington, DC 20036-1023. In the case of articles whose authors are employees of the United States Government or its contractors or grantees, the Optical Society of America recognizes the right of the United States Government to retain a nonexclusive, royalty free license to use the author's copyrighted article for United States Government purposes.

Printed in the U.S.A.



## Contents

Agenda of Sessions	v
<b>BWA</b> Blood Constituent Monitoring I	1
<b>BWB</b> Blood Constituent Monitoring II	17
<b>BWC</b> Cell Analysis and Properties I	31
<b>BWD</b> Cell Analysis and Properties II	43
<b>BThA</b> Poster Session	53
<b>BThB</b> Diagnostic Scattering Properties of Particles and Tissues	125
<b>BThC</b> Raman and Fluorescence in Tissues I	139
<b>BThD</b> Raman and Fluorescence in Tissues II	151
<b>BFA</b> Dyes and Reporters <i>In Vivo</i> I	161
<b>BFB</b> Dyes and Reporters <i>In Vivo</i> II	171
Key to Authors and Presiders	181

**BIOMEDICAL OPTICAL SPECTROSCOPY  
AND DIAGNOSTICS  
TECHNICAL PROGRAM COMMITTEE**

David Benaron, *Stanford University, General Chair*

Eva Sevick-Muraca, *Purdue University, Program Chair*

Thomas Baer, *Biometric Imaging*

Irving Bigio, *Los Alamos National Laboratory*

Britton Chance, *University of Pennsylvania*

Michael Feld, *Massachusetts Institute of Technology*

Howard Nathel, *Lawrence Livermore National Laboratory*

Rebecca Richards-Kortum, *University of Texas at Austin*

Ries Robinson, *University of New Mexico*

Katarina Svanberg, *Lund Institute of Technology, Sweden*

Bruce Trombert, *Beckman Laser Institute and Medical Clinic*

Alan Waggoner, *Biological Detection Systems*

## WINDSOR BALLROOM

7:00am-6:00pm

**Registration**

## WINDSOR BALLROOM

8:00am-8:30am

**Introduction to Biomedical Optical Spectroscopy and Diagnostics**Eva Seveck-Muraca, *Purdue University*

8:30am-10:35am

**BWA • Blood Constituent Monitoring I**David Benaron, *Stanford University, Presider*

8:30am-8:35am

**Introduction to Blood Constituent Monitoring**, David Benaron, *Stanford Univ.*

8:35am (Invited)

**BWA1 • Digital filtering and multivariate analysis of near-infrared spectra for tissue diagnostics**, Mark A. Arnold, *Univ. Iowa*. Digital Fourier filtering is coupled with partial least squares (PLS) regression to enhance information extracted from near spectra of biological and clinical samples. The analytical benefits of this preprocessing step and strategies to optimize filter performance are discussed. (p. 2)

9:15am

**BWA2 • Spatially and spectrally resolved steady-state diffuse reflectance measurements of the optical properties of tissue-simulating phantoms**, M. G. Nichols, E. L. Hull, T. H. Foster, *Univ. Rochester*. We report steady-state diffuse reflectance determinations of hemoglobin absorption in tissue-simulating phantoms. This technique enables *in vivo* oxygen monitoring during photodynamic therapy. (p. 5)

9:35am

**BWA3 • Detection of changes in blood glucose concentration in vivo with spatially resolved diffuse reflectance**, J. T. Bruulsema, J. E. Hayward, T. J. Farrell, M. S. Patterson, *Hamilton Regional Cancer Centre, Canada*; M. Essenpreis, D. Böcker, *Boehringer Mannheim GmbH, Germany*; L. Heinemann, M. Berger, F. A. Gries, T. Koschinsky, *Univ. Düsseldorf, Germany*; J. Sandahl-Christiansen, H. Orskov, *Endocrinology and Diabetes, Denmark*. Spatially resolved diffuse reflectance measurements on diabetic subjects show a correlation between step changes in blood glucose concentration and tissue-reduced scattering coefficient. (p. 8)

9:55am

**BWA4 • A feasibility study on pulsed laser photoacoustic spectroscopy for noninvasive glucose monitoring**, Arlene Campbell, Hugh A. MacKenzie, *Heriot-Watt Univ., UK*; Peter W. H. Rae, *The Royal Infirmary of Edinburgh, UK*. A feasibility study shows a high correlation between trends in blood glucose and the photoacoustic response of tissue for diabetic and normal subjects. (p. 11)

10:15am

**BWA5 • In vivo measurements of blood flow changes using diffusing wave correlation techniques**, I. V. Meglinsky, D. A. Boas, A. G. Yodh, B. Chance, *Univ. Pennsylvania*. We use photon correlation spectroscopy with a simple correlation diffusion to study and quantify blood flow in the arm during cuff ischemia. (p. 14)

## SALONS V-VII

10:35am-11:00am

**Coffee Break/Exhibits**

## WINDSOR BALLROOM

11:00am-1:00pm

**BWB • Blood Constituent Monitoring II**David Benaron, *Stanford University, Presider*

11:00am

**BWB1 • Transurethral reflectometry using sliding fiber device for noninvasive measurement of in vivo optical properties of prostate**, Beop-Min Kim, Steven L. Jacques, Martin Ostermeyer, *Univ. Texas/M. D. Anderson Cancer Center*; Sohi Rastegar, *Texas A&M Univ.*; Massoud Motamedi, *Univ. Texas*. A new approach and device are designed to measure the *in vivo* optical properties of prostate in a noninvasive way. (p. 18)

11:20am (Invited)

**BWB2 • Frequency-domain photon migration (FDPM) measurements of cell and tissue optical properties for biomedical diagnostics**, Olivier Coquoz, Eric Anderson, Bruce J. Tromberg, *Beckman Laser Institute and Medical Clinic*; Lars O. Svaasand, *UC-Irvine*; Richard C. Haskell, *Univ. Trondheim, Norway*. A 1 GHz multi-frequency, multi-wavelength FDPM instrument is used to quantitatively measure optical properties of cell suspensions, biopsy specimens, and bulk tissues. (p. 21)

12:00m

**BWB3 • The frequency-domain multi-distance method in the presence of curved boundaries**, Albert Cerussi, John Maier, Sergio Fantini, Maria Angela Franceschini, Enrico Gratton, *Univ. Illinois-Urbana Champaign*. We investigate the ability of the semi-infinite frequency-domain multi-distance method to recover  $\mu_a$  and  $\mu_s$  for cylindrical tissuelike phantoms. (p. 24)

12:20pm

**BWB4 • The effect of water in the quantitation of hemoglobin concentration in a tissuelike phantom by near-infrared spectroscopy**, Maria Angela Franceschini, Sergio Fantini, Albert Cerussi, Enrico Gratton, *Univ. Illinois-Urbana Champaign*; Beniamino Barbieri, *ISS Inc.*; Britton Chance, *Univ. Pennsylvania*. The absorption of water may not be negligible in the spectroscopic quantitation of hemoglobin concentration and saturation in biological tissue. The effect of water absorption is investigated. (p. 27)

12:40pm

**BWB5 • Fetal brain oxygenation during labor studied by frequency domain spectroscopy**, R. Watson, M. Kohl, P. O'Brien, S. Lawrence, D. T. Delpy, M. Cope, *Univ. College Hospital, UK*. The influence of contractions on the Hb/HbO<sub>2</sub> status in the fetal brain is investigated in the frequency domain. The elimination of movement artefacts is discussed. (p. 30)

1:00pm-2:00pm

**Lunch Break**

WEDNESDAY

MARCH 20, 1996

## WINDSOR BALLROOM

2:00pm-3:45pm

### **BWC • Cell Analysis and Properties I**

Irving Bigio, Los Alamos National Laboratory, *Presider*

2:00pm-2:05pm

**Introduction to Cell Analysis and Properties**, Irving Bigio, Los Alamos National Laboratory.

2:05pm (Invited)

**BWC1 • Applications of laser optical microscopic techniques in deciphering disease specific mechanisms and diagnosis**, B. Herman, Univ. North Carolina. The use of lasers of various types in conjunction with fluorescence optical microscopy, allows quantitative, sensitive, and specific detection of disease specific markers in clinical specimens. The application of lasers to the diagnosis of cervical disease is described. (p. 32)

2:45pm

**BWC2 • Quantitative laser scanning confocal autofluorescence microscopy of normal, premalignant, and malignant colonic tissues**, Hsing-Wen Wang, Marcia I. Canto, Michael V. Sivak, Joseph A. Izatt, Case Western Reserve Univ.; Joseph Willis, Univ. Hospitals of Cleveland. Quantitative laser-induced fluorescence imaging is performed in unstained colonic tissue sections and bulk colon specimens to characterize autofluorescent properties of colon cancer. (p. 35)

3:05pm (Invited)

**BWC3 • Absolute enumeration of rare cell types in peripheral blood using laser induced fluorescence and volumetric microscopy**, Thomas M. Baer, Louis J. Dietz, Biometric Imaging. We describe a novel technique for the absolute enumeration of dye-labeled cells by use of laser-induced fluorescence and volumetric microscopy. (p. 38)

## SALONS V-VII

3:45pm-4:15pm

**Coffee Break/Exhibits**

## WINDSOR BALLROOM

4:15pm-5:15pm

### **BWD • Cell Analysis and Properties II**

Irving Bigio, Los Alamos National Laboratory, *Presider*

4:15pm

**BWD1 • Rapid analysis of fluorescence quenching of FITC-conjugated antibodies on individual cells by phase-sensitive flow cytometry**, C. Deka, B. E. Lehnert, N. M. Lehnert, J. A. Steinkamp, Los Alamos National Laboratory; G. M. Jones, L. A. Sklar, Univ. New Mexico. We demonstrate a high-speed method to analyze the impact of self-quenching on fluorescence lifetimes in individual cells by phase-sensitive flow cytometry with use of a model system consisting of FITC-labeled anti-mouse Thy 1.2 antibodies bound to murine thymus cells. (p. 44)

4:35pm

**BWD2 • Measurement of laser-excited fluorescence spectra of individual airborne biological particles**, Gang Chen, Richard K. Chang, Yale Univ.; Paul Nachman, Ronald G. Pinnick, Steven C. Hill, Gilbert L. Fernandez, Army Research Laboratory; Michael W. Mayo, Systems and Processes Engineering Corp. We report measurements of fluorescence spectra of individual airborne biological particles excited with a UV laser fired when particle scattering or fluorescence exceeds predetermined thresholds. (p. 47)

4:55pm

**BWD3 • Light scattering from cells**, Andrew Dunn, Colin Smithpeter, Rebecca Richards-Kortum, A. J. Welch, Univ. Texas-Austin. The contributions of cellular components to the scattering pattern from cells is determined by solving numerically Maxwell's equations within the cells. (p. 50)

## LOCATION TO BE ANNOUNCED

6:30pm-8:00pm

**Conference Reception**

## WINDSOR BALLROOM

7:00am–6:00pm

## Registration

## WINDSOR BALLROOM

8:30am–10:30am

## BThA • Poster Session

**BThA1 • Noninvasive determination of blood contents using a photoacoustic laser sensor**, G. Spanner, R. Niessner, *Technical Univ. Munich, Germany*. For the noninvasive determination of blood contents *in vivo* spectra of human blood are measured noninvasively with use of the photoacoustic response produced by modulated diode lasers. (p. 54)

**BThA2 • Optical metabolic imaging of ocular tissue with two-photon excitation laser scanning microscopy**, Barry R. Masters, *Unifomed Services Univ. Health Science*. Two-fold changes in cellular respiration are optically monitored as 1.2- $\mu$ m-thick images of NADP(H) fluorescence intensity across a 400- $\mu$ m *in situ* cornea and human lens epithelium. (p. 57)

**BThA3 • Measurement of the muscle optical properties on muscular dystrophy patients by a frequency-domain photometer**, Valentina Quaresima, Marco Ferrari, *Univ. L'Aquila, Italy*; Romina Sfarenì, *Istituto Superiore di Sanità, Italy*; Assunta Pizzi, *Fondazione Pro Juventute Don C. Gnocchi, Italy*. Muscle  $\mu_s$  and  $\mu_a$  (715 and 825 nm) mapped on controls and some muscular dystrophy patients suggest the utility of optical biopsy as an indicator of muscle damage. (p. 60)

**BThA4 • Optical mapping of the human breast using second derivative near-infrared spectroscopy**, Valentina Quaresima, Marco Ferrari, *Univ. L'Aquila, Italy*; Romina Sfarenì, *Istituto Superiore di Sanità, Italy*; Steve J. Matcher, *Univ. College London, UK*; Jeffrey W. Hall, *NIRSystems, Inc.* Second derivative near-IR (650–1100 nm) transillumination spectra from several breast sites are analyzed to identify the most significant wavelengths for breast optical imaging. (p. 63)

**BThA5 • Muscle near-infrared spectroscopy for critically ill patients management**, R. A. De Blasi, N. Almenröder, *Univ. Roma, Italy*; M. Ferrari, *Univ. L'Aquila, Italy*. Hb volume and oxygenation of sternomastoid muscle and forearm of patients with respiratory failure and sepsis are studied by NIRS.  $VO_2$  and blood flow are evaluated. (p. 65)

**BThA6 • Spectrophotometry for the assessment of pigmented skin lesions**, V. P. Wallace, J. C. Bamber, P. S. Mortimer, *ICR, Royal Marsden Hospital, UK*; D. C. Crawford, *Univ. Hospital of Wales, UK*. Optical reflectance spectra (320–1100 nm) are obtained from 121 skin lesions. Features correlated with histology correctly classified 73% benign naevi and 100% malignant melanoma. (p. 67)

**BThA7 • Single-fiber optical probe of two-photon induced fluorescence of biological markers**, A. T. Obeidat, A. E. Kaplan, J. B. Khurgin, M. D. Stern, *The Johns Hopkins Univ.* A single optical fiber was used to induce and collect simultaneously fluorescence through two-photon absorption in fluorophores. We show that a single-mode fiber is a more efficient source and detector than a multimode fiber. (p. 70)

**BThA8 • Broadband monitoring of physiological changes with a continuous light tissue spectrometer**, Judith R. Mourant, Andreas H. Hielscher, David M. Schmidt, John S. George, *Los Alamos National Laboratory*. A broadband (250–850 nm) cw spectrometer is developed to measure diffuse-backscattered light in tissue, and its sensitivity to physiological changes is demonstrated. (p. 73)

**BThA9 • Spectroscopy, photophysics, and detection limits in fluorescence microscopy of oligonucleotide arrays**, Mark O. Trulson, David Stern, Ian D. Walton, Richard P. Rava, *Affymetrix*. Spectral and photophysical properties of several fluorophores are measured and discussed in the context of detection limits in fluorescence microscopy of high-density oligonucleotide arrays. (p. 76)

**BThA10 • Fluorescence imaging of high-density oligonucleotide arrays**, Ian D. Walton, David Stern, Mark O. Trulson, Richard P. Rava, *Affymetrix*. Approaches to imaging of oligonucleotide probe arrays are discussed with regard to resolution, sensitivity, speed, background rejection, and the impact of image digitization on quantitation of fluorophore density. (p. 78)

**BThA11 • Quantitative flow transport imaging in tissuelike matrices using micro-endoscopic probes**, Michael P. Houlne, Darren Hubbard, Darryl J. Bornhop, *Texas Tech Univ.* Micro-endoscopes are used to quantify remotely fluid transport in tissuelike matrices and tissues with use of fluorescent, tissue-selective probe molecules. (p. 81)

**BThA12 • Nitrogen-laser-excited autofluorescence spectroscopy for discrimination of human breast malignancy**, S. K. Majumder, A. Uppal, P. K. Gupta, *Centre For Advanced Technology, India*. Results of an *in vitro* study on nitrogen-laser-excited autofluorescence spectra of human breast tissues are reported. Sensitivity and specificity toward cancer of 85% are obtained involving 15 patients. (p. 84)

**BThA13 • Fourier diagnostic analysis of fluorescence spectra from normal and malignant breast tissues**, A. Katz, Y. Yang, R. R. Alfano, *CUNY–City College*; Edward J. Celmer, Margaret Zurawska-Szczepaniak, *St. Vincent's Medical Center of Richmond*. Fourier analysis is applied to the fluorescence spectra of normal, malignant, and adipose breast tissues for the purpose of developing a spectroscopic diagnostic approach. (p. 87)

**BThA14 • Quantitative fluorescence in tissuelike media**, John S. Maier, Albert E. Cerussi, Sergio Fantini, Maria Angela Franceschini, Enrico Gratton, *Univ. Illinois–Urbana-Champaign*. We present a study focused on quantitative fluorescence in tissues at near-infrared wavelengths. Conclusions relevant to basic science and medical applications are presented. (p. 90)

**BThA15 • Optical constants of bone tissues and their variations related to bone mineral density**, Ryuichihiro Araki, Akira Takeuchi, Akira Itabashi, *Saitama Medical School, Japan*; Sergei G. Proskurin, Yukari Takahashi, Yukio Yamada, *AIST-MITI, Japan*. We measure optical constants of bone tissues and find correlation between  $\mu_s'$  and BMD. The feasibility of bone quality assessment by light is discussed. (p. 93)

**BThA16 • Fluorescence spectroscopy of *B. Subtilis* in solution and aerosol**, M. Seaver, J. F. Pinto, J. D. Eversole, *Naval Research Laboratory*. Fluorescence spectra are obtained from *Bacillus subtilis* samples by use of laser excitation at 248 nm (KrF excimer) and tripled tunable Cr:LiSAF (265–290 nm). (p. 95)

**BThA17 • Determining optical properties with fiber-optic oblique incidence reflectometry**, Shao-Pow Lin, Frank K. Tittel, *Rice Univ.*; Steven L. Jacques, Lihong Wang, *Univ. Texas/M. D. Anderson Cancer Center*. We deduce the absorption and reduce scattering coefficients of tissue phantoms by sampling the diffuse reflectance profile of obliquely incident light. (p. 98)

**BThA18 • A low-cost phase modulation system for tissue spectroscopy and oximetry**, Yunsong Yang, Hanli Liu, Britton Chance, *Univ. Pennsylvania*. A laser-based frequency domain spectrometer for tissue diagnosis is presented. Using I&Q demodulation and frequency-encoding techniques we measure the optical properties of a tissue-stimulating model. (p. 101)

**BThA19 • Investigation of exogenous contrast agents for biomedical optical imaging**, Tamara L. Troy, Lena Nelson-Larry, Christina L. Hutchinson, Eva M. Sevick-Muraca, *Purdue Univ.* Exogenous contrast agents were investigated. Fluorescent dyes appear to be more promising than light absorbing dyes for providing contrast for optical imaging. (p. 104)

**BThA20 • Optical properties of normal and diseased breast tissue**, Tamara L. Troy, Eva M. Sevick-Muraca, *Purdue Univ.*; David L. Page, *Vanderbilt Univ.* Optical property measurements of normal and diseased breast tissues show *in vitro* differences that may be commensurate, but are not always consistent, with histopathology. (p. 107)

**BThA21 • Frequency-domain photon migration in two-layered tissues**, Michal Rosen-Zvi, Haim Taitelbaum, *Bar-Ilan Univ., Israel*. We study frequency-domain spectroscopy for reflectance measurements in two-layered tissues, using a random-walk model of photon migration. (p. 110)

**BThA22 • Noninvasive spectroscopy of variously shaped turbid media like human tissue based on the microscopic Beer-Lambert law**, Yutaka Tsuchiya, Tsuneyuki Urakami, *Hamamatsu Photonics, Japan*. We propose and verify a new method to measure the absolute concentration of absorber in the turbid media that have variously shaped nonreentrant surface. (p. 113)

**BThA23 • Luminescence diffusion tomography**, Jenghwa Chang, Harry L. Graber, Randall L. Barbour, *SUNY Health Science Center*. Image operators are derived for luminescence diffusion tomography with time-harmonic sources with use of a set of coupled radiation transport equations. Experiments are performed and reconstructed images are presented. (p. 116)

**BThA24 • Spatially resolved spectroscopy for extracting spectrum of hemoglobin diluted in a highly scattering medium**, Yoshio Tsunazawa, Yukio Oikawa, Shin-itchi Iwamoto, Hideo Eda, Michinosuke Takada, *Shimadzu Corp., Japan*. We examine the diffusion equation for extracting pure hemoglobin spectra from measurement for blood cells in milk solution with varied probe distance with use of CCD spectrometer. (p. 119)

**BThA25 • Absolute  $SO_2$  measurements in layered tissue**, S. J. Matcher, K. Nahid, M. Cope, D. T. Delpy, *Univ. College London, UK*. The results of computer modeling of various schemes for absolute  $\mu_a$  (and hence  $SO_2$ ) measurements in inhomogeneous layered structures are presented. (p. 122)

#### SALONS V–VII

9:45 am–10:15 am

Coffee Break/Exhibits

#### WINDSOR BALLROOM

11:00 am–12:45 pm

**BThB • Diagnostic Scattering Properties of Particles and Tissues**

Howard Nathel, *Lawrence Livermore National Laboratory*,  
President

11:00 am–11:05 am

**Introduction to Diagnostic Scattering Properties of Particles and Tissues**, Howard Nathel, *Lawrence Livermore National Laboratory*.

11:05 am

**BThB1 • Theoretical and experimental investigations on solute-induced changes in optical properties in living tissues**, Hanli Liu, Yutao Zhang, Mika Kimura, Britton Chance, *Univ. Pennsylvania*. We show theoretically and experimentally that the solute-induced changes in absorption and scattering in living tissues depend on tissue osmolarity and tissue relative refractive index. (p. 126)

11:25 am (Invited)

**BThB2 • Elastic scattering spectroscopy for diagnosis of tissue pathologies**, Irving J. Bigio, Judith R. Mourant, James Boyer, Tamara M. Johnson, JoAnne Lacey, *Los Alamos National Laboratory*. Spectral analysis of sub-surface elastic-scattered light over a broad range of wavelengths is used as a method of noninvasive optical diagnosis for a variety of tissue pathologies. (p. 129)

12:05 pm

**BThB3 • The significance of fiber numerical aperture for optical measurements of turbid media**, Judith R. Mourant, Andreas Hielscher, *Los Alamos National Laboratory*. The effects of fiber numerical aperture on photon sampling volume and on the importance of details of the scattering phase function are studied by use of Monte Carlo simulations. (p. 132)

12:25 pm

**BThB4 • Influence of particle size and concentration on the diffuse backscattering of polarized light**, Andreas H. Hielscher, Judith R. Mourant, Irving J. Bigio, *Los Alamos National Laboratory*. We demonstrate that diffuse-backscattered polarized light yields information about particle size and concentration in turbid media. (p. 135)

12:45 pm–2:00 pm

Lunch Break

THURSDAY

MARCH 21, 1996

---

WINDSOR BALLROOM

2:00pm-4:05pm

**BThC • Raman and Fluorescence in Tissues I**

Thomas Baer, *Biometric Imaging, Presider*

2:00pm-2:05pm

**Introduction to Raman and Fluorescence in Tissues**, Thomas Baer, *Biometric Imaging*.

2:05pm (Invited)

**BThC1 • Raman and fluorescence spectroscopy for in vivo spectroscopy**, Rebecca Richards-Kortum, *Univ. Texas-Austin*. Fluorescence spectroscopy has been explored to diagnose cervical and oral cavity pre-cancer. High predictive value is achieved with spectra at multiple excitation wavelengths when inter-patient variation is considered. (p. 140)

2:45pm

**BThC2 • Raman measurements of concentrations in scattering media**, Jeffery S. Reynolds, Fred P. LaPlant, Charles A. Thompson, Kevin J. Webb, Dor Ben-Amotz, *Purdue Univ.* Raman spectroscopy is used to measure quantitatively solution concentrations in a highly scattering medium. This approach may prove useful in biological spectroscopy and imaging. (p. 143)

3:05pm (Invited)

**BThC3 • Raman histopathology and the Plotkin diamond**, Michael Feld, *MIT*. The use of Raman spectroscopy to provide quantitative biological diagnostic information will be discussed. (p. 146)

3:45pm

**BThC4 • Fluorescence spectroscopy and imaging in random media**, Christina L. Hutchinson, Tamara L. Troy, Eva M. Sevick-Muraca, *Purdue Univ.* A new referencing procedure is proposed for deconvolving the lifetime for short-lived fluorescent dyes from photon migration times in tissues and other scattering media. (p. 147)

---

WINDSOR BALLROOM

4:05pm-4:30pm

**Coffee Break**

---

WINDSOR BALLROOM

4:30pm-5:50pm

**BThD • Raman and Fluorescence in Tissues II**

Thomas Baer, *Biometric Imaging, Presider*

4:30pm

**BThD1 • Diffusive fluorescent waves in homogeneous and heterogeneous turbid media: Analytic solutions and sensitivity analysis**, X. D. Li, M. A. O'Leary, D. A. Boas, B. Chance, A. G. Yodh, *Univ. Pennsylvania*. Analytic solutions of fluorescent diffusive waves are presented for homogeneous and heterogeneous turbid media. The results are used to ascertain potential limitations of these probes. (p. 152)

4:50pm (Invited)

**BThD2 • Fluorescence lifetime imaging with frequency-domain photon migration measurement**, Dilip Y. Paithankar, Eva M. Sevick-Muraca, *Purdue Univ.* A new modality of fluorescence lifetime imaging for biodiagnostics within tissue is developed using frequency-domain measurements of photon migration. (p. 155)

5:30pm

**BThD3 • Concentration and lifetime images of fluorescent turbid media**, M. A. O'Leary, D. A. Boas, X. D. Li, B. Chance, A. G. Yodh, *Univ. Pennsylvania*. We derive simultaneously spatial maps of the concentration and lifetime of heterogeneous fluorophore distributions using fluorescent diffuse photon density waves. (p. 158)

---

WINDSOR BALLROOM

7:30pm-9:30pm

**Workshop: Industrial Challenges From the Medical Industry in Biomedical Optics, Diagnostics, and Imaging**

Eva Sevick, *Purdue University, Presider*

FRIDAY

MARCH 22, 1996

WINDSOR BALLROOM

7:30am–12:30pm

**Registration**

WINDSOR BALLROOM

8:30am–10:35am

**BFA • Dyes and Reporters In Vivo I**

Eva Sevick–Muraca, *Purdue University, Presider*

8:30am–8:35am

**Introduction to Dyes and Reporters In Vivo**, Eva Sevick–Muraca, *Purdue Univ.*

8:35am

**BFA1 • Dye-oligonucleotide conformational structures studied by satellite holes**, Ta-Chau Chang, Chien-Chih Chiang, *Academia Sinica, Taiwan*. The spectral features of satellite holes in nonphotochemical-hole-burned spectra provide a promising method to identify different conformational structures of dye-oligonucleotides. (p. 162)

8:55am (Invited)

**BFA2 • Photonic monitoring of infectious disease and gene regulation**, Christopher H. Contag, *Stanford Univ.* Bioluminescent proteins were used as reporters to determine, in real-time, the spatial and temporal distribution of pathogens, and regulated genes in living mammals. (p. 165)

9:35am (Invited)

**BFA3 • Phosphorescence probes for measurement of O<sub>2</sub> and NO in tissues**, Jane M. Vanderkooi, *Univ. Pennsylvania*. When molecules absorb light, they become more reactive. The reactivity of excited state molecules, relative to the ground state molecules, is the basis of the use of photoactivated molecules as sensors for the paramagnetic molecules, O<sub>2</sub> and NO. The concentration of these physiological diatoms can be determined by their effect in increasing the rates of the transition from the excited state to the ground state of probe molecules. The longer the probe lifetime, the greater the chance for contact between the sensor and sensed molecules. This means that long-lived phosphorescence will be sensitive to O<sub>2</sub> and NO at the low concentrations, while shorter-lived fluorescence will be less sensitive. Extrinsic probes added to tissue or cells allow one to make an image of the oxygen distribution. We are also examining the use of molecules that are intrinsic to the cell as use in oxygen sensor, and recent results will be presented. (p. 168)

10:15am

**BFA4 • Upconverting reporters for immunodiagnostics: Applications in immunohistochemistry and surgical imaging**, Gregory W. Faris, William H. Wright, David A. Zarling, Luke V. Schneider, *SRI International*. We describe the properties of near-infrared-excited upconverting phosphors for ultrasensitive detection and their application to immunohistochemistry and surgical imaging. (p. 169)

WINDSOR BALLROOM

10:35am–11:00am

**Coffee Break**

WINDSOR BALLROOM

11:00am–12:20pm

**BFB • Dyes and Reporters In Vivo II**

Eva Sevick–Muraca, *Purdue University, Presider*

11:00am (Invited)

**BFB1 • Laser spectroscopy in tissue characterization**, Katarina Svanberg, Claes af Klinteberg, Annika Nilsson, Ingrid Wang, Stefan Andersson-Engels, Sune Svanberg, *Lund Institute of Technology, Sweden*. Laser-based spectroscopic techniques were developed for tumor tissue characterization utilizing different tumor-localizing substances. Time-integrated laser-induced fluorescence measurements utilizing a point monitoring fluorosensor and a multi-color fluorescence imaging system were performed *in vivo* in patients with various malignant tumors. The autofluorescence as well as the substance-related fluorescence signals were monitored and tumor demarcation functions calculated for different tumors. (p. 172)

11:40am

**BFB2 • Spectroscopic characterization and biodistribution of tissue site-selective polyazacyclic terbium chelates**, Darryl J. Bornhop, Darren S. Hubbard, Michel P. Houlne, *Texas Tech Univ.* Terbium chelate fluorescence and tissue selectivity demonstrate the potential for *in vivo* cancer diagnosis. (p. 175)

12:00m

**BFB3 • Noninvasive technique for the diagnosis of diseased salivary glands in situ**, I. Gannot, *Food and Drug Administration*; A. H. Gandjbakhche, H. Koch, R. F. Bonner, *NIH*; G. Gannot, P. C. Fox, *National Institute of Dental Research*. Fluoresceinated antibodies that specifically bind to infiltrating lymphocytes in minor salivary glands are imaged to provide monitoring of the progression of Sjögren's syndrome. (p. 178)

12:20pm–12:30pm

**Closing Remarks**



Wednesday, March 20, 1996

# Blood Constituent Monitoring I

**BWA** 8:30 am-10:35 am  
Windsor Ballroom

David Benaron, *Presider*  
*Stanford University*

## Digital Filtering and Multivariate Analysis of Near-Infrared Spectra for Tissue Diagnostics

Mark A. Arnold, Department of Chemistry, University of Iowa, Iowa City, Iowa 52242

The significance of near infrared (near-IR) spectroscopy for clinical and biomedical measurements is the potential to extract analytical information from human subjects in a painless and noninvasive manner. The concept is to pass a selected band of near-IR radiation through the tissue of interest and then computationally extract chemical concentrations from the resulting spectral information. Reliable and accurate measurements require innovative data processing schemes capable of differentiating chemically similar analytes in the presence of strongly absorbing and scattering matrix components.

Our research efforts to develop and evaluate near-IR spectroscopy have focused on noninvasive measurements of blood glucose in human subjects. Our strategy has been to develop techniques for measuring glucose in matrices of increasing complexity. We started with glucose in a simple aqueous buffer solution and have progressed to measurements in complex biological fluids such as whole blood and undiluted serum. Overall, our results indicate that glucose information can be selectively extracted from near-IR spectra collected over the  $5000\text{--}4000\text{ cm}^{-1}$  ( $2.0\text{--}2.5\text{ }\mu\text{m}$ ) spectral range. Critical factors for success include signal-to-noise ratio (SNR) of the collected spectra, digital filtering of raw spectra, and multivariate calibration methods. The SNR must be sufficiently high to allow reliable absorbance measurements for analytes with low absorptivities in the presence of a strongly absorbing/scattering matrix. Digital filtering is one means for enhancing the SNR by effectively removing high frequency spectral noise. Digital filtering can also reduce the adverse effects of baseline shifts and curvatures. After this spectral processing, partial least squares (PLS) regression methods are used to generate calibration models that accurately relate spectral information to analyte concentration.

Digital Fourier filtering effectively enhances analytical information extracted from near-IR spectra of biological samples. The utility of subjecting raw absorbance spectra to this preprocessing step has been illustrated in several of our experiments. In all cases, the Fourier filtering step involves transforming a raw absorbance spectrum into the corresponding digital frequencies, multiplying the transformed spectrum by a Gaussian shaped filter response function, and then returning the spectrum back to the normal spectral domain (absorbance versus wavenumber). Successful filtering requires identification of the optimum Gaussian function that best discriminates spectral features specific for the analyte from all other spectral features which include random noise, baseline variations, and absorbance bands

associated with other matrix components. Filter optimization requires establishing the best combination of mean position and standard deviation width for the Gaussian function along the digital frequency axis. The filter must be positioned along the digital frequency axis to pass spectral information corresponding to the shaped of the analyte absorbance bands. In addition, the filter must be wide enough to pass all the relevant analytical information, yet thin enough to block unwanted noise and other spectral variations. We have developed a scheme for identifying the best Fourier filter parameters based on performance of the calibration model.

Digital Fourier filtering is able to reduce the effects of random noise and baseline variations within the spectral data set. These features were identified early in our work when attempting to establish the feasibility of measuring clinically relevant levels of glucose in a simple aqueous matrix. Noise and baseline variations in raw absorbance spectra prevented the development of accurate calibration models in these early experiments. By treating each spectrum with an appropriate Fourier filter, however, accurate predictions were possible based on a glucose absorption band centered at  $4400\text{ cm}^{-1}$ . Comparison of raw and filtered spectra clearly reveals the SNR enhancement provided by this preprocessing step.

All near-IR measurements in aqueous matrices will be subject to strong temperature effects caused by the temperature dependency of the underlying water absorption bands. Water absorption bands centered at  $5200$  and  $3800\text{ cm}^{-1}$  affect the  $5000$ - $4000\text{ cm}^{-1}$  spectral range. The high concentration of water and the broadness of these absorption bands result in significant absorption of light throughout the  $5000$ - $4000\text{ cm}^{-1}$  region. In addition, the exact position of these bands is temperature dependent because of the influence of hydrogen bonding. As a result, the overall absorption properties of aqueous samples vary with slight changes in solution temperature and these variations result in large baseline shifts and curvatures.

The adverse effects of temperature induced baseline variations can be eliminated by using a digital filter preprocessing step. In this experiment, the training set consisted of near-IR spectra collected at  $37^{\circ}\text{C}$  for aqueous solutions with known levels of glucose. The prediction data set consisted of analogous spectra collected at temperatures ranging from  $33$  to  $41^{\circ}\text{C}$  at  $1^{\circ}\text{C}$  increments. Background spectra were collected at  $37^{\circ}\text{C}$  for both the training and prediction data sets. The resulting baseline variations were nearly an order of magnitude greater than the absorbance from glucose. Nevertheless, application of a suitable digital Fourier filter removed all evidence of this strong background variation and provided accurate glucose measurements.

The final example of measurement enhancement by digital Fourier filtering involves attempts to measure glucose in multiple matrices of whole blood. In this experiment, spectra were collected from samples composed of six unique bovine blood matrices. Approximate 25 samples were used for each matrix and triplicate spectra were collected for each sample. Calibration models were generated by using a training

data set composed of all spectra from five of the six blood matrices. Glucose concentrations were then predicted from all spectra in the remaining sixth blood matrix. This process was then repeated in a "leave one out" fashion where a different blood matrix is used as the prediction set until all matrices serve as the prediction set. Analytical performance was judged by comparing the predicted glucose concentrations with the actual, known values for each sample. Concentration correlation plots were constructed by plotting predicted glucose concentrations versus the known values. Ideally, such plots are linear with a unity slope and zero intercept.

Analysis of models constructed without the Fourier filtering step reveals a systematic error in the glucose predictions when the sample matrix is not represented in the calibration training set. Concentration correlation plots are linear with unity slopes, but the intercepts are offset from zero. The degree and direction of this offset vary for each matrix and seem to depend on the level of protein present in the matrix. Preliminary indications suggest protein interferes with the measurement when the natural variation of protein is not incorporated into the calibration model through the sample matrices used for the training set.

Glucose predictions are significantly more accurate when spectra are treated with an optimized digital Fourier filter before the PLS regression. It must be stressed that only spectra in the training set were used for both filter optimization and model construction. With the digital filtering step, correlation plots for glucose predictions revealed none of the offset behavior observed without Fourier filtering. Elimination of this matrix dependent bias results in a combined standard error of prediction (SEP) of 0.94 mM for all six independent prediction matrices.

# Spatially and Spectrally Resolved Steady-State Diffuse Reflectance Measurements of the Optical Properties of Tissue-Simulating Phantoms

M. G. Nichols, E. L. Hull and T. H. Foster

University of Rochester,

Department of Physics and Astronomy, Rochester, NY 14627 (M.G.N., E.L.H., T.H.F.)

Department of Radiology, 601 Elmwood Ave Box 648, Rochester, NY 14642 (T.H.F.)

Phone: (716)-275-1366 (M.G.N, E.L.H), (716)-275-1347 (T.H.F), FAX: (716)-273-1033

Email: mike (M.G.N), edhull (E.L.H), tom (T.H.F) @plato.rad.rochester.edu

The oxygenation status of tumors is of great importance in radiation and photodynamic therapy (PDT). A noninvasive method of monitoring tumor oxygenation would be valuable in treatment planning and in monitoring response to various therapeutic interventions (Stone *et al.*, 1993). In PDT, for example, several reports have demonstrated a relationship between tumor response in animal models and the fluence rate of the incident irradiation (for example, Gibson *et al.*, 1994). We have suggested that the fluence rate dependence of tumor regrowth rates following PDT could be explained on the basis of photochemical oxygen consumption. While we have validated this hypothesis in multicell tumor spheroids *in vitro*, photodynamic oxygen depletion has yet to be demonstrated in those animal tumor models which exhibit a fluence rate dependent response to PDT. In order to investigate this and related problems, we are exploring an optical method for noninvasively monitoring tumor oxygenation by measuring the tissue near IR absorption spectrum.

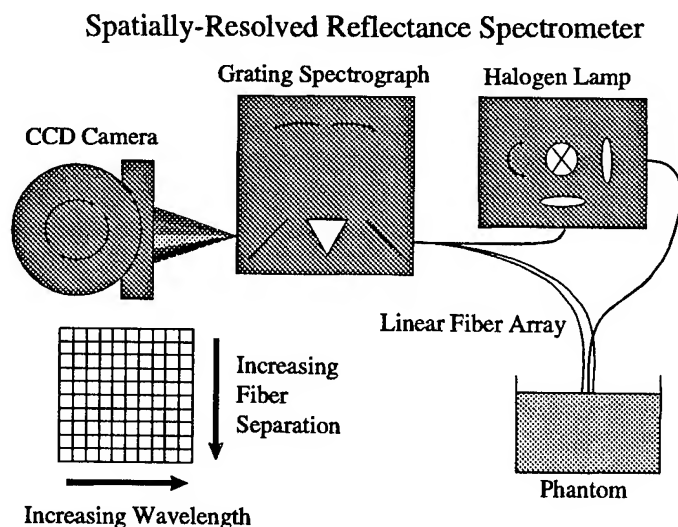


**Figure 1.** The experimental apparatus used to obtain spectrally and spatially resolved diffuse reflectance from optically turbid materials.

The experimental apparatus is illustrated in **Figure 1** and is based on concepts first suggested by Wilson *et al.* (1990). Briefly, light from a halogen lamp is launched into a subcutaneous tumor or tissue-simulating phantom through a single 400  $\mu\text{m}$  source fiber. Fifteen 200  $\mu\text{m}$  detector fibers placed at various distances from the source collect the diffuse reflectance re-emitted from the tumor volume and a reference fiber monitors lamp fluctuations. These optical fibers are arranged in a

linear array and imaged onto the entrance slit of a grating spectrograph. The spectrograph is fitted with a low resolution grating (300g/mm) which spectrally disperses the reflectance from each fiber onto a distinct portion of a CCD array, allowing all sixteen radially resolved spectra to be obtained simultaneously. The CCD has sixteen bits of dynamic range permitting source-detector fiber separations of 1 to 10 mm over the surface of the tumor or phantom. The diffuse reflectance spectra are fit to a steady-state diffusion model of photon transport to obtain the transport scattering ( $\mu'_s$ ) and absorption ( $\mu_a$ ) coefficients as a function of wavelength over a 160 nm interval. Complete data sets can be acquired in under 5 s enabling assessment of oxygen dependent chromophores on time scales relevant to PDT.

Our effort recently has involved instrument calibration and verification. Optical phantoms consisting of a scattering solution and known quantities of chromophore, such as cytochrome c, hemoglobin and various photosensitizers, have been used to gauge performance. Absorption spectra of a phantom consisting of 12.5% stock Liposyn-II® (10%) and various concentrations of manganese meso-tetra (4-sulfonatophenyl) porphine (MnTPP) obtained from this apparatus are shown in Figure 2. It is clear that the absorption spectrum of the phantom (data points) can be determined from the diffuse reflectance provided scattering is properly accounted for. Indeed, the recovered absorption spectrum is very similar to that obtained in a clear homogeneous aqueous solution in a conventional spectrometer (lines).

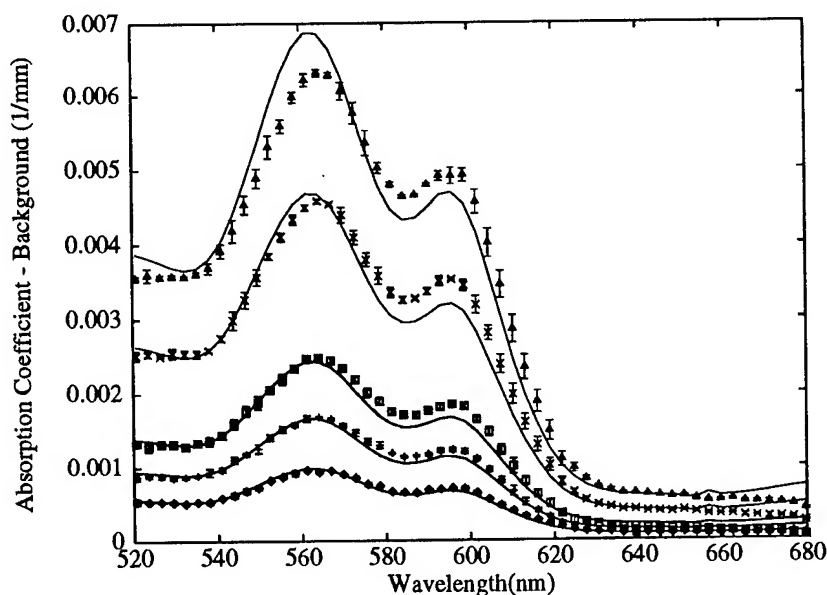


**Figure 2.** Background-subtrated absorption spectra (data points) of several concentrations of manganese meso-tetra (4-sulfonatophenyl) porphine (MnTPP) in 12.5% stock Liposyn-II® (10%) reconstructed from diffuse reflectance measurements. The lines are absorption spectra from spectrophotometer measurements of nonscattering samples with amplitudes scaled to provide the best fit to the data. The single, fitted scaling parameter reveals the concentration of MnTPP in the phantom.

In a similar manner, the hemoglobin oxygen saturation can be determined by reconstructing the absorption spectrum and fitting it to a superposition of oxygenated and deoxygenated hemoglobin spectra obtained from nonscattering samples and a conventional spectrometer. In this case, the

concentrations of the two forms are determined as independent fitting parameters and the fractional saturation can then be determined. Figure 3 depicts the oxygenated hemoglobin spectrum obtained for several hemoglobin concentrations in a 12.5% Liposyn-II® (10%) phantom.

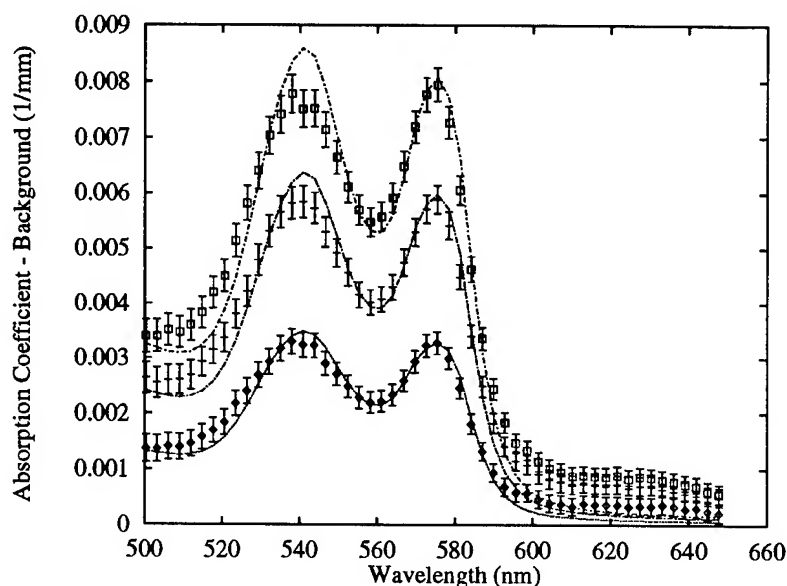


**Figure 3.** Background-subtracted absorption spectra of several concentrations of human hemoglobin, obtained from hemolysed blood, in a 12.5% Liposyn-II® (10%) phantom. These data were fit in the same manner as the data in Figure 2.

We are currently conducting experiments wherein the absorption spectrum of a hemoglobin, yeast and Liposyn-II® phantom is obtained concurrently with oxygen electrode measurements while the yeast deoxygenates the phantom. By measuring the hemoglobin oxygen saturation as a function of the oxygen partial pressure, the hemoglobin oxygen dissociation constant can be measured. These data may provide a calibration that will enable correlation of measured hemoglobin oxygen saturation with average tissue oxygen concentration *in vivo*.

### References

- S.L. Gibson, T.H. Foster, R.H. Feins, R.F. Raubertas, M.A. Fallon and R. Hilf (1994). Effects of photodynamic therapy on xenografts of human mesothelioma and rat mammary carcinoma in nude mice. *Br. J. Cancer* 69:473-481.
- H.B. Stone, J.M. Brown, T.L. Phillips and R.M. Sutherland (1993). Oxygen in tumors: correlations between methods of measurement and response to therapy. *Radiat. Res.* 136:422-434.
- B.C. Wilson, T.J. Farrell and M.S. Patterson (1990). An optical fiber-based diffuse reflectance spectrometer for noninvasive investigation of photodynamic sensitizers *in vivo*. *Proc. SPIE IS* 6:219-232.

## Detection of Changes in Blood Glucose Concentration *in vivo* with Spatially Resolved Diffuse Reflectance

J. T. Bruulsema<sup>1</sup>, M. Essenpreis<sup>2</sup>, L. Heinemann<sup>3</sup>, J. E. Hayward<sup>1</sup>, M. Berger<sup>3</sup>, F. A. Gries<sup>4</sup>, T. Koschinsky<sup>5</sup>, J. Sandahl-Christiansen<sup>6</sup>, H. Orskov<sup>6</sup>, T. J. Farrell<sup>1</sup>, M. S. Patterson<sup>1</sup>, D. Böcker<sup>2</sup>

<sup>1</sup>Hamilton Regional Cancer Centre, 699 Concession St., Hamilton, Ontario, Canada, L8V 5C2. Phone: (905)387-9495. Fax: (905) 575-6550.

<sup>2</sup>Boehringer Mannheim GmbH., Sandhofer Strasse 116, D-68305 Mannheim, Germany. Phone: 621-759-4746. Fax: 621-759-6340.

<sup>3</sup>Klinik für Stoffwechsel und Ernährung, MNR Klinik, Universität Düsseldorf, Moorenstrasse 5, 40225 Düsseldorf, Germany. Phone: 0211-3118771. Fax: 0211-3118772.

<sup>4</sup>Diabetes-Forschungsinstitut, Universität Düsseldorf, Auf'm Hennekamp 65, 40225 Düsseldorf, Germany. Phone: 0211-3382-200. Fax: 0211-342080.

<sup>5</sup>Diabetes-Forschungsinstitut, Universität Düsseldorf, Auf'm Hennekamp 65, 50225 Düsseldorf, Germany. Phone: 0211-338227. Fax: 0211-3382603.

<sup>6</sup>Medical Department M., Endocrinology and Diabetes, DK-8000 Aarhus C., Denmark. Phone: 0045-89493333. Fax: 0045-89492010.

Continuous, non-invasive monitoring of blood glucose levels may be possible with a technique which relates changes in tissue reduced scattering coefficient ( $\mu_s'$ ) to changes in blood glucose concentration. *In vitro* measurements of glucose effects with tissue simulating phantoms predict a decrease in  $\mu_s'$  of 0.05 % mM<sup>-1</sup> glucose for adipose tissue and 0.1 % mM<sup>-1</sup> glucose for muscle [Kohl *et. al.*, 1995]. An optical measurement system which is sensitive enough to detect small  $\mu_s'$  changes would enable diabetics to monitor their glucose levels continuously between their standard measurement procedure which requires them to obtain blood samples several times daily.

Spatially resolved diffuse reflectance has been used successfully to measure tissue optical properties. In this technique, a narrow beam of light from a broadband source is directed through the tissue surface and diffusely reflected light is collected at several distances from the entry point. The optical properties can be obtained by fitting a diffusion model [Farrell *et. al.*, 1992 (1)] to the measured reflectance. In this measurement a surface probe consisting of a source fiber, a calibration fiber, and eight detection fibers was used. Detectors were situated between 1 to 10 mm from the source. The detected light is passed through an imaging spectrometer and onto a CCD. In this way, spectral and spatial information are obtained simultaneously.

A total of 15 diabetic volunteers were enrolled in the clinical study. The probe was applied to the abdomen of the volunteer. Reflectance measurements were acquired at 15 second intervals while the blood glucose concentration of the volunteer was consecutively clamped with a Biostator [Clemens *et. al.*, 1977] at target concentrations of approximately 3.5 mM, 9mM, 14 mM and 5mM. The first concentration was held for about 2 hours and the remaining



concentrations were held for about 1 hour, resulting in a total measurement time of about 5 hours. A bolus of glucose or insulin was given to induce a step change for each change in concentration. For three of the volunteers a single large glucose step (3.5 mM  $\rightarrow$  14 mM) was given to increase the observed signal change. The volunteer remained as still as possible throughout the measurement to avoid artifacts from movement.

A neural network trained on a diffusion model was used to extract optical properties from the reflectance data [Farrell *et. al.*, 1992 (2)]. The time evolution of  $\mu_s'$  was compared to the monitored blood glucose concentration changes. The expected scattering change was small compared to the observed physiological drift in  $\mu_s'$  which was frequently quite large (about 5% over the 5 hour period). Some factors potentially contributing to the physiological noise in the derived scattering coefficient are temperature and volunteer motion.

A typical  $\mu_s'$  (800 nm) and glucose plot is shown in Figure 1. In this case a single large increase of blood glucose concentration was induced at 12:02 with a nominal step in blood glucose concentration of 3.5 mM to 14 mM. The corresponding measured change in  $\mu_s'$  was about 0.1%  $\text{mM}^{-1}$ , comparing well with what Kohl *et. al.* predicted (0.05% to 0.1%  $\text{mM}^{-1}$ ). A correlation between estimated  $\mu_s'$  change and blood glucose concentration was found in 11 out of 15 volunteers. For some of the volunteers the relative change in  $\mu_s'$  was slightly larger than the change predicted by Kohl *et. al.* The results are encouraging and further studies will emphasize optimization of detector design, measurement location and reduction of signal shifts.

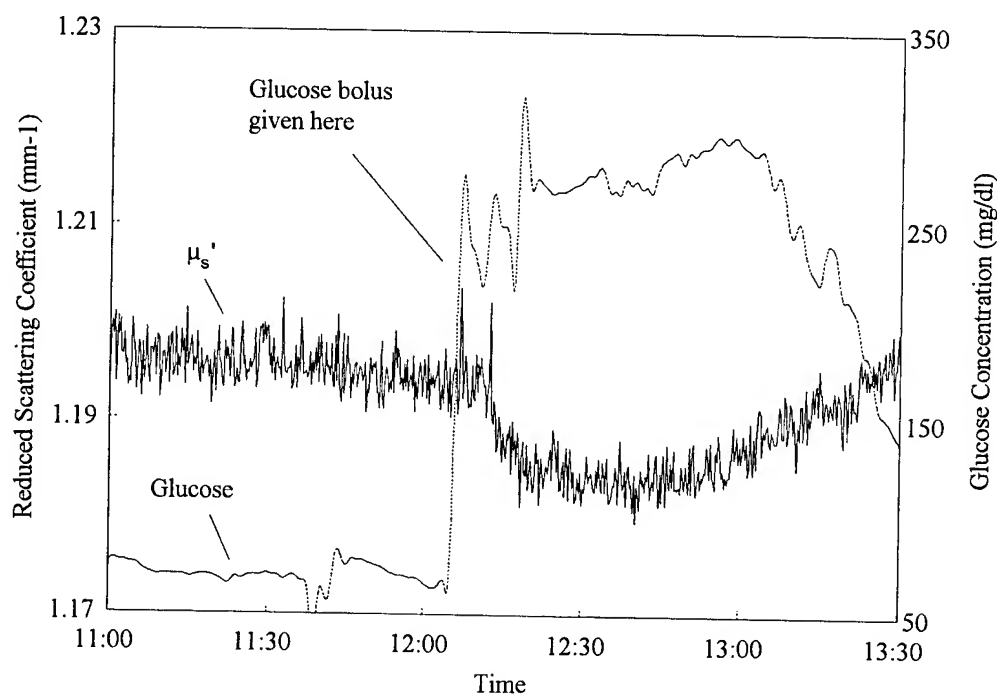


Figure 1: Reduced Scattering Coefficient and Blood Glucose Concentration Versus Time for a Diabetic Volunteer. A single glucose bolus was given at 12:05 with a nominal concentration change of 70 mg/dl  $\rightarrow$  280 mg/dl (3.5 mM  $\rightarrow$  14 mM).

## References

Kohl, M., Cope, M., Essenpreis, M. and Böcker, D. Influence of glucose concentration on light scattering in tissue-simulating phantoms. *Optics Letters* **19** 2170-2172 (1994).

Farrell, T. J., Patterson M. S. and Wilson, B. C. A diffusion theory model of spatially resolved, steady-state diffuse reflectance for the noninvasive determination of tissue optical properties in vivo. *Med. Phys.*, **19** 879-888 (1992).

Clemes, A. H., Chang, P. H. and Myers, R. W. The development of Biostator, a glucose controlled insulin infusion system (GCIIS). *Horm. Metab. Res. (Suppl.)*, **8** 23-33 (1977).

Farrell, T. J., Wilson, B. C. and Patterson, M. S. The use of a neural network to determine tissue optical properties from spatially resolved diffuse reflectance measurements. *Phys. Med. Biol.*, **37** 2281-2286 (1992).

## A Feasibility Study on Pulsed Laser Photoacoustic Spectroscopy for Non-Invasive Glucose Monitoring

Arlene Campbell, Peter W.H. Rae\* and Hugh A. MacKenzie

Heriot-Watt University, Department of Physics, Riccarton, Edinburgh, EH14 4AS, U.K.

Tel: (+44) 131 451 3053, Fax: (+44) 131 451 3036, Email: phyad@bonaly.hw.ac.uk

\*The Royal Infirmary of Edinburgh, Department of Clinical Biochemistry, Lauriston Place, Edinburgh, EH3 9YW, U.K. Tel: (+44) 131 229 2477, Fax: (+44) 131 229 3543

A range of non-invasive monitoring techniques for the determination of blood glucose are being actively pursued worldwide<sup>1-5</sup>. An instrument using diffuse reflectance measurements on the forearm has recently become available for diabetic home use<sup>6</sup>. Further instruments are available for research and, after successful clinical trials, are expected to reach the marketplace<sup>7</sup>. Current measurements are based on near infrared spectroscopy (NIRS), a technique which has been successful in the monitoring of cerebral oxygenation and haemodynamics<sup>8</sup>. Here the relatively large concentrations of haemoglobin and oxyhaemoglobin, which have opposing characteristics and strong spectral features in the NIR, make detection easier, but absolute determination is made difficult due to the highly scattering nature of tissue. In contrast, the absorption of glucose in the NIR is orders of magnitude lower, the spectral features are subtle and concentrations found in the human body are small. As a result, the limited success at glucose determination has only been made possible by the application of advanced chemometric analysis<sup>9</sup>.

In the work reported here, the photoacoustic technique has been utilised in a feasibility study for non-invasive blood glucose monitoring. Photoacoustic spectroscopy (PAS) has been used for the detection of low absorbing analytes in liquids and gases for many years<sup>10</sup>. The recent availability of laser diodes coupled with fast microprocessors has brought a resurgence of the technique as new applications are realised. We have developed pulsed laser photoacoustic spectroscopy (PLPAS) for non-invasive monitoring due to its many advantages over the limitations imposed by NIRS, namely:

- geometrical position of source and detector is non-critical.
- immunity to scattering.
- insensitivity to water absorption.
- requirement of low power laser diode sources.
- use of cheap rugged lightweight piezoelectric detector.

A laser pulse is fired into the tissue. The small increase in temperature causes localised heating and consequently thermal expansion occurs and a pressure wave is generated. This sound wave is detected on the skin surface by a piezoelectric element. Due to the short pulse duration ( $\sim 100$ ns), multiple pulses over a small measurement time ( $\sim 5$ sec) allow for signal averaging to produce favourable signal to noise values. The amplitude of this averaged waveform is recorded as the photoacoustic response. Figure 1 shows a typical photoacoustic response obtained from a finger<sup>11</sup>. The source was a laser diode at 904nm, 2 $\mu$ J energy and 200ns pulse duration, the detector a 4mm disc of PZT-5A ceramic and the response obtained, after amplification, over 256 samples at a rep. rate of 200Hz. The initial ringing is a result of 'pickup' from the laser diode power supply, but sufficient shielding can remove this.

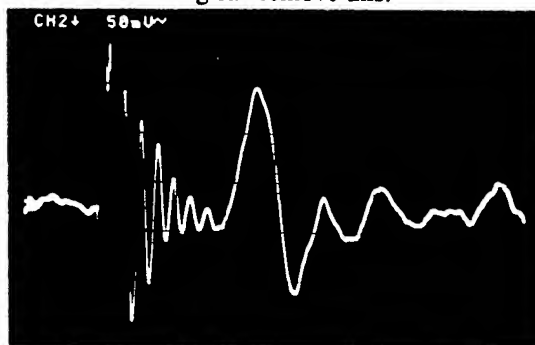
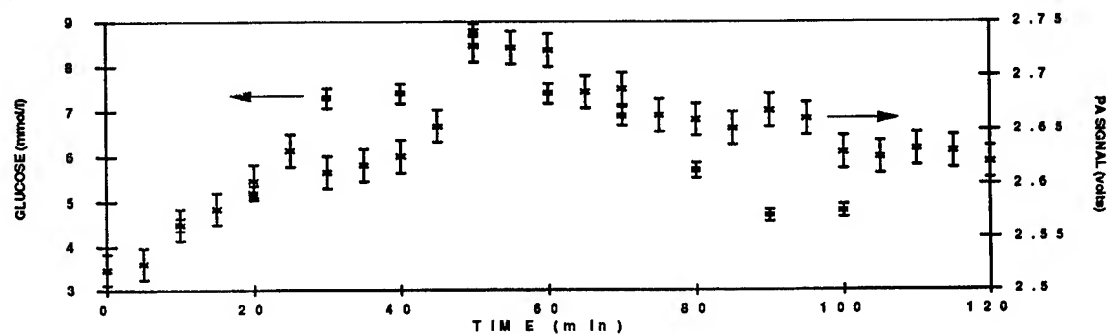


Figure 1. Photoacoustic response from a finger. The response occurred 5 $\mu$ s after the laser pulse was fired.

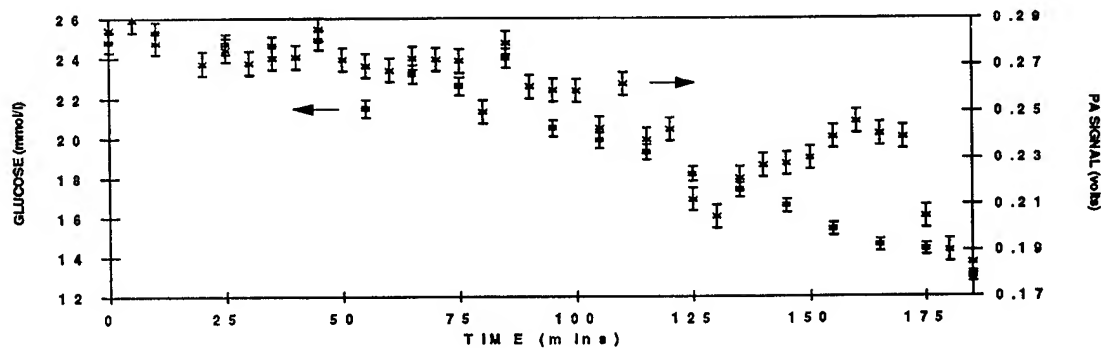
A feasibility study was performed to determine if the photoacoustic response of tissue could be shown to monitor changes of blood glucose concentration across the physiological range (3-30mmol/L, ~60-600mg/dL). A standard oral glucose tolerance test (OGTT) was performed on a group of eight volunteers, two Type 1, two Type 2 and four normal. The protocol for an OGTT is to fast for a twelve hour period, consume a 75g dose of D-glucose in under five minutes, with venous blood samples taken at the start and end of a two hour period for analysis on a standard laboratory instrument. For the study, a photoacoustic measurement was taken every 5 minutes and a standard venous blood sample taken every 10 minutes. The procedure was approved by the local ethical committee.

For the purposes of this study, the source used was a Q switched Nd:Yag laser fired down a doped Raman fibre. Individual wavelengths were selected on a monochromator. A small portion of the 60 $\mu$ J beam was picked off for energy monitoring. The sampling head consisted of micro-optics for focusing the beam and a piezoelectric detector (described earlier). An index finger was held against the source and detector by means of a metal clip. The entire head size was 25x35x90mm. The photoacoustic signal was amplified and read by an ADC card within a PC. For each response, 1024 pulses were averaged, taking ~5sec, and the amplitude recorded.

(a)



(b)



(c)

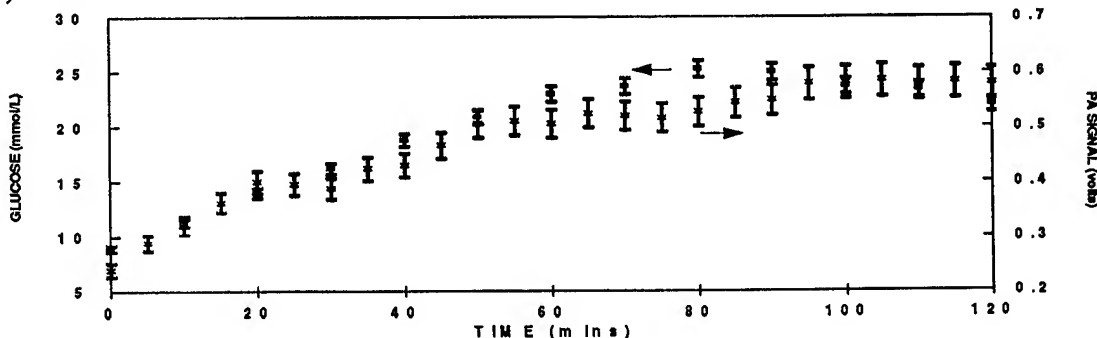


Figure 2. OGTT's performed on (a) normal subject, (b) Type 1 diabetic and (c) Type 2 diabetic. In each case the photoacoustic response has been overlaid onto the results from a standard glucose oxidase method on a venous blood sample.

Figure 2 shows the results for one subject from each class. Diabetic subjects omitted their morning insulin. In the case of Type 1's insulin was injected during the monitoring period, for the case shown this was at 20, 80 and 145 minutes. The photoacoustic response has been overlaid on the clinical (venous blood) results for the figures. In all cases the photoacoustic response closely matched the true blood glucose result. The range of amplitudes of the photoacoustic response varied from subject to subject. In order to predict a correlation between the photoacoustic response and the true blood glucose response, a linear regression was applied between the blood glucose concentration and the photoacoustic response for each subject. From these regression equations a correlation of  $r^2 = 0.959$  was obtained between the paired points of equivalent blood glucose concentration with true blood glucose. Figure 3 shows the percentage difference of the equivalent blood glucose concentration from the photoacoustic response to the true blood glucose concentration. This shows an appreciable number of the points lie within a  $\pm 10\%$  band, the approximate error value of conventional test strip technology.

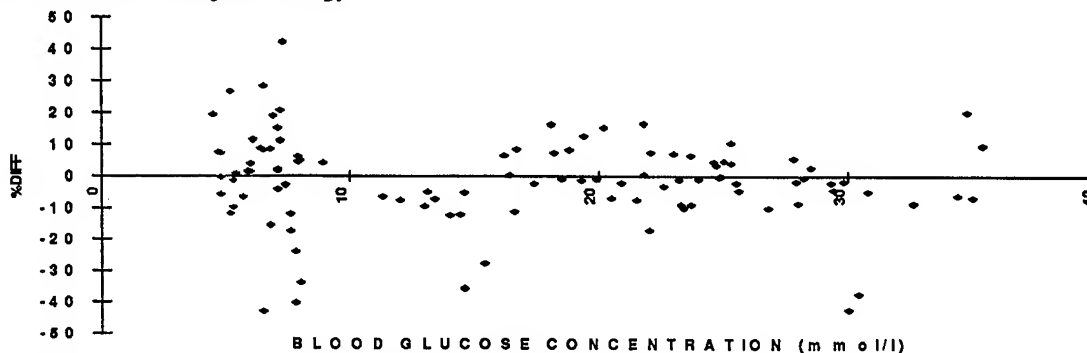


Figure 3. The percentage difference between the equivalent blood glucose concentration calculated from the photoacoustic response and the blood glucose concentration measured from the venous blood samples

These results have shown that the photoacoustic response of tissue may be used to determine blood glucose. Much work remains in evaluating the subject to subject variability, quantitating the signal and testing with a normal diet in order to ensure that other analytes do not influence the response.

#### References

1. Robinson, M.R., Eaton, R.P., Haaland, D.M., Koepp, G.W., Thomas, E.V., Stallard, B.R., and Robinson, P.L. "Noninvasive glucose monitoring in diabetic patients: a preliminary evaluation," *Clin Chem.* 38, 1618-1622, 1992.
2. Marbach R., Koschinsky, T.H., Gries, F.A., and Heise, F.A., "Noninvasive blood glucose assay by near-infrared spectroscopy of the inner human lip," *Appl. Spectro.* 47, 875-881, 1993.
3. Quan, K.M., Christison, G.B., and MacKenzie, H.A., "Glucose determination by a pulsed photoacoustic technique using a gelatin based phantom," *Phys. Med. Biol.* 38, 1911-1922, 1993.
4. Maier, J.S., Walker, S.A., Fantini, S., Franceschini, M.A., and Gratton, E., "Possible correlation between blood glucose concentration and the reduced scattering coefficient of tissues in the near infrared," *Opt. Lett.* 19, 2062-2064, 1994.
5. Cote, G.I., Fox, M.D., and Northrop, R.B., "Noninvasive optical parametric glucose sensing using a true phase measurement technique," *IEEE Trans. Biomed. Eng.* 39, 752-756 1992.
6. Diasensor 1000, Diasense, U.K. Ltd (an affiliate of Biocontrol Technology, Inc.) London, U.K.
7. Futrex 9100, Futrex Inc., Gaithersburg MD.
8. Wyatt, J.S., Cope, M., Delpy, D.T., Edwards, A.D., Wray, S.C., and Reynolds, EOR., "Quantification of cerebral oxygenation and hemodynamics in sick newborn infants by near infrared spectrophotometry," *Lancet* ii, 1063-1066 1986.
9. Heise, H.M., Marbach, R., Janatsch, G., and Kruse-Jarres, J.D., "Multivariate determination of glucose in whole blood by attenuated total reflection infrared spectroscopy," *Anal. Chem.* 61, 2009-2015 1989.
10. Tam, A.C., "Applications of photoacoustic sensing techniques," *Rev. Mod. Phys.* 58, 381-431 1986.
11. Duncan, A., Hannigan, J., Freeborn, S.S., Rae, P.W.H., McIver, B., Greig, F., Johnston, E., Binnie, D.T., and MacKenzie, H.A., "A portable non-invasive blood glucose monitor," *Transducers'95-Euroensors IX*, Sweden, June 1995.

**In vivo Measuring of Blood Flow Changes using Diffusing Wave Correlation Techniques**I.V. Meglinsky<sup>\*,†</sup>, D.A. Boas<sup>\*,†</sup>, A.G. Yodh<sup>†</sup> and B.Chance<sup>\*</sup>

<sup>\*</sup> Department of Biochemistry and Biophysics, <sup>†</sup> Department of Physics,  
University of Pennsylvania, Philadelphia, PA 19104-6089;  
Phone: (215)-898-4342, (215)-898-6354, Fax: (215)-898-1806,  
E-mail: igor@sol1.lrsrn.upenn.edu

<sup>†</sup> Department of Physics, Saratov State University, Saratov 410071, Russia

**Introduction:** In recent years there has been a growing interest in the study of flow phenomena in complex fluids using photon speckle correlation techniques<sup>1,2</sup>. The best-known applications of these studies in biology and medicine are the non-invasive measurements of blood flow in large and small blood vessels, as well as the blood volume changes in capillary loops of muscles and other biological tissues<sup>1</sup>. In this contribution, methods for probing the spatially varying dynamics of blood flow in heterogeneous turbid media with diffusing light are applied. The method utilizes the Doppler broadening of light that arises in a multiply scattering dynamical media, but the method is also responsive to  $\mu_a$ ,  $\mu_s$ ' changes. Specifically, we use correlation techniques to monitor blood flow in the arm during cuff ischemia. Our measurements clearly show blood flow changes with cuff pressures, including the hyperemic overshoot after cuff release. In this paper we describe experiments, and discuss the results with some theoretical explanation and correlation with physiological phenomena.

**Background:** The possibility of using laser Doppler flowmetry to measure blood flow perfusion has been described by different authors (see for example [1] and references therein). The motions are probed by monitoring the time dependence of the fluctuations of the scattered light. These fluctuations are usually characterized by the normalized single scattering temporal autocorrelation function<sup>1,2</sup>,

$$g_1(\tau) = \frac{\langle E(0)E^*(\tau) \rangle}{\langle |E(0)|^2 \rangle} \quad (1)$$

where  $E$  is the electric field of the scattering light, collected by the detector and  $\tau$  is the delay time. Experimentally, one typically measures the normalized temporal intensity correlation function which is related to the correlation function  $\langle I(0)I(\tau) \rangle / \langle I^2 \rangle$  by the Siegert relation<sup>3</sup>,

$$\frac{\langle I(0)I(\tau) \rangle}{\langle I^2 \rangle} = 1 + \beta |g_1(\tau)|^2 = g_2(\tau), \quad (2)$$

where  $\beta$  is determined primarily by the collection optics  $0 \leq \beta \leq 1$ <sup>4</sup>.

Recently, it has been shown that the temporal field correlation function in a heterogeneous medium is accurately modeled by the correlation diffusion equation<sup>2</sup>:

$$(D_\gamma \nabla^2 - \nu \mu_a - \nu \mu_s' \langle v^2 \rangle \kappa_0^2 \tau^2 / 3) G_1(r, \tau) = -\nu S(r), \quad (3)$$

where  $\kappa_0$  is the wavenumber of the photon in medium,  $\nu$  is the speed of light in the medium,  $\mu_a$  is the absorption coefficient,  $\mu_s'$  is the scattering coefficient,  $\langle v^2 \rangle$  is the second moment of the particle speed distribution,  $G_1(r, \tau)$  is the unnormalized temporal correlation function which is a function of position  $r$  and correlation time  $\tau$ ,  $S(r)$  is the source distribution, and  $D_\gamma = \frac{\nu}{3\mu_s'}$  is the photon diffusion coefficient. This model will be used to interpret our results.

**Experimental method:** Light with a wavelength of 800 nm is generated by a Ti:Sapphire laser, and is coupled into a fiber optic cable then delivered to our sample (human arm). The silica multimode fiber, has a diameter 200  $\mu\text{m}$  and numerical aperture  $0.16 \pm 0.02$ . Remission of the light is collected from the sample by a single-mode fiber in order to observe the intensity fluctuation of a single speckle (mode), the diameter of the single-mode fiber is 3  $\mu\text{m}$  (see Fig.1.). Single-mode fibers provide good receiver optics for dynamic light-scattering measurements<sup>5</sup>. The pair of multimode and single-mode fibers is effective for achieving high output radiation from the illuminating fiber, high signal-to-noise ratio, and low modal noise from the vibration of the fiber. The light collected by the single-mode fiber is delivered to a photon-counting photo-multiplier tube, after that to commercial digital autocorrelator (Model BI-9000AT, Brookhaven Instruments Corporation, Holtsville, NY, USA)

which calculates the temporal intensity autocorrelation function.

**Results and discussion:** In Figure 2 and 3 we present some results using the arrangement in Fig.1. Fig.2a represents a autocorrelation function of the backscattering light from arm. As shown in Fig.1, we are using medical aneroid sphygmomanometer for the control and variation of blood pressure in the vessels inside arm. We can see that the slope of the autocorrelation function is different for different blood pressures. The changes in the slope arise from blood flow changes (see Fig.2). In Fig.2b we plot  $\ln g_1(\tau)$  and in Fig.3 the slope of the autocorrelation function as a function of measurement time is plotted. The results represent a physiological behavior of vascular system. Each measurement of autocorrelation function was repeated for 3 minutes. The magnitude of arm cuff pressure is plotted in Fig.3 around each point (in Torr). The results agree with physiological behavior of blood flow in the cardiovascular system. Furthermore, the suggested method of observing of blood flow changes gives a possibility for observation of a hyperemic phenomenon which is manifest by a higher flow after release of cuff (see Fig.3, point number 15). Concomitant blood concentration changes are also recorded at 800 nm especially on releasing the cuff. Simultaneous recording with an tissue absorption spectrophotometer ("Run-Men") is essential to deconvolute the flow and concentration signals.

**Summary:** This work reviews the experimental methods for *in vivo* measurements of blood flow in living tissue. The speckle fluctuation has a dependence on blood flow, that is present from the results of our experiments (Fig.2a, b). This technique is sensitive for observation of blood volume changes in living tissue. Furthermore, we have demonstrated that the changing slope of the autocorrelation function is directly connected to the changes of cardiovascular system state, see Fig.3. Our results agree with physiological explanation of blood volume changes in muscles with different pressure on the arm (see Fig.3), that shows validity of results and adequate using this method and gives a good reason for extension of this technique.

**Conclusions and remarks:** The dynamic region behavior of speckles depends on various factors within the living objects, such as the spatial structures of tissues and vessels, and absorption and diffusion characteristics. These factors may be quantified by using the correlation diffusion equation to interpret the experimental results. We are investigating this possibility. The detailed observation and experimental analysis of temporal fluctuations are effective for the development of their potential applicability. We anticipate that dynamic temporal fluctuations phenomena will be useful in future for studies of various kinds of living objects and will be applied for the measurement of these objects' physiological behavior. This method may be quite useful for non-invasive measurement of blood flow in living tissue, determination of shear flow rate, effective diameter of scatterers (red blood cells) and as follows gives useful information for physiological, medical and biological fields.

#### References

1. A.P.Shepherd, P.A.Oberg, eds., "Lasers Doppler Blood Flowmetry", Kluwer Academic Publishers, 1990.
2. D.A.Boas, L.E.Cambell, and A.G.Yodh, "Scattering and Imaging with Diffusing Temporal Field Correlations", *Phys. Rev. Lett.*, vol.75, No.9, pp.1855-1858, 1995; D.A.Boas, L.E.Cambell, and A.G.Yodh, "Fluctuation Imaging", *Proc. SPIE*, vol.2389, part 1, pp.220-227, 1995.
3. B.J.Ackerson, R.L.Dougherty, N.M.Regugui, and U.Nobbman, "Correlation Transfer: Application of Radiative Transfer Solution Methods to Photon Correlation Problems", *J.Thermophys and Heat Transfer*, vol.6, No.4, pp.577-588, 1992.
4. E.Jakerman, C.J.Oliver and E.R.Pike, "Clipped correlation of intensity fluctuations digital autocorrelation of photon-counting fluctuations", *J.Phys A: Gen.Phys.*, vol.4, pp.827-835, 1971.
5. J.Ricka, "Dynamic Light Scattering with Single-mode and Multimode Receivers", *Appl. Optics*, vol.32, No.15, pp.2860-2874, 1993.

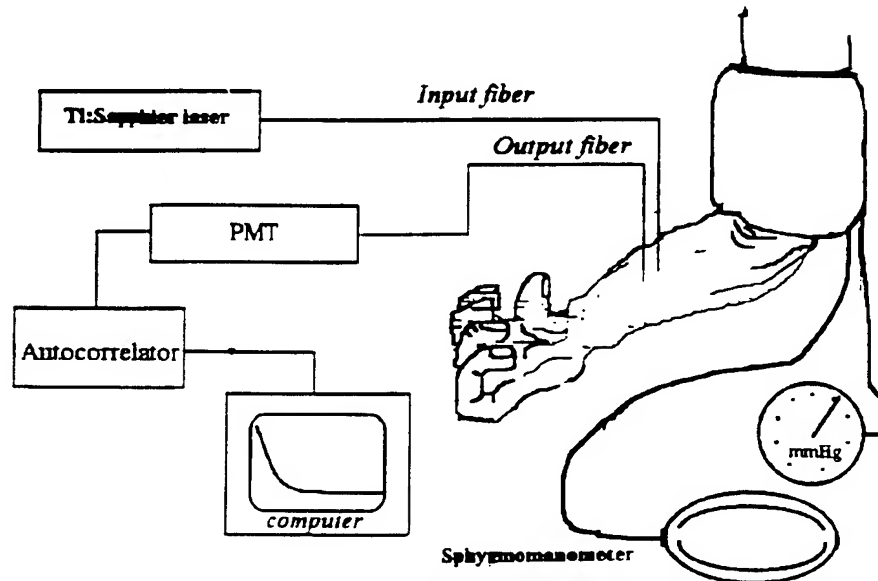


Fig.1 Experimental setup. The 800 nm line from Ti:Sapphire laser (operated at 0.1 W) is coupled into a multi-mode fiber optic cable and delivered to the surface of arm. Laser beam incident on the skin from multimode fiber (source), diameter of which is 200  $\mu\text{m}$ . Remission of the light is collected from the sample by a single-mode fiber (detector) in order to observe the intensity fluctuation of a single speckle (mode), diameter of the single-fiber is 3  $\mu\text{m}$ . A single-mode fiber collects light at a known position and delivers it to a photo-multiplier tube (PMT), whose output enters a digital autocorrelator to obtain the temporal intensity correlation function. The temporal intensity correlation function is related to the temporal field correlation function by Siegert relation. The fiber can be moved to any position on the sample surface. Source-detector separation is 6 mm. Using sphygmomanometer we can control and change of blood flow.

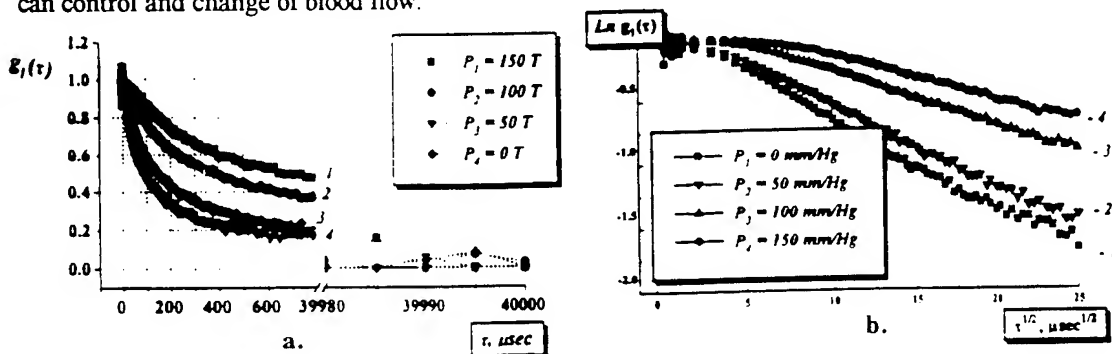


Fig.2. (a) - typical normalized autocorrelation function  $g_1(\tau)$  depending on arm suppression changes; (b) -  $\ln g_1(\tau)$  with arm suppression changes; slope of this function characterizes scatterers motion.

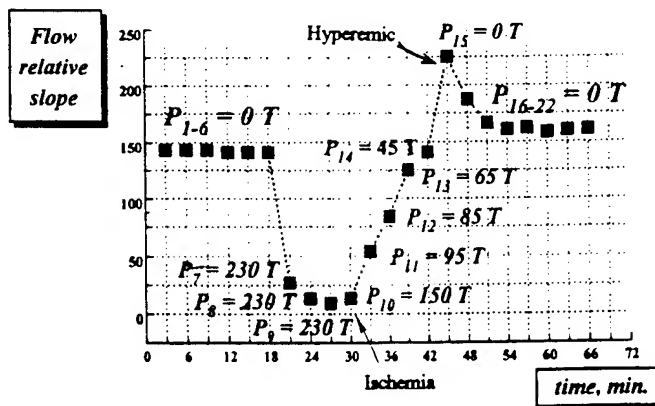


Fig.3. Changes of flow relative slope of autocorrelation function with the arm suppression changes in real time of experiment. Each measurement duration is 3 minutes.



Wednesday, March 20, 1996

# Blood Constituent Monitoring II

**BWB** 11:00 am-1:00 pm  
Windsor Ballroom

David Benaron, *Presider*  
*Stanford University*

## Transurethral Reflectometry using a Sliding Fiber Device for Noninvasive Measurements of *in vivo* Optical Properties of Prostate

Beop-Min Kim<sup>1,2</sup>, Steven L. Jacques<sup>1</sup>, Sohi Rastegar<sup>2</sup>, Martin Ostermyer<sup>1</sup>, Massoud Motamedi<sup>3</sup>

<sup>1</sup>Laser Biology Research Laboratory, Box 17, The University of Texas M.D. Anderson Cancer Center, 1515 Holcombe Blvd., Houston, TX 77030

<sup>2</sup>Bioengineering Program, Texas A&M University, College Station, TX 77843

<sup>3</sup>Biomedical Lasers and Spectroscopy Laboratory, Jennie Sealy Hospital Rt. D56, The University of Texas Medical Branch, Galveston, TX 77555

### INTRODUCTION

Knowledge of tissue optical properties (absorption coefficient  $\mu_a$  and reduced scattering coefficient  $\mu_s'$ ) is essential for all kinds of laser applications in medicine. However, it is quite difficult to obtain the *in vivo* optical properties for internal organs such as prostate in a noninvasive way. A new device composed of two parallel optical fibers was designed to detect spatially resolved diffuse reflectance and hence to noninvasively measure *in vivo* optical properties. It was tested for canine prostate at a wavelength of 633 nm.

### METHODS AND MATERIALS

**Reflectometry** The fluence rate of a tissue irradiated by an infinitely narrow beam can be modeled by a pair of real and imaginary isotropic sources near the surface boundary [1-2]. In this model, the fluence rate at the extrapolated boundary reduces to zero. Based on this model, the Green's function for the diffuse reflectance becomes:

$$R(r) = \frac{1}{4\pi} \left[ z_0 \left( \mu_{\text{eff}} + \frac{1}{r_1} \right) \frac{e^{-\mu_{\text{eff}} r_1}}{r_1^2} + (z_0 + 2z_b) \left( \mu_{\text{eff}} + \frac{1}{r_2} \right) \frac{e^{-\mu_{\text{eff}} r_2}}{r_2^2} \right] \quad (1)$$

where  $z_0$  is the depth of the real source from the tissue surface,  $z_b$  is the position of extrapolated boundary where the fluence rate reduces to zero,  $\mu_{\text{eff}}$  is the effective attenuation coefficient, and  $r_1$  and  $r_2$  are the distances from the real and imaginary sources respectively. For the inverse problem, the diffuse reflectance is obtained using CCD camera or optical fibers. However, additional information is required to deduce both unknowns ( $\mu_a$  and  $\mu_s'$ ). Total reflectance ( $R_d$ ) is expressed as the integration of the diffuse reflectance over the entire surface as shown below.

$$R_d = \int_0^\infty R(r) 2\pi r dr \quad (2)$$

It is known that  $R_d$  depends upon the reduced scattering/absorption ratio ( $N'$ ) and the internal reflection parameter  $A$ . If the internal reflection parameter  $A$  is known (matched or mismatched boundary), we can determine both optical properties by integrating the diffuse reflectance as shown in equation (2) and by fitting the profile to equation (1). Usually, the diffuse reflectance is measured in arbitrary units. Therefore, it is necessary to estimate the scaling factor that is required to obtain absolute units.

$$R_d = \int_0^\infty k M(r) 2\pi r dr \quad (3)$$

where  $M(r)$  is the diffuse reflectance profile in arbitrary units (actual measurement) and  $k$  is the scaling factor. Once the scaling factor is determined, the spatially resolved diffuse profile in arbitrary units can be used to deduce both optical properties.

**Structure Of Sliding Fiber Device** The device is an optical fiber which slides within a cylindrical housing (stainless steel) with a series of collection windows along its length. The tip of the fiber has a short section of diffusive medium (titanium dioxide in epoxy) which serves as an isotropic collector coupling light into the optical fiber for detection. Sliding the fiber within the housing passes the diffusive collection tip past each of the collection windows. A second fiber which is glued on top of the stainless steel housing serves as the light source. Hence the device measures fluence rate interstitially or reflectance topically as a function of distance from the source. The collection light is detected by a PMT and the signal routed to a digital oscilloscope for data acquisition.

## RESULTS

**Studies in Phantom and Calibration** Tissue simulating phantoms were made by mixing water with polystyrene sphere (PS, a scatterer) and trypan blue (TB, an absorber). Four different mixtures were used for device calibration and the optical properties for the mixtures were measured using video reflectometry, a method that has been tested rigorously. Table 1 shows the different combinations of absorber and scatterer per 500 ml of water and their optical properties.

Table 1

	PS	TB	$\mu_a$ (cm <sup>-1</sup> )	$\mu_s'$ (cm <sup>-1</sup> )
Mixture 1	3 ml	0.1 ml	0.05593	1.21
Mixture 2	3 ml	0.2 ml	0.11276	1.247
Mixture 3	6 ml	0.1 ml	0.0578	2.59
Mixture 4	6 ml	0.2 ml	0.1179	2.751

The sliding fiber device was placed on the surface of each phantom. Then, while slowly moving the detection fiber along the stainless steel housing, the oscilloscope recorded the detected signal. An example of the detected raw signal is shown in Fig. 1. The peak to peak values were fitted to equation (1) using its known optical properties and the scaling factor was estimated as shown in Fig. 2. The calculated scaling factors are 1122.3, 915.76, 965.59, and 845.65 for mixtures 1, 2, 3, and 4 respectively. The average value was 962.33 and this value was used to deduce the optical properties of the canine prostate.

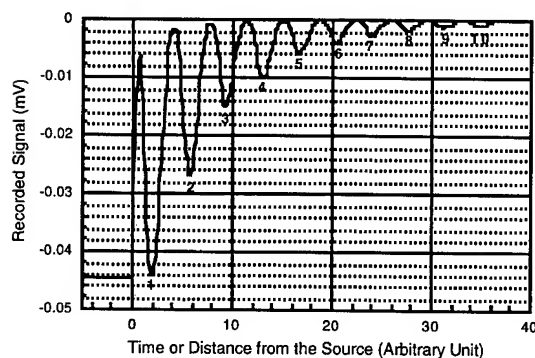


Fig. 1. Raw signal recorded in oscilloscope

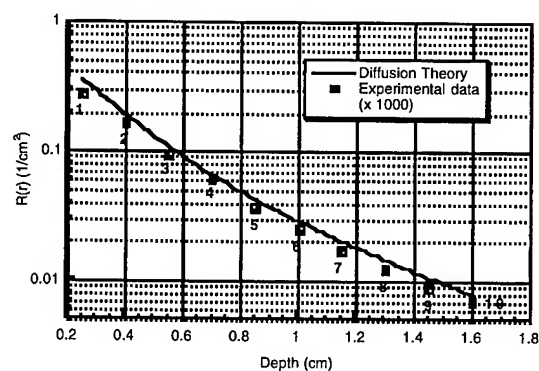


Fig. 2. Experimental data and a theoretical diffuse reflectance curve (diffusion theory) based on true optical properties. By curve fitting, the scaling factor was estimated ( $k \approx 845.65$ , Mixture 4)

**Animal Experiment** The new device was inserted through urethra of the canine prostate and the signal was read in the same way as in the phantom work. Both optical properties were deduced using 633 nm red light. The optical properties of the prostate are shown in table 2 and the diffuse reflectance profile is shown in Fig. 3.

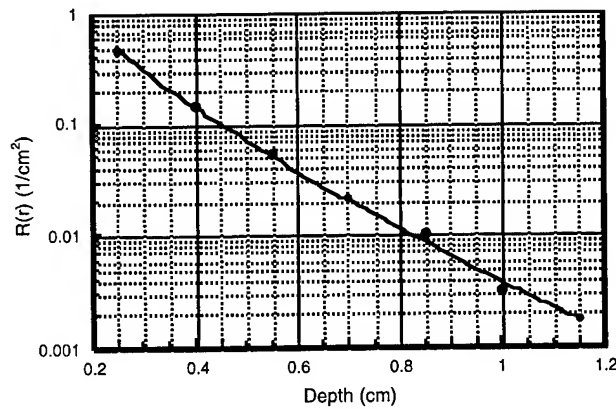


Table 2

at 633 nm	$\mu_a$ (cm <sup>-1</sup> )	$\mu_s'$ (cm <sup>-1</sup> )
Canine prostate	0.35057	10.705

Fig. 3. Diffuse reflectance data for canine prostate at 630 nm and a curve fitting

## DISCUSSION

Optical property measurement using a CCD camera and topical diffuse reflectance profile has been shown to be accurate and effective. The only shortcoming of this method is that it requires a separate measurement of total diffuse reflectance which is difficult to obtain for human internal organs. Our sliding fiber device can be used for internal organs such as the prostate and the rectum in a very noninvasive way. For the first time, the *in vivo* optical properties of the canine prostate have been measured using this device. To make this new device more applicable for general purpose, a spectrum of diffuse reflectance over a range of wavelengths needs to be estimated. Currently, it is applicable for only one particular wavelength. An OMA system will be used for full spectrum investigation in the near future.

## REFERENCE

1. T. J. Farrell, M. S. Patterson, and B. Wilson, "A diffusion theory model of spatially resolved, steady state diffuse reflectance for the noninvasive determination of tissue optical properties *in vivo*," *Med. Phy.*, vol. 19, pp. 879-888, 1992
2. R. C. Haskell, L. O. Svaasand, T-T Tsay, T-C Feng, M. S. McAdams, and B. J. Tromberg, "Boundary conditions for the diffusion equation in radiative transfer," *J. Opt. Soc. Am. A*, vol. 11, no. 10, pp. 2727-2741, 1994

# Frequency-Domain Photon Migration (FDPM) Measurements of Cell and Tissue Optical Properties for Biomedical Diagnostics

Olivier Coquoz<sup>1</sup>, Lars O. Svaasand<sup>2</sup>, Eric Anderson<sup>1</sup>, Richard C. Haskell<sup>3</sup>, Bruce J. Tromberg<sup>1,2\*</sup>

1. Beckman Laser Institute and Medical Clinic, University of California, 1002 Health Sciences Rd. East, Irvine, CA 92717-1475

2. Department of Physiology and Biophysics, UC Irvine

3. University of Trondheim, 7000 Trondheim, Norway

2. Department of Physics, Harvey Mudd College, Claremont, CA 91711

\*Corresponding author: Phone: (714) 824-8705; FAX: 714 824 8413;

email: tromberg@nova.bli.uci.edu

## Introduction

Rapid, accurate determination of tissue optical properties is essential to nearly all aspects of Photomedicine, from predicting photon dosimetry during therapeutic procedures, to forming optical images of tissue physiology. Measurements depend on the availability of suitable instrumentation and models for analyzing the complex information content of light that is backscattered, transmitted, or re-emitted from tissues.

Frequency-domain photon migration (FDPM) is a non-invasive technique that can be used to quantitatively characterize tissue optical properties.<sup>1-6</sup> We have constructed a portable, high-bandwidth (0.3 MHz - 1 GHz), multi-wavelength FDPM system which distinguishes between tissue absorption, scattering, and fluorescence processes in a single measurement.<sup>2</sup> FDPM challenges include assigning optical properties to discrete tissue volumes and correlating these parameters with useful physiological information during diagnostic and therapeutic procedures.<sup>3,4</sup>

In FDPM, the intensity of light incident on an optically turbid sample is modulated at high frequencies, and the diffusely reflected or transmitted signal is measured with a phase-sensitive detector. Amplitude-modulated light propagates through multiple-scattering media with a coherent front, forming photon density waves (PDW)<sup>5,6</sup>. Wave dispersion is highly dependent on the optical properties of the medium. Thus, measurements of the frequency- or distance-dependent phase and amplitude of photon density waves can be used to derive scattering and absorption coefficients.

There are basically two ways to perform FDPM measurements, either varying the source-detector distance while modulating light at a fixed frequency, or keeping the source and the detector at fixed positions and sweeping over a range of frequencies.<sup>3</sup> Most FDPM techniques assume either infinite or a semi-infinite sample geometries. We have recently developed a cuvette which can be used to characterize photon density wave behavior in confined geometries. Our objective is to extend FDPM applications to recording optical properties of tissue biopsies, cell suspensions and biochemical assays. Highly reflecting materials are used to build the cuvette in order to take advantage of multiple wall interactions. In this way, it is possible to increase the optical pathlength and raise a small phase-shift or demodulation signal to detectable levels in extremely small volumes (typically 0.45 mL).

## Materials and Methods

### Theory

The diffusion approximation can be used to obtain exact analytic expressions for the propagation of photon density waves in various geometries. The optical fluence satisfies a diffusion equation of the following form:

$$\nabla^2 \phi - \frac{3}{c^2 \tau_l \tau_{tr}} \phi - \left(1 + \frac{\tau_{tr}}{\tau_l}\right) \frac{3}{c^2 \tau_{tr}} \frac{\partial \phi}{\partial t} = -\frac{3}{c \tau_{tr}} q \quad (1)$$

where  $q$  is the diffuse photon source density and  $c$  is the velocity of light in the medium. The parameters  $\tau_l$  and  $\tau_{tr}$  are, respectively, the loss relaxation time and the transport relaxation time. They are related to the absorption coefficient  $\mu_a$ , the reduced scattering coefficient  $\mu_s'$  and the diffusion constant  $\zeta$  by the following expressions:

$$\tau_l = \frac{1}{\mu_a c}; \quad \tau_{tr} = \frac{1}{(\mu_a + \mu_s') c}; \quad \zeta = \frac{c \tau_{tr}}{3} \quad (2)$$

When the scattering medium is assumed to be of infinite extent, the general solution of (1) for the fluence rate is expressed in the form<sup>5</sup>:

$$\phi \propto e^{-kr} \cdot e^{i\omega t} \quad (3)$$

where  $r$  is the distance from the source,  $\omega$  is the source angular modulation frequency, and  $k$ , the complex wavenumber, is given by:

$$k = k_{real} + ik_{imag} = \frac{\sqrt{3}}{c} \sqrt{\frac{1}{\tau_l \tau_{tr}} + \left(1 + \frac{\tau_{tr}}{\tau_l}\right) \frac{i\omega}{\tau_{tr}}}; \quad k_{real} = \sqrt{\frac{3}{2}} \frac{1}{c \sqrt{\tau_l \tau_{tr}}} \sqrt{\sqrt{1 + (\tau_l \omega)^2} + 1}$$

$$k_{imag} = \sqrt{\frac{3}{2}} \frac{1}{c \sqrt{\tau_l \tau_{tr}}} \sqrt{\sqrt{1 + (\tau_l \omega)^2} - 1} \quad (4)$$

These expressions provide all parameters defining photon density wave propagation, namely the phase velocity  $v_{ph} = \omega/k_{imag}$  and the two parameters coming out of the measurements, i.e. the phase  $\phi = k_{imag}r$  and, the ac amplitude,  $m$ , given by  $\ln(m) = -k_{real}r$ .

#### Sample in a spherical cuvette

The geometry considered here consists of a spherical scattering medium (the actual sample) confined in a metallic container. The refractive index of metals contains an imaginary part which accounts for partial light absorption within the first atomic layers. This loss of light can be described, to a first approximation, in terms of a radiative-type boundary between the sample and metal. Thus, the absorption of photons in the metallic wall is equivalent to the loss of photons at an air-tissue boundary. The source is set at the center of the sphere and the fluence rate in the scattering medium is defined by:

$$\phi_1 = \frac{A_1}{r} e^{-k_1 r} + \frac{B_1}{r} e^{k_1 r}, \quad r < a \quad (5)$$

where  $\phi_1$  and  $k_1$  are, respectively, the fluence rate and wavenumber in the sample. The coefficients  $A_1$  and  $B_1$  are determined by the boundary and initial conditions. The boundary conditions require the continuity of fluence rate and flux at the surface of the sphere (i.e. at  $r=a$ , where  $a$  is the sphere radius), and the total flux at the origin equal to the power of the source:

$$P = \lim_{r \rightarrow 0} 4\pi r^2 j_1 \quad (6)$$

The radiative boundary between conditions at the interface between a diffusive and a non-diffusive medium can be approximated as:

$$\phi_1|_{r=a} = \Omega j_1|_{r=a}; \quad \text{where } \Omega \text{ is defined as: } \Omega = 2 \frac{1 + R_{eff}}{1 - R_{eff}} \quad (7)$$

and, for a radiative boundary,  $R_{eff}$  is the effective reflection coefficient. In our case, we set  $R_{eff}$  = the diffuse reflectance of the metal (i.e. aluminum), and make further adjustments to take into account losses due to holes in the cuvette wall (source, detection and supply channels). If the metal were perfectly reflective,  $R_{eff} = 1$ , and  $\Omega \rightarrow \infty$ . In that ideal case,  $j = 0$  at the cuvette boundary, as expected.

Using equations (5)-(7), we can derive the distance- and frequency-dependent behavior of both the phase and ac amplitude, the two measured FDPM parameters. The expression for fluence rate is:

$$\phi_1 = \frac{P \left\{ (a - \Omega \zeta_1) \sinh(k_1(a-r)) + \Omega \zeta_1 k_1 a \cosh(k_1(a-r)) \right\}}{4\pi \zeta_1 r \left\{ (a - \Omega \zeta_1) \sinh(k_1 a) + \Omega \zeta_1 k_1 a \cosh(k_1 a) \right\}} \quad (8)$$

To obtain the exact optical properties, phase and amplitude data is fit to analytical expressions obtained above.

#### Experiment

A portable, high-bandwidth instrument is used for all FDPM tissue and cuvette measurements.<sup>1</sup> It is based on the use of intensity-modulated laser diodes as sources and an avalanche photodiode detector. A network analyzer (Hewlett Packard model 8753C) is used to produce RF swept from 300 kHz to 1 GHz superimposed on the direct current of the laser diode (e.g. SDL, Inc. model 7420). Several different wavelengths are available, ranging from 670 nm to 950 nm, and each diode is addressed serially using an RF switch. In the case of cuvette measurements, the laser output is directly coupled onto a 200  $\mu$ m-diameter fiber terminated with a diffusing micro-sphere to ensure isotropic illumination within the sample (PDT systems, Inc. model 2808-A03). The optical power coupled into the sample averages approximately 30 mW. The tip of the source fiber is positioned at the center of the spherical cuvette. An avalanche photodiode (APD, Hamamatsu, model C5658) biased at 12 V is used to detect the diffuse signal through a thin glass window. A 100- $\mu$ m-diameter gradient-index fiber is used for tissue measurements with the APD in direct surface contact at a fixed source-detector separation. Measurement time depends on the precision required and the number of sweeps performed. Phase and amplitude data are typically acquired for the entire 300 kHz to 1 GHz region in a few seconds. The network analyzer is driven by a computer (MacIntosh Quadra) and virtual instrument software (LabView, National Instruments).

Experiments were performed on well-characterized phantoms to confirm the ability of our method to derive the optical properties of turbid 0.45 mL samples. In this paper we describe a series of cell suspension studies designed to address the physiological importance of optical property changes in cells and tissues under different environmental conditions. FDPM measurements were recorded at a concentration of approximately  $10^8$  cells/ml (lymphocytes (P388 D1 mouse tumour-derived macrophages) and human breast carcinoma cells (MCF7)). Although this is about one order

of magnitude smaller than typical tissue cell densities, it was used in order to avoid experimental problems such as cell aggregation, necrosis, or masking effects characteristic of high-density suspensions. Inert polystyrene microspheres were added to bring the scattering properties to a level ensuring the diffusion regime. Cells were treated with Trypsin-EDTA before centrifugation to prevent excessive aggregation and resuspended in small volumes of 1X PBS without calcium salts at 37°C.

## Results and Discussion

Fig. 3 shows phase measurements in comparison with analytical model functions for polystyrene microsphere - MCF7 human breast cancer cell suspensions under different environmental conditions. MCF7 cell size was measured to be 21.8  $\mu\text{m}$  and 15.2  $\mu\text{m}$  under normal and 2% saline conditions respectively. Cell density is  $0.7 \cdot 10^8/\text{ml}$ .

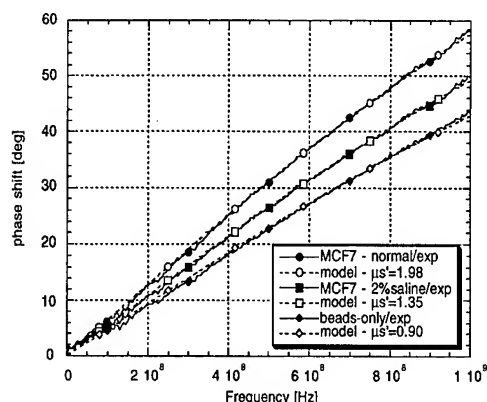


Fig. 3. Phase vs. freq. for MCF7 human breast cancer cells. transformations will be examined.

Reduced scattering cross-sections,  $\sigma_s'$  (defined as  $\sigma_s' = \sigma_s(1-g)$ , where  $\sigma_s$  is the scattering cross-section and  $g$  the anisotropy factor) obtained experimentally for lymphocytes and MCF-7 cells are compared to Mie theory predictions in Table 1. Cell size was measured by flow cytometry and an average refractive index (1.395) was selected based upon the range of values found in the literature. Cells are assumed to be spherical and scattering events independent.

These data show good agreement between FDPM measurements and Mie theory. However, Mie calculations demonstrate that small variations in the refractive index ratio (cells/matrix) can lead to dramatic changes in the reduced scattering cross-section. In view of this, the sensitivity of cells to a variety of different environmental conditions (osmotic and non-osmotic effects) will be discussed. Applications to monitoring tissue physiology and identifying malignant

Table 1: Measured reduced scattering cross-sections for different cell lines compared to Mie predictions.

Cell line	Wavelength [nm]	Cell size [ $\mu\text{m}$ ]	Mie $\sigma_s'$ [ $\times 10^{-8} \text{cm}^2$ ]	Exper. $\sigma_s'$ [ $\times 10^{-8} \text{cm}^2$ ]
Lymphocyte	674	12	3.33	3.08
MCF7	674	19.2	10.98	6.13

## Acknowledgements

This work was supported by the Whitaker Foundation (WF16493), the National Institutes of Health (GM50958), Beckman Instruments Inc., and the Swiss National Science Foundation (O.C.). In addition, we acknowledge Beckman Laser Institute programmatic support from the Office of Naval Research (N00014-91-0134), the Department of Energy (DE-FG-3-91-ER61227), and the National Institutes of Health (SP41RR01192).

1. B.J. Tromberg, L.O. Svaasand, S. J. Madsen, R.C. Haskell, C. Chapman,, "Frequency-Domain Photon Migration Spectroscopy in Turbid Media," in *Advances in Optical Imaging and Photon Migration*, B. Chance and R. Alfano, eds., Proceedings of The Optical Society of America, **21**, 93-95, (1994).

2. S. J. Madsen, R. C. Haskell and B. J. Tromberg, "A portable, high-bandwidth frequency-domain photon migration instrument for tissue spectroscopy", *Opt. Lett.* **19**, 1934-1936, (1994).

3. B.J. Tromberg, R.C. Haskell, S.J. Madsen, L.O. Svaasand, *Characterization of Tissue Optical Properties Using Photon Density Waves*, Comments on Molecular and Cellular Biophysics, **8**, 359-386 (1995).

4. S. J. Madsen, P. Wyss, L. O. Svaasand, R. C. Haskell, Y. Tadir and B. J. Tromberg, "Determination of the optical properties of human uterus using frequency-domain photon migration and steady-state techniques", *Phys. Med. Biol.*, **39**, 1191-1202, (1994).

5. B. J. Tromberg, L. O. Svaasand, T.-T. Tsay and R. C. Haskell, "Properties of photon density waves in multiple-scattering media", *Appl. Opt.*, **32**, 607-616, (1993).

6. J. B. Fishkin and E. Gratton, "Propagation of photon-density waves in strongly scattering media containing an absorbing semi-infinite plane bounded by a straight edge", *J. Opt. Soc. Am. A*, **10**, 127-140, (1993).

# The Frequency Domain Multi-Distance Method in the Presence of Curved Boundaries

Albert Cerussi, John Maier, Sergio Fantini, Maria Angela Franceschini, and Enrico Gratton

University of Illinois at Urbana Champaign  
Department of Physics  
Laboratory for Fluorescence Dynamics  
1110 West Green Street, Urbana, IL 61801-3080

## **Introduction**

Diffusion theory is widely used to describe near-infrared light propagation in highly scattering media such as biological tissues. The application of boundary conditions to the diffusion equation presents a challenging problem. The very presence of any boundary violates one of the approximations of diffusion theory, namely that it is valid at positions that are many scattering events removed from non-isotropic disturbances.<sup>1</sup> However, in the real world of non-invasive tissue diagnostic monitoring, boundaries are unavoidable. If photon migration methods are to play a role in the development of clinical *in vivo* spectroscopic and imaging instruments for the investigation of tissues, then the effects of boundaries must be included. The infinite medium is hardly an adequate geometry for non-invasive applications. The semi-infinite geometry is more practical, but cylindrical and spherical geometry more closely resemble human limbs and heads. We have investigated the effects of cylindrical boundaries upon our photon migration measurements.

## **Purpose of Study**

Given the complexity of the solutions for curved boundary conditions<sup>2</sup>, we would first like to know how existing semi-infinite models perform in the investigation of curved surfaces. The frequency-domain multi-distance protocol with a single modulation frequency as presented by Fantini *et al.* offers an analytic solution in both infinite<sup>3</sup> and semi-infinite<sup>4</sup> geometries.

*Our goal was to test the sensitivity of the semi-infinite multi-distance protocol to perturbations to the semi-infinite geometry (i.e., curvature).* We measured the absorption coefficient ( $\mu_a$ ) and the reduced scattering coefficient ( $\mu_s'$ ) with this protocol for both a semi-infinite slab and for cylinders composed of the same phantom material. We can then obtain information on how well the multi-distance method masks perturbations to the semi-infinite boundary.

## **Basic Theory**

The frequency-domain approach offers heavily damped spherical photon density waves as solutions of the photon density  $U(r,t)$  for the diffusion equation in an infinite medium.<sup>5</sup> The method of images allows us to derive the semi-infinite solutions from the infinite medium solution.<sup>6</sup> Forcing  $U(r,t)$  to vanish upon an extrapolated boundary located about 0.1 cm above the semi-infinite boundary allows the use of diffusion theory in modeling a flat tissue surface. Since we modulate a laser source at frequency  $\omega/2\pi$ , we create a total photon density wave of the form  $U(r,t) = U_{DC}(r) + U_{AC}(r)e^{-i(\omega t + \phi)}$ , where  $r$  is the source-detector separation.



We can easily obtain expressions for each of the measurable frequency-domain parameters (i.e., the *DC* intensity  $U_{DC}$ , the *AC* intensity  $U_{AC}$ , and the phase shift relative to the source  $\phi$ ):<sup>4</sup>

$$\begin{aligned}\ln(U_{DC}F_{DC}(r, \mu_a, D)) &= -r\sqrt{\frac{\mu_a}{D}} + G_{DC}(D, S), \\ \ln(U_{AC}F_{AC}(r, \mu_a, D, \omega)) &= -r\sqrt{\frac{\mu_a}{2D}} V_+(\mu_a, \omega) + G_{AC}(D, S, A), \\ \phi &= -r\sqrt{\frac{\mu_a}{2D}} V_-(\mu_a, \omega) - \tan^{-1}[F_{PH}(r, \mu_a, D, \omega)],\end{aligned}$$

where 
$$V_{\pm}(\mu_a, \omega) = \sqrt{1 + \left(\frac{\omega}{v\mu_a}\right)^2} \pm 1 \quad D = \frac{1}{3\mu_s'},$$

$F_{DC}$ ,  $F_{AC}$ , and  $F_{PH}$  are known analytical functions of their arguments;  $S$  is the source strength,  $A$  is the source modulation (i.e., *AC/DC*), and  $\omega$  is the angular modulation frequency of the source. The important points about these equations are:

- (1) All of the left hand sides contain the measurable frequency-domain parameters.
- (2) Only the *intercepts* (i.e., terms not dependent upon  $r$ ) contain the information about the source (i.e., the source phase, the source strength, and the source modulation).
- (3) The only unknowns in the *slopes* of these lines are  $\mu_a$  and  $\mu_s'$ , which is precisely what we wish to find. We can use the slopes associated with any two experimental quantities (say, *AC* and  $\phi$ ) to find  $\mu_a$  and  $\mu_s'$  (using an iterative method).

### **Experiment**

In order to test how well the semi-infinite multi-distance method fairs against the complications of curved boundaries, we prepared tissue-like phantoms composed of hot-mold glue and black India ink, cast into cylinders of 5 different diameters ranging from 4.2 cm to 10.2 cm. As a control, we also prepared a 5 cm thick slab of the same material which mimics the semi-infinite geometry. The optical coefficients of this material, measured on the flat sample with the semi-infinite multi-distance method, were  $\mu_a = 0.046 \text{ cm}^{-1}$  and  $\mu_s' = 7.0 \text{ cm}^{-1}$ . Using an optical fiber coupled to a 780 nm laser diode modulated at 100 MHz, we measured the photon density waves over a range of  $r$ 's in a reflectance-style measurement. The measurement was easily reproducible because of the use of machined templates that fit over the cylinders and the slab; this ensured that the fiber placements were identical each time. We also measured the photon density along two different directions on the cylinder surface; (1) along the  $\hat{z}$  axis (i.e., the long axis of symmetry), and (2) along  $\hat{\phi}$  (i.e., the circumferential direction).

### **Results**

We found that the semi-infinite protocol was able to recover  $\mu_a$  within 3% (please refer to figure 1) and  $\mu_s'$  within 10% when measured along the  $\hat{z}$  axis for all but the smallest diameter cylinders (less than  $\sim 5$  cm). This is quite promising for current *in vivo* hemoglobin saturation measurements that rely upon a frequency-domain instrument using this same protocol on human limbs.<sup>7</sup> These results indicate that at least the curvature itself may not create additional complications, provided that the measurement is performed along the  $\hat{z}$  axis.

Along the  $\hat{\phi}$  direction the curvature effect is stronger. The absolute values of the measured  $\mu_a$  and  $\mu_s'$  deviated by more than 50%, indicating that the method may fail if used on the skull. However, relative measurements may still be done and without corrections.

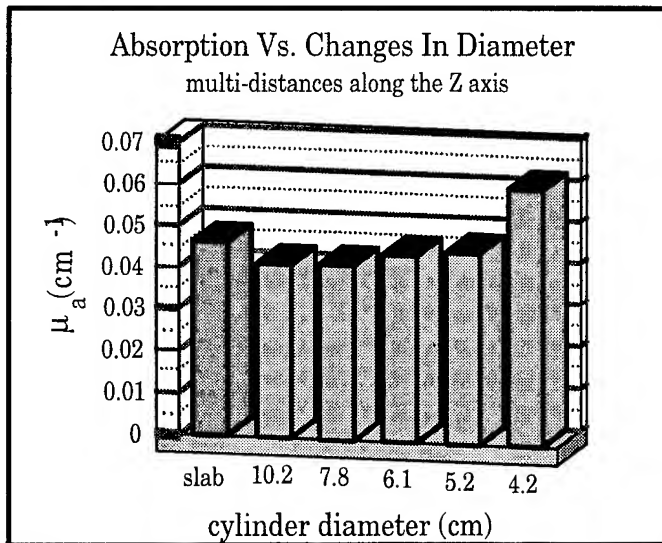


**Figure 1** - Results of the frequency-domain multi-distance method applied to 5 cylinders of varying diameter. Here we present the recovered values of  $\mu_a$ , as measured along the  $\hat{z}$  axis of the cylinder. Except for the smallest cylinder diameter, all values were measured within 3% of the slab coefficient ( $\mu_s'$  values were within 10% for this measurement). Also, it is interesting to note that the closest agreement lies between the 5 cm thick slab and the 5.2 cm diameter cylinder. This suggests that the loss of photons is mainly due to the narrowing thickness, and not necessarily the curvature.

We believe that the success of the  $\hat{z}$  axis measurements can be attributed to the fact that the multi-distance method turns slopes, not absolute values, into quantitative measurements of  $\mu_a$  and  $\mu_s'$ . Although the absolute values of the directly measured quantities (intensity and phase) may be changed dramatically by the curved boundary, the relative changes with respect to  $r$  remain approximately the same. In the  $\hat{z}$  axis measurement, the photon density as a function of  $r$  has a consistent symmetry that the  $\hat{\phi}$  direction measurement lacks (smaller  $r$ 's will feel the effect of the curvature more than the larger  $r$ 's).

**Conclusion** We have seen that the multi-distance protocol shows a small sensitivity to perturbations from curvature to a semi-infinite geometry. The perturbations incurred during measurements along the long  $\hat{z}$  axis of the cylinders are probably small enough to justify the protocol's use for a cylindrical geometry.

## References

- 1 J. J. Duderstadt and L. J. Hamilton, *Nuclear Reactor Analysis* (John Wiley & Sons, New York, 1976).
- 2 S. R. Arridge, *et al.*, "Theoretical basis for the determination of optical path lengths in tissue: temporal and frequency analysis," *Phys. Med. Biol.*, **37**, 1537-60 (1992).
- 3 S. Fantini, *et al.*, "Quantitative determination of the absorption spectra of chromophores in strongly scattering media: a LED based technique," *Appl. Opt.*, **33**, 5204-5213 (1994).
- 4 S. Fantini, *et al.*, "Semi-infinite-geometry boundary problem for light migration in highly scattering media: a frequency-domain study in the diffusion approximation," *J. Opt. Soc. Am. B*, **11**, 2128-38 (1994).
- 5 J. B. Fishkin and E. Gratton "Propagation of photon-density waves in strongly scattering media containing an absorbing semi-infinite plane bounded by a straight edge," *J. Opt. Soc. Am. A.*, **10**, 127-40 (1993).
- 6 M. S. Patterson, *et al.*, "Time-resolved reflectance and transmittance for the non-invasive measurement of tissue optical properties," *Appl. Opt.*, **28**, 2301-6 (1989).
- 7 S. Fantini, *et al.*, "Frequency-domain multi-channel optical detector for non-invasive tissue spectroscopy and oximetry," *Opt. Eng.*, **34**, 32-42 (1995).

## The Effect of Water in the Quantitation of Hemoglobin Concentration in a Tissue-Like Phantom by Near-Infrared Spectroscopy

Maria Angela Franceschini<sup>1</sup>, Sergio Fantini<sup>1</sup>, Albert Cerussi<sup>1</sup>,  
Beniamino Barbieri<sup>2</sup>, Britton Chance<sup>3</sup>, and Enrico Gratton<sup>1</sup>

<sup>1</sup> University of Illinois at Urbana Champaign, Department of Physics, Laboratory for Fluorescence Dynamics, 1110 West Green Street, Urbana, IL 61801-3080 Telephone: (217) 244-5620 Telefax: (217) 244-7187

<sup>2</sup> ISS Incorporated, 2604 North Mattis Avenue, Champaign, IL 61821

<sup>3</sup> University of Pennsylvania, Department of Biophysics/Biochemistry, D501 Richards Building and 37th & Hamilton Walk, Philadelphia, PA 19104-6089

**Introduction.** The use of time-resolved spectroscopy, in conjunction with diffusion theory<sup>1</sup>, has recently led to the development of tissue oximeters operating in both the frequency-domain<sup>2</sup> and the time-domain.<sup>3</sup> These instruments are capable of measuring the absorption ( $\mu_a$ ) and the reduced scattering ( $\mu_s'$ ) coefficients of tissue without making any assumptions on the optical path length. As a result, these instruments provide an absolute measurement of the optical coefficients of tissue. To translate the information about the optical properties of tissues into the determination of hemoglobin concentration and of hemoglobin saturation, it has been assumed that the absorption of near-infrared light in tissues is solely due to oxy- and deoxy- hemoglobin.

**Materials and Methods.** We performed near-infrared frequency-domain spectroscopy on a turbid suspension made of bovine blood (93 mL, hemoglobin concentration of 23  $\mu$ M), pH buffer (9 L), Liposyn 20% (231 mL, 0.5% solids content), and yeast (47 g). The optical properties of this suspension mimic those of tissue in the near-infrared ( $\mu_a \sim 0.05$  cm<sup>-1</sup>,  $\mu_s' \sim 6$  cm<sup>-1</sup>). The medium was enclosed in a sealed bag, and a constant flux of either oxygen or nitrogen was maintained through the medium via a tube located on the bottom part of the container. In this way a 100% oxygen, or 100% nitrogen atmosphere was attainable in the sealed bag. Consequently, the hemoglobin saturation could be varied (reversibly) from 100% to 0%. The OMNIA oximeter (ISS Inc.), placed on the surface of the medium, enabled us to continuously monitor the absorption and reduced scattering coefficients of the medium at two wavelengths ( $\lambda_1 = 715$  nm and  $\lambda_2 = 825$  nm), the hemoglobin saturation ( $Y$ ), the concentrations of oxy- and deoxy-hemoglobin ( $[\text{HbO}_2]$  and  $[\text{Hb}]$ ) and the total hemoglobin content ( $THC$ ). An oxygen electrode was located 1 cm below the surface of the medium to monitor the dissolved oxygen in the medium. A stirrer was used to prevent hemoglobin and suspended particles from settling.

**Results.** We initially did a measurement on the medium without the yeast. In this initial stage the hemoglobin was completely saturated, because the partial pressure of oxygen in air (150 mmHg) is sufficient to saturate the hemoglobin.<sup>4</sup> At time  $t=10$  min. we started the oxygen flux. Figure 1 reports the uncorrected hemoglobin saturation readings of the OMNIA instrument ( $Y^*$ ) and the oxygen electrode readings as a function of time. The duration of the oxygen and nitrogen fluxes are indicated in the figure. We initially maintained the oxygen flux for about 90 minutes. In this period of time, we registered changes only in the dissolved oxygen concentration measured by the oxygen electrode. The hemoglobin is fully saturated and no changes are observed. At  $t=100$  min., we stopped the oxygen flux, added the yeast to the medium, and started the nitrogen flux. The readings of the oxygen electrode started immediately to decrease, while the readings of  $Y^*$  with the OMNIA started to decrease at a later time. Both readings reached a minimum value after about 50-60 minutes. At time  $t=210$  min. we stopped the nitrogen flux, and started again the oxygen flux and maintained it

until the end of the experiment. The dissolved oxygen in the medium and the hemoglobin saturation increased again.

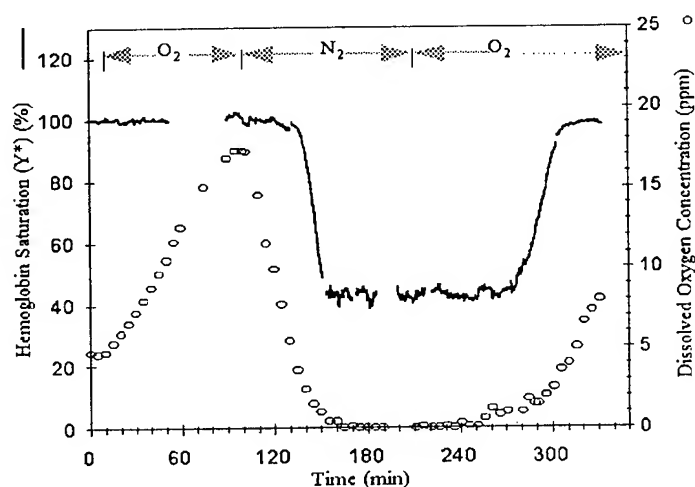


Fig. 1. Hemoglobin saturation readings of the OMNIA oximeter (continuous line, left y axis) and dissolved oxygen concentration (open circles, right y axis) as a function of time. The oxygen and nitrogen fluxes through the medium are indicated by the arrows.

**Discussion.** The relationship between the measured absorption coefficient at wavelength  $\lambda$  and the concentrations of chromophores in the medium is given by  $\mu_a(\lambda) = \sum_i \epsilon_i^\lambda [C_i]$ , where  $\epsilon_i^\lambda$  is the extinction coefficient at  $\lambda$  of the chromophore  $C_i$ , and  $[C_i]$  is the concentration of the chromophore  $C_i$ . In tissues, the summation is usually limited to the terms relative to oxy- and deoxy-hemoglobin.<sup>5,2,3</sup> To calculate  $Y^*$ , the OMNIA software is currently assuming that oxy- and deoxy-hemoglobin are the only absorbers for near-infrared light in tissue. The results for the hemoglobin saturation shown in Fig. 1 are not as we expect. While we correctly measure a 100% saturation in oxygen atmosphere, we do not obtain 0% saturation in nitrogen atmosphere. The main constituent by volume in our medium is water, and its contribution in the equation should be considered. By taking the water absorption into account, we find the water-corrected value of hemoglobin saturation ( $Y$ ). Figure 2 reports the hemoglobin saturation with and without the water correction ( $Y^*$  and  $Y$ , respectively). In our experimental conditions, the effect of this correction is negligible in the high saturation limit, but it becomes increasingly important at lower saturation values.

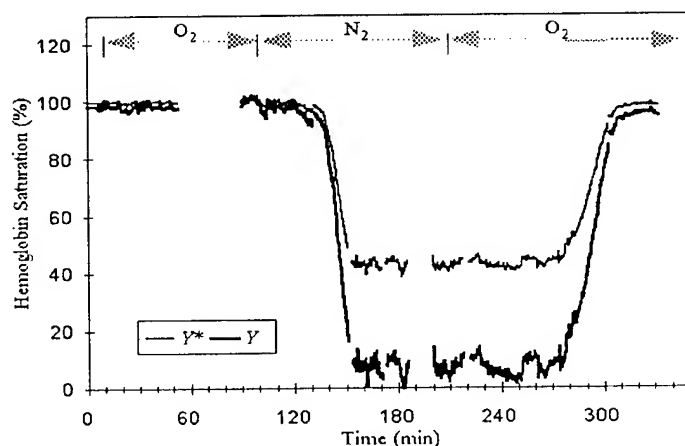


Fig. 2. Measured hemoglobin saturation without water correction ( $Y^*$ ) and with water correction ( $Y$ ) as a function of time.

We have calculated the dependence of uncorrected hemoglobin saturation ( $Y^*$ ) on hemoglobin concentration for the pair of wavelengths employed in this study ( $\lambda_1=715$  nm and  $\lambda_2=825$  nm). In Fig. 3 we report  $Y^*$  versus  $THC$  for different values of  $Y$  (11 curves for  $Y$  ranging

from 0% to 100% at increments of 10%). The vertical line in the figure indicates the concentration of hemoglobin used in our experiment. For the hemoglobin concentration employed in our *in vitro* experiment, the water-correction is important. However, for the hemoglobin concentration in tissues (80-150  $\mu\text{M}$ ), this correction would be important only at low saturation values.

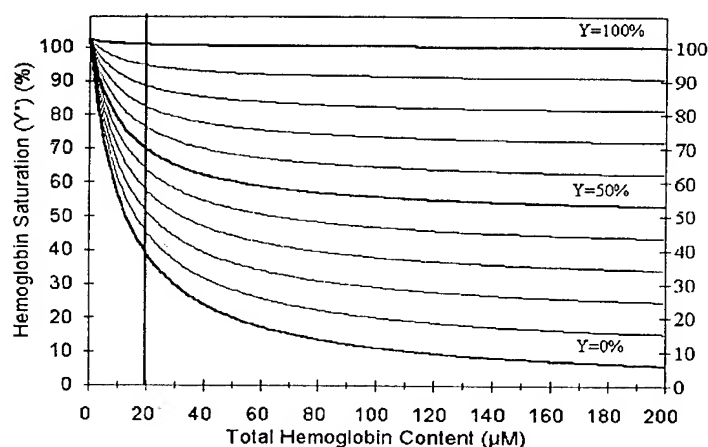


Fig. 3. Calculated hemoglobin saturation ( $Y^*$ ) as a function of total hemoglobin concentration for different values of actual saturation ( $Y$ ). The vertical line indicates the concentration of hemoglobin used in our experiment. These calculations employ the pair of wavelengths used in the OMNIA oximeter ( $\lambda_1=715\text{ nm}$ ,  $\lambda_2=825\text{ nm}$ ).

**Conclusions.** Near-infrared spectroscopy has the potential to determine quantitative values of hemoglobin concentration and saturation in blood perfused tissues. This potential has already been exploited by quantitative oximeters in the frequency-domain<sup>2</sup> and in the time-domain.<sup>3</sup> However, these instruments work under the assumption that hemoglobin is the only absorber in the near-infrared. While this is a reasonable first step approximation, it might lead to systematic errors. We have investigated the effect of water absorption in the quantitative determination of hemoglobin concentration and saturation in turbid media by near-infrared spectroscopy. Our results show that the effect of water depends on the total hemoglobin content and on the pair of wavelengths used by the optical oximeter. For the total hemoglobin content (19  $\mu\text{M}$ ) and the wavelengths (715 and 825 nm) employed in this study, the water correction has little effect on the determination of both the Hb concentration and the high saturation values. On the contrary, the water correction is relevant in the determination of both the HbO<sub>2</sub> concentration and the low saturation values. Water is an important absorber in biological tissue. However, its absorption properties may be affected by its bound state in tissues. Furthermore, background absorption could be due to other chromophores. Intrinsic tissue inhomogeneities might also play a role in the complication of quantitative optical measurements. Additional studies are required to correctly treat the background absorption of tissues.

## References

1. M. S. Patterson, B. Chance, and B. C. Wilson, "Time Resolved Reflectance and Transmittance for the Non-Invasive Measurement of Optical Properties," *Appl. Opt.* **28**, 2331-2336 (1989).
2. S. Fantini, M. A. Franceschini, J. S. Maier, S. A. Walker, B. Barbieri, and E. Gratton, "Frequency-Domain Multichannel Optical Detector for non-Invasive Tissue Spectroscopy and Oximetry," *Opt. Eng.* **34**, 32-42 (1995).
3. M. Miwa, Y. Ueda and B. Chance, "Development of Time Resolved Spectroscopy System for Quantitative Non-Invasive Tissue Measurement," *Proc. SPIE*, **2389**, 142-149 (1995).
4. C. R. Cantor and P. R. Schimmel, *Biophysical Chemistry part III*, pp. 963-964, (W. H. Freeman and Company, New York, 1969).
5. E. M. Sevick, B. Chance, J. Leigh, S. Nioka, and M. Maris, "Quantitation of Time- and Frequency-Resolved Optical Spectra for the Determination of Tissue Oxigenation," *Anal. Biochem.* **195**, 330-351 (1991).

## Fetal Brain Oxygenation during Labor studied by Frequency Domain Spectroscopy

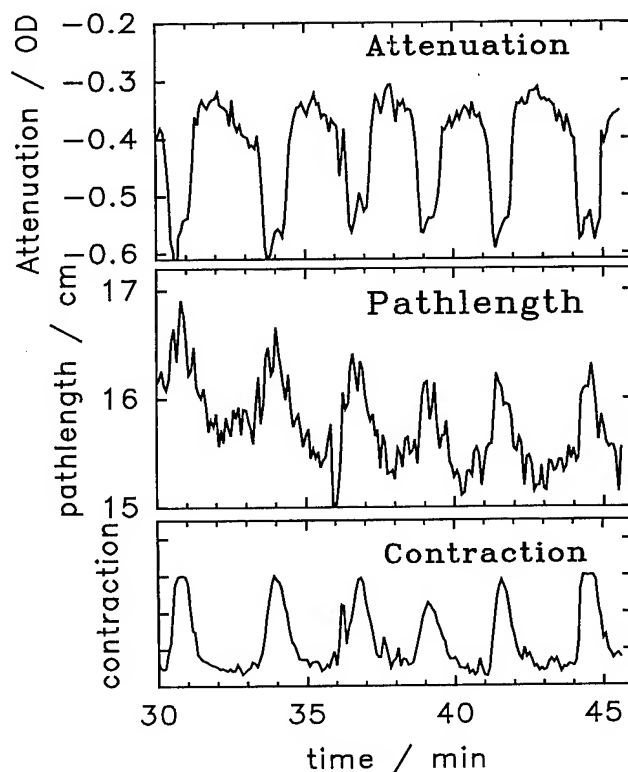
R Watson, M Kohl, P O'Brien\*, S Lawrence<sup>+</sup>, DT Delpy, M Cope

Department of Medical Physics and Bioengineering, University College London,  
11 - 20 Capper Street, London WC1E6JA, UK  
(44)-(171)-209- 6262 (Tel) - 6269 (Fax)  
e-mail: watsonrw@medphys.ucl.ac.uk

\*Department of Obstetrics, University College Hospital, 86-96 Chenies Mews,  
London WC1E 6AU, UK

<sup>+</sup>Department of Paediatrics, Rayne Institute, University College Hospital, 5 University Street,  
London WC1E 6AU, UK

The oxygenation status in fetal brains during birth was studied with phase resolved, frequency domain near infrared spectroscopy. In the figure below an example of the correlation between contractions, attenuation and optical pathlength (phase) changes measured on a fetal head is shown for a wavelength of 744 nm and a light source detector separation of 35 mm. Each contraction gives rise to a decrease in blood volume in the fetal brain accompanied by a decrease in attenuation and an increase in pathlength. The advantage of the additional pathlength information, compared with conventional attenuation measurements, for the assessment of haemoglobin concentration, oxygen saturation and the possible elimination of movement artefacts is discussed.



Wednesday, March 20, 1996

# Cell Analysis and Properties I

**BWC** 2:00 pm-3:45 pm  
Windsor Ballroom

Irving Bigio, *Presider*  
*Los Alamos National Laboratory*

APPLICATIONS OF LASER OPTICAL MICROSCOPIC TECHNIQUES IN DECIPHERING  
DISEASE SPECIFIC MECHANISMS AND DIAGNOSIS B. Herman, Department of Cell Biology  
& Anatomy, University of North Carolina, Chapel Hill, NC 27599

Accumulating evidence strongly associates human papillomavirus infection with the development of cervical cancers. However, it has also become increasingly clear that HPV infections of the cervix span a wide clinical spectrum from benign lesions to precancerous lesions, with only a minority of infections resulting in invasive cancers, although the reasons for this are not clear. Longitudinal epidemiologic studies using cytologic methods to detect HPV infection have shown that the majority of women infected with HPV will regress spontaneously. In addition, age-stratified data for rates of HPV positivity from cross-sectional studies also suggest that many women clear the infection spontaneously. These results support the concept that many women may be only transiently infected with HPV during their life span and only in women with persistent HPV infection does cervical cancer progress. In addition to persistence of HPV infection, recent epidemiological studies indicate that the amount of high-risk HPV (viral load or HPV gene copy number) in cervicovaginal epithelial cells may be a risk factor for cervical cancer. Thus, a technique which could detect, genotype and quantitate HPV in smears of cervicovaginal epithelial cells would be of major import in assessment of patient clinical status as well as in epidemiological studies relating HPV infection to cervical cancer.

The primary screening test for cervical abnormalities is the Papanicolaou (PAP) smear. Unfortunately there are certain disadvantages to this test. These include its lack of sensitivity when used as a triage method for colposcopy, detecting only 50 to 80% of abnormalities subsequently found by histologic examination, and a false negative rate of between 5 to 20%. Lastly, it is often difficult to identify HPV specific viral infection by cytologic examination of a PAP smear. For these reasons, we have been developing a microscopic imaging system which, when coupled to fluorescent in situ hybridization (FISH) techniques is capable of detection of *one to two copies* of HPV per cell, can genotype and quantitate the amount of HPV present at a single cell level in cervical PAP smears. This system is able to automatically identify each individual cell in a PAP smear, and quantitate HPV copy number, allowing assessment of cellular cytoarchitecture and HPV status at the single cell level. This FISH technique was combined with the microscopic imaging system and used to screen cervical specimens in comparison to polymerase chain reaction (PCR), to investigate the prevalence of HPV-16 in women with varying grades of cervical dysplasia/carcinoma. 29% of the specimens tested were positive for HPV-16 by PCR while 14% of the specimens tested were positive for HPV-16 by the FISH procedure. When the sensitivity and specificity of the FISH procedure was compared to that of PCR in terms of HPV detection and clinical disease status, it was found that the specificity of FISH and PCR with respect to predicting CIN 2-3 and carcinoma in situ was 90% and 75% respectively, while the sensitivity of FISH and PCR with respect to predicting CIN 2-3 and carcinoma in situ was 21% and 36% respectively. Because the FISH procedure preserves cellular morphology, has a higher specificity yet comparable sensitivity to PCR, use of the FISH procedure for detection of high risk HPV may serve as a useful adjunct to cytological screening for detection of high grade cervical disease. The microscope imaging system has also been used to determine the DNA ploidy distribution of PAP smears and to quantify the expression of the HPV-16 early protein, E6 in the cytoplasm of individual cells in the PAP smear. These studies demonstrated that the DNA ploidy distribution of HPV-16 E6 positive cells was the same as non infected (negative) cells. This result suggests that expression of E6 is an earlier event in the development of cervical disease than chromosomal instability; in addition, these reports demonstrate our ability to use quantitative fluorescence microscopy to detect target DNA using FISH, and to measure DNA ploidy and nuclear morphology using fluorescence microscopic techniques.



The development of a large number of fluorescence dyes and the ability to attach them to specific molecular cell constituents allows real-time observation and quantitation of the activities of these constituents in cells and tissue. For example, the availability of bioreagents such as monoclonal antibodies and nucleic acid probes have opened up new possibilities for the localization and analysis of proteins and nucleic acid sequences in cells, tissues and chromosomes. Unfortunately, theoretically obtainable sensitivity is never achieved due to autofluorescence from solvents, solutes, cells, tissues, fixatives employed, and optical components of the microscope system. This is a common problem affecting essentially all studies employing fluorescence microscopy, whether in living cells, fixed tissues, or clinical samples. Autofluorescence effectively decreases the signal-to-noise ratio of detection. This is the case even though a number of improvements have been made in the optics, digital computers, digitizers, image analysis algorithm and low-light-level sensitive detectors used in light microscopy.

Our FISH assay requires the use of fresh cervicovaginal cell preparations and cannot be used on standard PAP smears (i.e. those already stained and read by a cytopathologist), due to the fact that the absorption stains used by cytopathologists are intensely (auto)fluorescent and interfere with the FISH signal. This (auto)fluorescence has a defined lifetime (i.e. the average time that a molecule remains in an excited state prior to returning to the ground state); if it was possible to conjugate the HPV cDNA probe to a compound which was fluorescent but whose fluorescence was emitted after the fluorescence from the absorption stains had decayed, then it would be possible to observe and quantitate HPV in standard PAP smears without interference from the routine histological stains. We have developed an approach which overcomes these limitations- time-gated fluorescence microscopy (TGFM). This technique enables the separation of true fluorescence emitted from HPV cDNA probes (labeled with long-lifetime probes (lifetimes on the order of 1  $\mu$ sec - 1 msec)), from autofluorescence of PAP absorption stains (lifetimes on the order of 1-100 nsec).

In vitro studies using reticulocyte lysate systems has demonstrated a specific interaction between high risk HPV-16 E6 and the tumor suppressor gene product, p53. This interaction has been hypothesized to lead to degradation of p53 and loss of p53's growth suppressive activity. To determine whether this interaction occurred in intact cells, we investigated the localization of the HPV-16 E6 and endogenous p53 proteins in HPV positive and negative cervical carcinoma cell lines. E6 and p53 were predominantly in the cytoplasm of the HPV+ cells (Hela, CaSki, SiHa), while p53 was predominantly in the nuclei of the HPV- cells (C33-A and HT-3). To investigate further why p53 was unexpectedly in the cytoplasm of HPV+ cells, we used confocal microscopy to investigate the co-localization of the proteins. Confocal microscopy can be thought of as a CAT scanner for cells in that it allows the 3 dimensional distribution of cellular components to be examined. Results showed that these two proteins had very similar distributions in these cells, implying the proteins may exist in a bound complex. To substantiate this observation, we used Fluorescence Resonance Energy Transfer (FRET) microscopy, a technique which can document the physical proximity of two proteins. The basis of this technique is that the two proteins are labeled with different fluorescent molecules, called donor and acceptor respectively. By design, the emission spectrum of the donor overlaps the excitation spectrum of the acceptor fluorophores. When the donor and acceptor are within 50 Angstroms ( $10^{-10}$  meters) or less of one another, energy from the excited donors can be nonradiatively transferred to the acceptor. This results in an increase in the intensity of emission fluorophore ( $I_A$ ) and a concomitant decrease in the emission of the donor ( $I_D$ ), which is proportional to the distance between the proteins (i.e. the closer the two proteins are together, the greater the emission intensity of the acceptor and hence the ratio  $I_A/I_D$ ). Our findings

indicated that E6 and p53 were separated by a distance  $\leq 50$  Angstroms, and hence are most probably bound together in a complex. These studies suggest that part of the mechanism by which HPV-16/18 could cause cervical neoplasia may be that cytoplasmic HPV E6 binds to p53 protein after its transcription in the cytoplasm, preventing p53 from entering the nucleus where it performs its normal growth (tumor) suppressor function.

P53 has also been shown to regulate the expression of bcl-2 a protein that inhibits programmed cell death (*apoptosis*). Therefore, we examined bcl-2 transcription and expression in cervical carcinoma cell lines and keratinocytes. Findings from these studies demonstrated increased bcl-2 expression in cervical carcinoma cell lines that contain mutated or E6-inactivated p53. Western blotting and immunofluorescence microscopy demonstrated bcl-2 expression in the cytoplasm of four out of five cervical carcinoma cell lines examined while bcl-2 protein expression was undetectable in normal keratinocytes. Northern blot analysis demonstrated low levels of bcl-2 transcription in HeLa, CaSki, and C-33A cells, while reverse transcriptase (RT)-PCR demonstrated bcl-2 transcription in all cervical carcinoma cell lines which had Bcl-2 protein expression. Thus, inactivation of p53 function, which can induce apoptosis in certain cells, is associated with increased Bcl-2 expression. Increased Bcl-2 expression under conditions of p53 inactivation may provide cells with a selective advantage for survival and consequently play a role in the development of cervical carcinogenesis.

Based on these findings, we examined PAP smears from 94 women with varying degrees of cervical disease for the presence or absence of p53, HPV 16/18-E6 and bcl-2 protein using immunofluorescence microscopy. Our findings indicate that there is a statistically significant inverse association between the presence of p53 and invasive cervical disease (odds ratio (OR)=0.3, 95% confidence interval (CI)=0.13-0.73). Moreover, the odds of being diagnosed with an invasive stage of cervical cancer was 3.69 times higher (95% CI=1.55-8.80) for women positive for E6, and 17 times higher (95% CI=5.52-58.29) for women positive for bcl-2 expression compared to women negative for E6 or bcl-2. Women with invasive cervical cancer were also 4.59 times more likely to test positive for the expression of more than one marker (95% CI=1.78-11.78). Chi square analysis demonstrated a strong association between E6 and bcl-2 expression ( $p<0.001$ ) as well as between E6 or bcl-2 expression and diagnosis ( $p=0.015$ ,  $p<0.001$  respectively). In multivariate analysis the presence of bcl-2 (OR=18.82, 95% CI=5.52-67.82), and age at diagnosis ( $\geq 50$ , OR=7.83; 95% CI=2.50-24.47) showed significant association with invasive cervical disease after adjusting for the presence of p53 and E6. These findings indicate that 1) expression of bcl-2 is strongly associated with the development of high grade cervical disease; 2) the pattern of expression of high risk HPV E6, p53 and bcl-2 proteins may be useful for identifying women at increased risk for the development of cervical cancer; and 3) a defect in apoptosis may partially underlie the development of cervical cancer.

## Quantitative Laser Scanning Confocal Autofluorescence Microscopy of Normal, Premalignant, and Malignant Colonic Tissues

Hsing-Wen Wang<sup>1</sup>, Marcia I. Canto<sup>2</sup>, Joseph Willis<sup>3</sup>, Michael V. Sivak<sup>2</sup>, and Joseph A. Izatt<sup>1,2</sup>

Departments of <sup>1</sup>Biomedical Engineering and <sup>2</sup>Medicine  
Case Western Reserve University, Cleveland, OH 44106  
(216)844-7928; Fax:(216)844-8011

Department of <sup>3</sup>Pathology  
University Hospitals of Cleveland, Cleveland, OH 44106

### Introduction

Laser-induced fluorescence (LIF) spectroscopy has received considerable attention as an application of lasers and fiber optics to noninvasive tissue diagnosis, particularly in early detection of cancer in the breast<sup>1</sup>, lung<sup>1,2</sup>, esophagus<sup>3</sup>, and colon<sup>4-7</sup>. LIF spectroscopy is currently under study as a noninvasive method of tissue diagnosis in the colon due to its potential for future routine application in gastrointestinal endoscopy. The distinction of normal colon from premalignant and malignant lesions is of potential clinical importance because the early detection of these lesions is important in the treatment of patients. Previously published analyses of ultraviolet LIF spectral and intensity differences have correctly differentiated adenomas from normal colonic mucosa and hyperplastic polyps with resulting sensitivity, specificity, and PPV of 80-100%, 77-95%, and 82-94%, respectively<sup>4-7</sup>. Although these initial studies have provided compelling evidence supporting the use of LIF spectroscopy in early colon cancer diagnosis, there remains little information available regarding the specific origins and biochemical correlates of LIF spectra in colonic tissue. Proposed theories for the source of LIF differences in the colonic polyp model have included changes in gross polyp morphology<sup>7</sup>, microvascular changes<sup>7</sup>, differences in crypt architecture<sup>8</sup>, and biochemical differences characteristic of dysplastic epithelial cells<sup>8</sup>.

We have a particular interest in the development of LIF diagnosis in colonic tissues for clinical application during endoscopy, particularly in the immediate, noninvasive diagnosis of small or microscopic dysplastic lesions not readily diagnosed by routine examination. In order to address the morphological and cytological origins of colonic tissue autofluorescence and quantitatively assess the contributions of spectral signatures arising from different morphological tissue components, we have initiated studies of high-resolution ultraviolet laser scanning confocal fluorescence microscopy of unstained, excised samples of normal, premalignant, and malignant colonic tissues. Confocal microscopy is particularly well suited to this investigation because of its capability to provide quantitative measurements of remitted tissue fluorescence intensities localized with sub-micron resolution in three dimensions. Further, optical sectioning of thin tissue sections within relatively thick tissue specimens is possible, thus anomalous fluorescence signals arising from tissue sectioning artifacts are eliminated.

### Methods

Human colonic tissue samples were obtained from surgical resections with Institutional Review Board approval. Bulk tissue specimens were snap frozen and stored at -70°C. Frozen specimens were cut into 10 micron thick cryostat sections and stored at -70°C. Before use, slides were coverslipped with iced PBS. For histological comparison of fluorescence microscopy results, serial cryostat sections were fixed and stained with H&E. Initial studies of laser-induced fluorescence microscopy using optical sectioning in thick tissue samples were conducted in fresh excised colons of F344 rats.

Laser-induced fluorescence microscopy studies were performed using a state-of-the-art ultraviolet-corrected Olympus LSM-GB200UV confocal laser scanning microscope. Excitation wavelengths included selected lines from argon-ion (351-364 nm, 488 nm, 514 nm) and Helium-Neon (542 nm, 633 nm) lasers. Fluorescent light remitted from the specimen was separated from excitation light in a dichroic beamsplitter, and subsequently spectrally filtered using selectable barrier filters prior to photomultiplier tube detection. Quantitative imaging was performed using calibrated settings for laser power, confocal aperture size, image scanning speed, and photomultiplier tube gain.

### Preliminary Results

In preliminary studies, unstained frozen sections of normal colon, colonic tubular adenomas, and infiltrating adenocarcinomas have been examined to quantitate and compare autofluorescence intensities of cellular and morphological tissue components. Figures 1(a) and 1(b) illustrate LIF confocal microscopy of normal colon and low-grade dysplasia in colonic tubular adenoma, respectively, using 351-364nm excitation and a 515 nm barrier filter. In this and other normal samples, intense fibrillar fluorescence was observed in the collagen-rich connective tissues of the submucosa, muscularis mucosa, and to a lesser extent in the lamina propria. Brightly fluorescent granular deposits were observed which are tentatively identified as cytoplasmic eosinophil granules by comparison with an earlier study<sup>8</sup>. Minimal fluorescence was observed in mucosal columnar epithelial cells.

Marked differences in autofluorescence intensity and distribution were observed within regions of colonic tubular adenoma characterized as low-grade dysplasia by a clinical pathologist, as illustrated in Fig. 1(b). Notable differences included the presence of increased fluorescence within epithelial cell cytoplasm, and an increased quantity of eosinophils. Due to the presence of epithelial cell fluorescence, goblet cells can be identified based on the absence of fluorescence in mucin droplets contained within.

Subsurface optical sectioning in a bulk specimen of freshly excised colon tissue from a normal F344 rat is illustrated in Fig. 2. In this case, argon-ion excitation at 488nm and a barrier filter at 610 nm were used. The optical section was obtained at a depth of 100  $\mu$ m beneath the mucosal surface and parallel to it; colonic crypts are thus viewed from the top looking down. The structure of the crypts is made apparent primarily by fluorescence at the columnar epithelial cell borders, as well as the absence of fluorescence within the crypt lumens. Cytoplasmic granules of eosinophils were also observed.

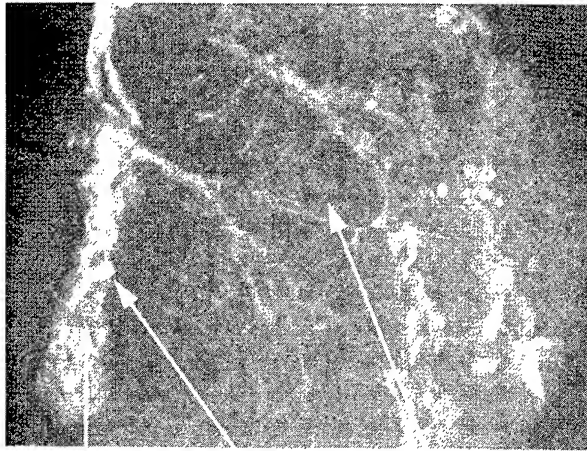
### Conclusion

The most important findings of our studies to date include observations of increased cytoplasmic fluorescence in dysplastic epithelial cells, and the demonstrated capability to perform fluorescence microscopy using confocal optical sectioning in bulk colonic tissue. Planned future study directions include 1) continued acquisition of a database of LIF images from normal, premalignant, and malignant colonic tissues, 2) performance of quantitative microspectrofluorimetry of localized cytoplasmic components, and 3) quantitative studies in thick unstained cryostat sections and bulk tissue specimens in order to take advantage of the confocal sectioning capability and eliminate cryostat sectioning artifacts.

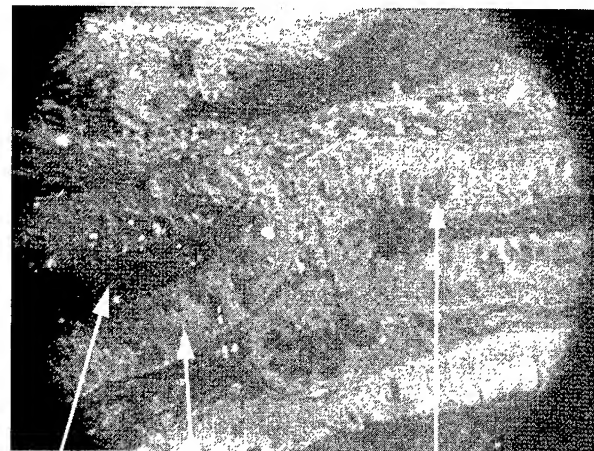
We gratefully acknowledge Olympus America, Inc. for research support and T. Pretlow for providing rat colon samples.

### References

1. Alfano RR, Tang GC, Pradham A, Lam W, Choy DSJ, Opher E. Fluorescence Spectra from Cancerous and Normal Human Breast and Lung Tissues. *IEEE J. Quant. Electron.* 1987;QE-23:1806-1811.
2. Lam S, MacAulay C, Hung J, LeRiche J, Profio AE, Palcic B. Detection of dysplasia and carcinoma in situ with a lung imaging fluorescence endoscope device. *J. Thorac. Cardiovasc. Surg.* 1993;105:1035-1040.
3. Panjehpur M, Overholt BF, Schmidhammer JL, Farris C, Buckley PF, Vo-Dinh T. Spectroscopic Diagnosis of Esophageal Cancer: New Classification Model, Improved Measurement System. *Gastrointest. Endosc.* 1995;41:577-581.
4. Cothren RM, Richards-Kortum R, Sivak MV, et al. Gastrointestinal tissue diagnosis by laser-induced fluorescence spectroscopy at endoscopy. *Gastrointest. Endosc.* 1990;36(2):105-111.
5. Kapadia CR, Kutruzzola FW, O'Brien K, Stetz M, Enriquez R, Deckelbaum LI. Laser-induced fluorescence spectroscopy of human colonic mucosa. Detection of adenomatous transformation. *Gastroenterol.* 1990;99:150-157.
6. Richards-Kortum R, Rava RP, Petras RE, Fitzmaurice M, Sivak M, Feld MS. Spectroscopic diagnosis of colonic dysplasia. *Photochem. Photobiol.* 1991;53(6):777-786.
7. Schomacker KT, Frisoli JK, Compton C, et al. Ultraviolet Laser-Induced Fluorescence of Colonic Tissue: Basic Biology and Diagnostic Potential. *Las. Surg. Med.* 1992;12:63-78.
8. Romer TJ, Fitzmaurice M, Cothren RM, et al. Laser-Induced Fluorescence Microscopy of Normal Colon and Dysplasia in Colonic Adenomas: Implications for Spectroscopic Diagnosis. *Am. J. Gastro.* 1995;submitted.

**a) NORMAL COLONIC MUCOSA**

**Connective Tissue**   **Eosinophil**   **Epithelial Cell Layer**

**b) LOW-GRADE DYSPLASIA**

**Crypt Lumen**   **Epithelial Cell Layer**   **Goblet Cell**

**Figure 1.** (a) Laser scanning confocal fluorescence microscope image of a 10 micron unstained frozen section of normal colonic tissue obtained using 351-364 nm argon-ion laser illumination with a 515 nm barrier filter. Intense fluorescence is observed in connective tissue and eosinophil granules. Minimal fluorescence is observed within columnar epithelial cells. (b) Corresponding image of low-grade dysplastic crypts within a tubular adenoma from a different patient obtained with the same illumination and filter. The photomultiplier gain was a factor of 2 x higher than in (a). Markedly increased fluorescence is visible within epithelial cells lining the crypts, and eosinophils are more numerous.

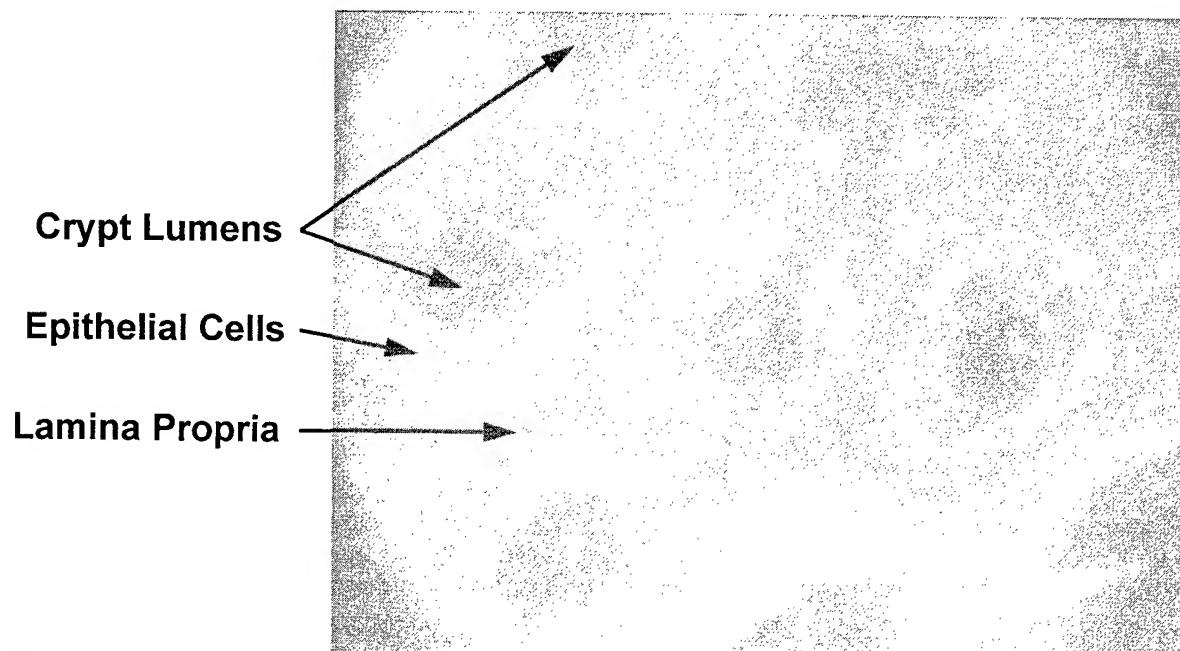


**Figure 2.** Laser scanning confocal optical section of normal rat colon obtained at a depth of 100  $\mu\text{m}$  beneath the mucosal surface and parallel to it. This image was obtained using 488 nm argon-ion laser illumination and a 610 nm barrier filter. Crypt structure is observed predominantly free of scattering interference from adjacent tissue layers.

**Absolute enumeration of rare cell types in peripheral blood  
using laser induced fluorescence and volumetric microscopy**

Thomas M. Baer and Louis J. Dietz

Biometric Imaging  
1025 Terra Bella Avenue  
Mountain View, CA 94043

**ABSTRACT**

This paper describes a novel technique for the absolute enumeration of dye-labeled cells using laser-induced fluorescence and volumetric microscopy. This technique has been used for the enumeration of CD4+ and CD8+ lymphocytes and CD34+ stem cells, quality checking of leukocyte-reduced blood products, and DNA ploidy measurements.

**INTRODUCTION**

Many applications exist for cell enumeration assays in both clinical and research laboratories. It is frequently desirable that these assays provide absolute cell enumeration, i.e. the result of the assay is a count of the cells of interest per unit volume of the original sample. One of the most common applications is the CD4+ lymphocyte count, used for monitoring the immune system of HIV-positive persons (4). This assay provides a measure of the absolute number of CD4+ lymphocytes per unit volume of whole blood. HIV-positive persons are identified as AIDS patients when their CD4+ count drops below 200 cells/ $\mu$ l. Other types of cell enumeration assays are useful in blood banking, cell culture, and cancer diagnosis and therapy.

These applications require that the cells of interest, which may be relatively rare, be identified without interference from the large majority of other cell types present in the sample. The applications described in this paper depend either on unique cellular surface markers or DNA staining to identify the particular cells of interest. To perform the CD4+ lymphocyte count, for example, a cell will be counted only if it has both the CD4 and CD3 antigens present on its surface. A typical CD4 lymphocyte will have many thousands of each of these antigens expressed on the cell surface. By using dye-labeled antibodies that bind specifically to these surface antigens, optical detection systems can be designed to identify and count the CD4 lymphocytes. By substituting antibodies that are specific to different surface markers, new assays can be designed with little or no change to the optical system. For example, CD8+ lymphocytes, also useful for monitoring the progress of AIDS, are identified by the presence of both CD8 and CD3 antigens. Hematopoietic stem cells, which are the precursor cells of all the various types of blood cells, can be identified by the CD34 surface antigen (1). Assays for CD34 stem cells are important for bone marrow transplant patients. DNA staining dyes (5), which

become fluorescent only when they are bound to DNA, are also useful for a different class of assays. These dyes can be used, again with little or no change to the optical system, for counting nucleated cells, which is important in blood banking and cell culture, or for DNA ploidy measurements (5), which can be used for cancer diagnosis.

### **FLUORESCENT DYES**

Fluorescent dyes, which are a critical part of these assay systems, have recently become available at longer wavelengths, in the red and near-infrared (2). These dyes enable the use of inexpensive helium-neon and diode laser sources and allow excitation in a region of the spectrum that has less absorption from biological sources. The dyes Cy5 and Cy5.5 (3), with emission peaks at 665 and 695 nm respectively, can both be excited at 633 nm, allowing a two-color fluorescence imaging system to be designed with a single excitation source. These dyes have been conjugated to antibodies for the CD3, CD4, CD8, and CD34 surface antigens. Other dyes which are suitable for protein labeling have been synthesized for use at longer wavelengths, such as BHMP, which has an emission peak at 800 nm. By adding a second excitation source at 780 nm, a third and possibly fourth color can be added to the system. DNA staining dyes, such as TO-PRO-3 (5), which emits at 661 nm, can also be excited by he-ne or diode lasers. These dyes can be used to detect nucleated cells or quantify DNA content within a cell.

### **INSTRUMENTATION**

A laser scanning fluorescence detection system was designed for the purpose of imaging and counting cells contained within a precision glass capillary. This capillary defines the volume of the sample, which is typically a few microliters. The laser beam illuminates a small cylindrical volume inside the capillary. This cylinder has a diameter of about 10  $\mu\text{m}$ , determined by the laser beam, and a depth of about 100  $\mu\text{m}$ , determined by the capillary thickness. The laser beam is raster-scanned across the capillary in one dimension by a scanning mirror. The second dimension of the image is obtained by translating the capillary relative to the optical system with a stepper-motor driven translation stage. The pixel spacing in both dimensions is 4  $\mu\text{m}$ . This spacing, as well as the laser spot size, is a compromise which allows adequate image resolution, depth of field, practical scan times, and reasonable data storage requirements. Photomultiplier tubes are used to detect the fluorescent signals, which are digitized and stored in a microcomputer. After the image acquisition is complete, image processing software is used to analyze the images and generate a count of the target cells per unit volume of the sample. The optical layout for a two-channel, single source system is diagrammed in Figure 1.

### **RESULTS**

Figure 2 shows a sequence of raster lines from a portion of a typical image. Note the baseline pedestal that is due to unreacted reagent left in the sample capillary, and the fluorescent



peaks from labeled cells. Custom image processing software is used to detect and quantify the peak intensity. For a two-color assay, such as the CD4<sup>+</sup> lymphocyte assay, each cell will be represented by two intensities, one from each different color detection channel. Figure 3 is a plot showing, for each detected cell, the intensities in both channels. The dot plot clearly shows separate populations of cells, indicating that some of the cells are labeled with varying amounts of the anti-CD3-Cy5 antibody, some with varying amounts of the anti-CD4-Cy5.5 antibody, and some with both. Only the cells that were determined by the software to be positive for both surface antigens are labeled with "+" marks, and the total number of these cells is calculated by the software. The absolute CD4<sup>+</sup> cell count per unit volume is calculated from the actual scan length, the capillary cross-sectional area, the sample dilution factor (if any), and the CD4<sup>+</sup> cell count.

### **REFERENCES**

1. Owens MA, Loken MR: Flow Cytometry Principles for Clinical Laboratory Practice. Wiley-Liss, Inc., New York, 1995.
2. Lee LG, Woo SL, Head DF, Dubrow RS, Baer TM: Near-IR Dyes in Three-Color Volumetric Capillary Cytometry: Cell Analysis With 633- and 785-nm Laser Excitation. *Cytometry* 21:120-128, 1995.
3. AS, Ernst LA, Mujumdar RB: Method for labeling and detecting materials employing arylsulfonate cyanine dyes. U.S. Patent 5,268,486, 1993.
4. Stein D, Korvick J, Vermund S: CD4<sup>+</sup> lymphocyte cell enumeration for prediction of clinical course of human immunodeficiency virus disease: a review. *Journal of Infectious Diseases* 165:352-63, 1992.
5. Shapiro HM: Practical Flow Cytometry. Wiley-Liss, Inc. New York, 1995.

### **LIST OF FIGURES**

Fig. 1. Layout of two-color optical detection system.

Fig. 2. Portion of a typical fluorescence image from one of the two detection channels. Note the baseline pedestal from unreacted reagent, and the peaks from labeled cells.

Fig. 3. Two-parameter fluorescence dot-plots of a normal blood sample. Cells which have been determined by the image-processing software to be positive for both CD3 and CD4 antigens are labeled with a "+" symbol. The overlap between the Cy5 and Cy5.5 emission spectra has been corrected mathematically to generate orthogonal axes representing relative fluorescence in each of the two channels.



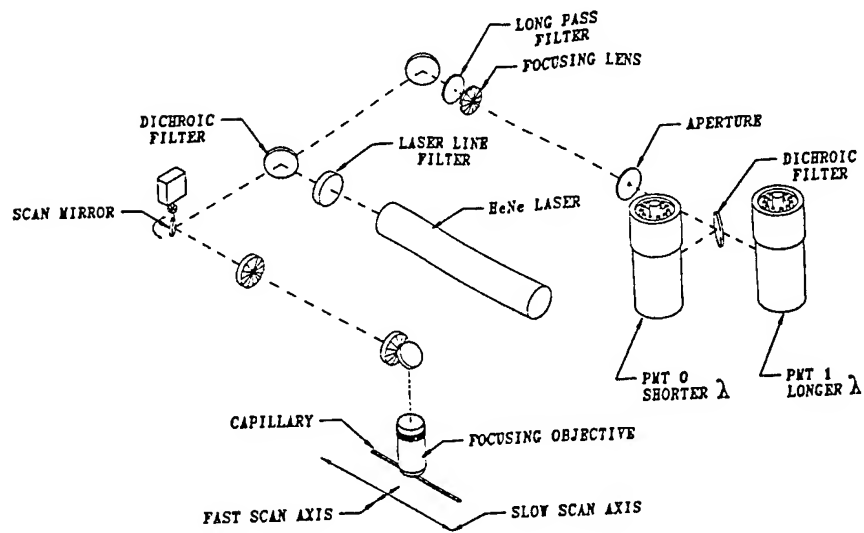


FIGURE 1

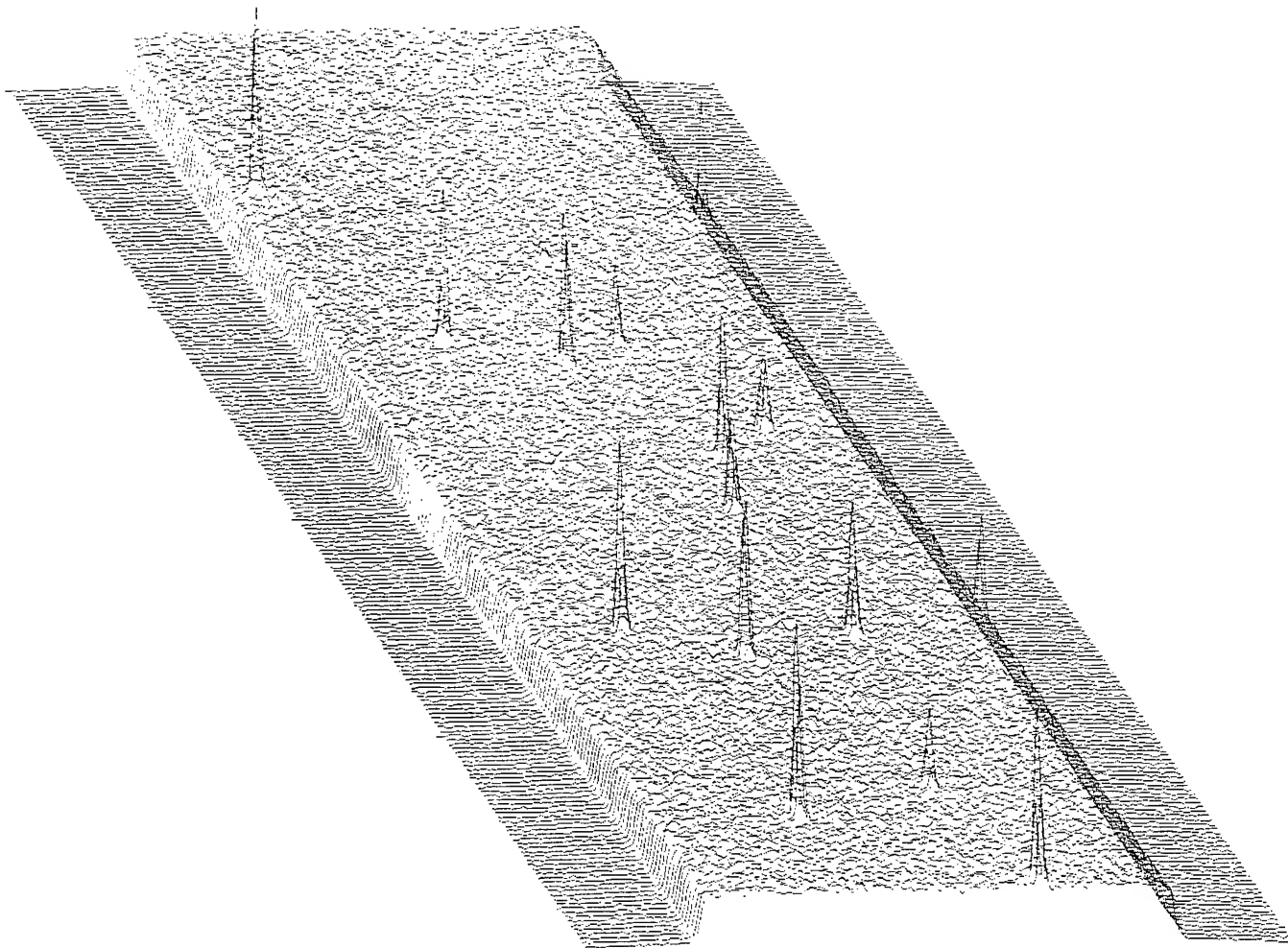


FIGURE 2

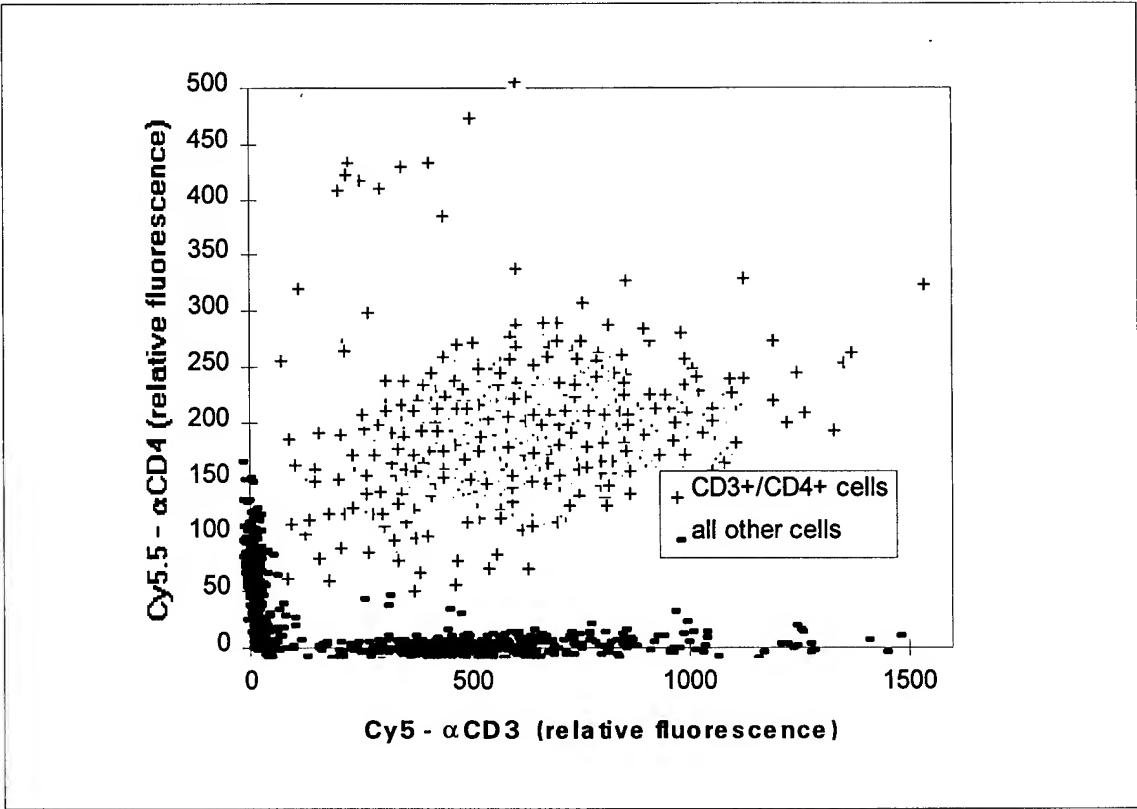


Figure 3

Wednesday, March 20, 1996

## Cell Analysis and Properties II

**BWD** 4:15 pm-5:15 pm  
Windsor Ballroom

Irving Bigio, *Presider*  
*Los Alamos National Laboratory*

**Rapid Analysis of Fluorescence Quenching of FITC Conjugated Antibodies on Individual Cells by Phase-Sensitive Flow Cytometry.** C. Deka, B. E. Lehnert, N. M. Lehnert, G. M. Jones<sup>+</sup>, L. A. Sklar<sup>+</sup>, J. A. Steinkamp. Los Alamos National Laboratory, Los Alamos, NM 87544. Telephone 505-665-1939 Fax 505-665-3024. (<sup>+</sup> GMJ and LAS are with the School of Medicine, University of New Mexico, Albuquerque, NM 87131.)

**Introduction:** In flow cytometry, fluorescence intensities from cells labeled with fluorescent antibodies are often used as a measure for the number of antibodies bound to specific receptor sites on the cells. Quantitative estimation of the number of receptor sites using this procedure assumes that the fluorescence intensity of the ensemble of antibody probes bound to a cell is proportional to the number of probes in that ensemble. However, in certain biological systems, non-linear effects such as fluorescence quenching may invalidate this assumption and lead to erroneous results. In most organic dyes, intermolecular interactions and energy transfer between molecules in close proximity to one another result in self-quenching of the fluorescence intensity [1,2]. This effect can manifest in antibody probes with a high fluorochrome to protein (F/P) ratio [2]. It can also occur due to close proximity of dye-conjugated probes relative to one another on a highly labeled cell surface. When the

probes are self-quenched due to probe-probe interactions, the measured total fluorescence intensity from a cell is no longer proportional to the number of probes bound to it. Therefore, experiments using fluorescent probes should be critically evaluated for quenching effects. Since self-quenching is accompanied by a change in the fluorescence decay and a decrease in the fluorescence lifetime, it may be conveniently identified using fluorescence lifetime spectroscopy. In this paper we apply the phase-sensitive detection method to investigate the impact of self-quenching on fluorescence lifetimes by flow cytometry. This permits hundreds of cells to be analyzed per second. Using a model system consisting of fluorescein isothiocyanate (FITC) labeled anti-mouse Thy1.2 antibodies bound to murine thymus cells, we demonstrate that, in addition to the expected variation of lifetimes as a function of F/P ratio of the probes, the fluorescence lifetime diminishes also as a function of antibody labeling concentration.

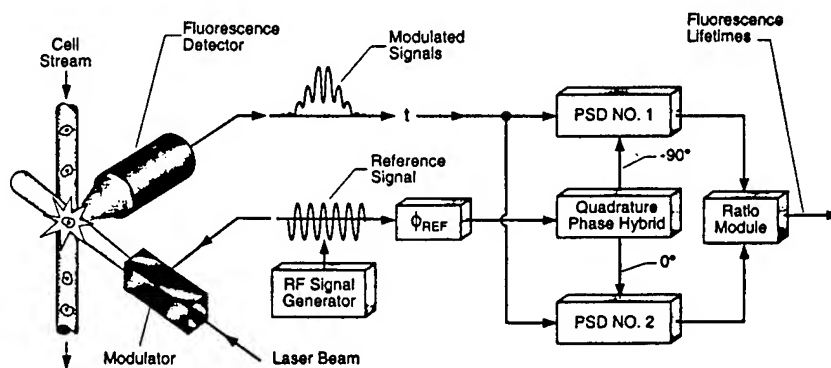


Fig. 1. Schematic diagram of the phase-sensitive flow cytometer. The fluorochrome labeled cells are excited by a modulated cw laser as they travel across the laser beam. The modulating fluorescence signal is detected at 90 to the plane containing the laser beam and the flow stream and processed by a phase-sensitive detection system. PSD1 and PSD2 are phase detectors (double balanced mixers).

When a reduction in the lifetime is observed in a labeled cell, it is important to distinguish quenching associated with clustered or randomly distributed antibody binding sites. For FITC, it is known that self quenching can be expected to play a significant role when the intermolecular distances are of the order of 50 angstrom [1]. For distances greater than this the intermolecular interaction decreases rapidly and the self quenching becomes insignificant. By correlating the fluorescence lifetime with intensity measurements in appropriate experiments, phase-sensitive flow cytometric analysis should be able to resolve these possibilities on a cell by cell basis.

**Lifetime Measurement in Flow:** For flow cytometric measurements, murine thymocytes labeled with the Thy1.2/FITC antibodies were excited at 488 nm by a cw laser beam from an Ar-ion laser (Model 2025: Spectra Physics, Palo Alto, CA) with the intensity being sinusoidally modulated at 29 MHz. The intensity modulation was accomplished using an electro-optic modulator Model 350 (Conoptics, Danbury, CT). The fluorescence from the cells was transmitted through a long-pass optical filter OG 515 (Melles Griot, Irvine, CA) and detected by a photomultiplier tube (PMT Model 4526, Burle Industries, Lancaster, PA). The modulated fluorescence signal was processed by analog phase-sensitive detection electronics to obtain the phase-shift and the lifetime at 29 MHz (FIG. 1). The measurement principles of the phase-sensitive flow cytometer used for the present experiment have been described in detail elsewhere [3].

Lifetime measurements were conducted on cells that were labeled at low, medium, and high concentration (antibody/cell ratio). The highest concentration labeling corresponded to the case when all the receptor sites on the cell were labeled by the antibodies. This case is designated herein as the 1:1 labeling concentration. The medium and low concentration labeling were obtained by diluting the antibody solution by 100 and

1000 folds prior to labeling the cells. These are designated as concentrations 1:100 and 1:1000 respectively. Figure 2a shows a comparison of fluorescence lifetime distributions of the cells labeled at the above mentioned concentrations with FITC/Thy1.2 antibodies having an average F/P ratio of 13.7. Figure 2b and 2c show comparison of the lifetimes for different

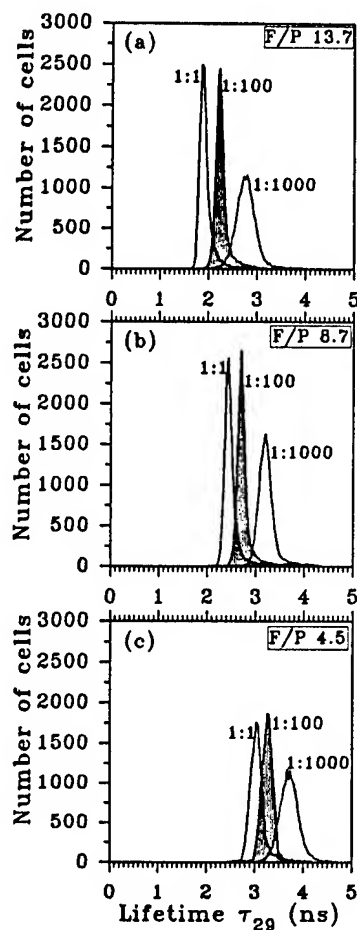


FIG. 2. Comparison of fluorescence lifetimes of FITC/Thy1.2 labeled mouse thymocytes for the three different antibody labeling concentrations of 1:1, 1:100 and 1:1000. Figures (a), (b), and (c) show the comparison using antibodies having F/P ratio of 13.7, 8.7, and 4.5, respectively.

**Table 1**

Fluorescence lifetimes of murine thymocytes labeled with FITC-conjugated Thy 1.2 anti-mouse antibodies measured in flow at a modulation frequency of 29 MHz.

F/P ratio	Lifetime in sparsely labeled cells (conc. 1:1000)	Lifetime in highly labeled cells (conc. 1:1)	Percentage Change in lifetime
4.5	3.7 ns	3.0 ns	19%
8.7	3.2 ns	2.4 ns	25%
13.7	2.8 ns	1.9 ns	32%

labeling concentrations of antibodies having F/P ratios of 8.7 and 4.5 respectively. For each F/P ratio, the lifetime was the shortest for the highest labeling concentration studied. The changes in the measured lifetime at the 1:1 labeling concentration relative to that at the 1:1000 labeling concentration are shown, as a percentage of the latter, in Table 1. The observed reduction in lifetime with increased binding is consistent with fluorescence self-quenching effects expected from probe-probe interactions in a densely packed ensemble.

**CONCLUSION:** Phase-sensitive flow cytometry permits efficient lifetime measurements on individual cells labeled with antibody-fluorochrome conjugates. Since changes in fluorescence decay and lifetime serve as indicators for fluorescence-quenching, phase-sensitive flow cytometry may be used to rapidly evaluate labeled cell samples for self-quenching effects. We have demonstrated this using antibody labeled murine thymus cells.

[This work was performed under the sponsorship of the United States Department of Energy, Los Alamos National Laboratory, the National Institute of Health (grant no. R01-RR07855 and RR01315). The portion of the work conducted at the University of New Mexico Cancer Center was supported by (grant nos. GM37696).]

## REFERENCES

1. Chen RF and Knutson JR: Mechanism of fluorescence concentration quenching of carboxyfluorescein in liposomes: energy transfer to nonfluorescent dimers. *Anal Biochem* 172, 61-77, 1988.
2. Haugland RP: *Molecular Probes Handbook of Fluorescent Probes and Research Chemicals*, 5th ed. Molecular Probes Inc. 1992.
3. Steinkamp JA, Yoshida TM and Martin JC: Flow cytometer for resolving signals from heterogeneous fluorescence emissions and quantifying lifetime in fluorochrome-labeled cells/particles by phase-sensitive detection. *Rev. Sci. Instrum.* 64 (12):3440-3450, 1993.

# Measurement of laser-excited fluorescence spectra of individual airborne biological particles

Gang Chen, Richard K. Chang  
Yale University

Department of Applied Physics and Center for Laser Diagnostics, New Haven, CT 06520-8284  
(203)432-4272, (203)432-4274(Fax)

Paul Nachman, Ronald G. Pinnick, Steven C. Hill, Gilbert L. Fernandez  
Army Research Laboratory, White Sands Missile Range, NM 88002-5501  
(505)678-4078/5634, (505)678-2432 (Fax)

Michael W. Mayo  
Systems and Processes Engineering Corp., Austin, TX 78746-6556  
(512)306-1100, (512)306-1122 (Fax)

We are developing laser based fluorescence particle counters and spectrum analyzers which should be useful for real-time monitoring of airborne bacteria, proteins or other particles. Improved methods for detecting and characterizing airborne particles could be useful in applications such as studying the spread of diseases of plants, animals, and humans, or determining the sources of particles in clean rooms. Many airborne bacteria, pollens and viruses are of medical, agricultural, or ecological interest. Some diseases of humans (e.g., tuberculosis), of farm animals, of agricultural crops, and of forest trees are commonly transmitted through the air. Some airborne pollens cause allergies in humans. Bacteria (e.g., *Bacillus thuringiensis*) used to control certain pests are commonly disseminated through the air.

Real-time measurements of fluorescence and/or fluorescence spectra of airborne particles should be useful for partial characterization of such particles and could help in understanding the generation and dispersal of pathogens or allergenic particles. The primary fluorescent materials in most bacterial cells are the same: the amino acids tryptophan, tyrosine, and phenylalanine (which cause proteins to have excitation/emission maxima at  $\sim 280/320\text{-}350\text{ nm}$ ); the reduced nicotinamide adenine dinucleotides (NADH, NADPH, with peak excitation/emission  $\sim 340/450\text{ nm}$ ); and the flavin compounds (e.g., FAD, riboflavin, with peak excitation/emission at  $\sim 450/515\text{-}565\text{ nm}$ ). Additional fluorescent molecules in biological particles can cause additional spectral features and thereby increase the differences among fluorescence spectra from different species.

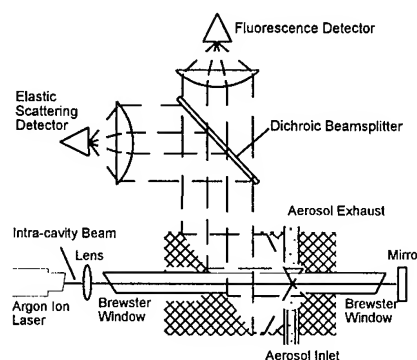


**Figure 1:** Schematic of the intracavity version of the fluorescence particle counter. An aerosol scattering cell is placed inside the cavity of an argon ion laser.

We first assembled a fluorescence particle counter[1] for detecting and partially discriminating between biological and nonbiological particles. A schematic is shown in Fig. 1. The instrument is basically a laser particle counter which measures the elastic scattering and undispersed fluorescence of single particles as they traverse an intense laser beam. Particles flow through the cell at about 20 m/s. Figure 2 shows the numbers of particles (vertical axis, log scale) in different bins, each corresponding to a range of elastic and fluorescence (normalized by elastic scattering) intensities. The particles are primarily *B. subtilis* spores. Similar measurements of a typical atmospheric dust,

kaolin, shows very little fluorescence.

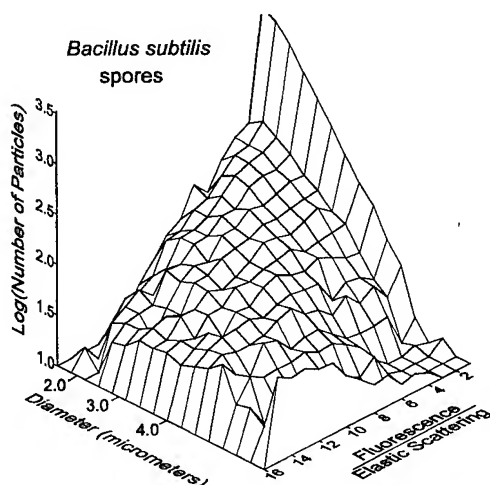


**Figure 2:** Histogram of *B. subtilis* spores measured with the extracavity FPC. The most numerous particles have a low fluorescence, and may be salts, proteins, or other nonfluorescing compounds.

Next, to measure the spectra of airborne particles, we assembled an aerosol fluorescence spectrum analyzer (AFS). [2] In the AFS, as particles flow through an intracavity 488 nm laser beam, the fluorescence is collected and dispersed in a spectrometer. The spectrum is recorded with a cooled CCD. The instrument is able to record spectra of groups of bacterial particles as they flow through the beam, but is not sensitive enough to record spectra of individual bacterial particles. However, the instrument is able to record spectra of individual polystyrene microspheres doped with laser dyes. Subsequent to our original description [2], we recorded spectra of biological particles excited with 363 nm light, which can excite fluorescence from both NADH and flavins. Example spectra with 363 nm excitation are shown in Fig. 3.

In order to record the spectra of individual airborne particles, we next assembled a conditional-sampling aerosol fluorescence spectrum analyzer [3]. As particles flowed into the 488 nm laser beam, their elastic scattering or fluorescence was detected with a PMT. The PMT signal was used to turn on the intensifier in front of a cooled CCD (placed at the output port of a spectrometer). In this way, the ICCD recorded spectra only when a particle was in the beam and its elastic scattering or fluorescence exceeded some preset threshold. Figure 4 shows example fluorescence spectra collected from

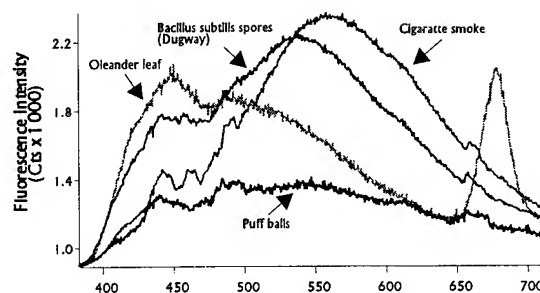


**Figure 3:** Fluorescence from aerosolized biological materials: *B. subtilis* spores, cigarette smoke, puff ball spores, aerosolized leaf materials. The excitation wavelength is 363 nm.

individual particles comprised of one or more *B. subtilis* spores. When the ICCD was not turned on by a signal from the PMT, most spectra had much smaller fluorescence levels.

A major limitation of the instruments described above is that because they require an intense cw laser beam, they are unable to excite fluorescence from proteins. Pulsed UV lasers are capable of exciting fluorescence from amino acids (e.g., tryptophan) in proteins. The problem with using a pulsed laser in a particle counter is that most pulses illuminate no particles (because the aerosol particles arrive at random times). Thus, in order to excite fluorescence in particles, the laser should be fired only when a particle is in its path.

In order to detect UV-induced fluorescence from airborne biological particles, we assembled a pulsed-UV-laser-based conditional-firing aerosol-fluorescence emission spectrum analyzer (CAFES). The frequency-quadrupled Nd:YAG laser (266 nm) fires only when a particle having an appropriate scattering characteristic moves into scattering region (as detected by a cw low power laser (HeNe or GaAlAs)). The CAFES measures the fluorescence spectra and elastic scattering intensity of individual airborne particles. We have detected the fluorescence spectra of airborne particles made from various biological materials, e.g., *B. subtilis* spores, *B. anthracis* spores, riboflavin, and tree leaves. This CAFES is useful for detecting and characterizing airborne bacteria and other airborne particles of biological origin which may be within a much larger number of non-fluorescent particles.

Fluorescence spectra should be useful for discriminating between biological and nonbiological airborne particles, and for discriminating among



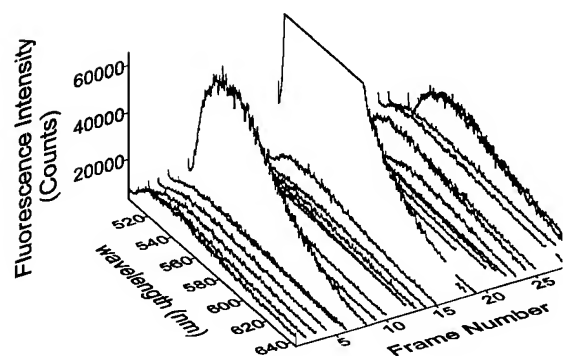


**Figure 4:** Fluorescence spectra of single particles composed of one or more *B. subtilis* spores recorded in the presence of nonfluorescing kaolin particles. The ICCD was triggered by signals from a PMT which records the total fluorescence from the particle. Each exposure was 200  $\mu$ s. Thirty successive spectra are shown. The highest intensity spectra presumably correspond to particles which contain many spores.

limited numbers of possible types of biological particles. An advantage of intrinsic-fluorescence based instruments is that they have no requirement for expendables. Fluorescence spectra in themselves are clearly inadequate for accurate species determinations. However, the relative nonspecificity of the AFS can be an advantage in cases where there are many types of unknown bacteria since it requires no prior synthesis of specific probes.

### References

- [1] R. G. Pinnick, S. C. Hill, P. Nachman, J. D. Pendleton, G. L. Fernandez, M. W. Mayo, and J. G. Bruno, "Fluorescence particle counter for detecting airborne bacteria and other biological particles," *Aerosol Sci. and Technol.*, in press.
- [2] S. C. Hill, R. G. Pinnick, P. Nachman, G. Chen, R. K. Chang, M. W. Mayo, and G. L. Fernandez, "Aerosol fluorescence spectrum analyzer: real-time measurement of emission spectra of airborne biological particles," *Appl. Opt.*, **34**, 7149-7155 (1995).
- [3] P. Nachman, G. Chen, R. G. Pinnick, S. C. Hill, R. K. Chang, M. W. Mayo, and G. L. Fernandez, "Conditional-sampling spectrograph detection system for fluorescence mea-

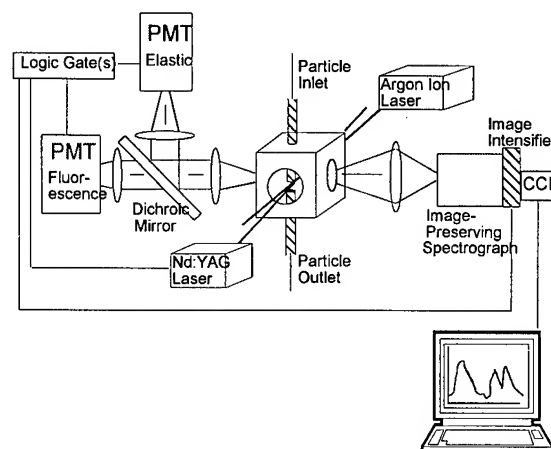


**Figure 5:** Simplified system schematic of the CAFES. The particle first flows through the cw beam (a semiconductor laser operating at 670 nm, or an argon ion laser at 488 or 363 nm, or a HeNe laser at 633 nm). The light scattered by and emitted from the particle is detected by the PMTs. The flashlamp of the Nd:YAG laser is triggered at 10 Hz. When one or both of the PMTs detects a particle in the scattering volume, and when the Nd:YAG laser is ready to fire (300 to 400  $\mu$ s after the lamp emission is initiated), then the laser is Q-switched. The fluorescence is spectrally analyzed using an image-preserving spectrometer and an intensified CCD or a liquid-nitrogen-cooled CCD.

surements of individual airborne biological particles," *Appl. Opt.*, in press.

# Light scattering from cells

Andrew Dunn, Colin Smithpeter, A.J. Welch, Rebecca Richards-Kortum  
Biomedical Engineering Program, University of Texas, Austin, TX 78712

## 1 Introduction

With the advent of optical imaging techniques capable of imaging on the cellular level, it is important to understand the contributions that each cellular constituent makes to the total image. This requires an understanding of how light interacts with each cell component.

Due to the inhomogeneities and complex structure of tissue, light propagation in biological tissue is difficult to describe analytically. Previous modeling techniques such as radiative transport theory, Monte Carlo modelling, and the diffusion equation approximated the microscopic structure of tissue as a collection of discrete scattering particles. To understand light interaction with cells however, this approximation is no longer valid. On the cellular level, the changes in index of refraction arise from the discrete cell components such as the extracellular fluid, cell membrane, cytoplasm, nucleus, and other organelles. To describe the interaction of light with cells and cell components on the microscopic level, it becomes necessary to adopt a model based on Maxwell's equations since the changes in index of refraction between cell components are on the order of the wavelength. In this paper we examine the phase function, or angular distribution of scattered light,  $P(\theta)$  from a single cell.

## 2 Finite Difference Model and Results

The finite difference time domain technique [1] was used to solve Maxwell's equations numerically within and around a cell. Using Yee's algorithm Maxwell's two curl equations are discretized in two dimensions yielding an electric field ( $E$ ) grid and a magnetic field ( $H$ ) grid which are spatially and temporally offset. A plane wave was incident on the cell and the fields over the grid are updated at each time step until steady state is reached. For example, the  $E_z$  component of the electric field was updated using

$$E_z^{n+1}(i, j) = E_z^n(i, j) + \frac{\Delta t}{\epsilon(i, j)\delta} [H_y^{n+1/2}(i-1, j) - H_y^{n+1/2}(i, j) + H_x^{n+1/2}(i, j-1) - H_x^{n+1/2}(i, j)] \quad (1)$$

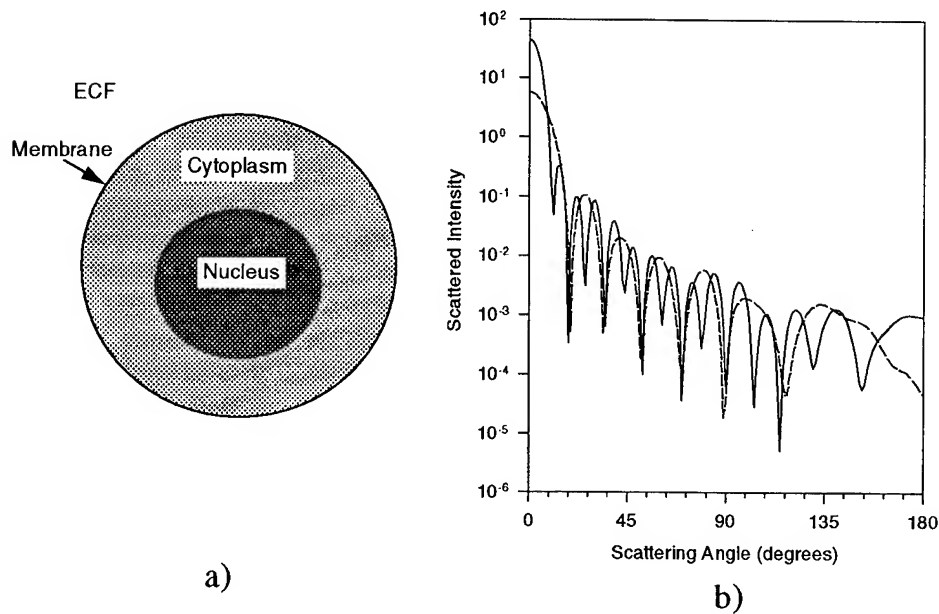


Figure 1: a) Cell used to compute scattered field pattern. The indices of refraction are:  $n_{ECF} = 1.35$ ,  $n_{membr} = 1.4$ ,  $n_{cyto} = 1.37$ ,  $n_{nucl} = 1.39$ . The cell diameter is  $7.5 \mu\text{m}$ . b) Scattered field pattern (arb. units) for entire cell (solid line) and the same cell with  $n_{cyto} = n_{ECF}$  (dashed line).

where  $\Delta t$  is the time step and  $\delta$  is the grid separation. The dielectric constant,  $\epsilon(i, j)$ , is assigned a different value over the grid according to the index of refraction of the cell components ( $n = \sqrt{\epsilon_r}$ ). Figure 1a demonstrates how the cell was created. After the fields within the cell were computed, the scattered field pattern,  $P(\theta)$ , was computed using a near field to far field transform.

Figure 1b shows the far field pattern for the cell shown on the left (solid line). The scattering angle was measured with respect to the center of the cell with 0 degrees being complete forward scatter and 180 degrees being backscatter. The scattered intensity is highly forward directed and contains numerous peaks and valleys due to interference effects.

By removing each of the cell components and computing the scattered pattern, it was determined that the overall shape of the scattering pattern is due mainly to the cytoplasm. This is seen in Figure 1 where the dashed line represents the scattered intensity of the cell in the absence of the cytoplasm (i.e.,  $n_{cyto} = n_{ECF}$ ). The nucleus contributes to the overall intensity level of the pattern and the membrane contributes only to the backscatter ( $180^\circ$ ).

Including melanin in the cell model has a significant effect on the scattered field pattern as shown in Figure 2b. Because of its high index of refraction ( $\sim 1.7$ ) [2] and

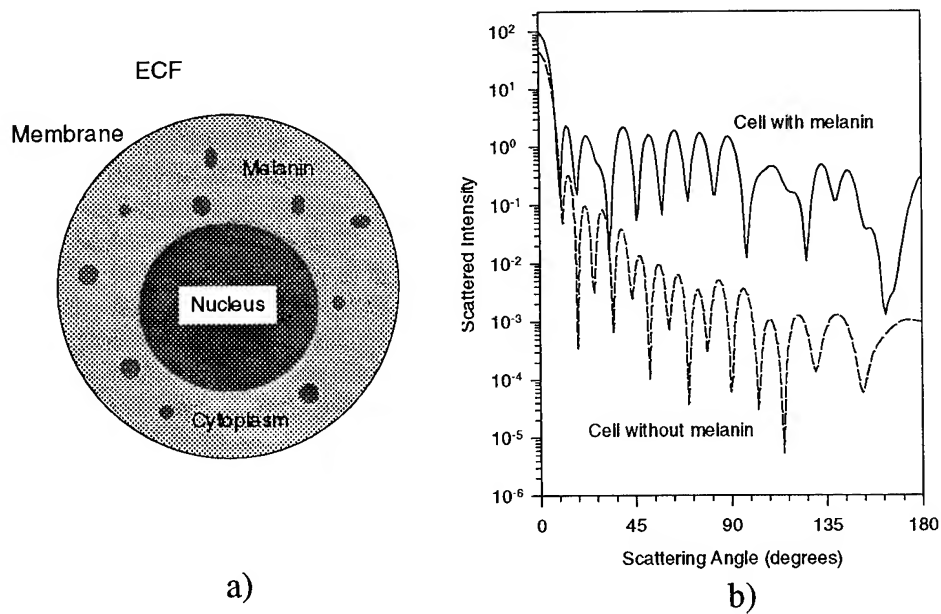


Figure 2: a) Cell containing melanin ( $n_{\text{melanin}} = 1.7$ ). b) Scattered field patterns (arb. units) for cell with (solid line) and without (dashed line) melanin.

small size, melanin causes a large increase in the backscattered light compared to a cell without melanin. This effect has been observed in confocal images of skin, which rely on backscattered light [2].

The finite difference time domain solution of Maxwell's equations is a powerful technique that can be used to determine the optical fields within a cell and the scattering pattern from that cell. Future work will focus on extending this technique to three dimensional cells and relating the scattering patterns to the scattering coefficient,  $\mu_s$  and anisotropy factor  $g$ .

## References

- [1] K. Yee, "Numerical solutions of initial boundary value problems involving maxwell's equations in isotropic media," *IEEE Transactions on Antennas and Propagation*, vol. AP-14, pp. 302–307, 1966.
- [2] M. Rajadhyaksha, M. Grossman, D. Esterwitz, R. Webb, and R. Anderson, "In-vivo confocal scanning laser microscope of human skin: melanin provides strong contrast," *Journal of Investigative Dermatology*, vol. 104, pp. 946–952, 1995.

**Thursday, March 21, 1996**

## Poster Session

**BThA** 8:30 am-10:30 am  
Windsor Ballroom

## Noninvasive Determination of Blood Contents Using a Photoacoustic Laser Sensor

G. Spanner and R. Niessner

Technical University of Munich, Institute of Hydrochemistry

D-81377 München, Marchioninstr. 17, Germany

### Introduction

The noninvasive determination of blood and tissue parameters is one of the most promising applications of photoacoustic laser spectroscopy (PALS). With PALS it is possible to obtain spectra from biomedical specimens that are completely opaque to transmitted radiation. Furthermore PALS provides the possibility of noninvasive depth profiling by using the delay time or the phase shift of the generated acoustic signal. Figure 1 shows the principle of noninvasive PALS generation. The creation of the photoacoustic signal in the sample is based on the conversion of absorbed light into heat by non-radiative processes. The heat-induced expansion generates acoustic shock waves. The waves transverse the sample and can be detected by a pressure-sensitive element [1]. Using the Q absorption band, which is located in the region of 500 to 600 nm, an absorption spectrum of hemoglobin can be obtained noninvasively.

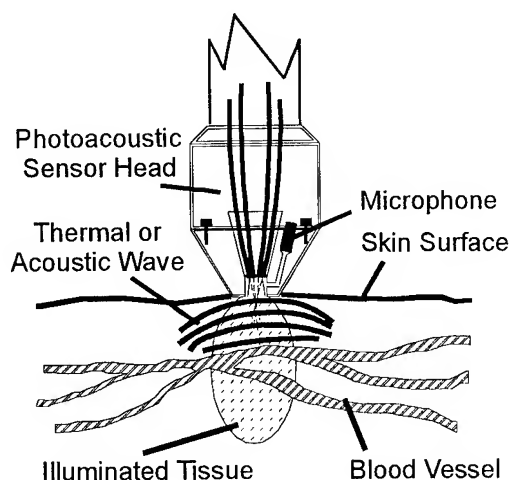


Fig. 1

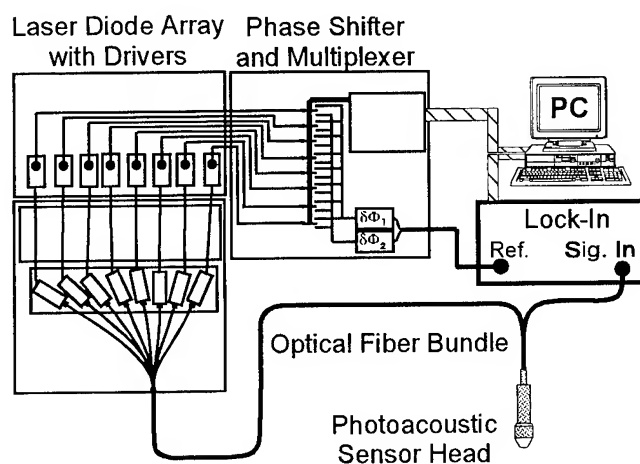


Fig. 2

The largest penetration depths of laser radiation into human tissue are obtained within the so-called therapeutic window which expands from about 600 nm to 2.5  $\mu\text{m}$ . In this near-infrared region the absorption of water and the main tissue chromophores are low enough to allow penetration depths up to several mm. Therefore this spectral region is well suited for the noninvasive detection of glucose, because the glucose molecule shows a significant absorption maximum at 1.57  $\mu\text{m}$ . Due to spectral interferences of other blood substrates like cholesterol, a single wavelength measurement cannot provide a reliable glucose determination. The influence of the spectral interferences, can be reduced by using several laser wavelengths and by applying the methods of multivariate calibrations. New developments in the area of laser diodes led to compact and high power narrow bandwidth light sources. These diodes are available at various wavelengths in the near infrared region. As the semiconductor devices are very compact and reliable devices, they are well suited for the development of a laser diode array with several independent laser elements. If up to 8 lasers with suitable wavelengths are selected, a single analyte like glucose can be determined even in a very complex matrix like whole blood.

### Experimental

First experiments were carried out using an excimer pumped dye laser as tunable laser source in the wavelength region between 520 nm and 600 nm. For the detection of the photoacoustic signal a piezoelectric ceramic was used. The ceramic was integrated into a photoacoustic sensor head which was coupled to the dye laser via an optical fiber. This experimental setup was mainly used for noninvasive measurement of hemoglobin spectra and the determination of the depth-resolving capabilities of the photoacoustic principle.

For measurements in the near infrared region, a laser diode array was developed. The whole experimental set-up is shown in Figure 2. For the detection of the photoacoustic signal, a lock-in amplifier was used. In order to increase the sensitivity of the system, a special modulation scheme was applied [2]. For this purpose, the phase shifter and multiplexer unit is necessary. The whole arrangement is controlled by a personal computer.

### Results

The in vitro photoacoustic spectra of whole blood taken through a highly light scattering vinyl membrane showed good agreement with reference spectra of diluted hemoglobin solutions which were obtained with a commercial spectral photometer. Small differences in the peak heights were mainly caused by influences of scattered light in the 0.12 mm thick membrane which served as a simple model of human skin. In vivo spectra taken from various parts of the human body also showed the two absorption peaks of oxyhemoglobin. This results confirmed, that the photoacoustic spectroscopy is an effective method for obtaining blood spectra in a noninvasive way. Additionally, a depth resolution of 0.1 mm can be obtained by measuring the delay time between

the laser pulse and the arrival of the acoustic signal at the surface of the sensor head. This depth information can be used for example for the normalization of signals from different tissue depths. Another application of this feature could be a depth-resolved angiographic method.

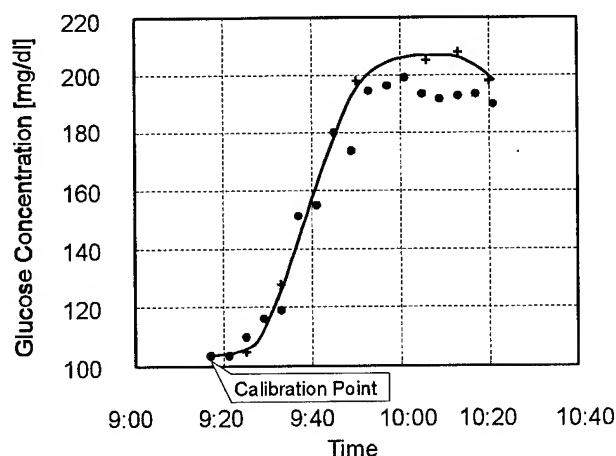


Fig. 3

The concentration values obtained from the invasively determined samples are interpolated by a spline fit. The predicted values of the calibrated photoacoustic sensor system are given by the filled circles. Only one calibration point is necessary to compensate absolute offsets. With the photoacoustic sensor a prediction error sum of squares of  $\text{PRESS}^{1/2} = 46.5 \text{ mg/dl}$  relative to the enzymatic method was obtained.

For the determination of glucose, the diode laser array was used. The wavelengths of the diodes were selected in a way, that the resulting calibration showed a minimum prediction error. With this arrangement, an oral glucose tolerance test was carried out. After an individual calibration of the sensor system the in-vivo blood glucose variations could be monitored with acceptable accuracy. Results obtained during a tolerance test are shown in Figure 3. Reference values were determined by a standard clinical enzymatic method and are indicated by crosses.

The concentration values obtained from the inva-

### Conclusions

The results obtained with a pulsed dye laser system have shown, that photoacoustic laser spectroscopy is well suited for the noninvasive determination of blood spectra. For absorbing layers, a depth resolution of 0.1 mm can be obtained.

The in-vivo determination of glucose concentrations at physiological levels showed, that variations of blood glucose levels can be monitored with acceptable precision using small and inexpensive laser diodes and a special modulation scheme. Highly integrated multiwavelength semiconductor laser arrays emitting at several wavelengths will soon become available. Such devices will lead to compact and affordable spectroscopic systems which can be applied for the development of small noninvasive glucose monitors for diabetic patients.

### References

1. S. A. Akhmanov, V. E. Gusev, A. A. Karabutov: Pulsed optoacoustics: Achievements and perspective. *Infrared Phys.* **29**, 815-838 (1989).
2. G. Spanner, R. Niessner: New concept for the noninvasive determination of physiological glucose concentrations using modulated laser diodes. *Fres. J. Anal. Chem.* In press (1995).



## Optical metabolic imaging of ocular tissue with two-photon excitation laser scanning microscopy

Barry R. Masters, Department of Anatomy & Cell Biology, Uniformed Services University of the Health Sciences, 4301 Jones Bridge Road, Bethesda, MD 20814.

Tel. 301-295-3204 Fax: 301-295-1715 e-mail: BMASTERS@USUHSB.USUHS.MIL

### Introduction

Light can be used as a noninvasive probe to monitor cellular function in cells, tissues and organs. Cellular metabolism can be noninvasively optically monitored by the technique of redox fluorometry. The probes are the intrinsic fluorescent pyridine nucleotides, and the flavoproteins. The pyridine nucleotides, NAD(P)H are excited in the region 365 nm and fluoresce in the region 400-500 nm. The flavoproteins are excited in the region 450 nm and fluoresce in the region 500-600 nm. Typically the fluorescence is imaged and changes in fluorescence intensity follow changes in cell and tissue oxidative metabolism.

Two-dimensional metabolic imaging based on redox fluorometry has two limitations. First, there is photobleaching of the fluorescent molecules during the measurement period. Second, the short wavelengths preclude deep penetration of highly scattering tissues such as human skin. Our previous work on the cornea in which we have used redox fluorometry is due to the low light scatter of the normal cornea Masters, 1990; Masters et al., 1993; Masters, 1993; Masters & Chance, 1993). However, further developments and applications of optical metabolic redox imaging of the ocular lens, and normal and pathological skin require longer wavelengths of light to penetrate deep into these highly scattering tissues.

### Methods

The technique of 2-photon excitation laser scanning microscopy has been used to overcome the two problems cited previously.

M. Goppert-Mayer developed the theoretical foundation for two photon excitation processes. The use of a laser scanning microscope for fluorescence imaging based on two-photon excitation microscopy was first developed by Denk et al., 1990. The principle is the simultaneous absorption of two photons; two photons of wavelength in the near infrared induce an electronic transition that normally required a ultraviolet photon. The experimental verification of the two-photon absorption process is that the number of electronic transitions from the ground state to the excited states is proportional to the square of the instantaneous intensity.

The practical instrument consists of a laser scanning confocal microscope that is used for scanning the laser beam and for detection of the specimen fluorescence. The optical sectioning is derived from the physics of the optical system. A series of 150-fs pulses of 700 nm light from a Nd:YAG pumped Satori dye laser are directed into the optical path of a scanning confocal microscope with the aperture opened up. The diffraction-limited focusing of the laser beam and the temporal concentration of the 100-fs pulses generated by the mode-locked laser result in two-photon excitation processes only in the region of focus. Outside of the focal region there is insufficient photon density, and therefore no absorption process occur. Therefore, outside of the focal regions there is no signal; this is the origin of the optical sectioning. To keep the biological samples in a viable state a pulse duty cycle of  $10^{-5}$  keeps the average power near 10 mW which is in the range of power normally used in a laser scanning confocal microscope.

The advantages of this imaging system are: (1) the near infrared light is less damaging to living cells and tissues, (2) there is deeper tissue penetration, and (3) photobleaching is limited to the region of focus. The 700nm light results in deep tissue penetration since both tissue absorption and scatter are reduced.

### Results

Two-photon excitation laser scanning microscopy was used to monitor the metabolic state of both an ex vivo rabbit eye and an ex vivo human ocular lens. These studies are based on the two-dimensional monitoring of NAD(P)H fluorescence intensity. The figures below show the applications of the methodology. The temporal changes in NAD(P)H were monitored over a two-fold change in fluorescence intensity following chemical induced cellular hypoxia.

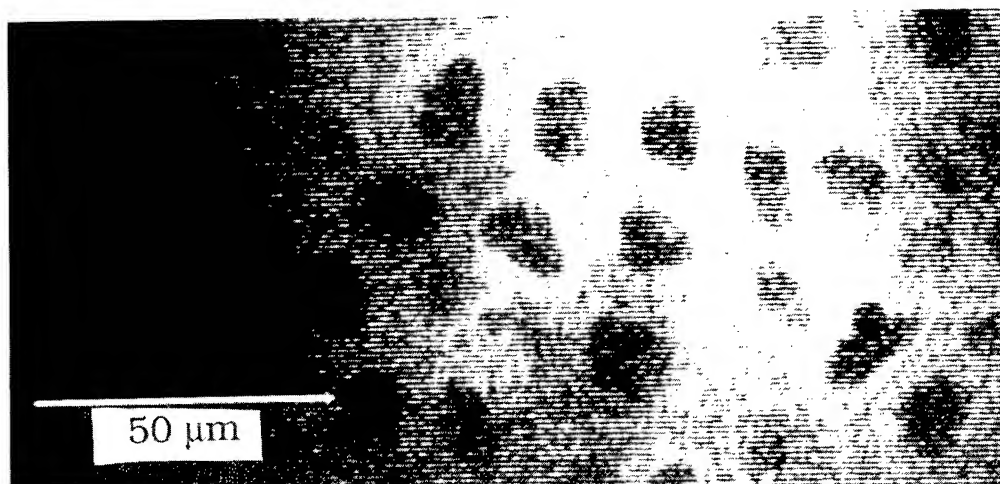


Figure 1. NAD(P)H fluorescence image showing basal epithelial cells in an *ex vivo* rabbit cornea. This image is located 50 μm below the surface of the cornea.

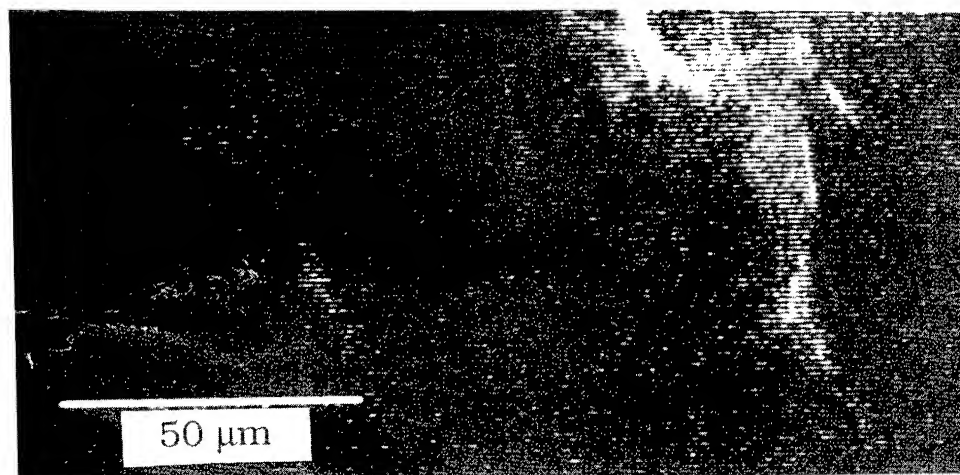


Figure 2. NAD(P)H fluorescence image showing keratocyte cellular processes in the corneal stroma of an *ex vivo* rabbit eye.

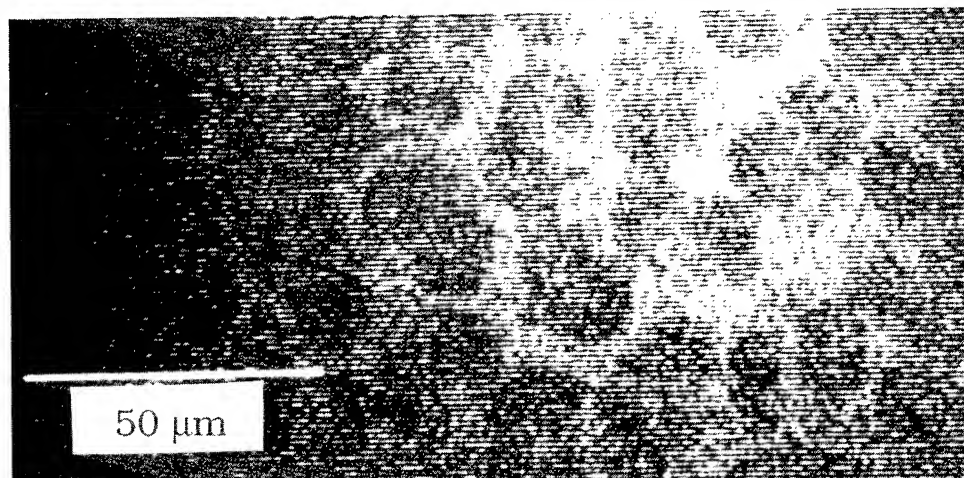


Figure 3. NAD(P)H fluorescence image showing corneal endothelial cells in an *ex vivo* rabbit eye. This image is located 400 μm below the surface of the cornea.

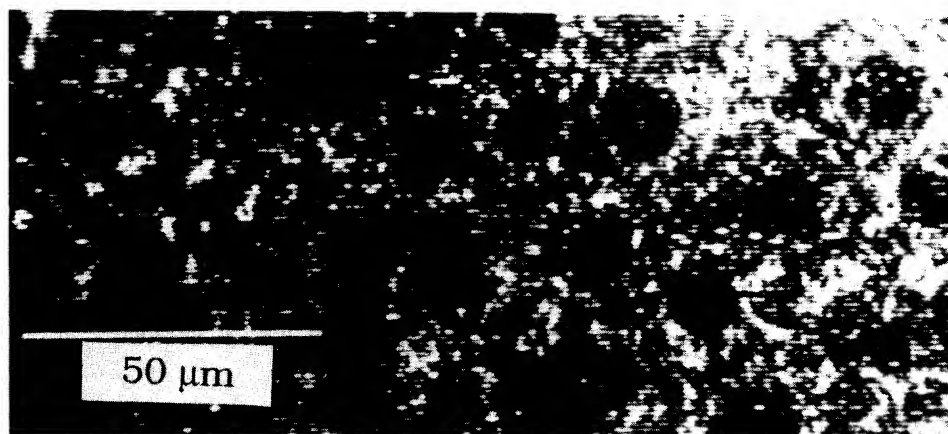


Figure 4. NAD(P)H fluorescence image showing epithelial cells on the surface of an *ex vivo* human ocular lens.

### Discussion

These studies demonstrate the feasibility of two-photon excitation functional microscopy on ocular tissue. The images are acquired through a tissue thickness of 400 nm. Further developments in progress involve the application of the methods to *in vivo* imaging of thicker and more highly scattering tissues. Our goal is the development of non-invasive optical methods for the diagnosis of pathology in human cells and tissues.

### References

1. Chance, B. and Thorell, B. (1959) Localization and kinetics of reduced pyridine nucleotide in living cells by microfluorometry. *J. Biol. Chem.* **234**, 3044-3050.
2. Masters, B.R. (1990). *In vivo* corneal redox fluorometry. *Noninvasive Diagnostic Techniques in Ophthalmology* (ed. by B.R. Masters) pp. 223-247, Springer-Verlag, New York.
3. Masters, B. R., Kriete, A. and Kukulies, J. (1993) Ultraviolet confocal fluorescence microscopy of the *in vitro* corneal: redox metabolic imaging. *App. Opt.* **32**, 592-596.
4. Masters, B.R. (1993) Functional imaging of cells and tissues: NADP(H) and flavoprotein redox imaging. in : *Medical Optical Tomography: Functional Imaging and Monitoring*, (Eds. G. Müller et al. ) SPIE Press, Bellingham.
5. Masters, B.R., Chance, B. Redox confocal imaging: intrinsic fluorescence probes of cellular metabolism, in: *Fluorescent and Luminescent Probes for Biological Activity*, (ed. W.T. Mason), Academic Press, 1993.
6. Goppert-Mayer, M. (1931). Über elementarake mit zwei quantersprungen. *Ann. Phys.* **9**, 273-294.
7. Denk, W. Strickler, J.H., and Webb, W.W. (1990). Two-photon laser scanning fluorescence microscopy. *Science*, **248**, 73-76.
8. Piston, D. W., Masters, B. R. , Webb, W. W. (1995) three-dimensionally resolved NAD(P)H cellular metabolic redox imaging of the *in situ* cornea with two-photon excitation laser scanning microscopy. *J. of Micros.* **178**, Pt. 1, 20-27.

## Measurement of the muscle optical properties on muscular dystrophy patients by a frequency-domain photometer.

Valentina Quaresima\*, Sfarenì Romina<sup>^</sup>, Assunta Pizzi<sup>&</sup>, Marco Ferrari\*<sup>^</sup>

\* Dip. Scienze e Tecnologie Biomediche, University of L'Aquila, 67100 L'Aquila, Italy;

<sup>^</sup> Lab. Biologia Cellulare, Istituto Superiore di Sanità, 00162 Roma, Italy;

<sup>&</sup> Fondazione Pro Juventute Don C. Gnocchi, 50020 Pozzolatico, Italy.

### Introduction

The novel therapeutic approaches such as gene therapy increase the need of quantitative methods to evaluate the progression of muscular dystrophy (MD) disease. Non invasive near infrared spectroscopy (NIRS) might play an important role in the evaluation of muscle tissue function.

Frequency-domain photometers can measure muscle optical parameters and calculate haemoglobin content and saturation.

We recently reported some preliminary results obtained using this instrument (1-3). Absorption ( $\mu_a$ ) and reduced scattering coefficients ( $\mu'_s$ ) at 715 and 825 nm as well as haemoglobin saturation (Hb Sat) and content (Hb tot) of the forehead, forearm and quadriceps were estimated. Hb Sat was measured during ischaemia and exercise.

The aim of this study was to explore the possibility to use this instrument to map the  $\mu_a$  and  $\mu'_s$  on different muscles of MD patients.

### Methods

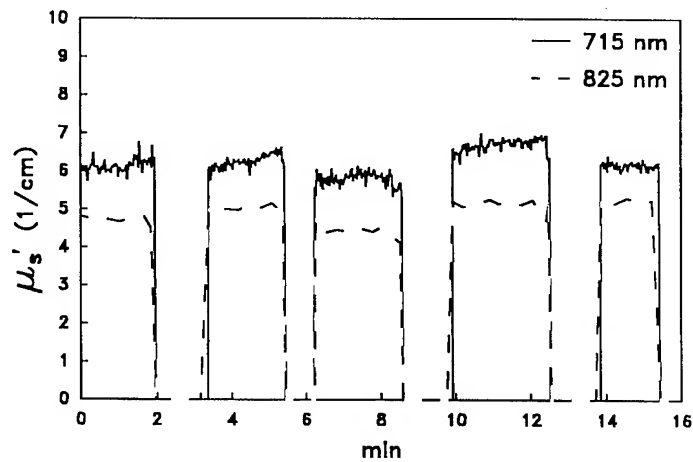
NIRS measurements were obtained by a frequency domain multi-source photometer (OMNIA, ISS, Champaign, Illinois) (4). Two near IR bands peaked at 715 and 825 nm were generated by two arrays of four intensity modulated light emitting diodes (LEDs). These LEDs are modulated at a frequency of 110 MHz. The LEDs and the bundle were included in a holder that was positioned on the monitored area. Oxy- and deoxy-haemoglobin concentrations were derived from extinction coefficients and absorption coefficients as previously described (4). The ratio oxy-haemoglobin/total haemoglobin was utilized to calculate Hb Sat.

Measurements were performed on untrained volunteers and muscular dystrophy MD patients. The sampling time was 1.6 s. Each subject gave informed consent before starting the study. Measurements were obtained on the forearm, the quadriceps, lateral and medial gastrocnemius and biceps.

### Results

The figure shows a typical recording of  $\mu'_s$  measured at 715 and 825 nm on 5 muscles. Some of the averaged data are summarized on the tables. A good reproducibility was found when the quadriceps  $\mu'_s$ ,  $\mu_a$ , Hb Sat and Hb tot measurements were repeated after 24 h (Tab.1). A significant difference of forearm  $\mu'_s$  was found between 12 controls and three Limb-girdle MD patients (Tab.2).

Different portable high-bandwidth frequency-domain photon migration instruments for tissue spectroscopy have been recently built (4-6). These results indicate that frequency-domain instruments can non-invasively map muscle absorption and reduced scattering coefficients providing information on muscle damage.



**Tab.1.** Measurement of quadriceps physiological and optical parameters ( $\mu_a$ : absorption coefficients;  $\mu_s'$ : reduced scattering coefficients)

N.	$\mu_a$ 715 nm ( $\text{cm}^{-1}$ )		$\mu_s'$ 715 nm ( $\text{cm}^{-1}$ )		$\mu_a$ 825 nm ( $\text{cm}^{-1}$ )		$\mu_s'$ 825 nm ( $\text{cm}^{-1}$ )		Hb Sat (%)		Hb tot ( $\mu\text{M}$ )	
C1 (r)	0.02		5.0		0.03		4.0		77		7	
C1 (l)	0.09		5.3		0.14		4.0		82		64	
C2 (r)	0.12		5.5		0.17		4.6		81		70	
C2 (l)	0.11		6.0		0.16		4.4		79		73	
C3 (r)	0.04		4.1		0.06		3.6		83		31	
C3 (l)	0.06		5.1		0.07		3.7		76		40	
C4 (r)	0.06		4.0		0.07		4.6		72		31	
C4 (l)	0.06		4.3		0.09		5.0		84		43	
FSO (r)	0.06		5.8		0.10		4.9		86		43	
FSO (l)	0.03		5.6		0.05		5.0		92		17	
NA1 (r)	0.01		3.7		0.02		3.0		99		9	
NA1 (l)	0.01		4.1		0.02		3.3		86		13	
NA2 (r)	0.03		6.2		0.05		5.5		91		30	
NA2 (l)	0.04		6.0		0.05		4.7		83		30	
H1 (r)	0.07	0.07*	4.7	4.0*	0.10	0.11*	4.5	3.4*	84	87*	44	55*
H1 (l)	0.07	0.07*	4.7	5.0*	0.10	0.10*	4.5	4.0*	84	87*	44	52*
H2 (r)	0.03	0.03*	5.2	5.2*	0.05	0.06*	4.6	4.9*	82	83*	18	20*
H2 (l)	0.04	0.04*	5.3	5.2*	0.06	0.06*	4.6	4.3*	82	74*	20	23*

C(1-4): Limb-girdle MD; FSO: facioscapulohumeral MD; NA(1-2): Neurogen atrophy; H(1-2): Control; \*: measurement repeated after 24h; r: right; l: left.

**Tab.2. Measurement of forearm physiological and optical parameters**  
 ( $\mu_a$ : absorption coefficient;  $\mu_s'$ : reduced scattering coefficient)

N.	$\mu_a$ 715 nm ( $\text{cm}^{-1}$ )	$\mu_s'$ 715 nm ( $\text{cm}^{-1}$ )	$\mu_a$ 825 nm ( $\text{cm}^{-1}$ )	$\mu_s'$ 825 nm ( $\text{cm}^{-1}$ )	Hb Sat (%)	Hb tot ( $\mu\text{M}$ )
C1	0.11	4.7	0.11	3.9	60	51
C2	0.09	4.4	0.14	4.6	83	63
C3	0.22	3.5	0.29	1.8	79	149
FSO	0.08	5.0	0.14	4.5	96	65
NA1	0.06	4.4	0.07	3.4	80	41
NA2	0.23	3.0	0.20	4.4	48	120
H	$0.14 \pm 0.02$	$2.7 \pm 0.4$	$0.20 \pm 0.02$	$2.2 \pm 0.3$	$77 \pm 2$	$100 \pm 7$

C(1-3): Limb-girdle MD; FSO: Facioscapulohumeral MD; NA(1-2): Neurogen Atrophy; H(n=12): Control.

(Support in part by Telethon-Italy Grant n° 501).

## References

1. R.A. De Blasi, S. Fantini, M.A. Franceschini, M. Ferrari, E. Gratton. *Medical & Biology Engineering & Computing* **33**: 228-230 (1995).
2. V. Quaresima, A. Pizzi, R.A. De Blasi, A. Ferrari, M. Ferrari. *SPIE* **2387**: 249-256 (1995).
3. M. Ferrari, R.A. De Blasi, S. Fantini, M.A. Franceschini, B. Barbieri, V. Quaresima, E. Gratton. *SPIE* **2389**: 868-874 (1995).
4. S. Fantini, M. A. Franceschini, J. S. Maier, S. A. Walker, B. Barbieri, E. Gratton. *Optical Eng.* **34**: 32-42 (1995).
5. A. Duncan, T. L. Whitlock, M. Cope and D. T. Delpy. *SPIE*, **1888**: 248-257 (1993).
6. S. J. Madsen, E. R. Anderson, R. C. Haskell and B. J. Tromberg. *Optics Letters* **19**: 1934-1936 (1994).

## **Optical Mapping Of The Human Breast Using Second Derivative Near Infrared Spectroscopy**

**Valentina Quaresima<sup>\*</sup>, Romina Sfareni<sup>^</sup>, Steve J. Matcher<sup>&</sup>, Jeffrey W. Hall<sup>@</sup>,  
Marco Ferrari<sup>\*^</sup>**

<sup>\*</sup> Dip. Scienze e Tecnologie Biomediche, University of L'Aquila, 67100 L'Aquila, Italy;

<sup>@</sup> NIRSystems, Inc., 12101 Tech Road, Silver Spring, MD, USA 20904;

<sup>^</sup> Lab. Biologia Cellulare, Istituto Superiore di Sanità, 00162 Roma, Italy.

<sup>&</sup> Dept. of Medical Physical and Bioengineering, 1st Floor Shropshire House, 11-20 Capper Street, University College London WC1E, UK.

### **Introduction**

Mammography is currently the only screening method with proven capability to diagnose nonpalpable cancers. Mammography, however, does not detect all cancers. Approximately 10% of clinically obvious breast cancers are not visible by mammography. Multiple areas of research have therefore been sought not only to improve mammography, but also to consider entirely new techniques in the study of breast cancer (1,2).

Sensible spectroscopic techniques can probe the biochemistry of tissue. Application of near infrared (IR) spectroscopy (650-1100 nm) to tissues has been limited to date mostly to the monitoring of brain and muscle oxygenation. Recently optical breast imaging instrumentations have been developed by several industries (3). Transillumination images of the breast were obtained by near IR phase modulation scanner prototypes using selected near IR wavelengths (3). However, very few *in vivo* breast spectral data are available (4). Derivative analysis have been proposed to quantify tissue chromophora (5,6).

We investigated the applicability of second derivative near IR spectroscopy to optimise the wavelengths for human breast imaging.

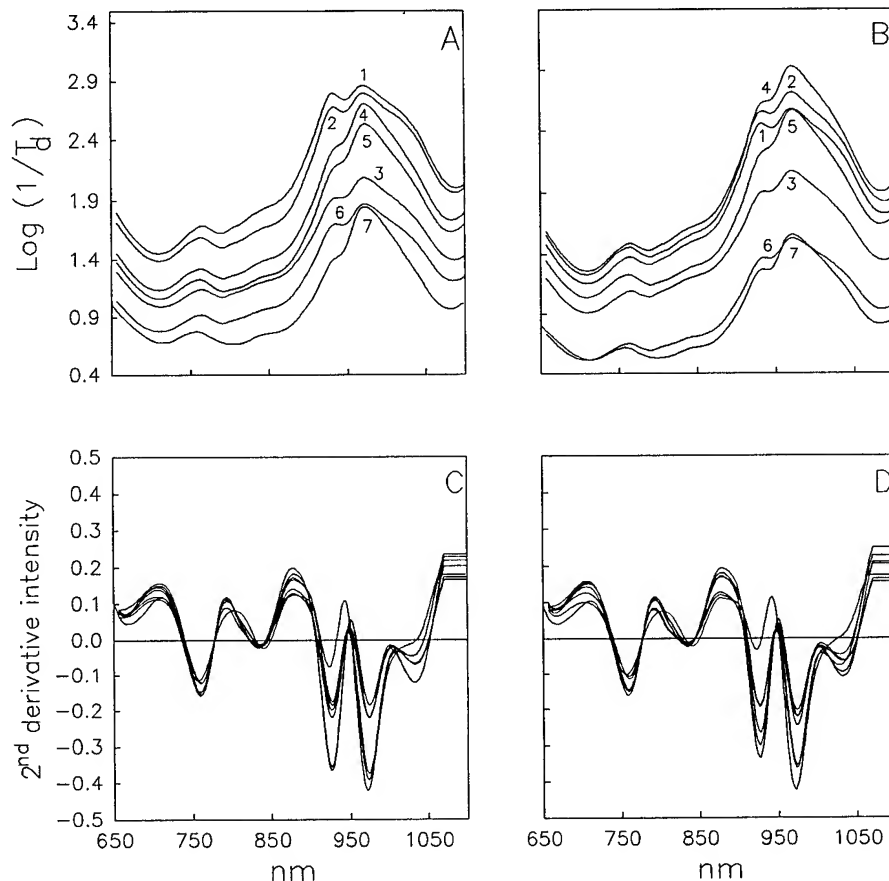
### **Methods**

Transillumination spectra of the female breast were collected using a NIRSystems, Inc. (Silver Spring, MD USA) model 6500 scanning spectrophotometer equipped with 2 optical fibers. Fibers were mounted in a hand held caliper device that could be adjusted for different thickness. Spectra were referenced to a 4 OD screen. Different locations (9-18) and/tickness (25-45 mm) on each breast were sequentially scanned. Second derivative spectra were calculated by using a sliding spectral segment of 20 nm and a gap between segments of 0 nm. Spectral data acquisition and mathematical treatments were accomplished using NIRSystems, Inc. Chemometric Software.

### **Results**

The figure shows transillumination spectra collected on seven locations of the right (panel A) and left (panel B) breast of a 25 year old woman. Measurements were made at the 7th day of the menstrual cycle. The breast was slightly compressed to a

thickness of 29-40 mm. Panel C and D are the corresponding second derivative spectra. Several absorption bands were found: deoxyhemoglobin contributes at 760 nm; water at 740, 860, and 965 nm; fat at 770, 820, 928, 1036 nm; proteins at 800, 910, 1020 nm. Therefore 800 nm is the unique finger print for proteins; 965 nm for water and 928 nm for fat. The separation of deoxyhemoglobin and fat contributions is difficult. Variations in the relative abundance of glandular and adipose tissue produced differences in the relative intensities of the hemoglobin, fat, water and protein absorption bands.



The preliminary results suggest that an accurate wavelength selection might improve the biochemical significance of the breast optical images.

## References

1. Adler D. D., Wahl R. L.; *American Journal Roentgenology* **164**:19-30 (1995).
2. Braeuning M. P., Pisano E. D.; *Breast Cancer Research and Treatment* **35**:31-38 (1995).
3. Reports of 1st and 2nd workshops on NIR Imaging in Medicine, EC Concerted Action Project on NIRS and Imaging 29-4, 1-5-1995; Florence.
4. Heusmann H., Kölzer J., Puls R., Otto J., Heywang-Köbrunner S., Zinth W.; *SPIE* **2389**: 798-808 (1995).
5. Ferrari M., Wilson D. A., Hanley D. F., Hartman J. F., Traystman R. J., Rogers M. C.; *American Journal of Physiology* **256**:H1493-H1499 (1989).
6. Matcher S. J., Cope M., Delpy D. T.; *Phys. Med. Biol.* **39**:177-196 (1994).



## Muscle Near Infrared Spectroscopy for Critically Ill Patients Management

De Blasi R.A., Ferrari M., Almenröder N.

\* Istituto di Anestesiologia e Rianimazione, I Università di Roma, Policlinico Umberto I, 00161 Rome, Italy.

& Dipartimento di Scienze e Tecnologie Biomediche, Università dell'Aquila, 67100 L'Aquila, Italy.

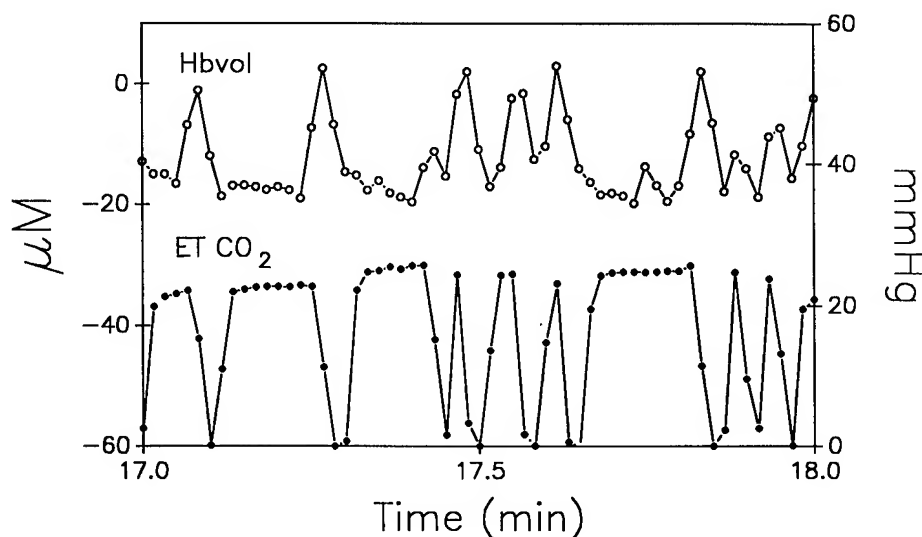
Near infrared spectroscopy (NIRS) technology can be employed for monitoring oxygenation and hemoglobin (Hb) changes in tissues during intensive care where such information may improve the clinical evaluation and treatment.

We apply NIRS on skeletal muscle in order to measure the Hb volume and oxygenation changes as well as the relationship between the oxygen consumption ( $\text{VO}_2$ ) and blood flow. The study was performed by a NIRO500 instrument (Hamamatsu Photonics, Japan). Sternomastoid muscle and forearm were investigated in two different studies. In the first study five patients with respiratory failure of different etiologies during weaning from mechanical ventilation were investigated (age  $58 \pm 7.5$ ). The sum of  $\Delta[\text{HbO}_2]$  and  $\Delta[\text{Hb}]$  (Hbvol) and the difference between  $\Delta[\text{HbO}_2]$  and  $\Delta[\text{Hb}]$  (Hbdif) were considered as an index of Hb volume and Hb oxygenation changes respectively. End-tidal  $\text{CO}_2$  and arterial oxygen saturation ( $\text{SaO}_2$ ) were continuously monitored. Muscle activation was evaluated by electromyography (EMG). All patients received assisted ventilation in pressure support mode. This mode of ventilation allows the patient to maintain his own respiratory rate. At the beginning of the study the highest level of pressure support was applied to prevent deep hypocapnia ( $\text{PaCO}_2 < 30 \text{ mmHg}$ ). A graded decrease of pressure support level was performed by 5  $\text{cmH}_2\text{O}$  steps. The lowest pressure value was at 10  $\text{cmH}_2\text{O}$ . The ventilatory parameters were measured for 10 min in each step 20 min after pressure support change.

The figure shows representative tracings of the end-tidal  $\text{CO}_2$  and Hbvol changes during pressure support ventilation in a patient with myasthenia gravis. Hbvol changes correspond to end-tidal  $\text{CO}_2$  changes. During inspiration an increase of Hbvol is observed; the opposite occurs during the expiration.

In a patient with chronic obstructive pulmonary disease, when the pressure support level was reduced, a rapid desaturation was accompanied with EMG activation.  $\text{SaO}_2$  remained stable during muscle desaturation. This patient failed his weaning within 48 hours.

No Hbdif changes were observed on patients with no EMG activation who were successfully weaned. A parallel decrease of Hbdif and  $\text{SaO}_2$  were observed on two patients who did not activate their sternomastoid muscle.



In a second study, NIRS was applied on the forearm of patients with severe sepsis, septic shock and no signs of sepsis in order to investigate if skeletal muscle can influence whole body  $\text{VO}_2\text{-O}_2$  delivery relationship and haemodynamics. Forearm  $\text{VO}_2$  and blood flow (FBF) were measured according to a method previously described (1). Forearm arteriolar resistance (FAR) were derived from the mean arterial pressure and FBF. In all patients forearm  $\text{O}_2$  delivery and  $\text{VO}_2$  did not correlate with the whole body  $\text{O}_2$  delivery and  $\text{VO}_2$ . A forearm  $\text{VO}_2\text{-O}_2$  delivery dependency was observed in non-septic patients, where no whole body  $\text{VO}_2\text{-O}_2$  delivery dependency appeared. No forearm  $\text{VO}_2\text{-O}_2$  delivery relationship was observed in septic and shock patients where whole body  $\text{VO}_2\text{-O}_2$  delivery dependency was found. In septic shock the lack of forearm  $\text{VO}_2\text{-O}_2$  delivery dependency was associated with low FAR even at a relatively low FBF. Low FAR were observed in septic shock indicating that in this condition haemodynamics could be influenced by skeletal muscle resistance.

In conclusion NIRS represents a useful tool to monitor skeletal muscle haemodynamics and oxygenation for the management of critically ill patients.

#### References

- 1- De Blasi RA, Ferrari M, Natali A, Conti G, Mega A, Gasparetto A. J Appl Physiol 76:1388-1393, 1994

## Spectrophotometry for the Assessment of Pigmented Skin Lesions.

V.P. Wallace, Department of Physics, Institute of Cancer Research, Royal Marsden Hospital, Sutton, Surrey, SM2 5PT, UK. Tel:0181 643 8901 ext:3314, Fax:0181 643 3812, E-Mail:vwallace@icr.ac.uk  
J.C. Bamber, address as above. D.C. Crawford, Department of Medical Physics and Bioengineering, University Hospital of Wales, Heath Park, Cardiff, CF4 4XW, UK. P.S. Mortimer, Consultant Dermatologist, Royal Marsden Hospital, as above.

### Introduction

With the increase in the incidence of Malignant Melanoma differential diagnosis of pigmented skin lesions becomes more important. Dermatologists have only limited success with diagnosing early melanoma<sup>1</sup> and a more objective method is needed that would improve diagnostic accuracy.

Scattering, the dominant optical process in tissue, arises from variations in refractive index. Melanin the major chromophore in pigmented lesions has been shown to act as a Rayleigh scatterer<sup>2</sup>. The major absorbers in skin are water, blood, keratin and melanin. Since the scattering and absorbing properties of tissue depend on biochemical composition, cellular structure and the wavelength of light, malignant tissues are expected to have different optical properties from that of normal tissue.

Reflectance spectrophotometry has been used since 1939 to study pigments of in vivo skin.<sup>3</sup> In 1991 Marchesini et al<sup>4,5</sup> used reflectance spectra to discriminate between benign naevi and malignant melanoma. The aim of the present study was to reproduce and extend the work of Marchesini et al. In particular, our optical system samples a smaller area of a lesion to study the variation of pigmentation within that lesion and extends the spectral measurements into the ultraviolet and infrared. We also have the histological diagnosis of all lesions.

### Materials & Method

Reflectance spectra ( $\lambda=320-1100\text{nm}$ ) were collected using 18 optical fibres from a xenon light source to illuminate small regions of the skin surface and 12 fibres coupled to a spectrophotometer (Photal MCPD-1000) to collect the reflected light (Fig 1). A solution of barium sulphate, 25% weight/volume, was used as a standard white reflector to calibrate the system.

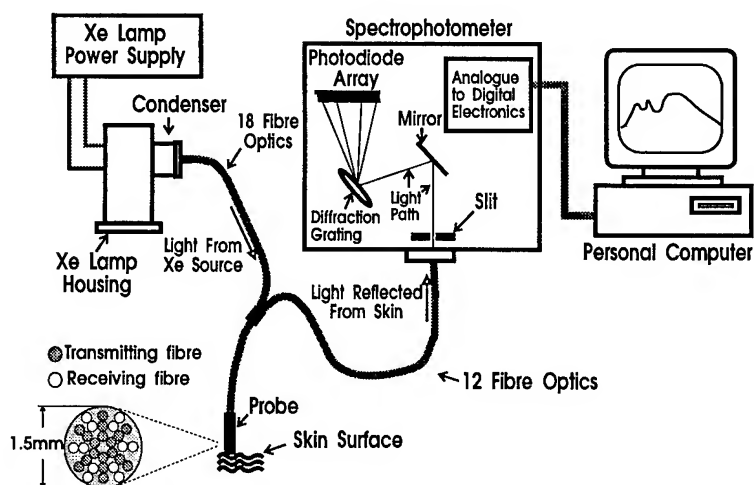


Figure 1. Schematic diagram showing layout of equipment used.

Patients were recruited from a Pigmented Skin Lesion Clinic. Three to five spectra were obtained from each lesion. To date a total of 399 spectra have been acquired from 121 lesions, all of which were subsequently excised for histological diagnosis, Table 1.

Histological Diagnosis	No. of cases	No. of spectra
Malignant Melanoma	15	55
Melanoma in situ	9	33
Dysplastic Naevus	11	36
Compound Naevus	30	98
Seborrhoeic Keratosis	14	42
Basal Cell Carcinoma	5	15
Other	37	120

**Table 1.** Lesions studied by histological type. Other includes Lentigo, Dermatofibroma, Junctional Naevus, Intradermal Naevus, Blue Naevus and Haemangioma.

## Results

Figure 2 shows the reflectance spectra for six groups important in differential diagnosis. The thick central line is the mean of the patient spectra for that group; the dotted line showing  $\pm 1$  standard deviation. The standard deviations are large and the groups tend to overlap; although, differences in shape can be detected. Between 400-800nm the slopes for dysplastic naevus are clearly steeper than for melanoma. Beyond 800nm the dysplastic naevus data have a negative slope whereas melanoma maintains a positive slope. In other groups the differences are not so apparent. Basal cell carcinoma is the easiest to differentiate since it distinctly shows features due to oxyhaemoglobin absorption

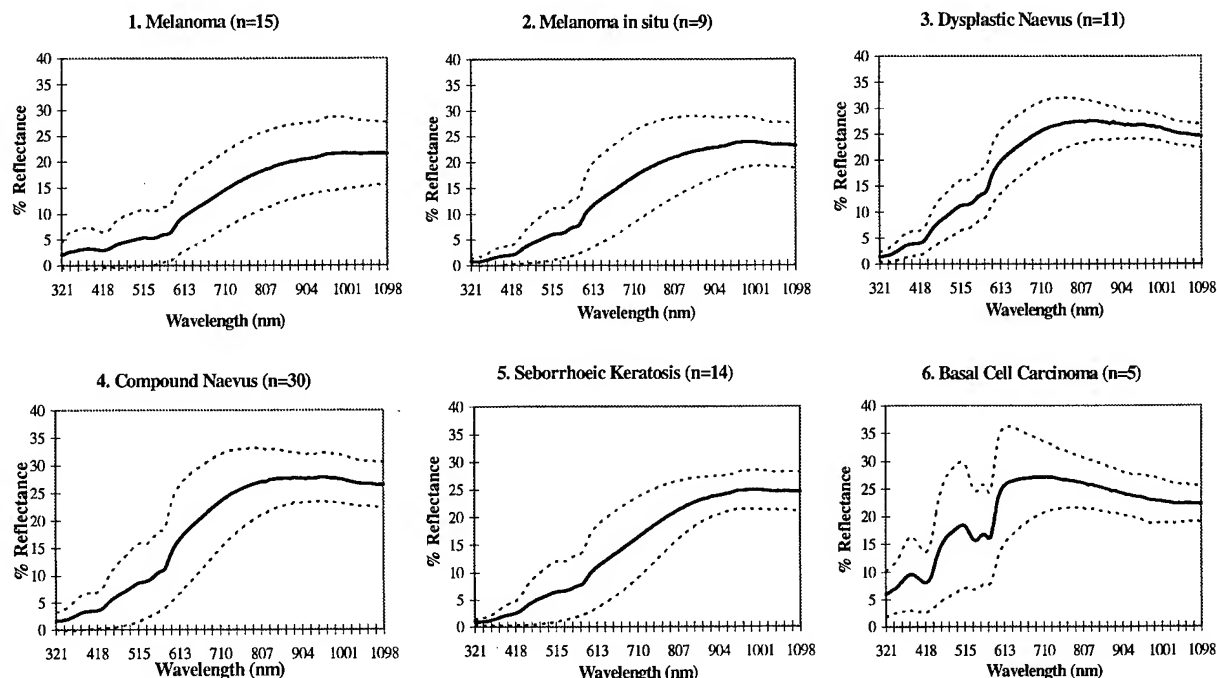


**Figure 2.** The mean ( $\pm 1$  standard deviation) reflectance spectra for six different types of lesion.

## Analysis

By visual assessment nineteen features, some of which are similar to those used by Machesini et al<sup>5</sup>, have been selected that were thought to best discriminate between the spectra in Figure 2. Nine of these features were slopes in different regions of the spectrum; e.g. the slope of the curve in the region between 616-748nm. Seven other features represent areas between lines connecting two points and the curve itself; e.g. the area between the straight line connecting 515nm and 616nm and the curve in that region. A

very small area suggests that the region is flat, a positive area suggests the curve is dome shaped and a negative area trough shaped. The final three features are: the mean value in the region 1039-1098nm, the total area under the curve and the variation between the spectra from within each lesion. Each parameter was calculated for each spectrum in the six groups (total of 279 spectra). A Student's t-test was used to assess the significance of the difference between the means of the features for all possible pairs of the six groups. The features that provided a significant difference in the pairs (i.e.  $P < 0.01$ ) between all groups were: the total area under the curve, the slope in the region 515-616nm, the area between the line and curve joining 578-1039nm, the slope in the region 826-958nm, and the area between the line and curve joining 609-772nm. All other features had significance for certain pairs; on average each pair of groups had approximately 10 features for which  $P < 0.01$ . There were three exceptions, the pair, dysplastic naevus and compound naevus had only two features at the  $P < 0.01$  level; the mean value between 1039-1098nm and the spatial variation of reflectance within a lesion. This is consistent with the fact that visual discrimination between these lesion types is based upon the variegated appearance of most dysplastic naevi. There were no features that discriminated between malignant melanoma and melanoma in situ; this pair being very similar visually and histologically. Also no features discriminated between malignant melanoma and seborrhoeic keratosis; these two are normally very different visually and the fact that their reflectance spectra were very similar remains at present unexplained.

Compound naevi are benign pigmented lesions that are most likely to be confused with melanoma. The difference between these diagnostically important groups was therefore studied in more detail by using the seven most significant features ( $P \leq 0.0001$ ) in a linear discriminate analysis procedure.<sup>6</sup> This involved 55 spectra from melanoma (15 lesions) and 98 spectra from compound naevi (30 lesions). Forty-four (80%) melanoma spectra were classified correctly and 77 (78.57%) naevi spectra were classified correctly. Since it is important that melanoma are not misclassified, an additional decision rule was created. If any one of the spectra from a lesion is classified into melanoma then that lesion should be classed as a melanoma. This resulted in all melanomas being classified correctly with the number of correctly classified naevi being reduced to 22 (73%).

## Conclusions

A new spectrophotometric system for wavelengths in the range 320-1100nm was used to obtain optical reflectance spectra from pigmented skin lesions; confirming the work of Marchesini et al.<sup>4,5</sup> Features of the reflectance spectra were found to correlate with histological diagnosis. Discrimination between benign and malignant lesions was good enough to suggest that the method has promise as an objective aid to the clinical diagnosis of skin tumours. Further work is required to confirm these preliminary findings and to more fully understand the mechanisms of interaction between light and skin that result in the observed reflectance spectra. The improved spatial resolution of the measurements permitted features associated with heterogeneity of colouration to be studied.

## References

1. Curley R. et al. Accuracy in Clinically Evaluating Pigmented Skin Lesions. *Br.Med.J* 299:16-18,1989.
2. Wobarst M. Melanin a Unique Biological Absorber. *App Optics* 20:2184-2186, 1981.
3. Edwards E.A. et al. The Pigments and Colour of Living Human Skin. *Am. J. Anat.* 65:1-33, 1939.
4. Marchesini R. et al. In vivo Spectrophotometric Evaluation of Neoplastic and Non-Neoplastic Skin Pigmented Lesions-I. Reflectance Measurements. *Photochem. & Photobiol.* 53 No.1:77-84, 1991.
5. Marchesini R. et al. In vivo Spectrophotometric Evaluation of Neoplastic and Non-Neoplastic Skin Pigmented Lesions-II. Discriminate Analysis between Naevus and Melanoma. *Photochem. & Photobiol.* 55 No.4:515-522, 1992.
6. SAS Institute Inc. SAS/STAT® User's Guide, Ver. 6, 4<sup>th</sup> Edition, Vol. 1, Cary, NC, 1989, 677-771

# Single-Fiber Optical Probe for Two-Photon Induced Fluorescence of Biological Markers

A. T. Obeidat, A. E. Kaplan, J. B. Khurgin

Department of Electrical and Computer Engineering

The Johns Hopkins University, Baltimore, Md 21218

(410) 516-5259, (410) 516-5566, nomad@doomsday.ece.jhu.edu

M. D. Stern

Department of Cardiology, The Johns Hopkins Medical Institution

The Johns Hopkins University, Baltimore, Md 21287

The use of fluorescent dyes which can be attached to specific cellular components as biological markers has become a well-established biomedical technique in recent years [1]. When optically stimulated, these dyes emit a characteristic fluorescence, enabling the structure and organization of the stained sample to be readily studied and visualized by means of fluorescence spectroscopy and confocal microscopy [2]. Moreover, some dyes exhibit enhanced fluorescence if attached to certain biological molecules. For instance, 4',6-diamidino-2-phenylindole (DAPI) exhibits such enhanced fluorescence when attached to the AT base pairs on a DNA strand [3]. Such properties are useful for mapping DNA structure or identifying the presence of particular molecules in a sample.

Typical dyes used in biological studies absorb and emit visible or UV light. However, UV light is strongly absorbed within a thin layer near the surface of the sample. Other problems with UV pumping include the lack of inexpensive UV laser sources, photobleaching of the dye molecules, and the anticipated photodamage of living cells by energetic UV photons. However, with the advent of ultrashort laser pulses, a new technique has emerged to excite these dyes with visible light which overcomes many of the aforementioned problems. This technique employs two-photon absorption in the dye, a third-order nonlinear process whereby a dye molecule absorbs two long-wavelength photons instead of a single short-wavelength photon. Subsequently, the dye emits its characteristic fluorescence and returns to its ground state. The whole process is referred to as two-photon induced fluorescence (TPIF) [4].

TPIF output intensity depends quadratically on the *peak* intensity of the pump laser pulse. Therefore, it is possible to observe TPIF with a modest *average* power if the laser pulse is sufficiently short. A major advantage of

TPIF over single-photon induced fluorescence is potentially higher resolution. This is a direct consequence of the fact that TPIF is observed only in the immediate vicinity of the focal spot, due to its quadratic intensity dependence. TPIF has already been proven useful in confocal laser scanning microscopy [5].

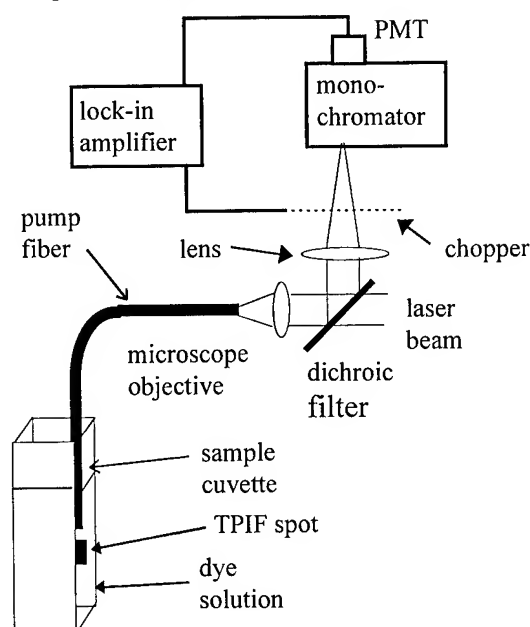


Fig. 1 The experimental setup.

However, TPIF encounters its own problems, the most obvious being its apparent inability to probe the *inhomogeneous* media widely present in biological research. Such media severely scatter incident laser light, thus preventing the tight focusing needed to observe TPIF, and seemingly limiting TPIF applications to investigating layers near the surface. It has already been shown that this shortcoming can be overcome by using optical fibers to deliver the pump light into the inhomogeneous medium [6]. Moreover, TPIF with fibers can be extended to biological media of very low transparency.

Optical fiber sensors are widely used in a variety of fields [7]. In experiments with TPIF, optical fibers offer enhanced resolution due to the very small spot sizes achievable within the specimen. Therefore, a smaller volume is exposed to laser intensity high enough to observe TPIF, which also limits the size of the region that could be damaged or photobleached. Moreover, the use of laser sources in the red part of the spectrum allows us to utilize off-the-shelf optical fibers instead of special expensive fibers required for UV radiation. In this paper we demonstrate that a single optical fiber can be successfully used to induce TPIF and collect the fluorescence to perform spectroscopic studies in liquid dye solutions. We also compare single-mode and multimode fibers and show that single mode fibers have the advantage for high resolution application.

The laser system used in our experiments consists of a Coherent 700 series dye laser pumped with the second harmonic of a mode-locked Coherent Nd:YAG Antares laser. The dye laser utilizes Pyridine as a gain medium with a saturable absorber, and a cavity dumper to shorten the pulses and to control the repetition rate. At a repetition rate of 7.6 MHz, the Pyridine laser produces 2 ps pulses at 730 nm with an average power of 70 mW; this corresponds to a peak power of 5 kW.

Five different optical fibers were used to deliver the laser light into the solution as indicated in table 1. The fibers were purchased from Thor Labs. The f\_5\_12 fiber supported only a single spatial mode, while the other four supported multiple modes as observed with a CCD camera. (The first number in a fiber's code is the core diameter in units of  $\mu\text{m}$  while the second number is the numerical aperture X 100).

Fiber	Core Diameter ( $\mu\text{m}$ )	N.A.	Coupling Efficiency (%)
f_5_12	5.5	0.12	10
f_5_12_10X	5.5	0.12	20
f_50_37	50	0.37	80
f_100_37	100	0.37	67
f_125_48	125	0.48	67
f_200_48	200	0.48	72

Table 1. Properties of the five fibers.

The laser beam was injected into the fibers with a 5X microscope objective one fiber at a time (except for one case where a 10X lens was used as indicated). We used a variable neutral density filter to change the input laser power. The output ends of the fibers were immersed in a dye solution contained within a standard fluorometer glass cuvette. The back-scattered sample fluorescence was collected from the pump fiber with a dichroic filter as shown in figure 1. It should be noted that a chopper placed in front of the monochromator was used with a lock-in amplifier to enhance the fluorescence signal.

The experiment was performed with a 5 mM solution of DAPI in Methanol. Figure 2 shows the one of the acquired spectra.

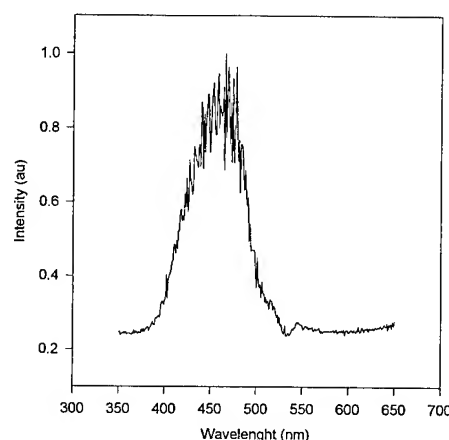


Figure 2. DAPI fluorescence spectrum.

The fluorescence spectra acquired at several values of input laser power were integrated over the entire fluorescence band to obtain the integrated intensity of TPIF. By varying the input power and computing the integrated fluorescence, we show in Fig. 3 the quadratic dependence of the fluorescence on the exiting power for the fibers we used.

Our previous work [6] revealed that the smaller core diameter of a fiber is, the more efficient a pumping source it is. As the core diameter increases, the generated fluorescence signal drops. The difference is due to the spatial profile of the beam exiting the fiber. The smaller the fiber is, the more tightly focused the beam is at the exit. Since the generated

fluorescence is quadratically proportional to the pump intensity, a higher fluorescence signal is generated with smaller fibers. Moreover, the exiting beam diverges more quickly for smaller fibers. Hence, the smaller the fiber, the more

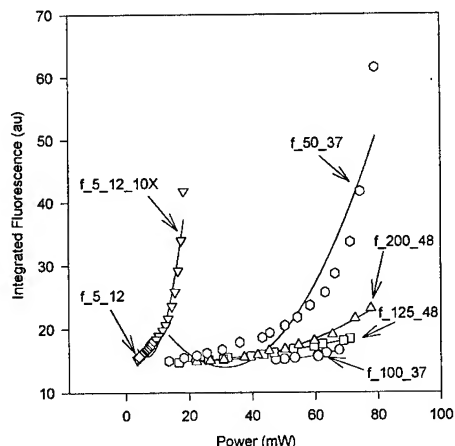


Fig. 3 Quadratic dependence of fluorescence on pump power for the different fibers.

intense and spatially confined its fluorescence. We have observed, with the aid of a CCD camera, that the fluorescence is more concentrated near the tip of smaller fibers. This trend was clearly observed as we compared the f\_5\_12 fiber with the f\_50\_37 fiber and was further verified by studying the f\_100\_37 fiber as well as the two other higher.

In this experiments, we collected the back scattered fluorescence signal with the aid of a dichroic filter. We had previously speculated that Multimode fibers can be more efficient at collecting the fluorescence. However, it is evident from figure 3 that this is not the case. The single mode fiber, despite its low coupling efficiency, proved to be best suited for the task. This somewhat surprising result is due to two factors. First, the fluorescence profile is fairly well matched to the numerical aperture of any given fiber. This is a direct result of the quadratic dependence of fluorescence on the pump intensity which serves to produce a tight fluorescence profile. Second, the single-mode fiber produces the highest intensity at its tip due to its narrow core diameter. This results in a strong fluorescence signal part of which is coupled efficiently back into the fiber and collected by our detection optics.

This arrangement has many useful applications in chemical, environmental and biological sensing. A single-fiber optical probe can be constructed to test for the presence of chemicals in various environments. Moreover, the small spot produced by the single mode fiber would ideal for TPIF fiber microscopy where a new class of samples can be accessed and imaged.

In conclusion, we have demonstrated the feasibility of using optical fibers to produce and detect two-photon induced fluorescence of two different biological markers. This technique is applicable to a variety of dyes important for biological research. It is shown that due to stronger fluorescence confinement near the fiber tip, single mode fibers are more suitable for high resolution applications.

#### References:

1. R. P. Haugland, *Molecular Probes Handbook of Fluorescent Probes and Research Chemicals* (Molecular Probes, Eugene, OR, 1992).
2. R. Y. Tsien, *Methods Cell Biol.* **30**, part B, 127 (1989); T. Wilson and C. Sheppard, *Theory and Practice of Scanning Optical Microscopy* (Academic Press, New York, 1984).
3. J. Kapuscinski and B. Skoczyla, *Nucleic Acids Res.* **5**, 3775 (1978); L. Masotti, P. Cavatorta, M. Avitabile, M. L. Barcellona, J. Von Berger, and N. Ragusa, *Ital. J. Biochem.* **31**, 90 (1982); J. Kapuscinski and W. Szer, *Nucleic Acids Res.* **6**, 3519 (1979).
4. J. R. Lakowicz, P. A. Koen, H. Szmazinski, I. Gryczynski, and J. Kusba, *J. Fluoresc.* **4**, 117 (1994).
5. W. Denk, J. H. Strickler, and W. W. Webb, *Science* **248**, 73 (1992); P. F. Curley, A. I. Ferguson, J. G. White, and W. B. Amos, *Optical and Quant. Electron.* **24**, 851 (1992).
6. A. Lago, A. Obeidat, A. Kaplan, J. Khurgin, P. Shkolnikov, and M. Stern, *Optic. Lett.* **20**, 2054 (1995).
7. R. B. Thompson and J. R. Lakowicz, *Anal. Chem.* **65**, 853 (1993); D. Wise, L. Wingard, Eds. *Biosensors with Fiber Optics* (Humana Press, Clifton, NJ 1991).



## Broadband monitoring of physiological changes with a continuous light tissue spectrometer

Judith R. Mourant<sup>1</sup>, Andreas H. Hielscher<sup>1</sup>, David M. Schmidt<sup>2</sup>, and John S. George<sup>2</sup>

Los Alamos National Laboratory, <sup>1</sup>Bioscience and Biotechnology, <sup>2</sup>Biophysics,  
CST-4, MS E535, Los Alamos, New Mexico 87545,  
Tel. 505 665 1190, Fax 505 665 4637, E-mail: jmourant@lanl.gov

**Introduction:** In recent years several authors have shown that physiological changes, such as variations in blood oxygenation or glucose concentration, can be detected by analyzing diffuse-backscattered light from biological tissues [1-7]. Methods that employ continuous light [1,2], short pulses [7] and sinusoidally amplitude-modulated light [4-6] have been used. However, all studies presented so far limit the collection of data to a few wavelengths in the near infrared. We have developed a continuous light tissue spectrometer that allows simultaneous measurement of the attenuation of diffuse-backscattered light over the wavelength range 250 to 850 nm. The collection of absorbance data over such a broad wavelength range results in a more thorough and reliable way of determining physiological parameters. Furthermore, our present system is sensitive enough to detect changes in absorption for up to 3 cm source-detector separations. Therefore, various tissue depths can be probed. For example, changes in superficial lesions can be monitored with adjacent source and detector fibers, while hemodynamic changes in the brain, which is covered by layers of other tissues, can be accessed by placing source and detector further apart. Multiple source-detector placements can provide spatial resolution in the order of fiber separation. In this work we describe the design of the device and some early applications that demonstrate its potential for research and clinical use.

**The Device:** Our system employs a xenon arc lamp, which emits light in the wavelength range from 250 to 1100 nm. The light is delivered to the tissue via a 400  $\mu\text{m}$  diameter fiber and collected by a 600  $\mu\text{m}$  diameter fiber. A separate fiber delivers light to a spectrally-flat diffuse reflecting reference. The purpose of the reference is to account for any fluctuations in the output of the light source during the measurements. The collection fibers from the tissue and reference are coupled to a spectrograph (Acton 275i). Light is dispersed over the wavelength range 250-850 nm using a grating blazed at 300 nm with 150 grooves/mm. Other wavelength ranges can be accessed with different gratings. The spectra from the two fibers is projected onto two regions of a 256x1024 element, thermoelectrically cooled, front-illuminated CCD (Princeton Instruments). The collection of data is computer controlled. The software allows control of data acquisition and integration times and on-line data analysis by computing differences or ratios between test and control spectra.

**Applications:** To examine the sensitivity of the system to changes in blood flow, diffuse-backreflection measurements were performed on the hand with and without a cuff applied to the arm. The light delivery and detection fibers were placed 2.4 cm apart on the back of the hand in close contact with the tissue. First, ten spectra were taken without the cuff. Then ten more spectra were recorded with a cuff applied to the upper arm. Finally, the cuff was released and ten more spectra were stored. The integration time for each measurement was 4 seconds.

The results of these measurements are shown in Fig. 1. Spectral changes due to the application and release of the cuff can be clearly seen from 600 to 850 nm. Application of the cuff resulted in a decrease in transmission. After the cuff was released the transmission recovered to its original state. The decrease in transmission when the cuff is applied can be explained by partial occlusion of the veins, which causes the blood volume, and therefore the absorption, to increase. Changes in blood oxygenation also contribute to the change in the signal. An examination of the time course of the changes shows that the response to the application of the cuff was faster than the response to its release.

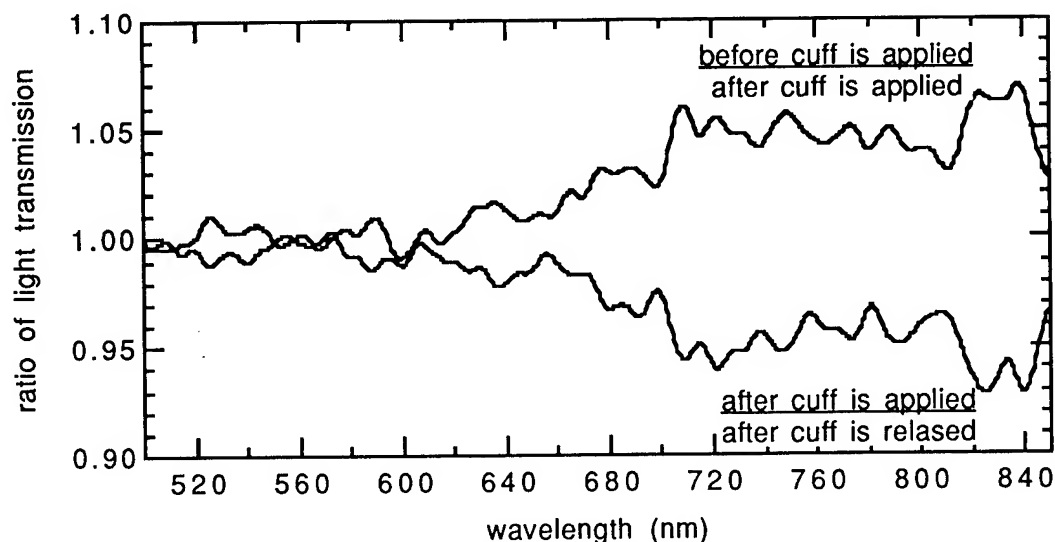


Fig. 1: Ratios of the diffuse-backscattered light from the hand before, during and after the application of a cuff to the upper arm. The top trace shows the ratio of spectra taken before application of the cuff to spectra taken after the cuff was applied. The bottom trace displays the ratio for spectra taken during constriction of the cuff divided by spectra taken after the cuff was released.

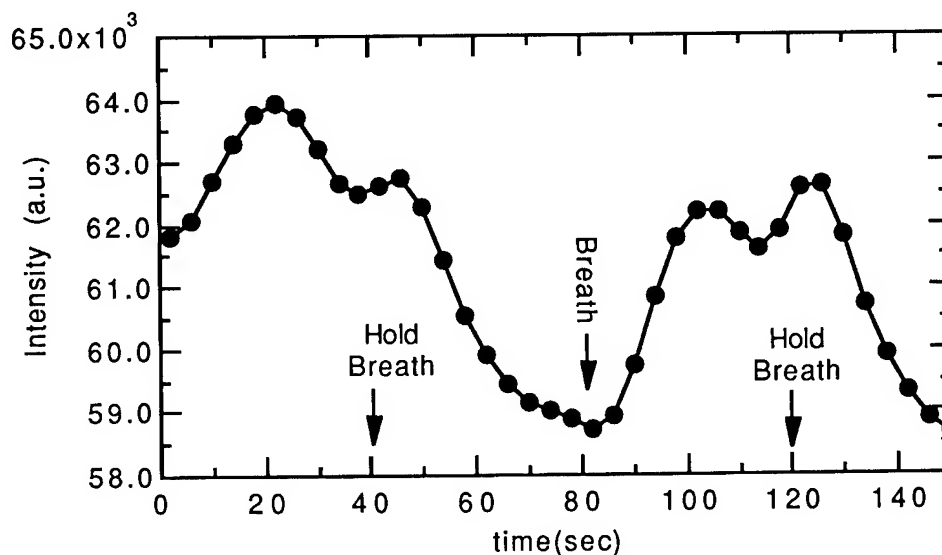


Fig. 2: The intensity of the diffuse-backscattered light, integrated from 720 to 840 nm, as a function of time.

We also tested if physiological changes in the brain can be measured with the device. Source and detection fibers were placed 2.5 cm apart on the back of the head, and changes in the diffuse-backscattered light due to alterations in breathing were monitored. The protocol was to collect ten spectra while the subject was breathing rapidly (~2 breaths/second), and then to take ten spectra while the subject held his breath. Spectra were taken every 4 seconds. For each spectra, the signal was integrated from 720 to 840 nm. This integrated signal is plotted as a function of time in Fig. 2. Changes in the intensity of the diffuse-backscattered light with breathing state are clearly visible. The initial observed rise reflects changes associated with transition from normal breathing to the accelerated rate used as the control condition. Breath holding initiated a pronounced fall in the observed transmission over this range, and this fall is reversed by the resumption of breathing.

In the future we plan to use the device for monitoring brain function. A range of historical and contemporary data has established that functional neural activation produced by sensory stimulation or motor control is associated with local hemodynamic changes. Changes include increases in blood flow and blood volume, and changes in blood oxygenation that reflect the discrepancy between blood oxygen delivery and tissue demands. These hemodynamic responses are the basis of widely used techniques for functional neuroimaging by PET and by functional MRI. We have undertaken experiments to demonstrate the expected changes in diffuse reflection spectra produced by visual stimulation. Results to date appear promising, but the expected changes are somewhat smaller than those associated with the manipulations described here. We expect that further refinement of the measurement methodology will allow these changes to be monitored routinely.

#### References:

- [1] C. E. Elwell, M. Cope, A. D. Edwards, J. S. Wyatt, D. T. Delpy and E. O. R., "Quantification of adult cerebral hemodynamics by near-infrared spectroscopy", *J. Appl. Physiol.* 77, pp. 2753-2760 (1994).
- [2] B. Chance, Z. Zhuang, C. Unah, C. Alter and L. Lipton, "Cognition-activated low-frequency modulation of light-absorption in human brain", *Proc. Nat. Acad. Sci. USA* 90, pp. 3770-3774 (1993).
- [4] M. Kohl, M. Essenpreis, M. Cope and D. Böcker, "The influence of glucose concentration upon the transport of light in tissue-simulating phantoms", *Phys. Med. Biol.* 40, pp. 1267-1287 (1995).
- [4] C. D. Kurth, J. M. Steven, D. Benaron and B. Chance, "Near-infrared monitoring of cerebral-circulation", *J. Clin. Monit.* 9, pp. 163-170 (1993).
- [5] R. A. Deblasi, S. Fantini, M. A. Franceschini, M. Ferrari and E. Gratton, "Cerebral and muscle oxygen-saturation measurement by frequency-domain near-infrared spectrometer", *Med. Biol. Eng. Comp.* 33, pp. 228-230 (1995).
- [6] S. Fantini, M. A. Franceschini, J. S. Maier, S. A. Walker, B. Barbieri and E. Gratton, "Frequency-domain multichannel optical-detector for noninvasive tissue spectroscopy and oximetry", *Opt. Eng.* 34, pp. 32-42 (1995).
- [7] H. Liu, A. H. Hielscher, B. Chance, F. K. Tittel and S. L. Jacques, "Influence of blood vessels on the measurement of hemoglobin oxygenation as determined by time-resolved reflectance spectroscopy", *Med. Phys.* 22, pp. 1209-1217 (1995).

## **Spectroscopy, photophysics and detection limits in fluorescence microscopy of oligonucleotide arrays**

Mark O. Trulson, Affymetrix, 3380 Central Expressway, Santa Clara, CA 95051 (408) 522-6032, FAX (408) 481-0422,

Mark\_Trulson@qmgates.affymetrix.com

David Stern, Ian D. Walton, and Richard P. Rava

We have been exploiting high density arrays of oligonucleotides to carry out sequence analysis of genetic material from diverse sources. The method utilizes the hybridization of fluorophore labelled DNA or RNA to the array, and interpretation of the resulting spatial pattern of fluorescence.

In the application of fluorescence detection to high density oligonucleotide arrays, the interplay of several factors defines our ability to obtain sequence information from a fluorescence image of the array. These factors include the photophysics of the fluorophores, sources of background interference, spatial resolution and image acquisition time requirements, and the chemistry of the hybridization process itself. Suitable nucleic acid-fluorophore conjugates must have high absorption cross sections, emission quantum yields, and low photobleaching quantum yields. They must be relatively immune to transient saturation under intense illumination. They must be insensitive to the sequence and hybridization state of the nucleic acids to which they are conjugated. Finally, they must be relatively insensitive to environmental conditions such as temperature, salt concentration, pH, and the local environment at the interface between the array surface and aqueous solution.

The performance of fluorophores in the high density oligonucleotide array system will be illustrated by detailed spectral and photophysical analysis of two candidate fluorophores: fluorescein and CY3, a commercially available carbocyanine dye. These fluorophores have been chosen on the basis of convenient excitation wavelength, availability as nucleotide triphosphate conjugates and the prospect for simultaneous use in a 2-color assay.

A confocal scanning fluorescence imaging system has been constructed to examine the spectral properties of candidate fluorophores in solution and immobilized on a surface. Off-axis illumination allows excitation wavelengths to be more readily changed than in an epi-illumination geometry, and provides small collection volumes even with collection optics of low numerical aperture. The high spatial and spectral

resolution allow characterization of emission spectra of fluorescent interferences in the assay, including the chip substrates, buffers, and the packaging material of the chip cartridge.

A method for the accurate measurement of fluorescence quantum yields in aqueous solutions has been developed. The technique utilizes the absolute Raman scattering cross section of the OH stretching vibration of water. Fluorescein conjugates have shown the expected sensitivity to solution pH and shift in  $pK_a$  with NaCl concentration, but are quite insensitive to other environmental parameters such as temperature and duplex formation. In contrast, CY3 conjugates are pH insensitive, but show dramatic reduction of emission quantum yield with increasing temperature and upon duplex formation. The environmental sensitivity of CY3 is tentatively ascribed to the conformational flexibility of the polymethine chain linking the carbocyanine moieties.

The absolute surface densities of fluorophores, the photobleaching quantum yields, and emission quantum yields of fluorophore-DNA conjugates hybridized to the array surface have been examined. Maximal densities of 10000 fluors per square micron, corresponding to intermolecular spacings in the range of 100 Ångstroms, have been observed. The onset of quenching at the highest fluorophore densities is evident from the data. Photobleaching quantum yields have been found to be  $2 \times 10^{-5}$  for fluorescein and  $4 \times 10^{-8}$  for CY3, and are nearly identical to solution values where comparison has been possible.

Transient saturation of fluorescence intensity of fluorophores has been observed to occur during the passage of a high intensity scanning laser spot, i.e. greater than 1 mW with a focussed spot size of 3 microns. The saturation behavior as a function of incident intensity and spot transit time has been interpreted in terms of a kinetic model that includes a slowly relaxing triplet state. Kinetic analysis of the data reveals that a triplet quantum yield of less than 1% may result in ground state depletion of more than 50% under the illumination conditions described above. The background luminescence of the glass substrate shows no saturation at high illumination intensities. For this reason, the background-limited signal to noise ratio for fluorescein conjugates reaches a maximum with approximately 3 mW incident power and decreases with further increases of power. In contrast, CY3 is far more immune to saturation and consequently produces maximum signal to noise at much higher intensities.

## **Fluorescence imaging of high density oligonucleotide arrays**

Ian D. Walton, Affymetrix, 3380 Central Expressway, Santa Clara CA 95051  
(408) 522-6034 FAX (408)481-0422 Ian\_Walton@qmgates.affymetrix.com  
David Stern, Mark O. Trulson, and Richard P. Rava

A newly developed technology that combines solid-phase oligonucleotide synthesis and photolithography is being used to spatially direct the synthesis of highly diverse arrays of immobilized oligonucleotide probes on a planar substrate. Hybridization events are detected by enzymatically incorporating fluorophores into unknown nucleic acids and allowing them to form double-stranded duplexes with the probe molecules in the array. The GeneChip™ array can be used to obtain detailed sequence information by analyzing the patterns of hybridization from unknown nucleic acids to the probes synthesized on the chip.

We can currently synthesize 256,000 distinct oligonucleotide sequences over an area of 1 square centimeter. Fluorescence detection of hybridization on these high density arrays requires that several potentially conflicting fluorescence imaging performance criteria be met:

High lateral spatial resolution: The optical resolution of the imaging system must be several times smaller than the feature size, currently 20 microns.

High axial spatial resolution: The axial response of the system must be limited to provide sufficient background rejection.

Large field of view: The imaging system must be able to provide high spatial resolution over an area of 1 square centimeter or greater.

Achromaticity: The broad emission spectra of organic fluorophores dictate the use of large detection bandwidths to maximize sensitivity. In addition, for some applications two or more spectrally distinct fluorophore species must be imaged simultaneously.

Low image distortion: To carry out automated analysis of fluorescence intensity patterns, a grid deliniating the synthesis sites on the array must be fitted to the image. The presence of random and systematic distortion complicates this process.

High sensitivity: The lowest observed fluorophore densities fall in the range of 1 to 50 fluors per square micron, i.e. fewer than 4000 fluorophores per 20 micron feature.

High dynamic range: DNA duplex stability varies markedly with sequence composition over the thousands of bases that are typically examined. For a single set of hybridization conditions with any real-world sample, a wide range of fluorophore surface densities is encountered. Maximum observed densities are greater than 1000 fluors per square micron.

The success of the GeneChip detection system in a commercial setting places additional requirements upon its design. First, sample throughput dictates image acquisition times of a few minutes. Second, the user must not be required to align each sample to the degree of precision required by the small depth of focus. An autofocus feature must therefore be incorporated into the design.

Two fundamental approaches to confocal fluorescence imaging of high density arrays have been explored. The primary distinction between them is the dimensionality of the excitation source and detection element.

#### Point scanners

In this approach, an excitation spot is focussed on the chip and scanned in one direction while the chip is slowly scanned in the orthogonal direction. Fluorescence is imaged through a spatial filter and directed onto a photomultiplier. Early embodiments of this method have achieved image acquisition rates of 2 lines per second. More recently, designs based on moving scan mirrors have achieved acquisition rates of 30 lines per second, which has been essential to the imaging of arrays with features as small as 20 microns in practical periods of time. The advantages of point scanning approaches include relatively straightforward optical design and control over the imaging volume by choice of spatial filter pinhole. However, the onset of transient fluorophore saturation under high intensity point-focussed illumination sets an upper limit to the usable laser power. For this reason, signal to noise performance decreases with increasing resolution for a given scan time.

#### Line scanners

In this approach, a tightly focussed laser line is used for excitation. The fluorescence thus excited is imaged onto a linear solid-state detection array. The finite width of the linear array itself provides spatial filtering to control the collection volume. Line illumination dramatically decreases the probability of fluorophore saturation, conferring the highest possible

sensitivity and speed as long as sufficient laser power is available. Short integration times result in low dark noise even without detector cooling, but the 30 to 100 electron read noise of commercially available linear CCD arrays places a strict limit on data acquisition rates for practical values of laser power and photobleaching quantum yields. Line illumination is also more difficult to employ, particularly with epi-illumination. The proper parallelism of the line focus to the long axis of the array raises new challenges in autoalignment. In addition, the spatial nonuniformity of line-focussed laser illumination must be corrected after scanning. Our progress in meeting these challenges in a practical line scanner will be discussed.



# **Quantitative Flow Transport Imaging in Tissue-Like Matrices using Micro-endoscopic Probes**

Michael P. Houlne, Darren Hubbard and Darryl J. Bornhop

Department of Chemistry and Biochemistry  
Texas Tech University  
Box 41061  
Lubbock, Texas 79409-1061

Tel: (806) 742-3142

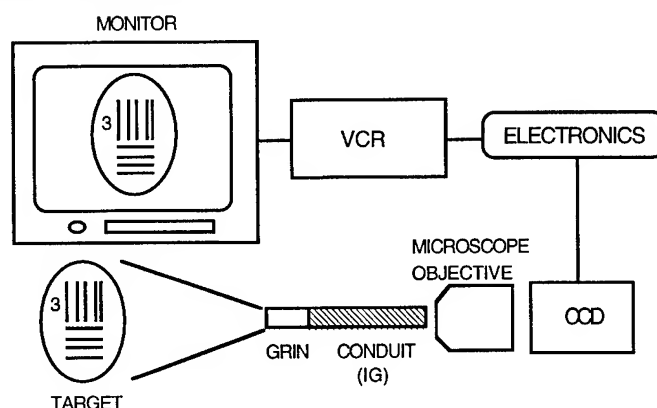
Fax: (806) 742-1289

e-mail: [qzlab@ttacs.ttu.edu](mailto:qzlab@ttacs.ttu.edu)

e-mail: [qzdjb@ttacs.ttu.edu](mailto:qzdjb@ttacs.ttu.edu)

Significant advances have been made in the area of tissue spectral analysis (1) and it appears possible to both identify and grade diseased tissue such as cancer tumors with the use of these approaches (2,3). Yet, progress is still needed in the general area of tissue spectroscopy (4-6), particularly in the arena of quantitative fluid transport in tissue matrices (7,8). The factors that affect movement of anti-cancer drugs through tumor tissues have not been clearly defined (9) and to this end, we have constructed a flexible microscope based on endoscopic imaging devices to investigate fluid transport in several tissue matrices.

Presented is the design, evaluation and implementation of this moderate resolution optical train. The simple optical configuration, illustrated below, employs flexible micro-endoscopic probes, an objective lens and a commercial for CCD.



This optical train produces resolution performance in the range of 25 - 40 Line Pairs/mm (LP/mm) with significant improvements predicted. Quantitative calibration is accomplished by relating gray-scale value to solute concentration. The endoscopes employed are 1-3 meters in length and range in outer diameter from 1.5 mm to 2.5 mm; some containing a working lumen for the introduction of a tool or a fluid at the site of investigation. A xeon discharge lamp provides lighting to the target externally or via illumination conduit in the endoscope.

Specialized image processing techniques allow for quantitative, time-sequenced imaging of marker dye transport in the matrix of interest. We employ minimally invasive quantitative mapping (concentration vs. time and position) of fluid transport to model first order convective versus diffusive flow properties

and to elucidate various transport mechanisms that drive anti-cancer therapeutic distribution in tumors. We specifically differentiate convective transport from diffusive transport and discuss the change in concentration of a probe molecule as a function of position and time.

### References

1. Numerous authors and topics; 1) "Joint Symposium on Advanced Optical Techniques for Medical Diagnosis: Spectroscopy 1 & 2, OSA Annual Meeting and the 10th Interdisciplinary Laser Science Conference, October, 1994. 2) "An International Symposium on Biomedical Optics.", February 1995, San Jose, CA.
2. A. Pradhan, B.B. Das, K.M. Yoo, J. Cleary, R. Prudente, E. Celmer, and R.R. Alfano, "Time-resolved UV photoexcited fluorescence kinetics from malignant and non-malignant breast tissues.", *Lasers Life Sci.*, 4(4), 225-235, 1992.
3. N. Ramanujam, A. Mahadevan, M. Follen-Mitchell, S. Thomsen, E. Silva, R. Richards-Kortum, "Flourescence spectroscopy of the cervix.", *Clinical Consul. OBGYN*, 6(1), 62-66, 1994.
4. R.R. Alfano, A. Pradhan, and G. C. Tang, "Optical spectroscopic diagnosis of cancer and normal breast tissues.", *J. Opt. Soc. of Am. B*, 6, 1015-1023, 1989.
5. M.S. Feld, Personal communication and data presented at the Optical Society of America Meeting, Dallas, Oct. 1994.
6. J.R. Less, M.C. Posner, Y. Boucher, D. Borochoviz, N. Wolmark, and R.K. Jain, "Interstitial hyertension in human breast and colorectal tumors.", *Cancer Research*, 52, 6371-6374, (1992).
7. R.K. Jain, "Transport of molecules across tumor vascualture.", *Cancer and Metastasis Reviews*, 6, 559-594, (1987).
8. R.K. Jain, "Barriers to drug delivery in solid tumors.", *Scientific American*, July, 1994.
9. R.K. Jain, "Physiological resistance to the treatment of solid tumors.", in *Drug Resistance in Oncology*, ed. by B.A. Teicher, Marcel Dekker, New York, 87-105, 1993.

# **Nitrogen laser excited autofluorescence spectroscopy for discrimination of human breast malignancy**

S K Majumder, A Uppal and P K Gupta

Laser Programme, Centre For Advanced Technology, Indore, India 452 013

Tel. : 091-731- 488438

Fax No. : 091-731-488430

We present results of our in-vitro studies on nitrogen laser excited autofluorescence from pathologically characterized cancerous and adjoining normal human breast tissues obtained after resection from 15 patients with breast cancer. The cancerous breast tissue samples were infiltrating duct carcinoma with involvement of lymphatic channels and adjacent skin. The fluorescence spectra were measured from a total of 247 sites of which 131 sites were from cancerous portion and the remaining 116 were from surrounding normal portion.

The mean spectra of the breast tissue samples are shown in fig.1. All the spectra (from both the cancerous and normal breast tissues) were characterized by two major emission bands centered at around 390nm and 480nm respectively with significant changes in spectral intensity distribution over the bands. The overall fluorescence yield was observed to be higher for cancerous breast tissues compared to the normal ones. A histogram of the overall fluorescence intensity values is displayed in fig.2. Although this observation is contrary to a general reduction in blue-green fluorescence reported from other human tissues by several researchers [1], the higher yield from cancerous tissues observed in our experiments is in agreement with the work of Alfano group on normal and malignant cultured human breast cell lines [2].

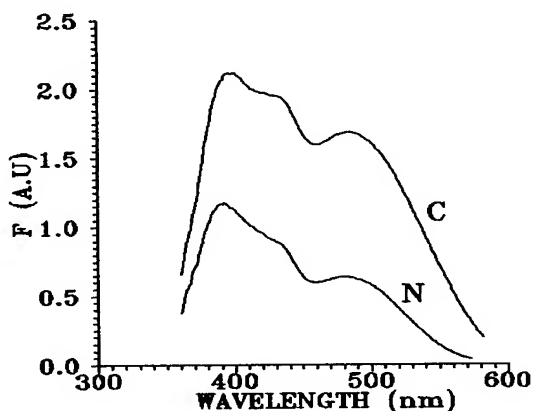


Fig.1: Mean breast tissue spectra from 131 cancerous (C) and 116 normal (N) sites.

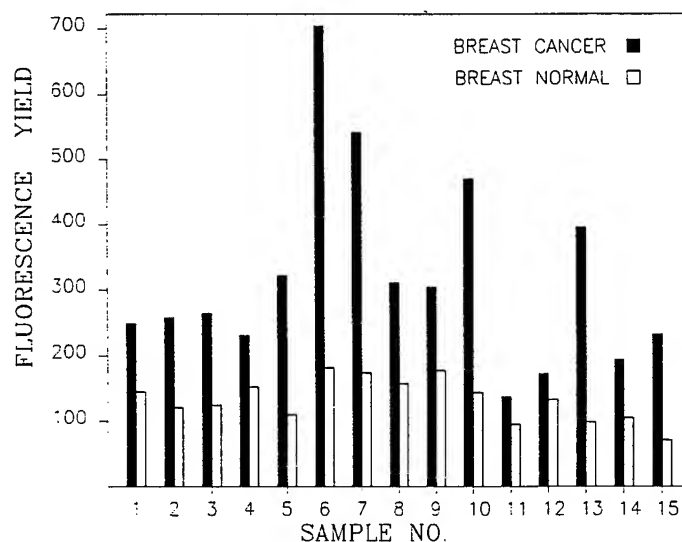


Fig.2: Histogram of the integrated fluorescence intensity values for paired samples from 15 patients.

The spectra normalized to the total integrated intensity are shown in fig.3. The 390nm band is seen to be stronger for normal and the 480nm band is more prominent for cancerous tissues.

In order to establish whether the observed differences in the spectra are statistically significant and to facilitate discrimination the spectral differences were quantified by forming 6 discrimination parameters on the basis of which tissue can be characterized as normal or cancerous. Two of these parameters were based on the value of fluorescence intensities at the peaks of 390nm and 480nm bands. Of the other four, three parameters were based on ratio of intensities at wavelength pairs (  $I(440)/I(380)$ ,  $I(450)/I(550)$  and  $I(480)/I(525)$  ) and the remaining one was based on the ratio of integrated intensities over the wavelength bands 450nm-550nm (BG) and 360nm-420nm (VB),  $I(BG)/I(VB)$ . A multivariate linear regression (MVLR) analysis was used for maximizing discrimination between the cancerous and the normal tissue spectra where these 6 parameters were used as input data for determining the discrimination function. The cut-off point for discrimination was taken as the weighted average of the mean scores of the discrimination function for normal and cancerous tissues. This correctly identified 112 out of 131 cancerous sites and 101 out of 116 normal sites investigated. The scatter plot for the values of the MVLR score is shown in fig.4.

The mean values of the 6 individual discrimination parameters for each tissue type were also calculated and discrimination power of these was tested by applying Student's t-test. All the parameters were found to be statistically significant with a p-value of better than 0.001. Table-1 lists the mean value  $\pm$  standard deviation of these parameters and table-2 lists the predictive values (sensitivity, specificity, predictive value positive and predictive value negative) of the MVLR score using the weighted average as the cut-off point.

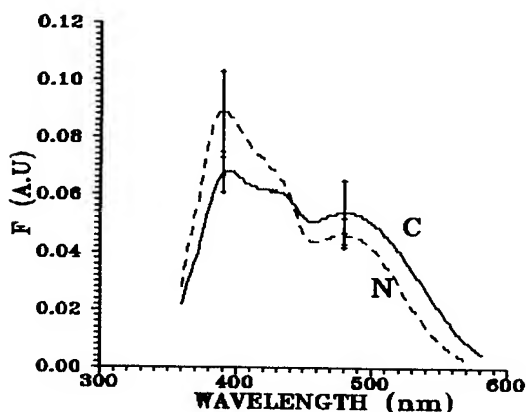


Fig.3: Mean breast tissue spectra from 131 cancerous (C) and 116 normal (N) sites normalized to the total integrated intensity.

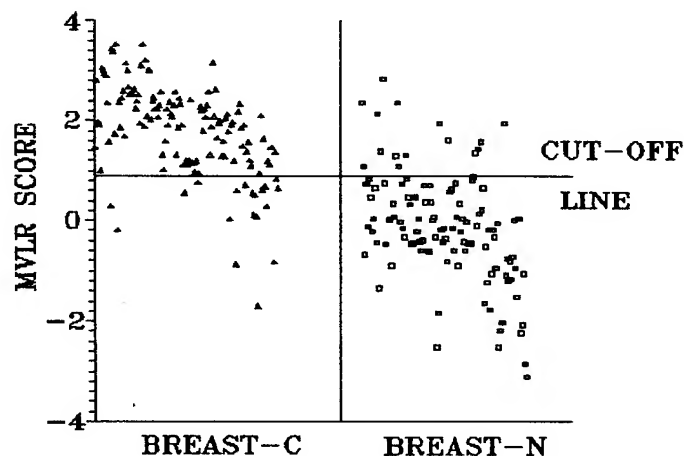


Fig.4: The scatter plot of the 6-variable MVLR score from cancerous (BREAST-C) and normal (BREAST-N) tissue sites.

TABLE-1:

Mean value  $\pm$  standard deviation of the statistically significant discrimination parameters for breast tissues.

Discrimination parameter	Cancerous	Normal
I(440)/I(380)	1.084 $\pm$ 0.165	0.793 $\pm$ 0.152
I(450)/I(550)	3.069 $\pm$ 1.703	5.639 $\pm$ 2.133
I(480)/I(525)	1.507 $\pm$ 0.372	2.006 $\pm$ 0.618
I(PEAK,BG)	0.056 $\pm$ 0.006	0.050 $\pm$ 0.005
I(PEAK,VB)	0.068 $\pm$ 0.011	0.090 $\pm$ 0.014
I(BG)/I(VB)	1.390 $\pm$ 0.325	0.880 $\pm$ 0.292

TABLE-2:

Sensitivity, specificity, predictive value positive (PVP) and predictive value negative (PVN) towards cancerous breast tissue using MVLR score.

Discrimination score	Sensitivity %	Specificity %	PVP %	PVN %
MVLR score (6 variable)	85.5	87.07	88.2	84.2

REFERENCES

- [1] Andersson-Engels S, Berg R, Johansson J, Svanberg S, Stenram U and Svanberg K, Laser spectroscopy in medical diagnostics. In: B W Henderson, Dougherty T J, eds., Photodynamic Therapy; Basic Principles and Applications, New York, Maccel Dekker, Inc. 1992
- [2] Glassman W S, Steinberg M and Alfano R R, *Lasers In The Life Sciences*, 6(2), 1994, 91-98

## Fourier Diagnostic Analysis of Fluorescence Spectra from Normal and Malignant Breast Tissues

A. Katz,\* Y. Yang,\* E. J. Celmer,\* M. Zurawska-Szczepaniak,\* and R. R. Alfano\*

\*Institute for Ultrafast Spectroscopy and Lasers,  
New York State Center for Advanced Technology for Ultrafast Photonic Materials and Applications,  
The City College and Graduate School of the City University of New York,  
New York, N.Y. 10031 (212) 650-5531, (212) 650-5530 (fax)

\*St. Vincent's Medical Center of Richmond Staten Island, N.Y. 10310-1699

Native tissue fluorescence spectroscopy allows for the development of a wide range of non-invasive diagnostic tools for *in-vivo* and *in-vitro* detection of the physical and chemical changes occurring in tissues and cells. There are several natural fluorophores that exist in tissue and cells which, when excited with ultraviolet and visible light, fluoresce in the ultraviolet and visible regions of the spectrum. Some of the important ones include tryptophan, elastin, collagen, nicotinamide adenine dinucleotide (NADH), adipose, flavins and porphyrins. The large number of fluorophore complicates interpretation of spectra. In the past decade, a number of research groups have made use of mediphotonic techniques for various medical diagnostic applications.(1-5) It has been shown that, with 300 nm excitation, the ratio of the emission intensities at 340 nm to 440 nm is a good discriminator between normal and malignant tissue.(3)

In this work, the emission spectra of 224 malignant, normal and adipose (fat) breast tissue samples were analyzed, using Fourier analysis, for the purpose of developing diagnostic tools for tumor detection in breast tissue. These diagnostic tools, incorporated into a fiber-optic needle based fluorescence instrument, can form a high spatial resolution, near real-time, *in-vivo* optical biopsy system.

Breast tissue is a complicated system, mainly composed of adipose, glandular and fibrous tissues and undesirable tumors, with underlying muscle and bone. Blood content and structure vary at different locations in the breast. During this work, all sample characterization was compared to pathology results and care was taken to insure that each excitation region only encompassed one tissue type.

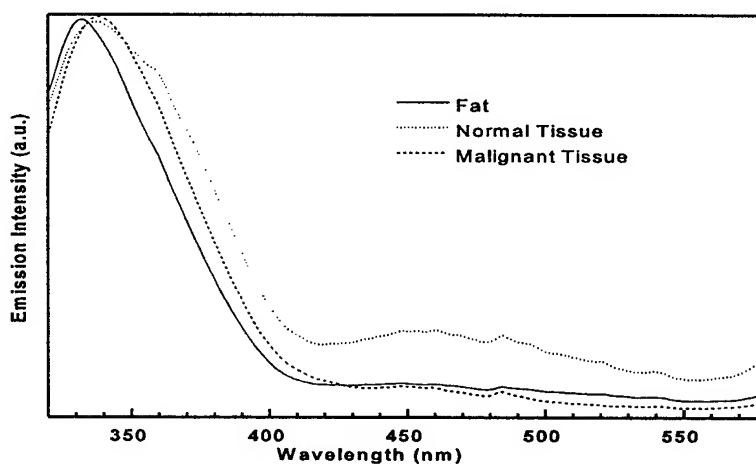


Figure 1. Average of emission spectra for fat, normal and malignant tissue.

The averaged emission spectra with 300 nm excitation, for fat, normal and malignant tissue is shown in Fig. 1. All spectra were normalized prior to generating the averages. Some significant features are: the peak emission from fat is shifted to shorter wavelengths as compared to normal and malignant tissue; the 340 nm emission band of normal tissue is broader than fat or malignant tissue; and the relative emission

intensity of normal tissue at 440 nm is greater than fat or malignant tissue. This last feature invites applying the  $I_{340\text{nm}} / I_{440\text{nm}}$  ratio test. This test successfully distinguished normal from malignant tissue in 60 of 61 normal samples and 92 of 97 malignant samples (sensitivity of 0.95); however, it sometimes misidentified fat as malignant tissue.

In order to examine the differences in the spectra, Fourier analysis was employed. A discrete Fourier transform was performed on each of the sample's spectra and the lower order harmonics were analyzed. The grating resolution and data smoothing function of the spectrophotometer acted as a low pass filter, limiting the usefulness of the higher order harmonics. Significant differences were observed in the magnitude and phase of the Fourier transform data. It was observed that the phase of the first three harmonics from the fat samples was significantly smaller than the phase of the malignant samples. The magnitude of the Fourier data was also examined. In order to correct for collection efficiency, the magnitudes of the harmonics were divided by the D.C. component of the Fourier data. The D.C. component is equal to the emission intensity averaged over the spectral range. It was observed that the magnitudes of the normal samples, for the first three harmonics, were smaller than that of the malignant and fat samples. These results are summarized in Table 1.

	Normal	Fat	Malignant
Relative magnitude of 1 <sup>st</sup> harmonic	$0.94 \pm 0.17$	$1.267 \pm 0.10$	$1.37 \pm 0.10$
Relative magnitude of 2 <sup>nd</sup> Harmonic	$0.72 \pm 0.11$	$0.94 \pm 0.057$	$0.95 \pm 0.07$
Relative magnitude of 3 <sup>rd</sup> Harmonic	$0.33 \pm 0.08$	$0.55 \pm 0.058$	$0.52 \pm 0.06$
Phase angle of 1 <sup>st</sup> harmonic	$50.41 \pm 6.32$	$41.34 \pm 2.63$	$47.34 \pm 2.15$
Phase angle of 2 <sup>nd</sup> harmonic	$82.77 \pm 5.72$	$72.28 \pm 4.02$	$80.07 \pm 3.08$
Phase angle of 3 <sup>rd</sup> harmonic	$108.93 \pm 3.20$	$92.95 \pm 6.24$	$103.74 \pm 3.20$

Table 1. Summary of Fourier transform data for first three harmonics. Phase angles are given in degrees. The magnitudes have been normalized by dividing by the D.C.

Since the main goal is to be able to detect malignancy, a two step approach was employed. First the magnitude of the harmonics were examined to discern malignancy from normal tissue. Next the phase angles were examined to distinguish malignancy from fat. The histograms of the relative magnitudes of the first harmonic for normal and malignant samples is shown in Fig. 2. Using a threshold value of 1.21, 94 of 97 malignant samples are correctly identified, with 1 false positive from 61 normal samples for a sensitivity of 0.97 and a specificity of 0.98. The histograms for the phase angles of the first harmonic for fat and malignant tissue are shown in Fig. 3. Using a threshold of  $44.5^\circ$ , 92 of 97 malignant samples are correctly identified for a sensitivity of 0.95. This threshold value gives 6 false positives from 66 fat samples for a specificity of 0.91. Combining these test, the average sensitivity is 0.92 and the specificity is 0.95. These statistical results, with the statistical results from the 2<sup>nd</sup> and 3<sup>rd</sup> harmonics, are summarized in Table 2.



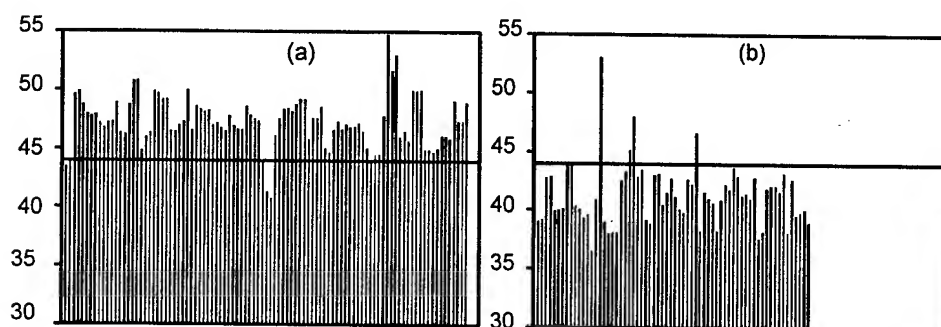


Figure 2. Phase angle (in degrees) of first harmonic for malignant (a) and fat (b).

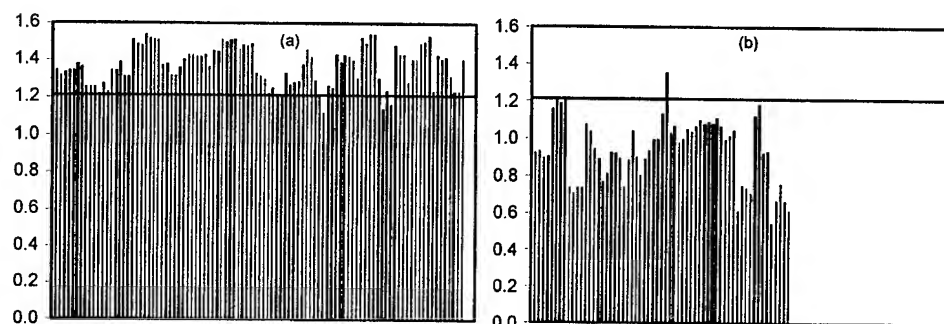


Figure 3. Magnitude of first harmonic for malignant (a) and normal (b) tissues.

	Magnitude		Phase		Combined	
	Sensitivity	Specificity	Sensitivity	Specificity	Sensitivity	Specificity
1 <sup>st</sup> harmonic	0.97	0.98	0.95	0.91	0.92	0.95
2 <sup>nd</sup> harmonic	0.93	0.90	0.97	0.91	0.90	0.91
3 <sup>rd</sup> harmonic	0.98	0.88	0.94	0.94	0.92	0.92

Table 2. Statistics of accuracy for separating fat, normal and cancer tissue.

## References

- 1) R. R. Alfano, D. B. Tata, J. J. Cordero, P. Tomashefsky, F.W. Longo, and M.A. Alfano, "Laser induced fluorescence spectroscopy from native cancerous and normal tissues." *IEEE J. Quantum Electron* **QE-20**, 1507-1511 (1984).
- 2) R. R. Alfano, G. C. Tang, A. Pradhan, W.Lam. D. S. J. Choy, and E. Opher, "Fluorescence spectra from cancerous and normal human breast and lung tissues." *IEEE J. Quantum Electron* **QE-23**, 1806. (1987).
- 3) R. R. Alfano, Bidyut B.Das, Joseph Cleary, Romulo Prudente, Edward J. Celmer, "Light sheds light on cancer-distinguishing malignant tumor from benign tissue and tumors." *The Bulletin of the New York Academy of Medicine* **67**, 143 (1991).
- 4) R. Richards-Kortum, R. P. Rava, R. E. Petras, N. Fitzmaurice, M. Sivak and M. S. Feld, "Spectroscopic Diagnosis of colonic dysplasia." *Photochem. Photobiol.* **50**, 777-786 (1991).
- 5) K. T. Shoemaker, J. K. Frisoli, C. C. Compton, T. J. Flotte, J. M. Richter, N. S. Nishioka and T. F. Deutsch, "Ultraviolet laser induced fluorescence of colonic tissue: Basic biology and diagnostic potential" *Lasers Surg. Med.* **12**, 63-78 (1992).

## **Quantitative Fluorescence in Tissue-like Media**

John S. Maier, Albert E. Cerussi, Sergio Fantini, Maria Angela Franceschini, and  
Enrico Gratton

Laboratory for Fluorescence Dynamics  
Department of Physics  
University of Illinois at Urbana-Champaign  
1110 W. Green Street  
Urbana, Illinois 61801-3080  
Telephone: (217) 244-5620  
Fax: (217) 244-7187  
  
e-mail: lfdwmeg@ux1.cso.uiuc.edu  
<http://www.physics.uiuc.edu/groups/fluorescence>

### **Introduction**

The study of near-infrared photon migration in tissues has matured to the point of the development of clinical instrumentation. The addition of fluorescence through the administration of exogenous fluorophores promises to improve the sensitivity and specificity of the already useful techniques developed in this field of study. We approach the problem of fluorescence in tissues focusing on a basic understanding of the physics, striving to attain quantitative information about parameters such as the fluorophore lifetime, concentration and quantum yield.

The clinical interest in fluorescence in tissues stems from the ability to label specific tissues through the administration of fluorescent antibodies which are specific for a certain pathological/physiological structure. In addition to increased sensitivity and specificity, entirely new information is available from fluorescent parameters such as the probe lifetime. The lifetime can be sensitive to environmental parameters such as local  $O_2$  concentration, pH, and binding state. For instance, a fluorescent probe that changes lifetime upon binding to a tumor could simplify the discrimination between background and tumor fluorescence.

In addition to the clinical applications, the potential to measure absolute concentrations or quantum yields indicates a new laboratory tool. Determining the quantum yield of a probe has traditionally posed a significant problem to fluorescence. The difficulties in accounting for the different excitation and emission geometries are not present in the highly scattering environment.

## Theory

To derive an expression for the frequency-domain fluorescence photon density in highly scattering environments, we start with the diffusion equation, which is the standard approximation used for strongly scattering media such as tissues. The spatial distribution of the excitation light is easily calculated from this equation. We then spatially convolute the Green's function of the diffusion equation ( $G_m(r)$ ) with the extended source of the emission photon density ( $q_m(r)$ ). We also temporally convolute the effect of the probe lifetime ( $\tau$ ) assuming a single exponential decay. The result is the density of emission photons  $U_m(r)$ , which is given by:

$$U_m(r) = G_m(r) \otimes q_m(r)$$

$$= \frac{S_x [F] \epsilon' \Lambda \int \phi_{\lambda_x}(\lambda_m') \gamma(\lambda_m') d\lambda_m'}{4\pi v D_m D_x} \left( \frac{1 + i\omega\tau}{1 + (\omega\tau)^2} \right) \frac{e^{-\alpha_x r} - e^{-\alpha_m r}}{(\alpha_m^2 - \alpha_x^2) r}, \quad (1)$$

where

$$D = \frac{1}{3\mu_s'}, \quad \text{and} \quad \alpha^2 = \frac{\mu_a}{D} \left( 1 - \frac{i\omega}{v\mu_a} \right).$$

$S_x$  is the strength of the excitation source in units of photons $\times$ s $^{-1}$ ,  $[F]$  and  $\epsilon'$  are the concentration and the molar extinction coefficient of the fluorophore respectively, and  $\Lambda$  is the fluorophore quantum yield. The integral represents the detector response to this specific system. Quantities with subscript  $m$  correspond to the emission wavelength, while those with subscript  $x$  refer to the excitation wavelength; for example,  $\mu_{ax}$  is the absorption coefficient of the medium at the excitation wavelength.  $v$  is the speed of light in the medium,  $\omega$  is the angular modulation frequency of the source, and  $r$  is the distance between the source and the detector.

Equation (1) is essentially identical in form to that derived by Patterson *et al.* [1]. We note that the dependence on lifetime is included in only one multiplicative complex term that does not have spatial dependence. The spatial dependence of the emission photon density is described in the final term and depends only on the optical coefficients of the medium at the excitation and emission wavelengths, and on the angular modulation frequency. The quantities  $\Lambda$  and  $[F]$  enter as multiplicative factors.

## Experiment Vs. Theory

We performed an experiment in a scattering fluorescent solution to test the accuracy of this model. In the experiment, a source of excitation light (532 nm) was used to excite a scattering medium composed of TiO<sub>2</sub>, black ink and rhodamine B (with a concentration of about 400 nM), with reduced scattering and absorption coefficients of  $\mu_s' \sim 9.2$  (cm $^{-1}$ ) and  $\mu_a \sim 0.15$  (cm $^{-1}$ ) respectively. A monochromator was used to selectively pass the emission light to our frequency-domain detector. We independently measured the absorption and reduced scattering coefficients of the medium at  $\lambda_x$  (532 nm) and at  $\lambda_m$  (600 nm) so that we

would have them for predictive purposes. This measurement also allowed us to characterize the source strength and phase. Based on these independent measurements, we predicted the fluorescence intensity at 600 nm (figure 1A) and the phase of the emission light (figure 1B) as functions of position. The plots in figure 1 show both the theoretical predictions and the experimental data. The quantitative theoretical predictions (continuous lines) were generated without any fit and without any free parameters. We assumed standard values of rhodamine B in water for  $\Lambda$  and for  $\tau$  (0.6 and 1.5 ns, respectively).

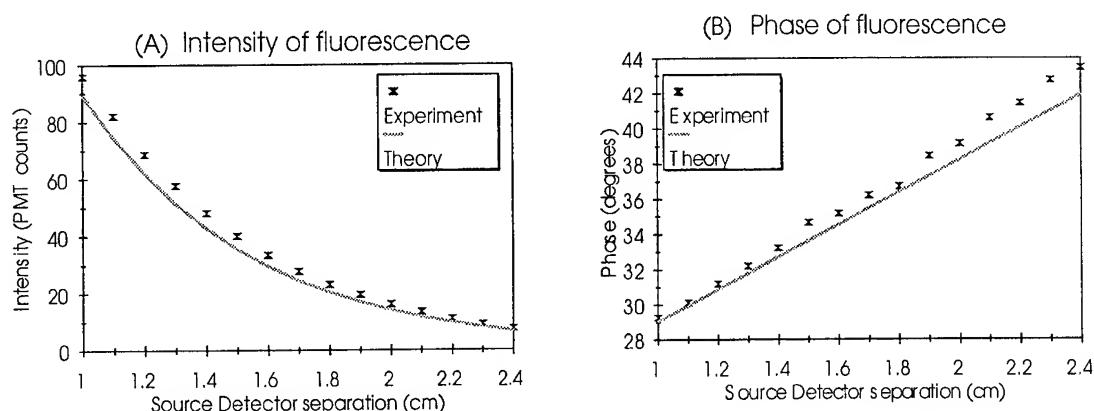


**Figure 1** -Theoretical predictions based upon equation (1) Vs. experimental data for rhodamine B in a highly scattering phantom. The solid lines represent the prediction. No free parameters are involved (we assumed standard values for rhodamine B in water as listed in the text). Panel (A) shows the DC emission intensity, and panel (B) shows the emission phase. Both are measured or calculated as functions of  $r$ .

## Conclusion

The above model can be used to answer many basic questions about the potential for the use of fluorescence in tissues. Our work focuses on the best ways to quantitatively measure the lifetime and the concentration of a fluorescent probe in a scattering environment. Additional possibilities include the characterization of the medium in terms of the absorption and scattering coefficients based on measurement of the emission light distribution, and a new method to measure the quantum yield of a fluorescent probe.

## References

- [1] M. S. Patterson and B. W. Pogue, "Mathematical model for time-resolved and frequency-domain fluorescence spectroscopy in biological tissues", *Appl. Opt.* **33**, 1963-1974 (1994).

## Optical Constants of Bone Tissues and Their Variations Related to Bone Mineral Density

Ryuichiro Araki\*, Akira Takeuchi\*\*, Akira Itabashi\*\*, Sergei G. Proskurin\*\*\*, Yukari Takahashi\*\*\* and Yukio Yamada\*\*\*

\*Department of Hygiene and Preventive Medicine, Saitama Medical School

\*\*4-th Department of Internal Medicine, Saitama Medical School

\*\*\*Biomechanics Division, Mechanical Engineering Laboratory, AIST-MITI

Return address: Dr. Ryuichiro Araki, Department of Hygiene and Preventive Medicine, Saitama Medical School, 38 Morohongo, Moroyama, Iruma-gun, Saitama 350-04, JAPAN

TEL: +81-492-76-1168 FAX: +81-492-94-6907 e-mail: raraki@saitama-med.ac.jp

Osteoporosis<sup>1</sup> causes decrease in bone mineral density (BMD, the quantity of hydroxyapatite crystals which act as scattering particles). This pathological change is directly associated with decrease in the volume of calcified bone matrix and result in replacement of the lost bone matrix with bone marrow which contains high concentration of Hb and thus acts as strong light absorber. These changes are expected to induce changes in optical properties of the bone tissues. The purpose of our study is to examine the fundamental optical properties of the bone tissues and their variations under various pathophysiological conditions by means of time-resolved spectroscopy.

Bone samples from cow thighbone and human spinal bone were cut to obtain 10 mm cube samples. The samples were placed in a glass cell filled with physiological saline. The laser pulse (FWHM=100 fs, wavelength=765 nm) from a Ti-Sapphire laser (Coherent, U.S.A.) was focused on the center of the cubic samples. Light emerged from the opposite side was guided into a streak scope (Hamamatsu Photonics, Japan), then temporal point-spread function (TPSF) was recorded<sup>2</sup>. BMD was determined with a DXA scanner (Lunar DPX-L) using animal-mode of the equipment.  $\mu_s'$  and  $\mu_a$  were estimated using MC-LUT method<sup>3</sup> based on the Monte Carlo simulation of light propagation within the samples.

As shown in Figure 1, tight correlation between BMD and  $\mu_s'$  was found. In contrast, there was no linear relationship between BMD and  $\mu_a$  among both trabecular and cortex bone samples, though there seems fairly good linearity between BMD and  $\mu_a$  among trabecular bone samples only. Since decrease in BMD indicates replacement of the lost bone matrix with bone marrow, this increase in  $\mu_a$  associated with increase in BMD is problematic. One possible explanation is as follows; in our experimental situation, Hb within the bone marrow tends to be lost into the saline during preservation. The bone samples with lower BMD is more porous than those which have higher BMD, and thus larger amount of Hb might be lost if BMD is lower. With respect to this point, more careful investigation is required.

The tight correlation between BMD and  $\mu_s'$  suggests the feasibility of noninvasive optical determination of BMD by means of *in vivo* time-resolved spectroscopy if influence of the surrounding soft tissue upon the optical signal can be satisfactorily excluded. Suggested

part of the human body for such optical measurement is the heel, in which the calcaneal bone exists and frequently used for ultrasonic bone-quality measurement. Using an X-ray CT system, we have confirmed that the skin, subcutaneous and fat tissues can be satisfactorily excluded by pressing the heel with moderate force.

Measurement of optical properties of bone tissues might give another useful information, *i.e.*, microstructure of the bone trabeculae, since the space between the bone trabeculae is filled with bone marrow which is the strong light-absorber. Such micro-structural information cannot be obtained with the existing equipments such as the DXA scanner, and thus might be a great advantage over the other existing techniques for bone-quality assessment based on X-ray or ultrasonic waves.

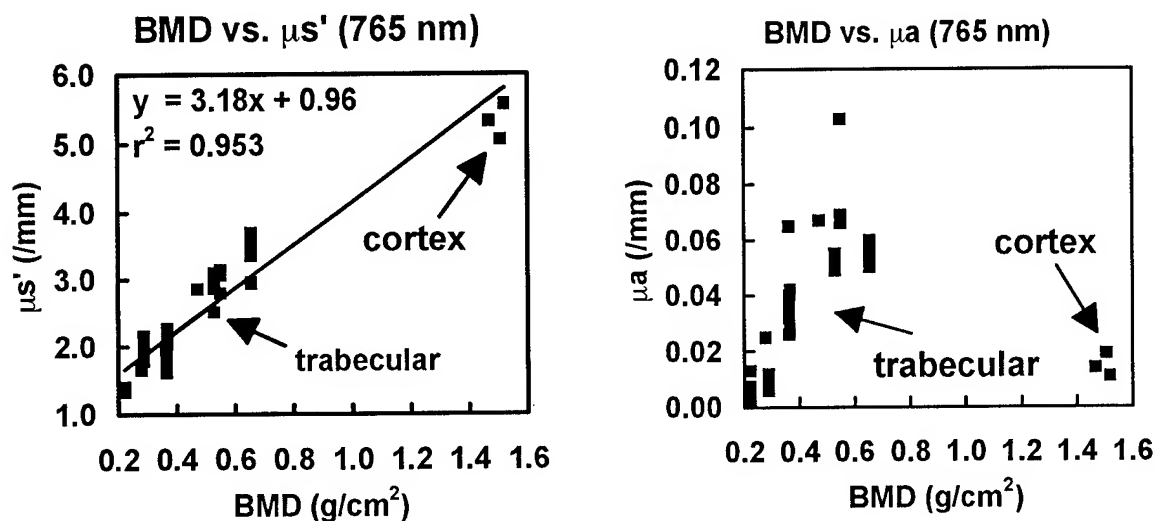


Figure 1. Relationship between BMD and  $\mu s'$  (left) and between BMD and  $\mu a$  (right) of trabecular and cortex bone samples taken from cow thighbone.

#### References

- 1) Consensus development conference: Diagnosis, prophylaxis, and treatment of osteoporosis, Am. J. Med., Vol.94, 646, 1993.
- 2) A. Takeuchi et al., Osteoporosis Japan, Vol.3, 11-13, 1995 (in Japanese).
- 3) R. Araki et al., Front. Med. Biol. Engng., in press.

## Fluorescence Spectroscopy of *B. Subtilus* in Solution and Aerosol

M. Seaver, J. F. Pinto, and J. D. Eversole

Code 5611  
Optical Sciences Division  
Naval Research Laboratory  
4555 Overlook Ave., S.W.  
Washington, DC 20375-5320

Phone: (202) 767-9523  
FAX: (202) 404-8114  
email: [eversole@nrlfs1.nrl.navy.mil](mailto:eversole@nrlfs1.nrl.navy.mil)

One-dimensional absorption or emission spectra do not usually provide adequate information to characterize biological material. However, development of tunable laser excitation sources provides another dimension to spectral analytic capability. Fluorescent spectra acquired as a function of excitation wavelength can be visualized as a two-dimensional surface. Such data is usually referred to as an excitation-emission matrix (EEM), and this approach has demonstrated significant diagnostic potential.<sup>1,2</sup> Recent research on *B. subtilus* spores indicates that there may be three main component chromophores that contribute significantly to fluorescent emission: tryptophan<sup>3</sup>, NADH<sup>4</sup> and other coenzymes, principally riboflavin<sup>5</sup>. These components are listed in order of decreasing emission strength and increasing emission wavelength. If this proves to be an accurate description of photo-emission in these types of bacterial spores, it suggests the potential for their spectrometric classification. An analogy may be drawn between such spores and phytoplankton which also has three main classes of chromophores: chlorophylls, carotenoids, and phycobilins.<sup>6</sup> In the case of phytoplankton, EEM analysis of fluorescence using conventional fluorimeters has produced a method of sample decomposition into algal classes based on the relative amounts of the three chromophore types which have reasonably well separated individual spectra.

Similar techniques for using spectral fingerprint analysis in a multidimensional data set have also been applied to population characterization for cell sorting using flow cytometry.<sup>7</sup> The application of this type of spectral analysis to bacteria and other microbes depends on extension of the spectral region into the far ultraviolet. Figure 1 shows a combined plot of emission and absorption spectra of two of the known chromophores present in *Bacillus* spores: Tryptophan<sup>8</sup> and NADH<sup>9</sup>. In these spectra, the emission profiles for both purified compounds overlap only slightly, while the two

absorption peaks, at 205 nm for tryptophan and 225 nm for NADH, are sufficiently far apart for a tunable excitation source to achieve discrimination capability using EEM data.

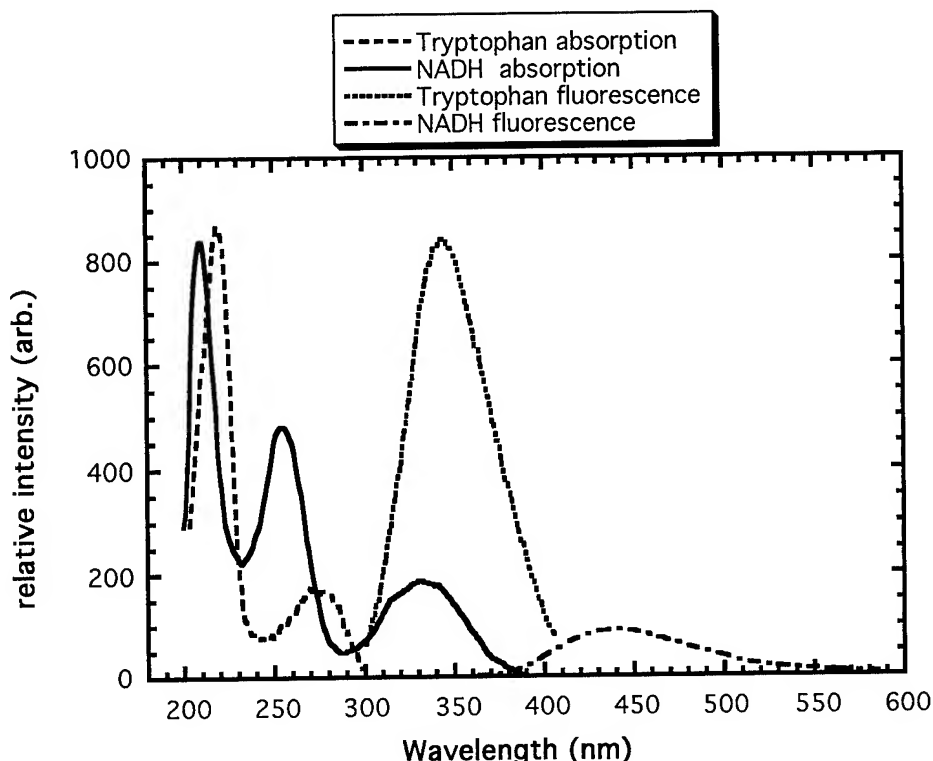


Figure 1. Absorption and emission spectra for both NADH and tryptophan.

Much of the previous work on spectral characterization of biological materials has used filtered continuum sources such as mercury or xenon arc lamps which can broadly tuned but have to trade off between low resolution and low intensity (especially in the far UV). Consequently, most previous study has been restricted to bulk samples; very little work has been published on bioaerosols. The higher intensity of tunable laser sources is critical to the issue of investigating biological material in aerosol form. While conventional dye laser sources may be used, they typically have limited tuning ranges in the UV.

Samples of *Bacillus subtilis* spores have been prepared as suspensions in water and as aerosols from both dry power and solution sprays. Particle densities are monitored in by attenuation of light at non-absorbing wavelengths. Fluorescence spectra from liquid samples were excited by either a KrF excimer laser at 248 nm or a tripled Cr:LiSAF laser tunable from 265 to 290 nm. Peak emission cross sections of individual spores has been estimated at  $\approx 2 \times 10^{-11} \text{ cm}^2/\text{str}/\text{nm}$ . This work is in progress, and will address several current issues including: excitation wavelength dependence of the fluorescence cross section, spectral differences between spore and vegetative cell states of the same species,



effect of water on sample spectra, and photo-bleaching rates as a function of excitation wavelength. Preliminary data such as shown in Fig. 2 indicate that flowing samples are required to obtain emission spectra free of complications due to photo-bleaching when using UV excitation even at moderately low fluences.

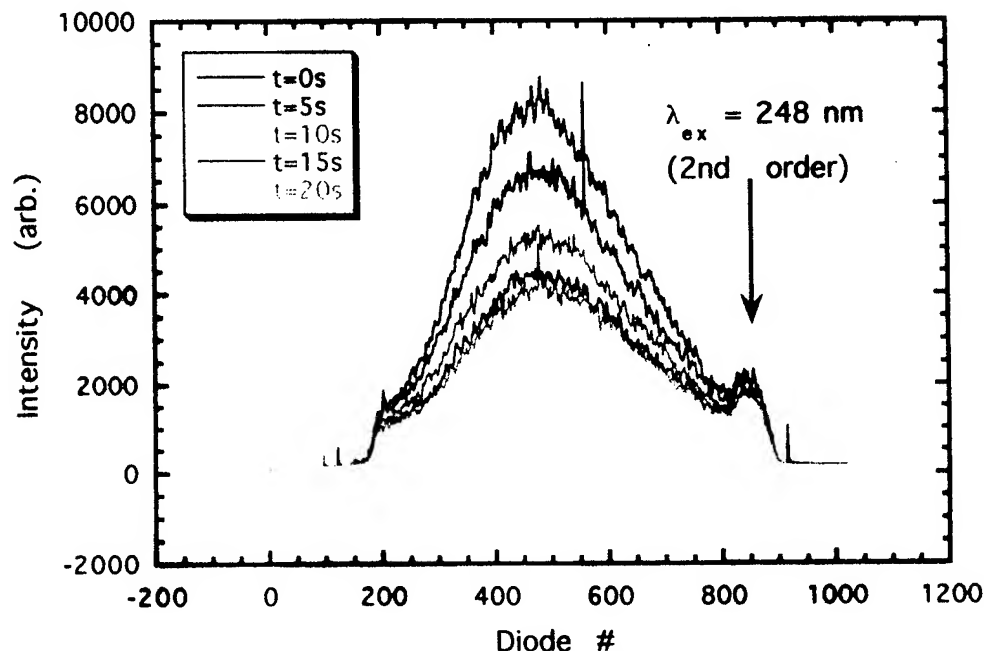


Figure 1. Fluorescence spectra from *B. subtilis* shown at 5 s intervals when exposed to 248 nm excitation at 200 pulses /s and  $\approx 8 \text{ mJ/cm}^2$  per pulse.

## References

1. M. W. Mayo, S. C. Hill, and R. K. Chang, "Fluorescence of bacteria, pollens and naturally occurring airborne particles: excitation /emission spectra", (submitted to Appl. Spectrosc.).
2. P. B. Oldham, "Multidimensional Fluorescence Identification of Phytoplankton", in Modern Techniques for Rapid Microbiological Analysis, W. H. Nelson, (VCH, New York, 1991) pp. 199-240.
3. M. Seaver and J. D. Eversole, "UV excited fluorescence from biological particles", presented at, Scientific Conference on Obscuration and Aerosol Research, ERDEC, APG, Aberdeen MD, June 1995
4. J. Ho and P. Hairston, "Development of a fluorescence aerodynamic particle sizer for biological aerosol detection", presented at, Scientific Conference on Obscuration and Aerosol Research, ERDEC, APG, Aberdeen MD, June 1995
5. R. G. Pinnick, S. C. Hill, P. Nachman, J. D. Pendleton, G.L. Fernandez, M. W. Mayo, and J. G. Bruno, "Fluorescence particle counter for detecting airborne bacteria and other biological particles", (submitted to Aerosol Sci. Tech.)
6. P. B. Oldham, "Multidimensional Fluorescence Identification of Phytoplankton", in Modern Techniques for Rapid Microbiological Analysis, W. H. Nelson, (VCH, New York, 1991) pp. 199.
7. for example: B. G. deGroot, M. van Dam, N. CX. Swart, A. Willemsen, and J. Greve, *J. Cytom.*, **8**, 445 (1987).
8. F. W. J. Teale and G. Weber, *Biochem. J.* **65**, 476 (1957), and Fluorescence and Phosphorescence of Proteins and Nucleic Acids, S. V. Konev, (Plenum, New York, 1967) pp 10.
9. K. Konig, Y Liu, G.J. Sonek, M.W. Berns and B. J. Tromberg, "Photoinduced autofluorescence modifications of cells in a optical trap", in Optical and Imaging Techniques in Biomedicine, A. Katzir, ed., Proc. SPIE **2329**, pp. 193, 1994

## Determining optical properties with fiber-optic oblique incidence reflectometry

S. Lin<sup>1,2</sup>, S. L. Jacques<sup>1,2</sup>, F. K. Tittel<sup>1</sup>, and L.-H. Wang<sup>2</sup>

- |  |   |
|--|---|
| 1. Dept. of Electrical and Computer Engineering<br>Rice University<br>P.O. Box 1892<br>Houston, TX 77251<br>shao@rice.edu<br>voice: (713) 792-3664 | 2. Laser Biology Research Laboratory<br>University of Texas<br>M.D. Anderson Cancer Center<br>1515 Holcombe Blvd.<br>Houston, TX 77030<br>fax: (713) 792-3995 |
|--|---|

### Introduction

We are interested in an inexpensive and non-invasive way to measure the absorption and reduced scattering coefficients,  $\mu_a$  and  $\mu_s'$ , of biological tissue. Optical properties can potentially be used for the diagnosis of diseases such as skin cancers as well as for accurate calculations of light dosimetry and monitoring of therapeutic laser procedures.

When a photon enters a tissue, it will generally scatter a few times before either being absorbed or escaping the tissue at a point other than its point of entry. This is diffuse reflectance. The diffuse reflectance of a normally incident beam is described by<sup>1</sup>

$$R(x) = z_o(\mu_{eff} + \frac{1}{\rho_1}) \frac{e^{-\mu_{eff} \rho_1}}{\rho_1} + (z_o + 2z_b)(\mu_{eff} + \frac{1}{\rho_2}) \frac{e^{-\mu_{eff} \rho_2}}{\rho_2}$$

where the source beam is modeled by a positive point source  $z_o$  deep and a negative image source  $z_o + 2z_b$  above the phantom surface.  $z_b = 2AD$  is the height of the extrapolated zero fluence boundary between the two lumped model sources. "A" describes the internal reflection of light back into the phantom from the surface; it is 1 for a matched boundary. D is the diffusion constant.  $\rho_1$  and  $\rho_2$  are the distances from the positive and negative lumped sources, respectively, to some point of interest x on the phantom surface.  $\mu_{eff}$  is the effective attenuation coefficient of the medium

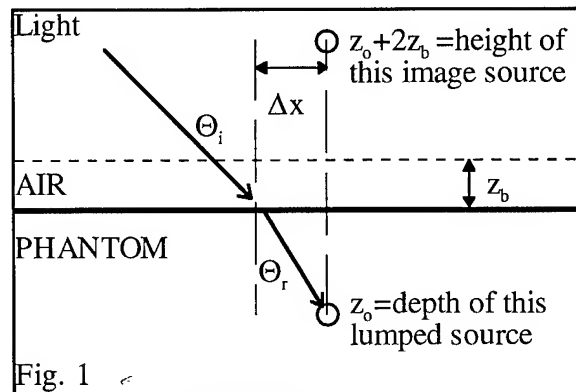
$$\mu_{eff} = \sqrt{\frac{\mu_a}{D}}$$

It is important to note that this reflectance expression does not conform to actual data at distances closer than 1 transport mean free path from the source because a lot of the reflected light is not actually diffuse<sup>1</sup>.

Delivering light at an oblique angle has two effects: first of all, the distances of the lumped sources above and below the phantom surface are smaller, and secondly, these sources are no longer directly above and below the light entry point, rather, they are shifted by a distance

$$\Delta x = \frac{\sin(\theta_r)}{0.35\mu_a + \mu_s'} = 3D\sin(\theta_r)$$

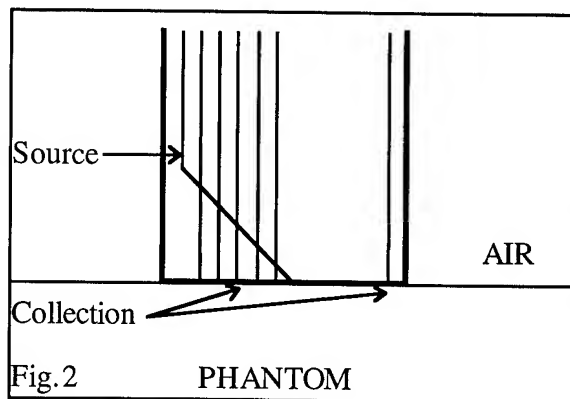
See Figure 1.<sup>2,3,4</sup> By sampling the diffuse reflectance profile with fibers of known position relative to an oblique source fiber, we measure  $\Delta x$ , calculate  $z_o$  and  $z_b$ , and do a curve fit to determine  $\mu_{eff}$ .  $\mu_a$  and  $\mu_s'$  are deduced from  $\Delta x$  and  $\mu_{eff}$ .



## Materials and Methods

The turbid tissue phantoms consisted of an absorber (Trypan Blue dye) and a scatterer (900 nm diameter Polystyrene spheres) in a water solution. We measured the absorption coefficient  $\mu_a$  of our stock Trypan Blue dye with a spectrophotometer and the scattering coefficient  $\mu_s$  of our stock Polystyrene by collimated transmission<sup>5</sup>. The anisotropy of scattering was calculated using Mie theory<sup>6</sup>. By adjusting the concentrations of the dye and the spheres, we made a number of phantoms with reduced scattering coefficients ranging from 4 to 10  $\text{cm}^{-1}$  and absorption coefficients ranging from 0.2 to 0.6  $\text{cm}^{-1}$  (all at 632.8 nm wavelength).

Our fiber optic probe both delivered source light as well as collected diffuse reflectance (see Figure 2). The source fiber was bent to deliver light to the phantom at an angle of 45 degrees, but each collection fiber was placed normal to the phantom surface. We used a HeNe laser (632.8 nm) as our source and measured the detected reflectance from each collection fiber with a power meter. The reflected power recorded for each collection fiber was calibrated against the average throughput of all the collection fibers when placed in a homogeneous light field. The position of each collection fiber relative to the source was taken from a digitized image (resolution of 45  $\mu\text{m}$  per pixel) of the probe.



We also constructed a flat black cover to attach to the face of our probe. When the probe face was placed in contact with the surface of the phantom, this cover contacted the remaining phantom surface and served to approximate a matched boundary condition. That is, there was minimal light reflected back into the phantom by the water-cover interface.

The data was fitted to the expression for diffuse reflectance with a nonlinear least-squares fit<sup>7</sup> to yield the shift in the center of diffuse reflectance  $\Delta x$  and the effective attenuation coefficient  $\mu_{\text{eff}}$  from which we deduced  $\mu_a$  and  $\mu_s'$ . This data analysis was implemented in C on a Sun SPARCstation 10.

## Results

Table 1 contains the computed results from data taken from our six tissue phantoms. The highest relative error in  $\Delta x$  was 8%, with most errors around 5% or better. The relative errors in  $\mu_{\text{eff}}$  were within 9%. For  $\mu_a$ , the error ranged from 6 to 19%, and for  $\mu_s'$  the error was within 10%.

Table 1.

Phantom		$\Delta x$ (cm)	$\mu_{\text{eff}}$ (1/cm)	$\mu_a$ (1/cm)	$\mu_s'$ (1/cm)
1	Expected	0.1875	2.2289	0.4	4
	Fitted	0.1725	2.0934	0.3246	4.3868
	% Error	8.01	-6.08	-18.85	9.67
2	Expected	0.1249	2.7305	0.4	6
	Fitted	0.1227	2.6074	0.3583	6.1997
	% Error	-1.77	-4.51	-10.43	2.09
3	Expected	0.0954	3.1254	0.4	8
	Fitted	0.0959	2.8575	0.3363	7.9754
	% Error	0.58	-8.57	-15.92	-0.31
4	Expected	0.0766	3.4883	0.4	10

	<b>Fitted</b>	0.0805	3.5121	0.4263	9.4964
	<b>% Error</b>	<b>5.13</b>	<b>0.68</b>	<b>6.57</b>	<b>-5.04</b>
<b>5</b>	<b>Expected</b>	0.1264	1.9198	<b>0.2</b>	<b>6.073</b>
	<b>Fitted</b>	0.1218	1.7905	0.1676	6.3153
	<b>% Error</b>	<b>-3.62</b>	<b>-6.74</b>	<b>-16.18</b>	<b>3.99</b>
<b>6</b>	<b>Expected</b>	0.1236	3.3629	<b>0.6</b>	<b>6.073</b>
	<b>Fitted</b>	0.1219	3.2805	0.5632	6.1722
	<b>% Error</b>	<b>-1.35</b>	<b>-2.45</b>	<b>-6.13</b>	<b>1.63</b>

### Conclusions

It is clear from our results that we can measure the shift in the center of diffuse reflectance,  $\Delta x$ , quite accurately. Since  $\Delta x$  is very closely related to  $\mu_s$ ' (particularly for relatively low absorbing media),  $\mu_s$ ' was deduced with roughly the same error. In addition, the 10% or less error we found in  $\mu_s$ ' is probably within the accuracy we can expect to achieve in mixing our phantoms to begin with.

For  $\mu_{\text{eff}}$ , the relative errors were somewhat higher, but all were still within 10%. The trend to note is that all but one of the fitted values of  $\mu_{\text{eff}}$  were low. This suggests that there was some effect that decreased the actual absorption of the phantom from what we expected. We are in the process of isolating this effect, which might be due to interactions between the Trypan Blue dye and Polystyrene spheres or simply due to adherence of dye to the container walls. The fact that increasing absorption from 0.2 to 0.6/cm (at the same scattering coefficient of 6.073/cm) decreases the error in  $\mu_{\text{eff}}$  is consistent with this hypothesis. Finally, since  $\mu_a = D\mu_{\text{eff}}^2$ , it is expected that its error should reflect the sum of the error in  $\Delta x$  and twice the error in  $\mu_{\text{eff}}$ , and it does.

Thus we have shown that with a single measurement of the relative profile of diffuse reflectance by fiber-optic oblique incidence reflectometry, we can accurately measure the shift in the center of diffuse reflectance from the light entry point and the effective attenuation coefficient. These two values in turn may be used to deduce both optical properties of absorption and reduced scattering.

### References

1. T. J. Farrell, M.S. Patterson, and B. C. Wilson, "A diffusion theory model of spatially resolved, steady-state diffuse reflectance for the non-invasive determination of tissue optical properties *in vivo*," Med. Phys. **19**, 879-888 (1992).
2. L.-H. Wang and S. L. Jacques, "Use of a laser beam with an oblique angle of incidence to measure the reduced scattering coefficient of a turbid medium," Applied Optics **34**, 2362-2366 (1995).
3. L.-H. Wang and S. L. Jacques, "Using an obliquely incident laser beam to measure optical properties of turbid media," Proc. Soc. Photo-Opt. Instrum. Eng. **2389**, 522-532 (1995).
4. S.L. Jacques, M. R. Ostermeyer, and L.-H. Wang, "On the diffusion constant of light transport in turbid media," in preparation (1995).
5. L.-H. Wang and S. L. Jacques, "Error estimation of measuring total interaction coefficients of turbid media using collimated light transmission," Physics in Medicine and Biology **39**, 2349-2354 (1994).
6. L.-H. Wang and S. L. Jacques, MIESPHR Program: Mie Theory for Scattering Spherical Particles (University of Texas M.D. Anderson Cancer Center, Houston, Texas, USA, 1995). Downloadable using anonymous ftp from laser.mda.uth.tmc.edu (129.106.60.92).
7. W. H. Press, B. P. Flannery, S. A. Teukolsky, and W. T. Vetterling, *Numerical Recipes in C*, 2nd ed. (Cambridge University Press, 1992).

## A low cost phase modulation system for tissue spectroscopy and oximetry

Yunsong Yang, Hanli Liu, Maureen O'Leary\*, Britton Chance

Department of Biochemistry and Biophysics and Department of Physics\*, University of Pennsylvania  
Philadelphia, Pennsylvania 19104

Tel: (215)898-4387; Fax: (215)898-1806; E-mail: yunsong@eniach.seas.upenn.edu

### Introduction

The determination of the optical properties of biological tissue is important in both diagnostic and therapeutic applications in medicine. Analytical expressions for frequency domain parameters (e.g., AC amplitude, phase shift) as the function of absorption coefficient( $\mu_a$ ) and the transport scattering coefficient( $\mu_s'$ ) have been demonstrated by using the diffusion approximation. Several modulation-detection techniques have been developed for frequency domain spectroscopy. Generally two frequencies are applied for phase detection. However in multi-channel or multi-wavelength applications, time sharing technique has to be employed, otherwise multiple number of frequencies will be needed, resulting more rigid requirement for instrumentation and higher cost.

### Method

We present a novel technique which uses the in-phase and quadrature(I&Q) demodulator and one frequency to detect both the amplitude and the phase. Figure 1. shows that an I&Q demodulator consists of a pair of double balanced mixers(DBMs) driven from a quadrature reference source, a pair of low pass filters(LPFs), a 90-degree power splitter and a 0-degree power splitter.

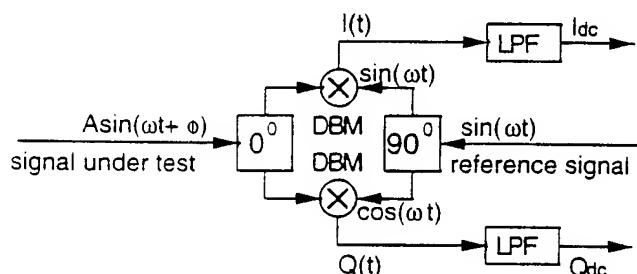


Figure 1. Diagram of an in-phase and quadrature demodulator.

Functioning like a multiplier, the in-phase mixer produces:

$$I(t) = A \sin(\omega t + \phi) \sin(\omega t) = 1/2 A \cos \phi - 1/2 A \cos(2\omega t + \phi) \quad (1)$$

and the quadrature mixer produces:

$$Q(t) = A \sin(\omega t + \phi) \cos(\omega t) = 1/2 A \sin \phi + 1/2 A \sin(2\omega t + \phi) \quad (2)$$

where  $\sin \phi$  term and  $\cos \phi$  term are DC signals which carry the amplitude and phase information, and  $\sin(2\omega t + \phi)$  term and  $\cos(2\omega t + \phi)$  term are radio frequency signals which will not pass through the LPFs. Therefore,

$$\phi = \tan^{-1} \left( \frac{Q_{dc}}{I_{dc}} \right), \quad A = 2 \sqrt{I_{dc}^2 + Q_{dc}^2} \quad (3)$$

Figure 2. shows the experimental setup of using a frequency-encoding dual-wavelength phase modulation system to test the optical properties of tissue-stimulating model. Our experiment was done in a large glass fish tank. Two radio frequency signal generators operate at slightly different frequencies, namely 140.00MHz and 140.01 MHz, and provide the driving signals for two laser diodes(LDs) which work at different optical wavelengths(i.e. 784nm and 810nm). The RF signal generators also provide the reference signals for two I&Q demodulators, respectively. Due to the narrow band of LPFs, each I&Q demodulator produces two DC signals which carry the amplitude and phase information for one wavelength, while two laser beams are combined and fiber-coupled to the model simultaneously. The collected optical signal is fiber-coupled to a photo-multiplier tube(PMT). The transformed electronic signal is amplified by a low noise amplifier(LNA) before

being split into two I&Q demodulators. The detected DC signals are digitized by an analog-to-digital converter(ADC). A stepping motor controlled mechanical holder was used here to change the separation between source fiber bundle and detector fiber bundle. The optical properties of the model are obtained by the following equations based on diffusion theory:

$$\mu_a = \frac{\omega}{c \tan(2 \tan^{-1}(\frac{\text{slope}_{\text{phase}}}{\text{slope}_{\text{amp}}}))}, \quad \mu_s' = \frac{(\text{slope}_{\text{phase}}^2 + \text{slope}_{\text{amp}}^2)}{3\sqrt{\mu_a^2 + (\frac{\omega}{c})^2}} - \mu_a. \quad (4)$$

where  $\text{slope}_{\text{phase}}$  is the slope of phase versus  $r$ ,  $\text{slope}_{\text{amp}}$  is the slope of  $\ln(r \times \text{AC amplitude})$  versus  $r$ ,  $r$  is the radial distance between source fiber bundle and detector fiber bundle,  $\omega$  is the modulation frequency, and  $c$  is the speed of light in the medium.

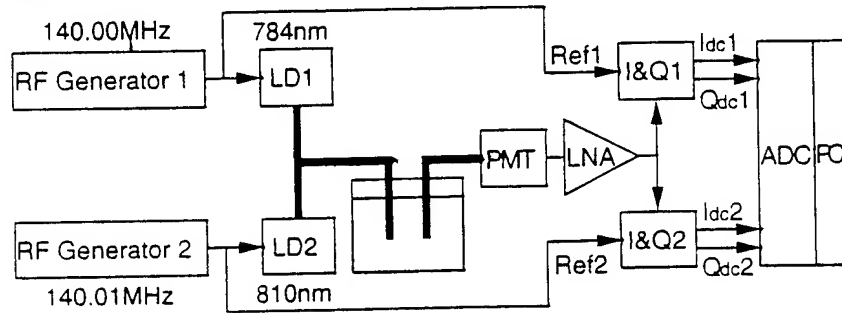


Figure 2. Experimental setup

## Results

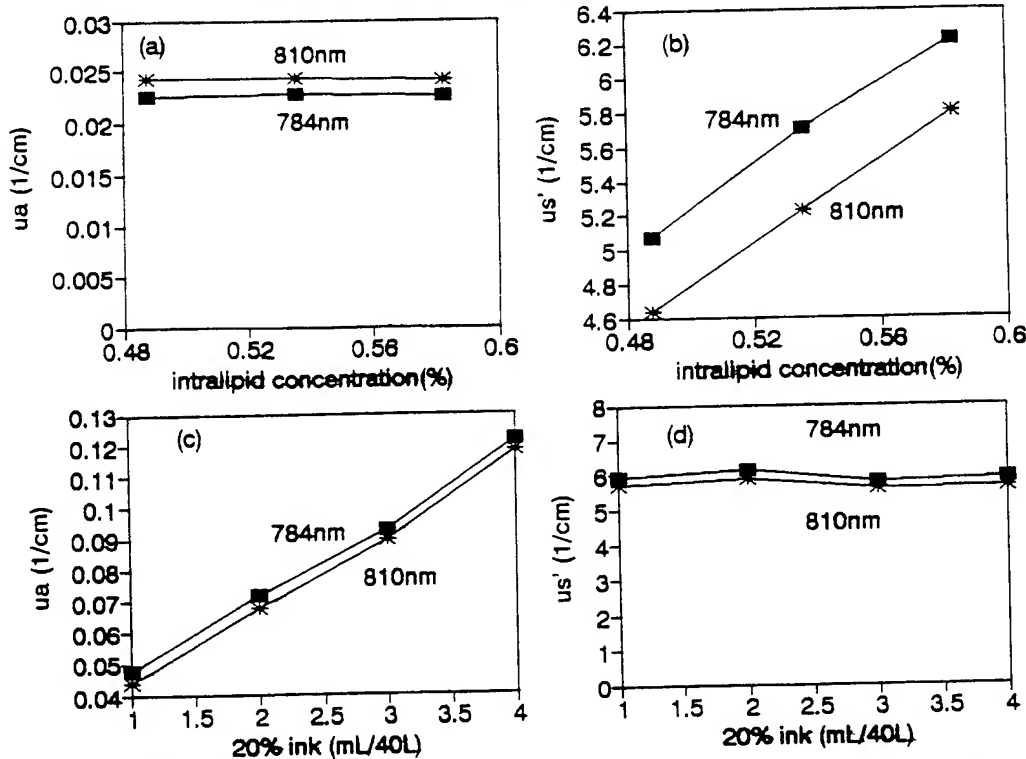


Figure 3. Experimental results of  $\mu_a$  and  $\mu_s'$  of a 40-liter intralipid solution measured with the Frequency-encoding Dual-wavelength Phase Modulation System.

Figures 3(a), 3(b), 3(c) and 3(d) show the results of  $\mu_a$  and  $\mu_s'$  of a 40-liter intralipid solution. In the case of 3(a) and 3(b), there was no ink in the solution, the concentration of intralipid was varied to obtain different  $\mu_s'$  values. From the graphs we can see that  $\mu_s'$  values are linear with the intralipid concentration for

both wavelengths, and  $\mu_a$  values remain constant. In the case of 3(c) and 3(d), intralipid concentration was kept at 0.6%, while the concentration of ink was varied to obtain different  $\mu_a$  values. The graphs show that  $\mu_a$  values are linear with the ink concentration, and  $\mu_s'$  values hold constant.

In clinical studies, particularly for imaging, the slope algorithm does not provide a spatial resolution of optical properties. On the other hand, the conventional method requires a calibration for absolute measurements of phase and amplitude. We thus propose a new approach to obtain optical properties at single source-detector separation without calibration. Based on the frequency-domain diffusion equation in an infinite medium, two equations F and G are introduced as:

$$F(\phi, A, \mu_a, \mu_s') = \phi - r \frac{\sqrt{\omega^2 + v^2 \mu_a^2} - v \mu_a}{\sqrt{2vD}} = 0, \quad (5)$$

$$G(\phi, A, \mu_a, \mu_s') = \ln A + \ln(4\pi r) + \ln D + r \frac{\sqrt{\omega^2 + v^2 \mu_a^2} + v \mu_a}{\sqrt{2vD}} = 0. \quad (6)$$

where  $\phi$  and  $A$  denote the measured phase and amplitude, respectively. According to the inverse function theory, following expressions are derived:

$$d\mu_a = - \frac{\begin{vmatrix} F_\phi & F_{\mu_s'} \\ G_\phi & G_{\mu_s'} \end{vmatrix}}{\begin{vmatrix} F_{\mu_a} & F_{\mu_s'} \\ G_{\mu_a} & G_{\mu_s'} \end{vmatrix}} d\phi - \frac{\begin{vmatrix} F_A & F_{\mu_s'} \\ G_A & G_{\mu_s'} \end{vmatrix}}{\begin{vmatrix} F_{\mu_a} & F_{\mu_s'} \\ G_{\mu_a} & G_{\mu_s'} \end{vmatrix}} \frac{dA}{A}, \quad d\mu_s' = - \frac{\begin{vmatrix} F_{\mu_a} & F_\phi \\ G_{\mu_a} & G_\phi \end{vmatrix}}{\begin{vmatrix} F_{\mu_a} & F_{\mu_s'} \\ G_{\mu_a} & G_{\mu_s'} \end{vmatrix}} d\phi - \frac{\begin{vmatrix} F_{\mu_a} & F_A \\ G_{\mu_a} & G_A \end{vmatrix}}{\begin{vmatrix} F_{\mu_a} & F_{\mu_s'} \\ G_{\mu_a} & G_{\mu_s'} \end{vmatrix}} \frac{dA}{A}. \quad (7)$$

where  $F_\phi$  is the partial derivative of  $F$  with respect to  $\phi$ , and so on. Given some perturbation to the optical properties, the relative phase change( $d\phi$ ) and relative amplitude change( $dA$ ) can be measured. Since equation(7) holds for different frequencies, if two frequencies are applied to the medium, four unknowns(i.e.  $d\mu_a$ ,  $\mu_a$ ,  $d\mu_s'$ ,  $\mu_s'$ ) can be obtained by four measurements(i.e.  $d\phi$  and  $dA$  for two frequencies). Theoretical simulations have shown that the optical properties can be determined in an error range of 5%; some experimental results are also obtained for comparison.

### Summary

This is an initial study of a new phase modulation system for tissue spectroscopy. The in-phase and quadrature demodulation technique was employed. Driven by the fast developing telecommunication market, I&Q demodulators are readily accessible and affordable. No synthesizer or high speed ADC is needed. Therefore the cost of the system is much lower. A frequency-encoding technique was developed to save the measurement time. In multi-channel or multi-wavelength application such as optical imaging, this advantage is necessary. A new perturbation algorithm was developed to calculate the optical properties without calibration. Further study has to be done in order to improve the performance of the system and its implementation in other applications.

### Reference

1. J.B. Fishkin and E. Gratton, "Propagation of Photon-Density Waves in Strongly Scattering Media Containing an Absorbing Semi-Infinite Plane Bounded by a Straight Edge", *J. Opt. Soc. Am. A* 10, 127-140(1993).
2. E.M. Sevick, B. Chance, J. Leigh, S. Nioka, and M. Maris, "Quantitation of time- and Frequency-Resolved Optical Spectra for the Determination of Tissue Oxygenation", *Anal. Biochem.* 195, 330-351(1991).
3. E. Gratton, S. Fantini, M.A. Franceschini, J.B. Fishkin, and J.S. Maier, "Near-Infrared Optical Spectroscopy of Tissues Using an LED Frequency Domain Spectrometer", in *OSA Proceedings on Advances in Optical Imaging and Photon Migration* edited by R.R. Alfano, Vol.21, 278-282(1994).
4. H. Liu, D.A. Boas, B. Beauvoit, E. Rachofsky, M.A. O'Leary, T. Kitai, and B. Chance, "Absorption and Scattering Properties in a Highly Absorbing Turbid Medium", in *OSA Proceedings on Advances in Optical Imaging and Photon Migration* edited by R.R. Alfano, Vol.21, 272-277(1994).

## Investigation of Exogenous Contrast Agents for Biomedical Optical Imaging

Tamara L. Troy, Lena Nelson-Larry, Christina L. Hutchinson and Eva M. Sevick-Muraca

School of Chemical Engineering  
Purdue University  
West Lafayette, IN 47907  
Phone: (317) 496-2739  
Fax: (317) 494-0805  
email: troy@ecn.purdue.edu

### Introduction

The success of frequency-domain biomedical optical imaging depends upon the ability to measure changes in photon migration due to differences in the optical properties of normal and diseased tissues. However, these differences may not be sufficiently large enough for consistent detection<sup>1</sup>. Exogeneous contrast can be imposed by drugs or dyes which provide optical contrast for diseased tissues. Therefore, the prospect of employing exogenous optical contrast for detecting tissue volumes was investigated in this study.

Exogenous contrast in tissues can be induced through injection of absorbing and fluorescing compounds which have an affinity for diseased tissues. One example concerns hematoporphyrin therapy whereby a photodynamic drug is administered for therapeutic reasons. These agents absorb as well as fluoresce and may provide contrast for imaging diagnostics in addition to providing therapy. In this study, we compare the contrast due to these two mechanisms: (i) absorption of light and (ii) fluorescent re-emission. In addition, we examine whether fluorescence quench kinetics can be monitored from within localized tissue regions in order to assess whether lifetime can provide contrast for optical imaging.

### Frequency-domain measurements of photon migration

In order to assess the contrast offered by these two mechanisms, we examined how

absorbing and fluorescing heterogeneities impact light propagation in random media. We measured light propagation using frequency-domain measurements of phase-shift and amplitude demodulation as a function of modulation frequency. Experimental measurements of phase-shift and amplitude demodulation of re-emitted fluorescent light were conducted at modulation frequencies between 80 and 240 MHz using a Ti:Sapphire laser (Spectra Physics, CA) at 780 nm. The laser was pulsed at a repetition rate of 80 MHz. The pulse train was delivered by a fiber optic to the surface of a cylindrical tank with diameter equal to 20 cm. The light was collected at a distance of 2.5 cm from the source by a second fiber optic and delivered to a PMT for detection. The gain of the PMT was modulated at a harmonic of the source frequency but offset by 100 Hz. The phase and modulation were extracted from the signal at this cross correlation frequency of 100 Hz through simple electronics (ISS, Champaign, IL). An 830 nm interference filter was used to make frequency-domain measurements at the emission wavelengths.

Phase-shift and amplitude demodulation were measured to evaluate the contrast offered by (i) a perfect absorber (ii) a fluorescent volume, and (iii) Indocyanine Green, an FDA approved dye with fluorescent re-emission at 830 nm. The perfect absorber consisted of a 6 mm diameter black rod. The fluorescent volume consisted of a 9 mm diameter tube filled with Intralipid solution containing a micromolar concentration of Diethylthiatricarbocyanine iodide (DTTCI) or IR-125, which are common laser dyes. Measurements of phase-shift were conducted as the heterogeneities



were moved from a peripheral location midpoint between the source and detector towards the center of the tank.

### Contrast due to absorption versus fluorescence

Figure 1 shows the phase-shift differences due to the presence of a heterogeneity measured at 80, 160, and 240 MHz modulation frequencies. Our results show that the best contrast available from absorption (i.e., a perfect absorber) causes a smaller measurable disturbance in photon migration than a micromolar concentration of fluorescent dye.

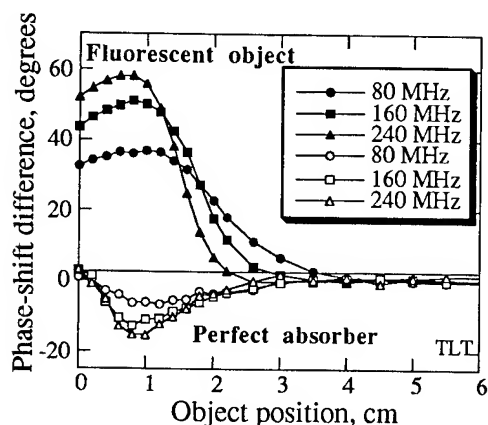


Figure 1: Measurements of phase shift difference vs. object position for a fluorescent object (closed symbols) and a perfect absorber (open symbols).

Figure 2 shows the similar measurements of phase-shift difference at excitation (780 nm) and fluorescent (830 nm) wavelengths for a 9 mm tube containing 0.1% Intralipid and micromolar concentrations of Indocyanine Green. As illustrated by the results in Figure 1, the contrast due to fluorescence exceeds that due to absorption.

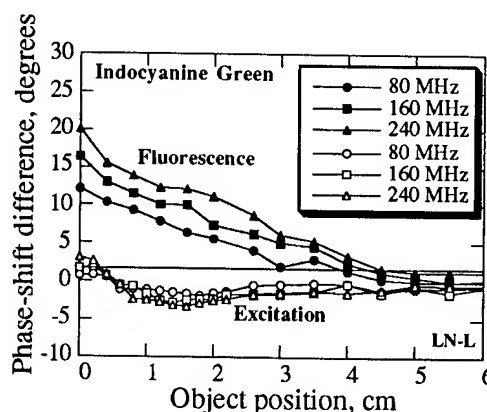


Figure 2: Measurements of phase shift difference vs. object position at the excitation (open symbols) and fluorescent (closed symbols) wavelengths for Indocyanine Green.

### Determination of lifetime of fluorescent heterogeneity

Recently, Hutchinson, *et al.*<sup>2</sup> showed that the lifetime of a heterogeneity can be determined from the demodulation of the re-emitted fluorescent light when it is referenced to the demodulation of a second fluorophore. Equation (1) shows the relationship between the measured modulation due to a "sampling" (superscript s) and "reference" (superscript r) fluorophore and the lifetime of the two probes.

$$\frac{M^s(\omega)}{M^r(\omega)} = \frac{\sqrt{1 + (\omega\tau^s)^2}}{\sqrt{1 + (\omega\tau^r)^2}} \quad (1)$$

This equation shows that lifetime determination can be made in a scattering media without prior knowledge of its optical properties.

In an analogous experiment to the ones described above, the fluorescent modulation was measured as a function of frequency as DTTCI and IR-125 scattering solutions were moved in separate experiments from the periphery to the center of the phantom. Figure 3 shows the ratio of modulation as a function of position of the fluorescent body. The solid lines denote the modulation ratio that is predicted by Eqn (1)

from measured and literature values for the lifetimes of the two dyes. At distances less

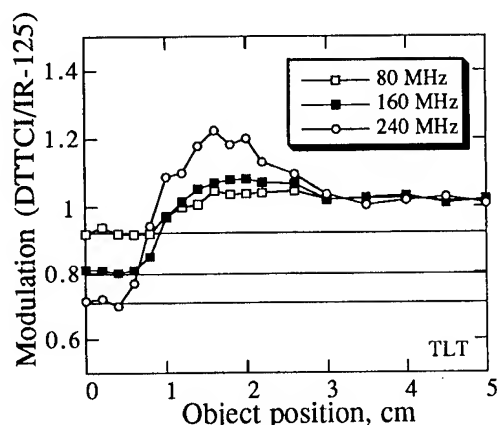


**Figure 3:** Measurements of the fluorescent modulation as a function of position for DTTCI and IR-125. Solid line denotes theory give by Eqn (1).

than 1 cm away from the source and detector, the agreement between theory and measurement is good. However, at distances farther away, the re-emitted fluorescent signal from IR-125 becomes weak and the modulation ratios become erroneous. Nonetheless, these results show that lifetime information is contained in the re-emitted signals which originate from the fluorescent body.

Paithankar and Sevick<sup>3</sup> have demonstrated fluorescent lifetime imaging using computational approaches. Our results suggest that experimental measurements can be conducted and used as input into their inverse imaging solution.

### Summary

These results show that exogenous contrast agents can be detected using photon migration techniques. Furthermore, these results indicate that fluorescence may offer the best contrast for optical imaging. In addition, we have experimentally shown that lifetime information is contained in the re-emitted fluorescent signal.

### Acknowledgment

This work is supported in part by the National Institutes of Health (CA61413 and K04-CA68374).

### References

1. Troy, T.L., Page, D.L., and E.M. Sevick-Muraca, "Optical Properties of Normal and Diseased Breast Tissue," This proceedings.
2. Hutchinson, C.L., Troy, T.L., and E.M. Sevick-Muraca, "Fluorescence-lifetime determination in tissues or other scattering media from measurement of excitation and emission kinetics," accepted, Applied Optics.
3. Paithankar, D.Y., and E.M. Sevick-Muraca, "Fluorescence lifetime imaging with frequency-domain photon migration measurement," this proceedings.

## Optical Properties of Normal and Diseased Breast Tissue

Tamara L. Troy and Eva M. Sevick-Muraca  
School of Chemical Engineering  
Purdue University  
West Lafayette, IN 47907

David L. Page  
Vanderbilt School of Medicine  
Vanderbilt University  
Nashville, TN 37205  
Phone: (317) 496-2739  
Fax: (317) 494-0805

### Introduction

Current statistics show that one in eight women in the U.S. will encounter breast cancer in her lifetime<sup>1</sup>. While x-ray mammography is an excellent tool for detecting the disease in postmenopausal women, this screening tool is insufficient for the general population. The increase in cellularity of breast tissues in premenopausal women causes an inability to accurately measure breast disease due to an increase in radiative scatter. Therefore, the small yet finite risks of x-radiation outweighs any possible benefits of detecting cancer in this age group using conventional mammography. Near-infrared (NIR) biomedical optical imaging may provide an alternate method for the detection of tumors in this population because unlike x-ray mammography, NIR techniques are not limited by but rather depend upon tissue scatter. However, the scattering and absorption properties of breast tissue need to be determined in order to assess the feasibility of NIR techniques.

### Method

In order to evaluate whether significant and consistent optical property differences exist between normal and diseased tissues, we measured the scattering coefficient,  $\mu_s$  and the absorption coefficient,  $\mu_a$  of excised normal and diseased breast tissues using the double integrating sphere apparatus shown in Figure 1.

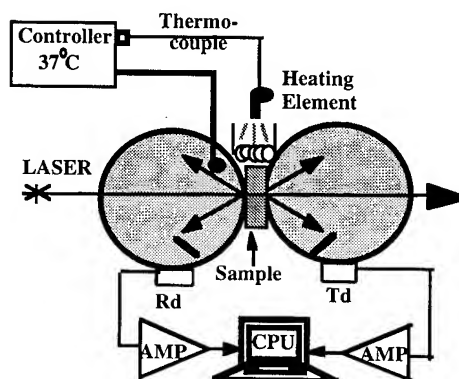


**Figure 1:** Schematic of the double integrating sphere apparatus.

This system was used to simultaneously measure diffuse reflectance,  $R_d$ , and diffuse transmittance,  $T_d$ , of a 1 mm thick tissue sample maintained at 37°C. Using these measurements, optical coefficients of the samples were obtained from an inverse adding doubling algorithm provided by Prahl<sup>2</sup>.

In order to validate our technique, measurements of monodisperse polystyrene suspensions with varying diameters and concentrations were made. From the values of isotropic scattering coefficient determined experimentally from the integrating sphere measurements, the scattering efficiency was determined for each bead size at various wavelengths. Figure 2 shows the typical agreement between the values predicted by Mie

theory (solid line) and that obtained experimentally.

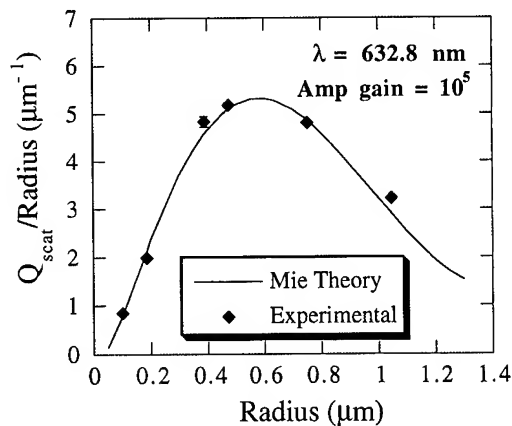


**Figure 2:** Comparison of Mie theory (solid line) with experimentally derived parameters (points).

Due to light losses at the edges of the sample, the absorption coefficient is over predicted. However, from experimental diffuse reflectance and transmittance measurements in a dye-scatter solution, we found that  $\mu_a$  was consistently higher by a constant factor. Using various concentrations of a broad band absorber in polystyrene suspensions, we calibrated the measurement of absorption from 0 to 0.1 cm<sup>-1</sup>.

### Comparison of frozen and freshly excised tissue

Breast tissue samples from both tumor biopsies and reduction surgeries were obtained from Vanderbilt University Hospital. Since the majority of diseased tissue specimens were available frozen, experiments were performed to determine if the process of freezing caused changes in tissue optical properties. Fresh samples from normal breast tissue were used in this investigation. The fresh sample was heated to body temperature, 37°C, and the optical properties were measured. The sample was then frozen for three minutes with liquid nitrogen and subsequently thawed back to 37°C. Again, the optical property measurements were made. Comparing the two sets of data, it was statistically shown to a 99% confidence level that no significant difference

exists between the optical properties of fresh and previously frozen tissue.

However, the temperature at which the sample is maintained during the measurement does impact the optical characteristics of the tissue. Experiments on canine prostate tissue (shown in Figure 3) demonstrate these temperature effects. Therefore, all tissue measurements were performed at 37°C to mimic body temperature conditions.

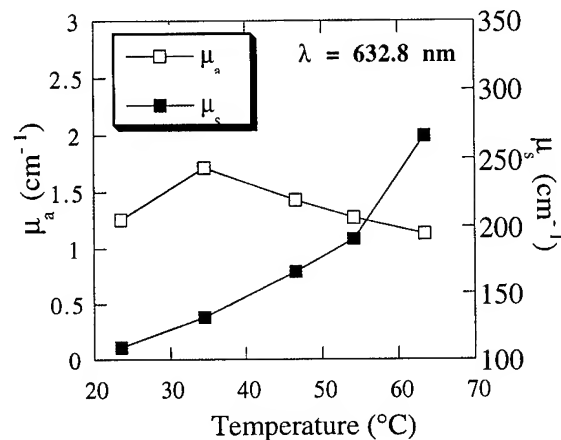


**Figure 3:** Dependence of the absorption coefficient and the anisotropic scattering coefficient on temperature for canine prostate tissue.

### Optical properties of breast tissues

In order to determine if significant optical contrast exists between normal and diseased tissue, data of  $\mu_a$  and  $\mu_s$  were analyzed to assess population differences. Figure 4 shows the measured data of  $\mu_a$  and  $\mu_s$  from normal and diseased tissues plotted at a wavelength of 749 nm. This figure shows that data from normal and diseased tissue do not fall into two distinct regions. Also, statistical analysis of the data shows that at a 99% confidence level no significant difference occurs.

However, small differences in the optical properties between normal and diseased tissue types have been revealed from histopathological characterization of the tissue. For example, we found that normal tissue tends to have greater scattering capacity than

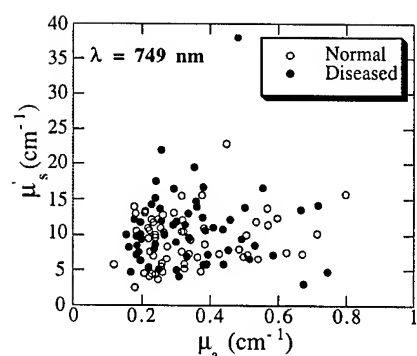


**Figure 4:** The absorption coefficient,  $\mu_a$ , plotted versus the anisotropic scattering coefficient,  $\mu'_s$ , for normal and diseased breast tissue data at  $\lambda=749\text{nm}$ .

fatty tissues. Fibrous tissues have greater scattering capacities than normal and fatty tissues. Nonetheless, the contrast available endogeneously may not be significant for detection of the disease with optical techniques. Our results point to the use of contrast agents.

### Conclusions

It is noteworthy that these measurements underestimate absorption due to blood drainage in excised tissue. Nonetheless, optical property measurements of normal and diseased breast tissue suggest a need for exogenous optical contrast that has a high selectivity for diseased tissues.

### Acknowledgments

We gratefully acknowledge the assistance of Julia Smith at the Vanderbilt University Medical School for her assistance in obtaining tissue samples; Scott Prahl at the Laser Research Center at St. Vincent Hospital in Portland, Oregon for his assistance with the double integrating spheres and the use of his inverse adding doubling algorithm. This work was supported by the National Institutes of Health CA61413-03 and the Research Career Development Award (EMS).

### References

1. Marshall, E., "Search for a killer: Focus shifts from fat to hormones in a special report on breast cancer," *Science*, 259: 618-621, 1993.
2. Prahl, S.A., van Gemert, M.C. and A.J. Welch, "Determining the optical properties of turbid media by using the adding doubling method," *Applied Optics*, 32: 559, 1993.
3. D.L. Page and T.J. Thomas, Diagnostic Histopathology of the Breast, Churchill Livingstone, Edinburgh, London, 1987.

# FREQUENCY-DOMAIN PHOTON MIGRATION IN TWO-LAYERED TISSUES

*Michal Rosen-Zvi and Haim Taitelbaum*

Department of Physics  
Bar-Ilan University  
Ramat-Gan 52900, ISRAEL

Tel: +972-3-531-8465  
Fax: +972-3-535-3298  
E-mail: haimt@eder.cc.biu.ac.il

Recently, a model of random-walk on a lattice has been suggested to describe photon migration in biological tissues [1-5]. In this model the *scattering* is simulated by a random change in the direction of travel of each photon on a lattice and the *absorption* occurring between nodes of the lattice is described by Beer's Law. This model has been applied to several typical biological systems, in various possible experimental schemes. For continuous light source, the random-walk model has successfully predicted the magnitude of reflected photon flux, the mean transit time and the optical penetration depth in *homogeneous* tissues. The assumption was then made that a single set of scattering and absorption parameters is sufficient to describe the entire bulk medium.

However, there are many biological tissues for which the homogeneity assumption is not justified. In particular, many tissues have *layered* structure, where each layer can be characterized by a different set of physical parameters [6-8]. Examples include skin (epidermis, dermis, subcutaneous fat), the walls of arteries (intima, muscle, adventitia), stomach, bladder, intestine and esophagus. Also, different tissues in contact, or tumors within a single tissue might be modeled as being such layers.

The basic multi-layer model is that of a two-region composite, with a surface layer lying on top of a semi-infinite substrate (Fig. 1). The thickness of the upper layer is taken equal to  $W$ , and the two layers differ only in their *absorption* coefficients,  $\mu_1$  for the upper layer, and  $\mu_2$  for the lower one. The case where the upper layer is the more absorptive one,  $\mu_1 > \mu_2$ , is more realistic and is typical for most biological applications, and has been found to have very interesting properties [4,9-11].

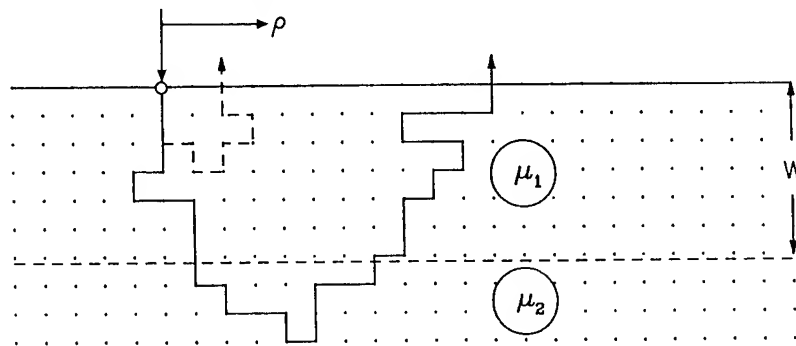


**Fig. 1:** A sketch of the lattice model for two-layered tissues.

In this case, short photon trajectories are likely to occur within the upper layer, but longer sojourns in the bulk imply that photons must travel in the lower, less absorptive, region, as otherwise they tend to be absorbed. This characteristics reflects in sharp *crossovers* in quantities measured as a function of the surface distance from the injection point, allowing one to determine the absorptivities of both layers, as well as the upper layer thickness.

The basic random-walk model for photon migration has been developed for measurements in the *time-domain*, in which a pulse of light is injected and measurements of the reflected intensity are made at a given distance, at a given time. However, the complex path and multiple scatters experienced by the light within the turbid tissue, result in a loss of amplitude and coherence so that the intensity of the reemitted light is several orders of magnitude smaller than the source intensity. Thus, predictions based on intensity measurements only might be very sensitive to signal-to-noise ratio problems. Contrary to these, measurements in the *frequency domain*, seem to suffer less from this drawback. In this domain, one can expect to obtain useful information from the *phase-shift* of the detected light with respect to the source. Moreover, most of the practical instrumentation are designed in the frequency-domain, where the phase-shift and demodulation of an amplitude-modulated light source is related to the mean transit time in the tissue, which by itself reflects the tissue's absorption and scattering parameters. This also helps to interpret Doppler measurements of blood flow in tissues [see, e.g., 12].

Some aspects of diffusive propagation of intensity-modulated light in tissues, and a corresponding frequency-resolved analysis have been recently studied by several groups [13-18]. In this paper we extend the random walk model of photon migration in two-layered tissues to include frequency-domain analysis. We present an analytical expression for the phase shift  $\Phi$  as a function of the source-detector separation  $\rho$ , which shows that there can be as many as three different types of behavior of this quantity, depending on the relation between the modulated frequency and the absorptivities of both layers. As a result, the possibility of determining the absorptivities of the two layers and the upper layer thickness from the phase shift is different in each regime. When the modulated frequency  $\omega$  is relatively small, one obtains that the phase shift of the reflected intensity is proportional to the mean path length of this radiation, a quantity whose dichotomous spatial behavior indicates the two-layer structure [4,10], and from which one can infer the absorption coefficients of the two layers, as well as the upper layer thickness. The specific result in this limit is

$$\Phi = \omega \langle n|\rho \rangle \approx \frac{1}{2} \sqrt{\frac{6}{\mu_1}} \omega \rho \left[ \frac{1 + \alpha(\rho)}{1 + \sqrt{\frac{\mu_2}{\mu_1}} \alpha(\rho)} \right], \quad (1)$$

where  $\alpha(\rho)$  is a crossover function which vanishes at small  $\rho$  and is very large for large  $\rho$ . As  $\omega$  becomes comparable with the absorptivities (in appropriate units), the possibility of observing the two-layer structure becomes worse, and finally, for much larger frequencies, it is impossible to make any diagnostic conclusions based on the phase shift. We discuss the applicability of these results for typical frequency-domain measurements in tissues.

## REFERENCES

- [1] R.F. Bonner, R. Nossal, S. Havlin and G.H. Weiss, "Model for photon migration in turbid biological media," *J. Opt. Soc. Am. A*, **4**, 423-432 (1987).
- [2] G.H. Weiss, R. Nossal, R.F. Bonner, J.E. Kiefer, H. Taitelbaum, and S. Havlin, "Random walk theory of photon migration in a turbid medium," in *Dynamical Processes in Condensed Molecular Systems*, J. Klafter, J. Jortner and A. Blumen, eds., (World Scientific, Singapore, 1989), pp. 147-174.
- [3] R.F. Bonner, R. Nossal, and G.H. Weiss, "A random walk theory of time-resolved optical absorption spectroscopy in tissue," in *Photon Migration in Tissues*, B. Chance, ed., (Plenum, New-York, 1990), pp. 11-23.
- [4] H. Taitelbaum, "Optical penetration depth in layered tissues", OSA Proc. on *Advances in Optical Imaging and Photon Migration*, R.R. Alfano, ed., **21**, 305-309 (1994).
- [5] A.H. Gandjbakhche and G.H. Weiss, "Random walk and diffusion-like models of photon migration in turbid media", *Prog. Opt.*, in press.
- [6] S. Takatani and M.D. Graham, "Theoretical analysis of diffuse reflectance from a two-layer tissue model," *IEEE Trans. Biomed. Eng.*, **26**, 656-664 (1979).
- [7] M. Keijzer, W.M. Star, and P.R.M. Storch, "Optical diffusion in layered media", *Appl. Opt.*, **27**, 1820-1824 (1988).
- [8] J.M. Schmitt, G.X. Zhou, E.C. Walker, and R.T. Wall, "Multilayer model of photon diffusion in skin," *J. Opt. Soc. Am. A*, **7**, 2141-2153 (1990), and references cited therein.
- [9] R. Nossal, J. Kiefer, G.H. Weiss, R. Bonner, H. Taitelbaum, and S. Havlin, "Photon migration in layered media," *Appl. Opt.*, **27**, 3382-3391 (1988).
- [10] H. Taitelbaum, S. Havlin, and G.H. Weiss, "Approximate theory of photon migration in a two-layer medium," *Appl. Opt.*, **28**, 2245-2249 (1989).
- [11] I. Dayan, S. Havlin, and G.H. Weiss, "Photon migration in a two-layer turbid medium: A diffusion analysis," *J. Mod. Opt.*, **39**, 1567-1582 (1992).
- [12] R.F. Bonner and R. Nossal, "Model for laser Doppler measurements of blood flow in tissue," *Appl. Opt.*, **20**, 2097-2107 (1981).
- [13] J. Fishkin, E. Gratton, M.I. vandeVen, W.W. Mantulin, "Diffusion of intensity modulated near-infrared light in turbid media", *SPIE Proceedings*, **1431**, 122-135 (1991).
- [14] M.S. Patterson, J.D. Moulton, B.C. Wilson, K.W. Berndt and J.R. Lakowicz, "Frequency-domain reflectance for the determination of the scattering and absorption properties of tissue", *Appl. Opt.*, **30**, 4474-4476 (1991).
- [15] E.M. Sevick, B. Chance, J. Leigh, S. Nioka and M. Maris, "Quantitation of time- and frequency- resolved optical spectra for the determination of tissue oxygenation", *Anal. Biochem.*, **195**, 330-351 (1991).
- [16] S.R. Arridge, M. Cope and D.T. Delpy, "The theoretical basis for the determination of optical pathlengths in tissue: temporal and frequency analysis", *Phys. Med. Biol.*, **37**, 1531-1560 (1992).
- [17] S. Jacques, A. Hielscher, L. Wang and F. Tittel, "How source/collector placement and subsurface absorbing layer affect time-resolved and phase/modulation-resolved photon migration", *SPIE Proceedings*, **1888**, 310-319 (1993).
- [18] A. Yodanis and B. Chance, "Spectroscopy and imaging with diffusing light", *Physics Today*, 34-40 (March 1995), and references cited therein.



# Non-invasive spectroscopy of variously shaped turbid media like human tissue based on the microscopic Beer-Lambert law

Yutaka Tsuchiya and Tsuneyuki Urakami

*Central Research Laboratory, Hamamatsu Photonics K.K.,*

*5000 Hirakuchi, Hamakita 434, Japan*

Fax.+81-53-586-6180, E-mail tsuchy@hamakita.hpk.co.jp

## 1. Introduction

Tissue spectroscopy is a diagnostic tool that has several potentials in the medical field. So far a variety of methods have been developed to measure the concentration of absorptive constituents such as hemoglobin in the living tissue [1-3]. These methods; continuous wave [4], time resolved [5-6] and frequency domain [7-8] techniques, are based on a model in which the diffusion approximation is applied on photon transport in homogeneous media.

While diffusion modeling with exact boundary conditions can be quite accurate [9-13], a practical problem limiting its use in tissue spectroscopy is that real tissue volumes are not simple shapes. The exact boundary conditions can be applied to the media that have simple shape such as spheres, cylinders, slabs, semi-infinite or infinite media [9]. Thus it is important to have a method measuring optical properties of variously shaped media.

Recently we have deduced fundamental, but simple formulas that represent the re-emission from media based on a model in which the microscopic Beer-Lambert law holds [14]. These formulas are valid for the homogeneous media having variously shaped non-reentrant surfaces. They can be extended to represent the re-emission in the time and the frequency domain as well as the steady state [14].

In this paper we propose a new method to measure the absolute concentration of the absorptive constituents in the homogeneous media that have variously shaped non-reentrant surfaces. In this method it was assumed that the scattering coefficient is invariant in the spectral range used for the measurement. The error of less than  $\approx 5\%$  has been obtained in absolute concentration by detecting the amplitude and the phase delay of the re-emission, when a photon-density wave was the incidence to a liquid phantom.

## 2. Theory

Consider the microscopic Beer-Lambert law in homogeneously turbid media. The impulse response of diffuse re-emission  $J(\mu_s, \mu_a, t)$  is expressed as

$$J(\mu_s, \mu_a, t) = b s(\mu_s, t) \exp(-\mu_a ct), \quad (1)$$

where  $\mu_s$  and  $\mu_a$  are the anisotropic scattering and the absorption coefficients of the medium, respectively [14]. The function  $s(\mu_s, t)$  and the constant  $b$  denote the probability of detecting photon at time  $t$  (i.e., photon path of  $\ell=ct$ , where  $c$  is the velocity of photon in the medium) and the intensity of injected light, respectively. The intensity  $I(\mu_s, \mu_a)$  that is temporal integration of  $J(\mu_s, \mu_a, t)$  satisfies

$$(\partial/\partial\mu_a) \ln I(\mu_s, \mu_a) = -c \langle t \rangle = -L(\mu_a), \quad (2)$$

where  $L(\mu_a)$  denotes the mean path length [14]. From Eq. (2) we obtain

$$\ln I(\mu_s, \mu_a) = -\int_0^{\mu_a} L(\mu_a) d\mu_a + \ln b + \ln \int_0^\infty s(\mu_s, t) dt. \quad (3)$$

Consider spectroscopy at wavelengths  $\lambda_1$  and  $\lambda_2$ , where  $\mu_a = \mu_{a1}$  and  $\mu_{a2}$ , respectively. If we assume  $s(\mu_s, t)$  is invariant, the relation between  $I(\mu_s, \mu_{a1})$  and  $I(\mu_s, \mu_{a2})$  is written as

$$\ln \frac{I(\mu_s, \mu_{a1})}{I(\mu_s, \mu_{a2})} = \ln \frac{I(\lambda_1)}{I(\lambda_2)} = \int_{\mu_{a1}}^{\mu_{a2}} L(\mu_a) d\mu_a + \ln \frac{b_1}{b_2}. \quad (4)$$

From the mean value theorem we obtain

$$\ln[I(\lambda_1)/I(\lambda_2)] = (\mu_{a2} - \mu_{a1})L(\xi) + \ln(b_1/b_2), \quad (5)$$

where  $\mu_{a1} \geq \xi \geq \mu_{a2}$  or  $\mu_{a2} \geq \xi \geq \mu_{a1}$ . The path length  $L(\xi)$  can be expressed by the mean path lengths  $L(\lambda_1) = L(\mu_{a1})$  and  $L(\lambda_2) = L(\mu_{a2})$  using  $p$  ( $0 \leq p \leq 1$ ) as

$$L(\xi) = pL(\lambda_1) + (1-p)L(\lambda_2). \quad (6)$$

On the other hand the concentration  $V$  of an absorber is expressed by the extinction coefficients  $\epsilon_1$  and  $\epsilon_2$  at  $\lambda_1$  and  $\lambda_2$ , respectively, as

$$V(\epsilon_2 - \epsilon_1) = \mu_{a2} - \mu_{a1}. \quad (7)$$

Thus we obtain the concentration  $V$  as

$$V = \frac{1}{(\epsilon_2 - \epsilon_1)L(\xi)} \ln \frac{b_2 I(\lambda_1)}{b_1 I(\lambda_2)} \quad (8)$$

Usually  $b_1 = b_2$ , and also we can assume  $p = 0.5$  since  $\partial L / \partial \mu_a|_{\mu_{a1}} \approx \partial L / \partial \mu_a|_{\mu_{a2}}$ .

In the case of photon density wave, the mean path length  $L(\mu_a)$  at modulation frequency  $\omega$  is given by

$$L(\mu_a) = c \partial \phi(\mu_a, \omega) / \partial \omega \approx c \phi(\mu_a, \omega) / \omega, \quad (9)$$

where  $\phi(\mu_a, \omega)$  denotes the phase-delay of the incident photon-density wave [15]. Measurements at least two points allows us to eliminate the factor  $b_2/b_1$  in Eq. (8) [15].

### 3. Experimental Results and Discussions

Figure 1 shows the experimental arrangement used to measure the absolute concentration of absorber in the tissue-like phantom. The incident light was the photon-density wave of which modulation frequency was 100 MHz and wavelength was either 784 or 832 nm; it was generated by a laser diode. The diffuse reflections of both wavelengths are detected at 30 mm away with an avalanche photo-diode.

The acrylic resin tank (210 mm  $\times$  50 mm  $\times$  135 mm) was filled with the 1% Intralipid suspension (1.2 liter), then Greenish Brown ink was added gradually. The absorption coefficients of the ink were previously measured by a spectrometer; they were 0.0131 and 0.0231 mm<sup>-1</sup>/ml at 832 and 784 nm in the water of 1.2 liter, respectively.

In Fig. 2 the measured volumes in unit of ml are plotted versus that of added Greenish Brown ink, as well as the difference of absorption coefficients at 784 and 832 nm. We see good coincidence in Fig. 2; the correlation factor is 1.05.

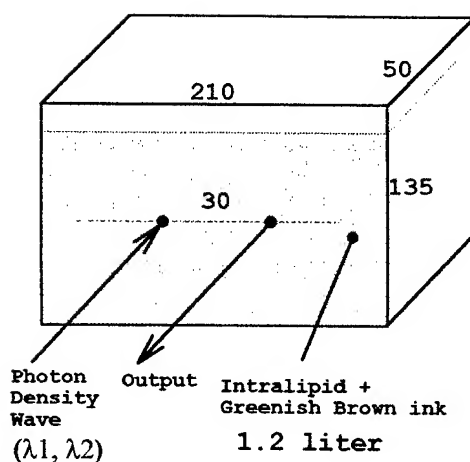


Fig. 1 Experimental Arrangement to measure the absolute concentration of absorber.

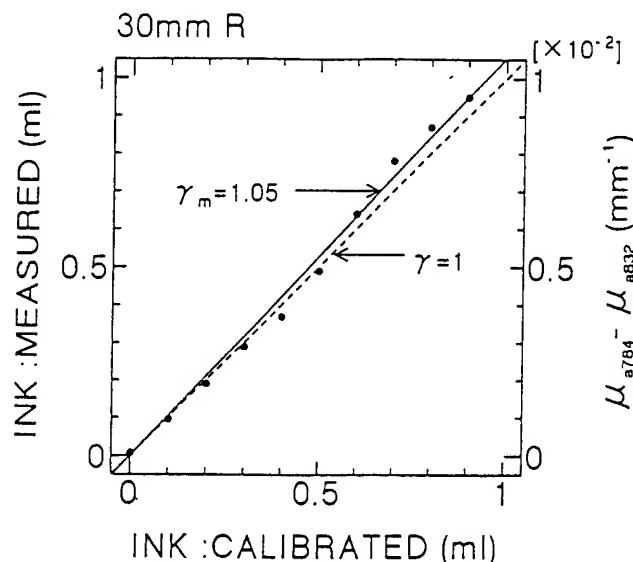


Fig. 2 Plots of measured volumes versus that of added Greenish Brown ink.

#### 4. Conclusions

Although human tissues are complex micro structures, for many applications we can assume them to be homogeneous and approximate them with the mean refractive index, the mean scattering and absorption coefficients. This is the case that we have proposed in this paper; that originates in the microscopic Beer-Lambert law in the turbid media and can measure the absolute concentration of absorptive constituents in the homogeneous media that have variously shaped non-reentrant surfaces. The experimental results showed that the measuring errors are less than  $\approx 5\%$  of the absolute concentration. In the experiment we used a simple setup where a photon-density wave was the incidence to a liquid phantom, re-emission was detected by an avalanche photo-diode, and the amplitude and the phase delay of the re-emission were detected. Although we approximated the mean path length by Eq. (9) and used the factor  $p=0.5$ , the measuring errors were very small, i.e., less than  $\approx 5\%$  of the absolute value.

#### References

1. B. C. Wilson and S. L. Jacques, *IEEE J. Quantum Electron.* **26**, 2186 (1990).
2. E. M. Sevick, B. Chance, J. Leigh, S. Nioka, and M. Maris, *Anal. Biochem.* **195**, 330 (1991).
3. B. C. Wilson, E. M. Sevic, M. S. Patterson, and B. Chance, *Proc. IEEE* **80**, 918 (1992).
4. T. J. Farrell, M. S. Patterson, and B. Wilson, *Med. Phys.* **19**, 879 (1992).
5. M. S. Patterson, B. Chance, and B. C. Wilson, *Appl. Opt.* **28**, 2331 (1989).
6. S. L. Jacques, *IEEE Trans. Biomed. Eng.* **36**, 1155 (1989).
7. J. M. Schmitt, A. Knüttel, and J. R. Knutson, *J. Opt. Soc. Am. A* **9**, 1832 (1992).
8. J. B. Fishkin and E. Gratton, *J. Opt. Soc. Am. A* **10**, 127 (1993).
9. S. R. Arridge, M. Cope, and D. T. Delpy, *Phys. Med. Biol.* **37**, 1531 (1992).
10. R. C. Haskell, L. O. Svaasand, T.-T. Tsay, T.-C. Feng, M. S. McAdams, and B. J. Tromberg, *J. Opt. Soc. Am. A* **11**, 2727 (1994).
11. S. J. Madson, B. C. Wilson, M. S. Patterson, Y. D. Park, S. L. Jacques, and Y. Hefetz, *Applied Optics*, **31**, 3509 (1992).
12. B. W. Pogue and M. S. Patterson, *Phys. Med. Biol.* **39**, 1157 (1994).
13. Y. Tsuchiya, K. Ohta, and T. Urakami, *Jpn. J. Appl. Phys.* **34**, 2495 (1995).
14. Y. Tsuchiya and T. Urakami, *Jpn. J. Appl. Phys.* **34**, L79 (1995).
15. Y. Tsuchiya and T. Urakami, *Pre. Proc. Japan Optics 95'*, 61 (1995) in Japanese.

## Luminescence Diffusion Tomography

Jenghwa Chang<sup>1</sup>, Harry Graber<sup>2</sup>, Randall L. Barbour<sup>1,2</sup>

Department of Pathology<sup>1</sup> and Department of Physiology and Biophysics<sup>2</sup>, SUNY Health Science  
Center at Brooklyn, Brooklyn, NY 11203, TEL: 718-270-1286, FAX: 718-270-3313

The excitation light and emission light associated with a luminescence process are governed by a set of coupled time-dependent radiative transfer equations (RTE) [1]. For details of these equations and notations, see accompanying paper [2]. Let  $R$  be the reading of a given detector for the emitted intensity, and  $r_2$  be the detector sensitivity function. Then

$$R = \int_V \int_{4\pi} r_2 \otimes \left( \int_{V'} \int_{4\pi} q_2' \otimes G_2(\mathbf{r}, \Omega; \mathbf{r}', \Omega'; t) d\Omega' d^3r' \right) d\Omega d^3r = \int_V \frac{\gamma}{4\pi\tau} N_s \otimes \bar{\phi}_2^+ d^3r, \quad (1)$$

where the  $\otimes$  symbol denotes a convolution in time,  $N_s$  is the fluorophore/phosphor concentration in the excited state,  $q_2 = \frac{\gamma}{4\pi\tau} N_s$  is the equivalent emission source,  $\gamma$  is the quantum yield,  $\tau$  is the mean lifetime,  $G_2(\mathbf{r}, \Omega; \mathbf{r}', \Omega'; t)$  is the Green's function at  $\mathbf{r}$  in direction  $\Omega$  with the source located at  $\mathbf{r}'$  in direction  $\Omega'$ , and  $\bar{\phi}_2^+ = \int_{4\pi} \int_{V'} \int_{4\pi} r_2' \otimes G_2(\mathbf{r}, -\Omega; \mathbf{r}', -\Omega'; t) d\Omega' d^3r' d\Omega$ . The frequency domain detector readings are obtained by Fourier transforming Eq. (1):

$$\tilde{R} = \int_V \frac{\gamma}{4\pi\tau} \tilde{N}_s \tilde{\phi}_2^+ d^3r, \quad (2)$$

where " $\sim$ " denotes the Fourier transform. Let  $N_0$  be the total fluorophore/phosphor concentration. Then the Fourier transforms of  $\tilde{N}_g$  and  $\tilde{N}_s$  are [2]:

$$j\omega\tau\tilde{N}_g = -\frac{\tau\Sigma_{T,1\rightarrow2}}{2\pi} \tilde{\phi}_1 \otimes \tilde{N}_g - \tilde{N}_g + 2\pi N_0 \delta(\omega) \quad \text{and} \quad \tilde{N}_s = 2\pi N_0 \delta(\omega) - \tilde{N}_g, \quad (3)$$

where  $\bar{\phi}_1 = \bar{\phi}_1(\mathbf{r}, t) = \int_{4\pi} \phi_1 d\Omega$  is the intensity [ $\text{cm}^{-2} \text{s}^{-1}$ ] of the excitation light. For time-harmonic excitation, that is,  $\tilde{\phi}_1 = 2\pi\phi_1^0 [\delta(\omega) + \eta\delta(\omega - \omega_0)]$ , where  $\eta$  is the modulation, Eq. (3) can be solved using the following approximations. When the saturation level is not significant, i.e.,  $N_g \approx N_0$ , we have

$$\tilde{N}_g(0) = 2\pi N_0 (1 - \tau\Sigma_{T,1\rightarrow2}\phi_1^0) \delta(0), \quad (4)$$

$$\tilde{N}_s(\omega_0) = -\tilde{N}_g(\omega_0) = \frac{2\pi\tau\Sigma_{T,1\rightarrow2}N_0\phi_1^0\eta}{1 + j\omega_0\tau} \delta(0). \quad (5)$$

When the saturation level is more significant, the coupling between DC and the fundamental frequency should be considered but the contribution of higher-order harmonics can be ignored, permitting the following approximations:

$$\tilde{N}_g(0) = \frac{2(1 + \tau\Sigma_{T,1\rightarrow2}\phi_1^0)^2 + 2(\omega_0\tau)^2}{2(1 + \tau\Sigma_{T,1\rightarrow2}\phi_1^0)^2 + 2(\omega_0\tau)^2 - (\tau\Sigma_{T,1\rightarrow2}\phi_1^0\eta)^2} \frac{2\pi N_0}{1 + \tau\Sigma_{T,1\rightarrow2}\phi_1^0} \delta(0), \quad (6)$$

$$\tilde{N}_g(\omega_0) = -\tilde{N}_s(\omega_0) = \frac{-\tau\Sigma_{T,1\rightarrow2}\phi_1^0\eta(1 + \tau\Sigma_{T,1\rightarrow2}\phi_1^0 - j\omega_0\tau)}{2(1 + \tau\Sigma_{T,1\rightarrow2}\phi_1^0)^2 + 2(\omega_0\tau)^2 - (\tau\Sigma_{T,1\rightarrow2}\phi_1^0\eta)^2} \frac{2\pi N_0}{1 + \tau\Sigma_{T,1\rightarrow2}\phi_1^0} \delta(0). \quad (7)$$

The goal of the inverse problem is to solve equation (2) for  $\mu_{T,1\rightarrow2}$ ,  $\gamma$ , and  $\tau$  under different source and detection conditions. This requires two reconstruction steps. In the first step, we solve for the background absorption and scattering coefficients,  $\mu_a$  and  $\mu_s$ , of the medium for the excitation and the emission photons separately using

previously developed techniques [3]. The second step is to reconstruct  $\mu_{T,1 \rightarrow 2}$ ,  $\gamma$ , and  $\tau$  using estimates of  $\tilde{\phi}_1$  and  $\tilde{\phi}_2^+$  calculated from Monte Carlo simulations or other numerical methods using the coefficients obtained from the first step. The following are two proposed methods for this second step.

(A) DC source

If we use DC sources, then equation (2) becomes

$$\tilde{R} = \int_V \frac{\Sigma_{T,1 \rightarrow 2} \tilde{\phi}_1 \tilde{\phi}_2^+}{4} (\gamma N_0) d^3r = \int_V w(\gamma N_0) d^3r, \quad (8)$$

where  $w \equiv w_{DC} = \Sigma_{T,1 \rightarrow 2} \tilde{\phi}_1 \tilde{\phi}_2^+ / 4$  is the weight function. If  $\Sigma_{T,1 \rightarrow 2}$  is known and  $\tilde{\phi}_1$  and  $\tilde{\phi}_2^+$  can be precalculated assuming that fluorophore is not present, then the unknown quantity  $\gamma N_0$  can be computed by solving a linear system obtained by discretizing (8). Here, only the product of quantum efficiency and fluorophore concentration is found, and they can not be directly separated.

(B) AC source

If modulated sources are used and  $\gamma N_0$  is solved for by analyzing the DC component of the response as described above and we adopt the approximation in Eq. (5), then equation (2) becomes

$$\tilde{R} = \int_V w \frac{1 - j\omega\tau}{1 + \omega^2\tau^2} d^3r, \quad (9)$$

where  $w \equiv w_{AC} = \gamma \Sigma_{T,1 \rightarrow 2} N_0 \phi_1^0 \eta \phi_2^+ / 4$ . Equation (9) can be discretized, and the real and imaginary parts of the detector readings give rise to two distinct systems of linear equations, from which  $1/(1 + \omega^2\tau^2)$  and  $-\omega\tau/(1 + \omega^2\tau^2)$  can be reconstructed. Because  $\omega$  is known,  $\tau$  can also be deduced. If the approximation in Eq. (7) is adopted, we get

$$\tilde{R} = \int_V w \frac{2(1 + \tau \Sigma_{T,1 \rightarrow 2} \phi_1^0 - j\omega_0\tau)}{2(1 + \tau \Sigma_{T,1 \rightarrow 2} \phi_1^0)^2 + 2(\omega_0\tau)^2 - (\tau \Sigma_{T,1 \rightarrow 2} \phi_1^0 \eta)^2} (1 + \tau \Sigma_{T,1 \rightarrow 2} \phi_1^0) d^3r, \quad (10)$$

where  $w$  is the same as that in Eq. (9). When  $\tau \Sigma_{T,1 \rightarrow 2} \phi_1^0 \ll 1$ , Eq. (10) reduces to Eq. (9).

A preliminary experiment was performed and reconstructed images are reported in this summary. Figure 1A shows the experimental tissue phantoms and Figure 1B illustrates the source and detector configurations. The experiment was performed with two balloons and no added dye in the background. A 0.75W, multi-line (average wavelength  $\sim 490 \mu\text{m}$ ) argon laser source was used to irradiate the phantom. A filter blocked excitation light from entering the detector. The detector was a Hamamatsu C3140 CCD camera directed normal to the phantom to collect the emission light. A limited illumination angle was used. The detectors were located at every  $30^\circ$  along the border of the cylinder and the source was positioned every  $10^\circ$  from  $90^\circ$  to  $150^\circ$  counterclockwise relative to the source. The source intensity was recorded for each measurement using a Coherent Labmaster-E. Each measurement was then corrected for the dark current, source intensity, and lens aperture. At least two measurements were taken and averaged to obtain the detector readings for each source-detector pair. In the first experiment, balloons containing different volumes (0.8 and 1.2 mL) of Rhodamine 6G dye at a concentration of  $\sim 50 \mu\text{M}$  were embedded in a 8 cm diameter cylindrical phantom filled with 0.2% Intralipid<sup>®</sup> (% lipid per unit volume). The same cylindrical phantom was used in the second experiment, but the Intralipid concentration was 0.33% and it contained  $0.1 \mu\text{M}$  dye. The volume of the balloon was 0.5 mL, and contained  $100 \mu\text{M}$  dye.

The optical thickness of the phantom medium was  $\sim 20$  and  $\sim 33$  transport mean free pathlengths, respectively, for the excitation and emission light. Weight functions for the corresponding reference media were computed by

Monte Carlo simulations assuming an optical thickness of 20 transport mean free paths. Image reconstructions were performed using three iterative algorithms — POCS, CGD, and SART — with a rescaling technique and positivity constraints [4]. 2-D reconstruction (Figure 2A) were performed by assuming symmetry along the  $z$ -axis and the weight function of voxels with the same  $z$ -coordinate were summed up to obtain an integrated value. Only the central plane of the reconstruction results are displayed. Figure 2B demonstrates the cylindrical coordinate system, where the  $\rho$ - and  $\phi$ - coordinates are shown in the figure and the  $z$ -coordinate is normal to the plane of paper. There are 400 voxels in each plane.

Figure 3 shows the reconstruction results using the CGD method after 10, 100, 1,000, and 10,000 iterations. The two balloons are located, and artifacts are present on the boundary. The two inhomogeneities are about the same size but with different intensities, which roughly coincides with the difference in balloon volume. The image quality improves as the number of iterations increases.

Additional results and work in progress include reconstruction of mean lifetime using time-harmonic sources, comparison of reconstruction results using different derived weight functions, and comparison of reconstruction for phantoms with and without added background fluorophores.

1. *Conceptual Basis for Calculations of Absorbed-Dose Distribution*, NCRP Report No. 108, 1991.
2. J. Chang *et al.*, "Fluorophore/Phosphor Emission Contains Higher Harmonics of the Excitation Modulation Frequency," accompanying paper.
3. J. Chang *et al.*, "Imaging diffusive media using time-independent and time-harmonic sources: dependence of image quality on imaging algorithms, target volume, weight matrix, and view angles," vol. SPIE-2389, (San Jose), Feb. 1995.
4. J. Chang *et al.*, "Image reconstruction of dense scattering media from CW sources using constrained CGD and a matrix rescaling technique," vol. SPIE-2389, (San Jose), Feb. 1995.

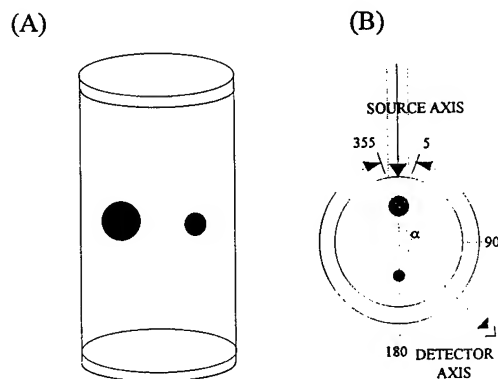


Figure 1. (A) Tissue phantom for the experiment, where two balloons were suspended in the cylinder; (B) Source and detector configurations.

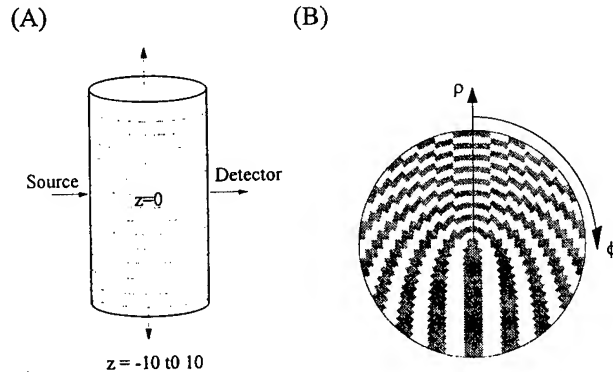


Figure 2. Three reconstruction types — (A) Type-1 reconstruction where axial symmetry was assumed along the  $z$ -axis. The cylindrical coordinate system used to discretize the phantom is shown in (D).

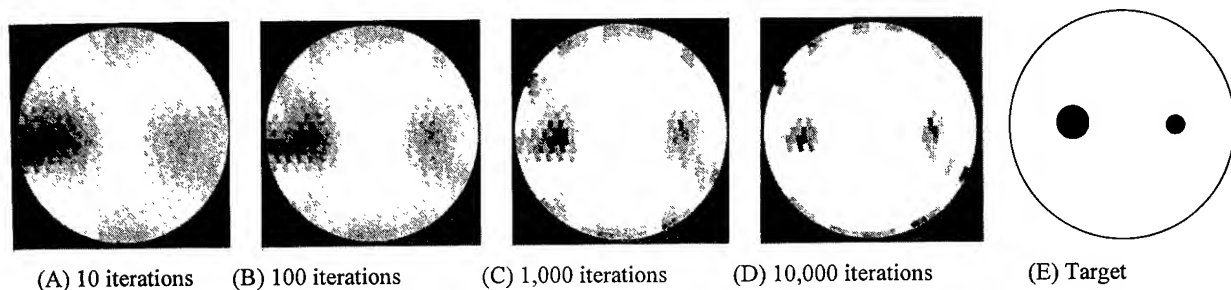


Figure 3. Type-1 reconstruction results from the first experiment using CGD method after (A) 10 iterations, (B) 100 iterations, (C) 1,000 iterations, and (D) 10,000 iterations. The target is shown in (E).

## Spatially resolved spectroscopy for extracting spectrum of hemoglobin diluted in a highly scattering medium

Yoshio Tsunazawa, Yukio Oikawa, Shin-itchi Iwamoto, Hideo Eda and Michinosuke Takada,  
Central Research Laboratory, Shimadzu Corporation

1 Nishinokyo Kuwabara-cho, Nakagyo-ku, Kyoto 604, Japan

Phone: +81-75-823-1190, Fax: +81-75-802-0318, E-mail: tunazawa@shimadzu.co.jp

### 1. Introduction

Determination of the absorption and scattering coefficient in the NIR spectral region for biological tissue is essential for the bio-optical research such as an optical CT and an oxygenation monitor. Methods using time resolved analysis were reported<sup>1,2</sup>, we adopted here an alternative method, the spatially resolved spectroscopy, to extract the absorption spectrum of the hemoglobin solved in a scattering solution, using a CCD spectrometer.

The principle is based on the analytical solution of the diffusion equation for the infinite and the semi-infinite media. Equations were derived for converting the measured spectra to the pure absorption spectra which were free from scattering material.

### 2. Experiment and Theory

We have examined the cases for the infinite and semi-infinite media as in the Fig.1. The light from the tungsten lamp were introduced via an optical fiber to the milk solution including 1.5 % bovine blood cells. Another fiber for detection was placed at  $r$  mm apart and was guided to the CCD spectrometer to obtain spectra of 700-900nm with varied optode distance  $r$ .

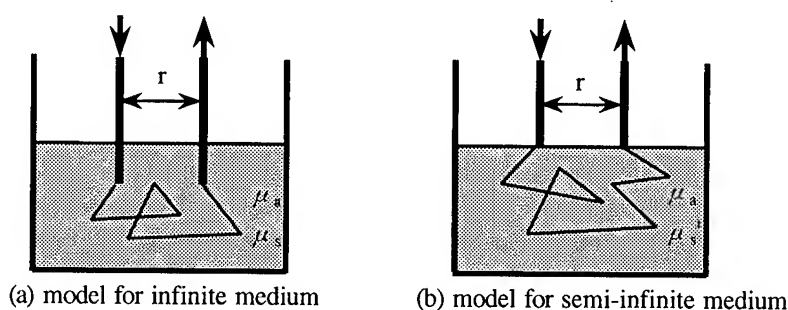


Fig.1 Experiment for the two cases

#### <Infinite medium >

The green function of the diffusion equation for the fluence rate  $\Phi(r)$  is known to be<sup>3</sup>

$$\Phi(r) = \frac{1}{4\pi D} \cdot \frac{\exp(-\mu_{eff} \cdot r)}{r} \quad \text{-----(1)}$$

which is considered as the fluence rate at a distance  $r$  from an isotropic point source in the infinite medium; where  $D$  is the diffusion coefficient ( $D = 1/3\mu_s'$ ),  $\mu_{eff}$  is the effective attenuation coefficient and equals to  $\mu_{eff} = \sqrt{(\mu_a / D)} = \sqrt{3\mu_a\mu_s'}$

There are some argument on the measurable light amount<sup>4</sup>, and we used the fluence rate after the following consideration. The diffuse intensity  $I_d(r, \hat{s})$  toward the direction  $\hat{s}$  should be the

measurable amount. In the diffusion approximation it is represented by<sup>5</sup>

$$I_d(r, \hat{s}) = \frac{\Phi(r)}{4\pi} + \frac{3}{4\pi} \cdot |\mathbf{F}_d(\mathbf{r})| \cdot \cos \theta \quad \text{-----} (2)$$

where  $\mathbf{F}_d(\mathbf{r})$  is the light flux given by  $\mathbf{F}_d(\mathbf{r}) = -D \cdot \text{grad} \Phi(r)$  ----- (3)

and  $\theta$  is the angle between  $\hat{s}$  and  $\mathbf{F}_d(\mathbf{r})$ .

In the case of infinite medium, substituting (1) and (3) into (2), we have

$$I_d(r, \hat{s}) = \left( \frac{\Phi(r)}{4\pi} \right) \cdot \left[ 1 + \frac{1}{\mu_s'} \cdot \left\{ \frac{1}{r} + \mu_{eff} \right\} \cdot \cos \theta \right] \quad \text{-----} (4)$$

Thus  $I_d(r, \hat{s})$  depends on  $\cos \theta$ , but if we measure from a direction perpendicular to the light flux as the case in (a) of Fig.1,  $I_d(r, \hat{s})$  becomes just  $\frac{\Phi(r)}{4\pi}$  and we can simply use  $\Phi(r)$  as the measurable amount. From (1), we have  $\ln(r \cdot \Phi(r)) = -\ln(4\pi D) - \mu_{eff} \cdot r$

Therefore by making semi-log plot " $\ln(r \cdot \Phi(r))$  versus  $r$ " we have  $\mu_{eff}$  from its slope, then  $\mu_a \cdot \mu_s'$  is obtainable using the relation  $\mu_a \mu_s' = \frac{1}{3} \mu_{eff}^2$

### <Semi-infinite medium>

For this we refer to Farrell et al.<sup>3</sup> who used extrapolated boundary as in Fig.2.

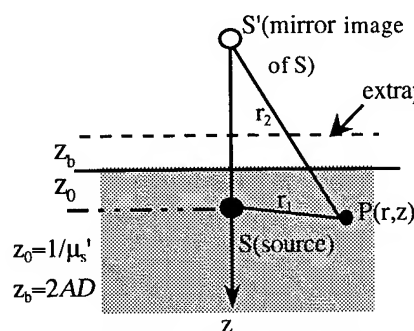


Fig.2 extrapolated boundary<sup>5</sup>

The boundary condition at the surface ( $z=0$ ) are given by

$$\Phi - 2AD \frac{\partial \Phi}{\partial z} = 0 \quad \text{-----} (5)$$

$$\text{where } A = \frac{1 + r_d}{1 - r_d} \text{ and}$$

$$r_d = -1.440n^{-2} + 0.710n^{-1} + 0.668 + 0.0636n \quad \text{---} (6)$$

$n$ : refractive index of the medium

From (5),  $\Phi$  and the  $F_d (= -D \frac{\partial \Phi}{\partial z})$  are proportional to each other at the surface, we can use the fluence rate also in this case as the measurable amount. The condition (5) is satisfied by adding a negative source  $S'$  at the mirror position of  $S$  with respect to the extrapolated boundary which locates outside the real surface by a distance  $z_b = 2AD$ .

Then the fluence rate at  $P$  is given as the sum of the effect of the positive and negative sources and given by<sup>3</sup>

$$\Phi(r, z) = \frac{1}{4\pi D} \left( \frac{e^{-\mu_{eff} \cdot r_1}}{r_1} - \frac{e^{-\mu_{eff} \cdot r_2}}{r_2} \right) \quad \text{-----} (7)$$

where  $r_1$  and  $r_2$  stand for the distance  $SP$  and  $S'P$  respectively.

We have measured many spectra of  $\Phi(r, 0)$  with varied  $r$ . From these we calculated  $\mu_{eff}$  as the function of wavelength, which is then converted to the spectrum of  $\mu_a \cdot \mu_s'$ .



### 3. Results

An example of recovered spectra of  $\mu_a \cdot \mu_s'$  are shown in Fig.3 which obtained with the configuration of Fig.1(a). Throughout the whole experiment,  $\mu_s'$  of the solutions were adjusted to about  $1 \text{ mm}^{-1}$ , therefore, the ordinate ( $\mu_a \cdot \mu_s'$ ) of the Fig.3 can be simply read as  $\mu_a$ .

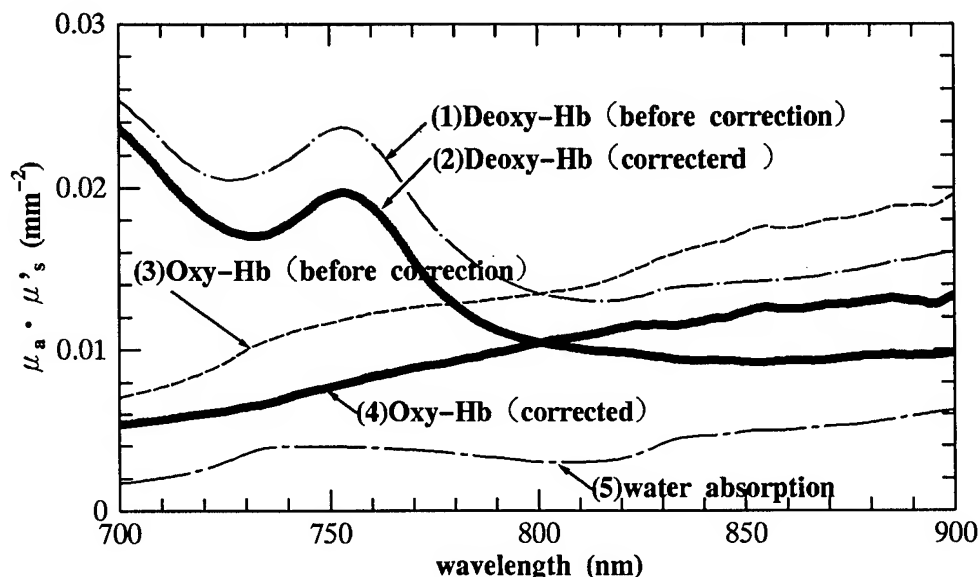


Fig.3 Spectra obtained with experiment after calculation

The curve (1) is for an oxidized solution while the curve (3) is for its reduced solution by adding sodium hydrosulfite. We found that the curve (3) was similar to the spectrum of oxy-hemoglobin but there was an abnormal bending around 730nm which seemed due to overlapped water spectrum. To make sure the cause of this bending we made another experiment with the same procedure but using a solution which had milk and no blood cell. The resulted spectrum was the curve (5) which is very close to the known spectrum of water. Finally we made a correction by subtracting the water like spectrum (5) from (1) and (3), thus we obtained (2) and (4). The corrected spectra (2) and (4) are very close to the known spectra of pure oxy and deoxy hemoglobin.

This work was performed as part of the National Research Development Programs for Medical and Welfare Apparatus under the New Energy and Industrial Technology Development Organization (NEDO).

### References

1. M.S.Patterson, B.Chance and B.C.Wilson, Appl. Opt., **28**, 2331-2336 (1989)
2. Y.Tsunazawa, I.Oda, H.Eda, and M.Takada, SPIE, **vol.2389**,75-86 (1995)
3. T.J. Farrell, and M.S.Patterson, Med. Phys.,**19**, 879-888 (1992 )
4. Feng Liu, K.M.Yoo, R.R.Alfano, Optics Letters, **18**, 432-434 (1993)
5. A.Ishimaru,"Wave Propagation and Scattering in Random Media" **vol.1**, chap. 9, p176, Academic Press Inc. (1978)

## Absolute $\text{SO}_2$ measurements in layered tissue.

S J Matcher, K Nahid, M Cope & D T Delpy

University College London Dept of Medical Physics and Bioengineering, 1st Floor Shropshire House, 11-20 Capper St, London. WC1E 6JA. UK.

Tel +44-171-209-6408 FAX +44-171-209-6269.

e-mail [sjm@medphys.ucl.ac.uk](mailto:sjm@medphys.ucl.ac.uk)

Absolute absorption coefficient measurement in highly scattering media represents a technically challenging problem, however it is of prime importance for the next generation of clinical NIRS monitors, which will offer an absolute index of tissue oxygenation rather than the current trend measurements. Various schemes have been proposed for this measurement, many of which assume a diffusion model of light transport. A common assumption is that the tissue being interrogated is homogeneous whereas, especially in the case of the adult head, it actually comprises layers of tissue with different blood and water content and scattering coefficients. Although some attempts have been made to discriminate surface and deep tissue effects<sup>1</sup>, their effectiveness has been questioned in clinical applications to adults and the region of localisation of the absolute  $\text{SO}_2$  signal remains poorly understood<sup>2,3,4</sup>. Little has been reported on possible methods of discriminating surface tissue and brain  $\text{SO}_2$ .

We have modelled the effects of heterogeneous (layered) tissue on several proposed schemes<sup>5,6,7,8,9</sup> for measuring absolute  $\text{SO}_2$  during various conditions (e.g. surface  $\text{SO}_2$  remaining constant whilst brain  $\text{SO}_2$  fluctuates etc) for various layer thicknesses and optical properties. using an FEM model of light transport<sup>10</sup>. Using a recently developed radiosity model of light transport through clear regions<sup>11</sup>, we also theoretically investigate the effect of the CSF layer on the  $\text{SO}_2$  estimates obtained by the various techniques.

1. P W McCormick, M Stewart, M G Goetting, M Dujovny, G Lewis and J I Ausman, "Non-invasive cerebral optical spectroscopy for monitoring cerebral oxygen delivery and haemodynamics", *Crit. Care. Med.* 19,89-97 (1991).
2. D N F Harris and S M Bailey, "Near infrared spectroscopy in adults: does the Invos 3100 really measure intracerebral oxygenation?" *Anaesthesia*, 48,694-696 (1993).
3. T J Germon, N M Kane, A R Manara and R J Nelson, "Near infrared spectroscopy in adults: effects of extracerebral ischaemia and intracranial hypoxia on estimation of cerebral oxygenation", *British Journal of Anaesthesia*, 73,503-506 (1994).
4. T J Germon, A R Manara, N M Kane and R J Nielson, "Possible limitations of cerebral oximetric monitoring in adults", *Anaesthesia*, 49, 639-652 (1994).
5. M Miwa, Y Ueda and B Chance, "Development of time-resolved spectroscopy system for quantitative noninvasive tissue measurement", *Proc SPIE* 2389, 142-149 (1995).
6. M Oda, Y Yamashita, G Nishimura and M Tamura, "Determination of absolute concentration of oxy- and deoxyhemoglobin in rat head by time-resolved Beer-Lambert law", *Proc SPIE* 2389, 770-778 (1995).

7. S J Matcher, P Kirkpatrick, K Nahid, M Cope and D T Delpy, "Absolute quantification methods in tissue near-infrared spectroscopy", *Proc SPIE* 2389, 486-495 (1995).
8. S Fantini, M A Francheschini-Fantini, J S Maier, S A Walker, "Frequency-domain multichannel optical detector for noninvasive tissue spectroscopy and oximetry", *Opt. Eng.* 34, 32-42 (1995).
9. M S Patterson, J D Moulton, B C Wilson, K W Berndt and J R Lakowicz, "Frequency domain reflectance for the determination of the scattering and absorption properties of tissue", *Appl. Opt.* 30, 4474-4476 (1991).
10. S R Arridge, M Schweiger, M Hiraoka and D T Delpy, "A finite element approach for modelling photon transport in tissue", *Med. Phys.* 20(2), 299-309 (1993).
11. M Firbank, S R Arridge, M Schweiger and D T Delpy, "An investigation of light transport through scattering bodies with non-scattering regions", *Phys. Med. Biol.* (in press).



Thursday, March 21, 1996

# Diagnostic Scattering Properties of Particles and Tissues

**BThB** 11:00 am-12:45 pm  
Windsor Ballroom

Howard Nathel, *Presider*  
*Lawrence Livermore National Laboratory*

## Theoretical and Experimental Investigations on Solute-Induced Changes in Optical Properties in Living Tissues

Hanli Liu, Yutao Zhang, Mika Kimura and Britton Chance  
Department of Biochemistry and Biophysics, University of Pennsylvania,  
D501 Richards Building, Philadelphia, PA 19104.  
TEL: (215) 898-4342; FAX: (215) 898-1806.

### 1. Background and Objective

A number of recent studies have focused on the possibility of using the NIR techniques to monitor a change of glucose concentration in tissue [1,2]. The basis of the method rests on the fact that a change of refractive index in the extracellular fluid due to the presence of additional glucose causes a small change in the overall scattering property of the tissue that could be detected by the NIR techniques. Chance et al [3] show that in lipid and yeast cell suspensions, an increase in concentration of a general solute, such as sugars and electrolytes, gives rise to a decrease in scattering factor of the suspension. These results are in good agreement with those given in Refs. 1 and 2. However, in the tissue measurement performed on a perfused rat liver, the results obtained by adding mannitol (or glucose) to the perfusate of the perfused liver displayed a behavior in contrast to those in the lipid suspensions [3] and can not be well explained by the change of only refractive index. In order to employ the NIR techniques for a broad use in noninvasive physiological monitoring, we wish to show in this paper the solute-induced correlation between optical properties in tissue and its refractive index as well as its osmolarity.

### 2. Theoretical Background

For biological tissues, Liu et al [4] have recently adapted the approximation method of the Mie theory, introduced by Graaff et al [5], and have expressed the reduced scattering coefficient,  $\mu_s'$ , as

$$\mu_s' = \frac{\phi(1-\phi)}{v_{par}} \sigma_s' = \frac{2.46}{a} \phi(1-\phi) \left( \frac{2\pi a}{\lambda} \right)^{0.37} \left( \frac{n_{in}}{n_{ex}} - 1 \right)^{2.09}, \quad (1)$$

where  $\sigma_s'$  is the scattering cross section,  $\phi$  is the volume fraction of the scattering particles relative to the total tissue volume,  $v_{par}$  is the volume of a single scattering particle and can be expressed as  $\frac{4}{3}\pi a^3$  for a spherical scatterer,  $a$  is the radius of the particle,  $\lambda$  is the wavelength of the scattered light,  $n_{in}$  and  $n_{ex}$  are refractive indexes of the intracellular and extracellular fluid, respectively. With the use of near-infrared light, eq. (1) is satisfied for scattering in living tissues and blood [4]. Eq. (1) shows that  $\mu_s'$  has both a refractive-index-dependent factor,  $\left( \frac{n_{in}}{n_{ex}} - 1 \right)^{2.09}$ , and a size-dependent factor,  $\frac{\phi(1-\phi)}{a} \left( \frac{2\pi a}{\lambda} \right)^{0.37}$ , for tissue. In

addition, based on the time-domain diffusion equation, it can be shown that the relationship between the mean optical pathlength  $\langle L \rangle$  and absorption,  $\mu_a$ , and reduced scattering,  $\mu_s'$ , coefficients is given as

$$\langle L \rangle = \frac{\sqrt{3}}{2} \rho \sqrt{\frac{\mu_s'}{\mu_a} - \frac{1}{2\mu_a}}, \quad (2)$$

which indicates that an increase in scattering results in an increase in optical pathlength.

### 3. Methods and Materials

In this study, we utilized time-domain, frequency-domain, and continuous-wave methods for different cases to show changes in absorption and scattering coefficients as well as in optical pathlength due to the introduction of a solute in the perfused rat liver or in the rat brain. The time-resolved spectroscopy is considered as a gold standard to measure the optical properties of a highly scattering medium; the frequency-domain method can give a transient response of mean pathlength change; the simple continuous-wave method can also give a fast response to a change in optical properties and quantify the scattering changes. Since these three methods have been well developed, for detailed instrumentation, we refer the

reader to ref. 6 for the time-domain method, refs. 7 and 8 for the frequency-domain method, and refs. 3 and 9 for the continuous-wave method. The wavelengths used in these methods were in the range of 780 nm-850 nm.

In rat liver perfusion, we used male SD strain rats of 300-350 g and anesthetized a rat by intraperitoneal injection pentobarbital (50 mg/kg weight). The rates were starved 24 hours in order to normalize the liver physiological conditions. After being removed from the rat, the liver was perfused by Krebs-Ringer buffer, which contained 2 mM glucose and was oxygenated by the gas mixture of 95% oxygen and 5% carbon dioxide. After the liver perfusion became stable (20-30 min), the perfusate can be switched between the buffer and others containing different concentrations of carbohydrates. The light source and detector were separated 1.5 cm apart and attached to the major lobes of the liver. In the rat brain measurements, a certain concentration of carbohydrates was injected through the tail veins, and the source and detector were placed 1 cm apart on the rat head.

#### 4. Results and Discussion

Figure 1(a) shows the simulated dependence of  $\mu_s'$  of a perfused rat liver on cell radius (top scale), with fixed parameters of cell volume fraction ( $\phi=0.8$ ), intracellular ( $n_{in}=1.465$ ), and extracellular ( $n_{ex}=1.33$ ) refractive indexes. This calculation illustrates that a decrease only in tissue cell size results in an increase in reduced scattering coefficient,  $\mu_s'$ , and thus in pathlength; *vice versa*. A decrease in cell size may be caused by an addition of a carbohydrate in tissue. Figure 1(a) also gives the dependence of  $\mu_s'$  on glucose concentration (bottom scale) introduced into liver.

The solid circles in Figure 1(b) are calculated for the relationship between  $\mu_s'$  and added glucose concentration with a variable cell radius,  $a$ , and a variable extracellular refractive index,  $n_{ex}$ , but a fixed cell volume fraction,  $\phi$  ( $=0.8$ ). On the other hand, the open circles in Figure 1(b) correspond to the simulation of  $\mu_s'$  for variable  $a$ ,  $n_{ex}$ , and  $\phi$  with a relationship of  $\phi = \frac{4}{3}\pi a^3/V_{total}$ , where  $V_{total}$  remains constant. Except for  $\phi$ , other parameters for these two traces are the same, namely,  $n_{in}=1.465$ ,  $n_{ex}=1.33+2.73 \times 10^{-5}[C]$ ,  $a=10.678-2 \times 10^{-3}[C]$  in  $\mu\text{m}$ , and  $\lambda=0.8 \mu\text{m}$ . These two circle traces show a contradictory behavior of  $\mu_s'$  as the carbohydrate concentration increases. After considering all effects of cell size, extracellular refractive index, and cell volume fraction, we show from the simulation data that in the addition of a solute/carbohydrate in tissue, the overall scattering of tissue can increase or decrease, depending on if  $\phi$  decreases or is unchanged, respectively.

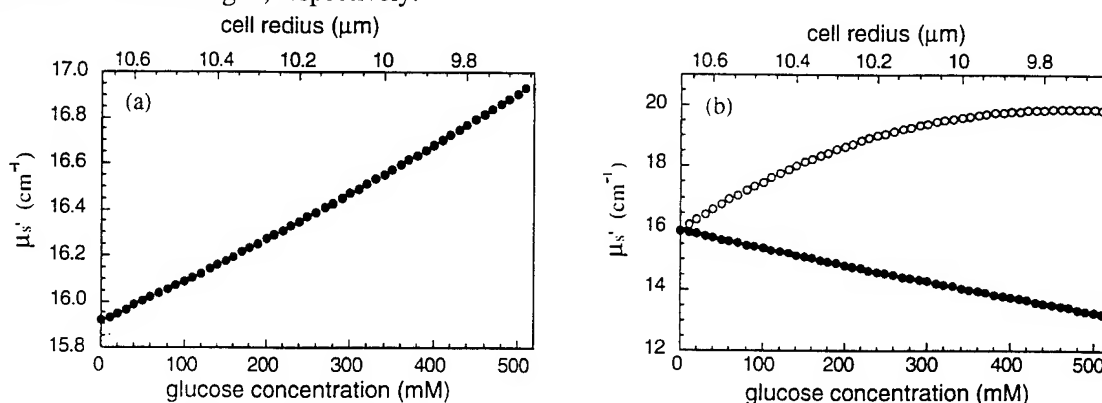


Figure 1. Simulated results of reduced scattering coefficient,  $\mu_s'$ , of the liver, calculated using eq. (1).

Experimentally, to study coupled effects on  $\mu_s'$  due to changes in both cell size and refractive index of the extracellular fluid, several carbohydrates were added in the perfusate for the liver perfusion experiments. Figure 2 is a set of time-dependent curves of pathlength measurements with the frequency-domain method during the liver perfusion with three kinds of carbohydrates. Curves (a), (b), and (c) correspond to a perfusate containing 200 mM glucose, 200 mM mannitol, and 200 mM sucrose,

respectively. Furthermore, Figure 3 shows a set of pathlength dependence of the rat brain on the injected carbohydrate concentrations.

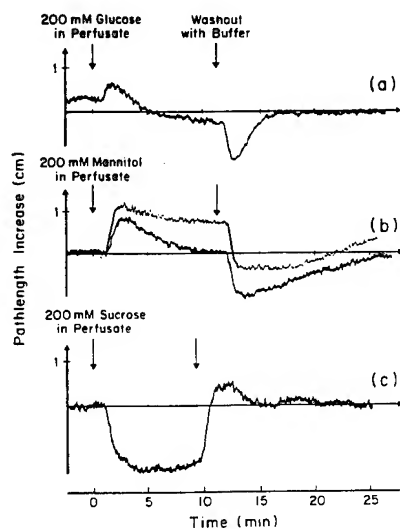


Figure 2.

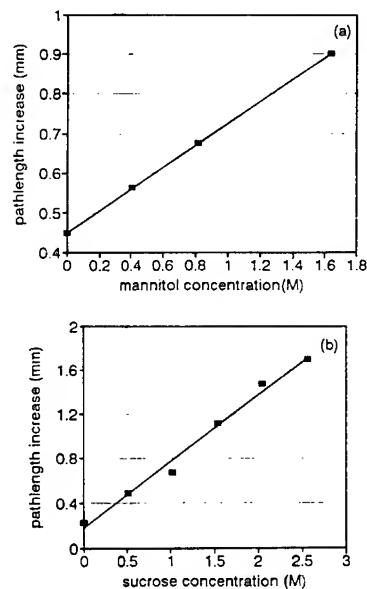


Figure 3.

Both Figure 2 and Figure 3 show that the pathlength, and thus the reduced scattering coefficient, increases as the carbohydrate is introduced into the perfusion liver or in the rat brain, except in the case of sucrose perfusion. This increase of scattering with an increase of carbohydrate concentration can be explained only by considering the shrinkage of the cell sizes of the tissue. The decrease in pathlength for the liver sucrose perfusion can be explained by a large amount of water loss in tissue, which makes  $\phi$  keep constant.

## 5. Summary:

In summary, an approximated approach of the Mie theory, suggested by Graaff et al, is used in calculating the effects of refractive index and osmolarity on reduced scattering coefficient of tissues. Furthermore, photon diffusion theory enables us to associate the reduced scattering coefficient to the optical pathlength. Experimentally, we employed the three NIR techniques to measure the changes of optical properties due to addition of a solute in perfused rat livers and in the rat brain. Based on the Mie calculations, we show that changes of scattering in tissue depend not only on the change in extracellular refractive index but also on the change in extracellular osmolarity, and thus on the change in cell volume. The consistency between the theoretical and experimental results clearly demonstrates that the variation of cell size plays an important role in determining changes in scattering properties of tissue. This study demonstrates that the NIR technique has a significant potential for noninvasive, physiological monitoring.

## 6. References:

1. J. S. Maier, S. A. Walker, S. Fantini, M. A. Franceschini, and E. Gratton, *Opt. Lett.* **19**(24), 2062-2064 (1994).
2. M. Kohl, M. Cope, M. Essenpreis, and D. Böcker, *Opt. Lett.* **19**(24), 2170-2172 (1994).
3. B. Chance, H. Liu, T. Kitai, and Y. Zhang, *Anal. Biochem.* **227**, 351-362 (1995).
4. H. Liu, B. Beauvoit, M. Kimura, B. Chance, submitted to *Biomedical Optics*.
5. R. Graaff, J. G. Aarnoudse, J. R. Zijp, P. M. A. Slood, F. F. M. de Mul, J. Greve, and M. H. Koelink, *Appl. Opt.* **31**(10), 1370-1376 (1992).
6. H. Liu, M. Miwa, B. Beauvoit, N. G. Wang, and B. Chance, *Anal. Biochem.* **213**, 378-385 (1993).
7. S. Fantini, M. A. Franceschini-Fantini, J. S. Maier, S. A. Walker, B. Barbieri, and E. Gratton, *Optical Engineering* **34**, 32-42 (1995).
8. E. M. Sevick, B. Chance, J. Leigh, S. Nioka, and M. Maris, *Anal. Biochem.* **195**, 330-351 (1991).
9. H. Liu, D. A. Boas, Y. Zhang, A. G. Yodh, and B. Chance, *Phys. Med. Biol.* **40**, 1983-1993 (1995).



## Elastic scattering spectroscopy for diagnosis of tissue pathologies

Irving J. Bigio, Judith R. Mourant, James Boyer, Tamara M. Johnson & JoAnne Lacey  
 Los Alamos National Laboratory  
 CST-4, MS-E535  
 Los Alamos, NM 87545, USA  
 IJB: tel: 505-667-7748; fax: 505-665-4637; e-mail: [ijb@lanl.gov](mailto:ijb@lanl.gov)

We have utilized elastic-scattering spectroscopy (ESS) to generate optical signatures for noninvasive diagnosis of various tissue pathologies in a variety of organ sites. Tissue pathologies, malignancy being of special interest, are detected and diagnosed using spectral measurements of the elastic optical transport properties of the tissue, scattering and absorption, over a wide range of wavelengths.

The use of elastic scattering as a method for optical tissue diagnosis is based on the fact that many tissue pathologies, including a majority of cancer forms, exhibit significant architectural changes at the cellular and sub-cellular level. Elastic-scattering spectral signatures are altered by changes in the same tissue parameters that pathologists address visually: the sizes and shapes of cells and nuclei, the ratio of nuclear to cellular volume, intra-nuclear components, clustering patterns, etc. ESS signatures are also affected by variations in the concentrations of mitochondria, which are posited as a primary source of scattering in some tissues.[1] Since the cellular components that cause elastic scattering have dimensions typically on the order of visible to near-IR wavelengths, the elastic scattering properties will exhibit a wavelength dependence that is more complex than for simple  $(1/\lambda^4)$  Rayleigh scattering. Thus, pathological changes can be expected to cause significant changes in an optical signature that is derived from the wavelength-dependence of elastic scattering.

The ESS probe is designed to be used in optical contact with the tissue under examination and has separate illuminating and collecting fibers. Thus, the light that is collected and transmitted to the analyzing spectrometer must first scatter through a small

volume of the tissue before entering the collection fiber(s). (See Figure 1.)

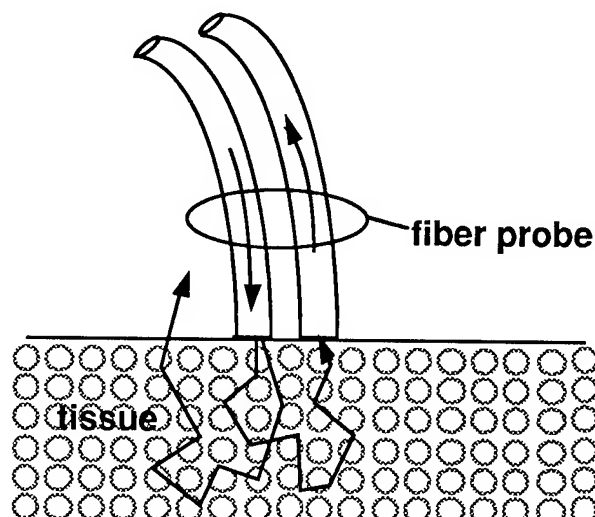


Fig. 1. The optical geometry of signal collection for ESS diagnostics.

The resulting effective path length of the collected photons is generally several times greater than the actual separation of the fiber tips. Consequently, the system has good sensitivity to the optical absorption bands that result from biochemical changes of the tissue components, over the instrument's effective operating range of 300 to >750 nm. Such absorption features add valuable complexity to the ESS signature. Although the instrument used in these experiments generates a spectrum that reflects the wavelength dependence of both scattering and absorption without separating those contributions, these composite signatures appear to correlate well with differences in tissue types and condition.

It is important to note that the fiber probe, being used in optical contact with the tissue, examines only that site and does not image the tissue surface. While this is an inherent

limitation for any type of spectroscopy performed with a contact probe, our approach to ESS does offer other advantages when compared to methods based on laser-induced fluorescence (LIF) and Raman spectroscopies. The use of less expensive detectors is enabled with ESS because the optical signals are much stronger. Furthermore, a white-light source can be employed rather than a laser. The data acquisition, storage and display time with the our instrument is  $<1$  second. Thus, in addition to the reduced invasiveness of this technique compared with current state-of-the-art methods (surgical biopsy followed by microscopic examination), ESS offers the possibility of impressively faster diagnostic assessment.

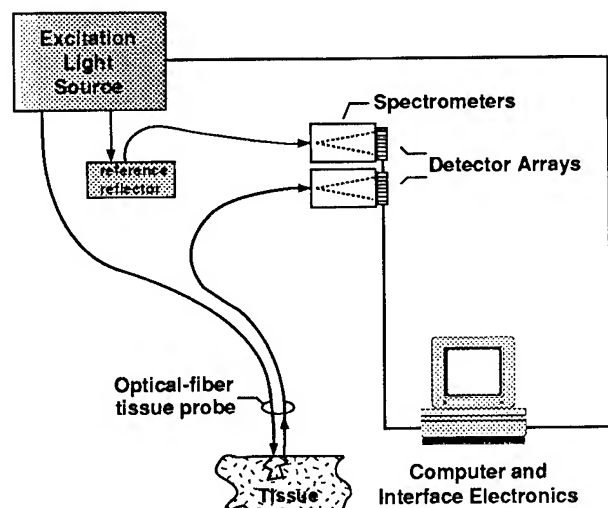


Fig. 2. System schematic.

The system, depicted schematically in Figure 2, consists of a white-light source, fiber-optic delivery and collection fibers, spectrometers for dispersion of the collected light and linear CCD's for detection. The wavelength range of the system is 300-750 nm (extendible to 250-1000 nm). The white-light source is a Xenon arc lamp, and two pairs of spectrometer/detectors are employed, one for measuring the signal returned by the collection fiber from the tissue, and the other for measuring a reference spectrum from a spectrally-flat, diffuse-scattering material. High OH<sup>-</sup> optical fibers of 200-500 microns in diameter were used for light delivery and collection. The complete optical probe, including an outer jacket, is  $\leq 2$  mm in

diameter and fits through the working channels of various endoscopes.

The small diameter of a probe for endoscopic use requires that the source and collection fibers be in close proximity to each other. (Thus, only a small volume of tissue,  $\leq 1$  mm<sup>3</sup>, is examined with each measurement.) For these short distances and for these geometries, computational modeling with the diffusion approximation is not valid, and physical relevance requires the use of Monte Carlo techniques and a correct form for the scattering phase function. To this end we have been investigating the use of Mie theory.[2] More detailed discussions of the operating principles and specifications of our instrumentation have appeared in earlier publications.[3,4,5]

Several different organ areas and tissue types have been the subjects of clinical testing with a portable version of our instrument. Our first *in vivo* data were taken in the bladder, for which a sensitivity and specificity of 100% and 97% respectively were obtained when the spectral data were compared with 50 biopsy reports from 12 patients.

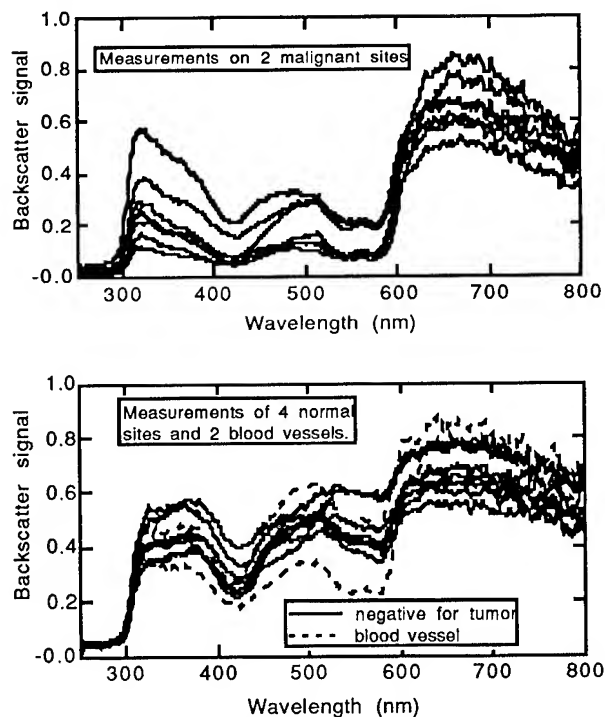


Fig. 3. ESS spectral signatures from bladder wall.

Figure 3 shows a comparison of typical spectral signatures, for both malignant and non-malignant diagnoses, taken from two of the bladder patients. With the bladder data, the spectral signature used for correlation with pathology was the slopes of the spectra in the UV range 330-370 nm.

Data have been taken in several locations of the GI tract.[6] Optical measurements were made on 73 biopsy sites in the colon/rectum, in 16 patients. Spectral criteria were chosen so as to yield 100% sensitivity for identifying the 6 malignant and dysplastic lesions, that were found, with a consequent specificity of 96% (i.e., no false negatives, and 4% false positives).

In the case of gastric lesions, 34 biopsy sites were examined in the stomachs of 17 patients. None were malignant, and only one site was dysplastic. While this one dysplastic site had a clearly different spectral signature than the other 33 sites, more data will be required before anything can be said about the repeatability of any signature. Data that we have taken to date in the esophagus are inconclusive.

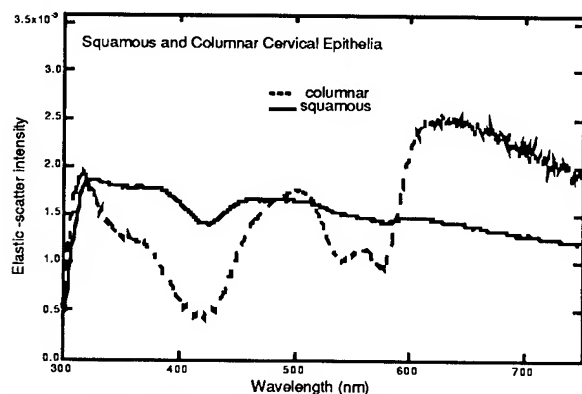


Fig. 4. Cervical epithelia spectra.

More recently we have investigated an interesting different application of this diagnostic: locating the transition zone between columnar and squamous-cell epithelia near the opening of the cervix. In pregnant women, the location of this epithelial transition zone moves outward during several days to weeks prior to delivery, and may be used as a predictive indicator of the onset of labor. Thus, noninvasive monitoring of the

movement of the transition zone could be used as an indicator for women at risk for preterm delivery, allowing safer and earlier intervention to try to delay labor. With women who were undergoing cervical biopsies for other reasons, we have made ESS measurements of the transition zone. Consistent spectral differences between the columnar-cell and squamous-cell epithelia were found for all the measured sites. The typical spectral differences are illustrated in Figure 4.

In summary, elastic-scattering spectroscopy appears to hold promise as a low-cost tissue diagnostic with a variety of potential applications.

1. B. Beauvoit, T. Kitai, H. Liu and B. Chance, "Time-resolved spectroscopy of mitochondria, cells and rat tissues under normal and pathological conditions," *Proc. SPIE* **2326**, pp. 127-136 (1995).
2. James Boyer, Judith R. Mourant and Irving J. Bigio, "Monte Carlo investigations of elastic scattering spectroscopy applied to latex spheres used as tissue phantoms", *Proc. SPIE* **2389**, pp. 103-112 (1995).
3. Irving J. Bigio, Thomas R. Loree, Judith Mourant, Tsutomu Shimada, K. Story-Held, R.D. Glickman and Richard Conn, "Optical diagnostics based on elastic scattering: recent clinical demonstrations with the Los Alamos Optical Biopsy System", *Proc. SPIE* **2081**, p.174, (1993).
4. Irving J. Bigio, Judith R. Mourant, James Boyer, Tamara Johnson and Tsutomu Shimada, "Noninvasive identification of bladder cancer with sub-surface backscattered light", *Proc. SPIE* **2135**, pp .26-31 (1994).
5. Judith R. Mourant, Irving J. Bigio, James Boyer, Richard L. Conn, Tamara Johnson and Tsutomu Shimada, "Spectroscopic diagnosis of bladder cancer with elastic light scattering", *Lasers in Surgery and Medicine* **16**, pp. (1995).
6. Judith R. Mourant, James Boyer, Tamara M. Johnson, JoAnne Lacey and Irving J. Bigio, "Detection of gastrointestinal cancer by elastic scattering and absorption spectroscopies with the Los Alamos Optical Biopsy System", *Proc. SPIE* **2387**, pp. 210-217 (1995).

# The significance of fiber numerical aperture for optical measurements of turbid media

Judith R. Mourant and Andreas Hielscher  
 Bioscience and Biotechnology Group CST-4, MS E535,  
 Los Alamos National Laboratory,  
 Los Alamos, NM 87545  
 ph: (505)665-1190 fax:(505)665-4637 e-mail: jmourant@lanl.gov

Optical techniques for tissue diagnosis often employ fiber probes which fit through the working channel of an endoscope. The delivery and collection fibers of these probes are either in close proximity,<sup>1,2,3</sup> or, in some cases, light delivery and collection is performed with the same fiber.<sup>4</sup> An important parameter in this geometry is the numerical aperture of the light delivery and collection fibers. By using Monte Carlo simulations we have found that the numerical aperture is an critically influences the photon sampling volume. We have also determined that for small values of numerical aperture details of the scattering phase function become more significant.

## Methods: Monte Carlo simulations

The geometry employed for the Monte Carlo simulations is shown in Fig. 1. The fibers have the same diameter and are adjacent with a fiber center-center distance  $d$ . This geometry is similar to those used in clinical tests of optical diagnostics in the esophagus, bladder, and cervix.<sup>2,3,5</sup>

Photons are launched by choosing two random numbers,  $\xi_1$  and  $\xi_2$ , to determine the point on the fiber face from which the photon is emitted. This point is specified by a radial distance and azimuthal angle as in equations 1 and 2. The deviation in initial direction of travel from the  $z$ -axis is defined by the polar angle,  $\theta$ , in Eq. 3, where  $NA$  is the numerical aperture of the delivery fiber, and  $n_f$  and  $n_m$  are the refractive indices of the delivery fiber and medium, respectively. Eq. 3 restricts  $\theta$  to be within limits set by the numerical aperture and takes into account Snell's law at the medium's surface. An azimuthal angle,  $\Psi_2$ , is also needed to define the direction of travel. From  $\theta$  and  $\Psi_2$  the unit vectors for the

direction of travel are calculated as in equations 4-6.

$$r = a\sqrt{\xi_1} \quad \text{and} \quad \Psi = 2\pi\xi_2 \quad (1,2)$$

$$\theta = (\sin^{-1}(NA n_f / n_m)) * \xi_3, \quad (3)$$

$$u_x = (\cos \Psi_2)(\sin \theta) \quad (4)$$

$$u_y = (\sin \Psi_2)(\sin \theta) \quad (5)$$

$$\text{and} \quad u_z = \cos \theta \quad (6)$$

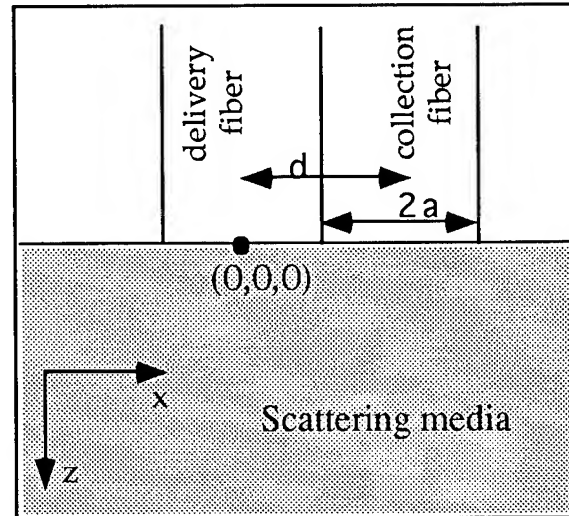


Fig. 1 Geometry for the simulations

Photon propagation is handled in the same general manner as described by Jacques and Wang.<sup>6</sup> However, our implementation allows for either a Henyey-Greenstein (HG) phase function or a phase function computed from Mie theory. The implementation of the Mie phase function is based on calculating a table of the cumulative distribution for the phase function  $P(\theta)$  which can be sampled with a random number.

Photons are terminated from the simulation when they exit the surface of the medium or travel too far from the midpoint between the fibers. Maxima for the depth and radial distance from  $(d/2, 0, 0)$  are set. These values were determined by running the simulation to find values for these cut-offs that had negligible effect on the simulation results. A photon is collected when it crosses  $z=0$  at a point under the collection fiber within the detection angle of the fiber. For collected photons the positions of scattering events are stored on an x-z grid (integrated over all y values).

#### The effect of numerical aperture on photon sampling volume

For any optical diagnostic technique, it is important to know the region of tissue that is being measured. The volume of tissue through which the collected photons traveled has been referred to as the photon sampling volume.<sup>7</sup> We have found that this volume depends on the numerical aperture of the delivery and collection optical fibers. For small numerical aperture fibers a relatively narrow and deep region is sampled. For larger numerical aperture fibers, the sampled region is less deep, but broader. This is illustrated in Fig. 2. Photon sampling volumes for adjacent 100  $\mu\text{m}$  delivery and collection fibers are shown. The medium was nonabsorbing with  $g = 0.85$  and  $\mu_s = 74.5 \text{ cm}^{-1}$ . In the top and bottom figures, the numerical apertures of both the delivery and collection fibers were 0.42 and 0.22 respectively. The number of scattering events per bin has been divided by the number of collected photons. Therefore, Fig. 2 shows contours of the probability that a collected photon scattered at a particular position in the x-z plane. In both figures the contours go from 0.005 to 0.025 in intervals of 0.005. Photon penetration is clearly deeper when the smaller numerical aperture fibers are employed.

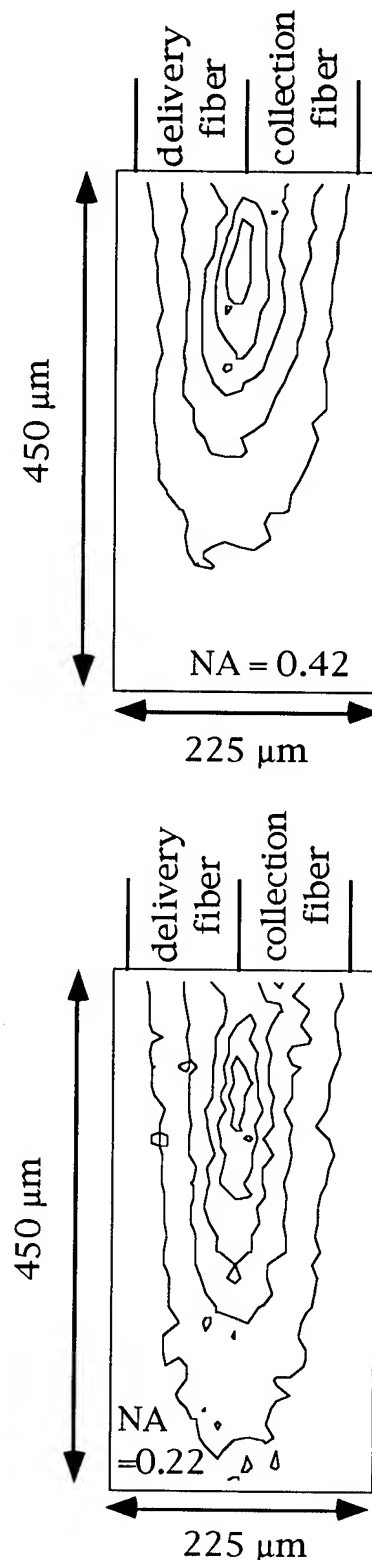


Fig. 2 Photon sampling volume for two different fiber numerical apertures. See text for details.

### Sensitivity to details of the scattering phase function for small numerical apertures

Simulations were performed with  $g = 0.85$  using the Mie and Henyey-Greenstein phase functions displayed in Fig. 3. The numerical aperture of the delivery fiber was fixed at 0.22, while the numerical aperture of the adjacent collection fiber was varied. Both fibers were 200 microns in diameter. Fig 4. shows that more photons are collected when a Mie angular scattering distribution is used rather than a HG angular scattering distribution. The percent difference in the fraction of photons collected,  $100*(F_{\text{Mie}}-F_{\text{HG}})/F_{\text{HG}}$ , is plotted as a function of numerical aperture. Here  $F_{\text{Mie}}$  is the fraction of photons collected when a Mie phase function is used and  $F_{\text{HG}}$  is the fraction of photons collected when a HG phase function is used. As NA increases  $100*(F_{\text{Mie}}-F_{\text{HG}})/F_{\text{HG}}$  decreases. This is attributed to the fact that for higher acceptance angles, the change in a photons direction of travel between emission and collection does not have to be as large. Therefore, high angle scattering events are not as important. Similar reasoning explains the fact that  $100*(F_{\text{Mie}}-F_{\text{HG}})/F_{\text{HG}}$  is greater for larger  $\mu_a$ .

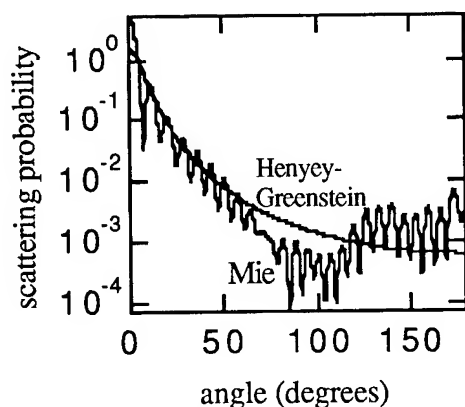


Fig. 3 The Mie and Henyey-Greenstein phase functions used in the Monte Carlo simulations.

### Conclusion

We have shown that fiber numerical aperture is a critical parameter in the design of systems for optical tissue diagnosis.

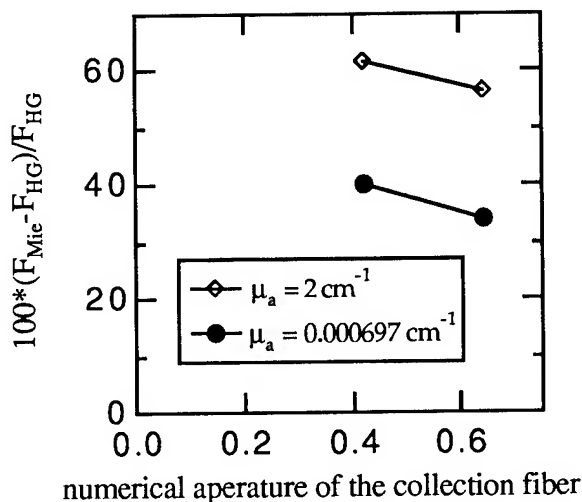


Fig. 4 The percent difference in the fraction of collected photons for a Mie phase function as compared with a Henyey-Greenstein phase function.  $g=0.8626$ ,  $\mu_s = 85.7 \text{ cm}^{-1}$ , and the NA of the delivery fiber was 0.22.

1. R. M. Cothren, R. Richards-Kortum, M. V. Sivak, M. Fitzmaurice, R. P. Rave, G. A. Boyce M. Doxtader, R. Blackman, T. B. Ivanc, G. B. Hayes, M. S. Feld, and, R. E. Petras, *Gastrointestinal Endoscopy* **36**:105-111, (1990).
2. T. Vo-Dinh, M. Panjehpour, B.F. Overholt, C. Farris, F.P. Buckley III, and R. Sneed, *Lasers Surg. Med.* **16**: 41-47 (1995).
3. J. R. Mourant, I. J. Bigio, J. Boyer, R. L. Conn, T. Johnson, and T. Shimada, Accepted by *Lasers in Surgery and Medicine* in 1994.
4. K.T. Schomacker, J.K. Frisoli, C C. Compton, T.J. Flotte, J.M. Richter, N.S. Nishioka, and T.M. Deutsch, *Lasers Surg. Med.* **12**:63-78 (1992).
5. N. Ramanujam, M. F. Mitchell, A. Mahadevan, S. Thomsen, E. Silva, R. Richards-Kortum, *Gynecological Oncology* **52**:31-38 (1994).
6. L. H. Wang, S. L. Jacques, and L. Zheng, *Computer Methods and Programs in Biomedicine* **47**: 131-146 (1995).
7. E.M. Sevick, J.R. Lakowicz, H. Szmanski, K. Nowaczyk and M.L. Johnson, *J. Photochem. Photobiol. B: Biol.* **16**:169-185 (1992).

## Influence of particle size and concentration on the diffuse backscattering of polarized light

Andreas H. Hielscher, Judith R. Mourant and Irving J. Bigio

Los Alamos National Laboratory, Bioscience and Bioengineering,  
CST-4, MS E535, Los Alamos, New Mexico 87545,  
Tel. 505 667 7270, Fax 505 665 4637, E-mail: hielsch@lanl.gov

That polarization effects in scattered light can yield useful information about biological material has been shown as early as 1976, when Bickel *et al.* announced a "new biophysical tool" [1]. Surprisingly, very few authors have used this new tool. Only a couple of studies exist that are concerned with polarization of forward scattered and transmitted light [2-4]. However, there are many biomedical applications where only backward scattered light is available for diagnostics, as, for example, in most endoscopic procedures. Recently Wang *et al.* addressed this issue for the first time by reporting angular variations of intensity in the diffuse-backscattered polarized light around the polarized-light input point [5]. In this study we investigate in detail the effects of particle sizes and concentration on the diffuse backscattering of linearly polarized light. We demonstrate that different particle size and concentrations lead to differences in the spatial pattern of backscattered light when viewed through a polarizer. These differences can be explained by Rayleigh and Mie theory, and can be used to characterize biomedical tissues.

The experimental set up is depicted in Fig. 1. A linear polarizer LP1 is placed in front of a HeNe laser. The polarized light is reflected by mirror M1 onto the surface of the turbid medium under investigation, through a hole in the center of mirror M2. The pattern of the backscattered light is observed by imaging the surface around the entrance point via M2 onto a cooled CCD camera. In order to reject the specular reflection from the surface, a mask is used at the intermediate imaging plane 1. Another, rotatable, polarizer LP2 is placed in front of the CCD camera and acts as an analyzer. Typically, images were taken either with LP1 and LP2 crossed or parallel with respect to each other. We used polystyrene-sphere-solutions with various sphere diameters and concentrations as tissue phantoms with controllable optical parameters. We also analyzed the diffuse-backscattered polarized light from milk with various fat contents.

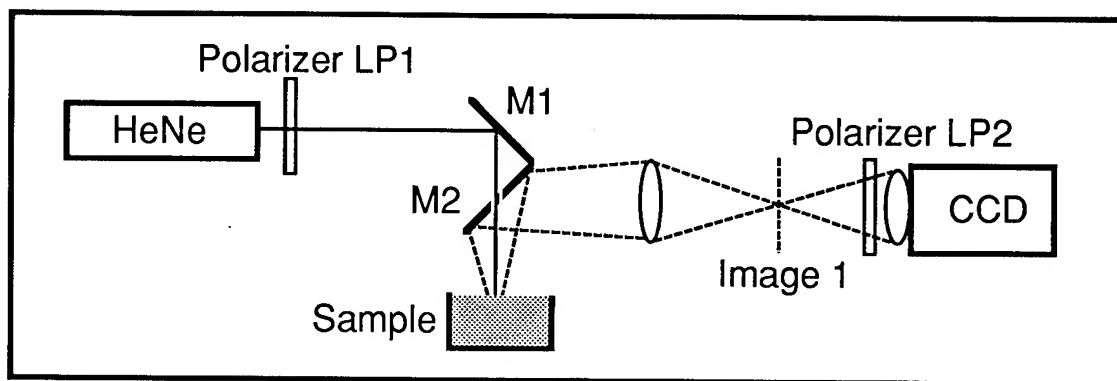


*Fig. 1: Experimental set up for measuring diffusely backscattered polarized light.*

Three examples of our measurements are shown in Fig. 2. The polarized light enters the medium in the center of the figures. The line-like disturbance that enters all of the pictures from the left is caused by a 0.5-mm diameter needle that holds the mask, which rejects the specular reflectance from the surface of the medium at the light input point.



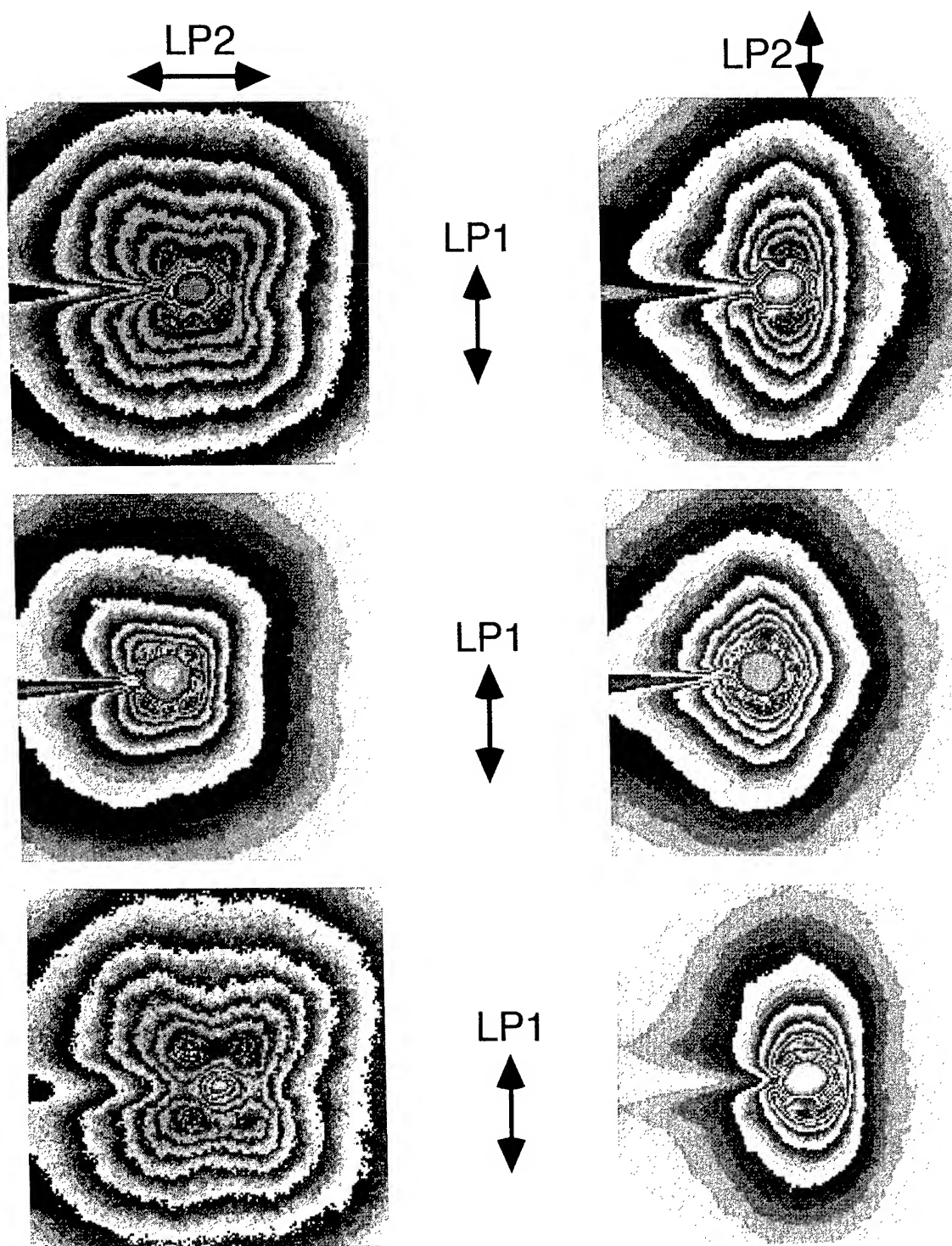


**Fig. 2:** Intensity patterns of diffusely backscattered light. The incoming light enters the medium in the center of the figures. The polarizations of the incoming light, given by LP1, and the orientation of the analyzer LP2 are indicated by the double-arrows. The figures show an area of 1cm x 1cm around the light entrance point. (Top) A 0.12% (by weight) solution of 0.497- $\mu\text{m}$ -diameter polystyrene spheres, with  $\mu_s = 15 \text{ cm}^{-1}$ ,  $g = 0.72$ , and  $\mu_s' = (1-0.72)*15 = 4.2 \text{ cm}^{-1}$ . (Middle) A 1.7% (by weight) solution of 3.4- $\mu\text{m}$ -diameter polystyrene spheres with  $\mu_s = 14 \text{ cm}^{-1}$ ,  $g = 0.86$ , and  $\mu_s' = 1.96 \text{ cm}^{-1}$ . (Bottom) Fat free milk..



The upper pictures in Fig.2 display results for particles with a diameter of 0.497  $\mu\text{m}$ . In the case of crossed polarizers (left side) a four-lobe pattern is clearly visible. The four maxima occur at  $45^\circ$  and  $135^\circ$  with respect to the polarization of the incoming light. This pattern extends out to approximately 0.5 cm from the center, which equals  $\sim 2$  times the reduced mean-free-path ( $\text{mfp}'$ ), where  $1 \text{ mfp}' := 1/(\mu_a + \mu_s')$ . When the analyzer is parallel with the incoming polarization, a two-lobe pattern appears with maxima along the direction of the polarization. These lobes also extend  $\sim 2 \text{ mfp}'$  out from the center. The two middle pictures in Fig. 2 show results for spheres with a diameter of 3.7  $\mu\text{m}$ . The scattering coefficient  $\mu_s$  is approximately the same as in the case of the 0.497- $\mu\text{m}$  spheres. The larger particle size results in a higher g-value, and therefore in a smaller  $\mu_s'$ . The four-lobe pattern for the crossed analyzer (middle left) is maintained but appears smaller. In the case of a parallel analyzer, one observes a four-lobe pattern that could not be seen with the smaller spheres. The maxima of these four lobes appear at  $0^\circ$  and  $90^\circ$  with respect to the polarization of the incoming light. Finally, the results of a measurement on a fat-free milk solution are shown. The patterns extend as far out as in the case of 0.497- $\mu\text{m}$  particles. However, the two lobe pattern in the case of a parallel analyzer is narrower.

We can summarize that with crossed polarizers one always observes a four-lobe pattern with maxima at  $45^\circ$  and  $135^\circ$  with respect to the direction of polarization of the incoming light. If the analyzer is oriented in parallel with the polarization of the incoming light, 2- or 4-lobe patterns are possible, depending on the particle size. The spatial extent of this pattern appears to decrease with increased sphere diameter. In other experiments we observe furthermore a decrease in pattern extent as the particle concentration is increased.

Most of the observed effects can be understood by Rayleigh and Mie theory. As an example, we give here an explanation for the two-lobe patterns. The basic argument is that for particles small compared to the wavelength, the probability for light scattering perpendicular to the plane of polarization is very small. Therefore, only little light can be seen in a plane perpendicular to the plane of polarization of the incident light and a two lobe pattern appears. This effect is enhanced when viewed at through a parallel analyzer. The largest particles in fat free milk are much smaller than the wavelength of visible light. Therefore, a clear two-lobe pattern appears in the fat free milk solution. The 0.497- $\mu\text{m}$  spheres are only slightly smaller than the wavelength of the incident light. Therefore, two additional lobes start to form. Finally, the 3.7  $\mu\text{m}$  spheres are much larger than the wavelength and four lobes become visible, since light scattering in  $0^\circ$  and  $90^\circ$  direction are now equally likely.

We have demonstrated that the diffuse-backscattered polarized light can be used to distinguish particle size and concentration in a highly scattering medium. Differences in cell sizes and nuclei are often observed between healthy and cancerous tissues. Therefore, this method has the potential of becoming a new diagnostic tool.

## References

- [1] W. S. Bickel, J. F. Davidson, D. R. Huffman and R. Kilkson, "Application of polarization effects in light scattering: A new biophysical tool", *Proc. Nat. Acad. Sci. USA* 73, pp. 486-490 (1976).
- [2] W. P. Van Demerwe, D. R. Huffman and B. V. Bronk, "Reproducibility and sensitivity of polarized-light scattering for identifying bacterial suspensions", *Applied Optics* 28, pp. 5052-5057 (1989).
- [3] J. M. Schmitt, A. H. Gandjbakhche and R. F. Bonner, "Use of polarized-light to discriminate short-path photons in a multiply scattering medium", *Applied Optics* 31, pp. 6535-6546 (1992).
- [4] D. D. Royston, J. H. Torres, S. L. Thomsen, P. S. Sriram and A. J. Welch, "Comparison of thermal tissue effects produced by sapphire and silica hemispherical tips", *Las. Surg. Med.*, pp. 47-58 (1994).
- [5] L. Wang, D. V. Stephens, S. L. Thomsen, S. L. Jacques and F. K. Tittel, "Polarized diffuse reflectance of laser light on a turbid medium", *International Conference on Future Directions of Lasers in Surgery and Medicine*, Engineering Foundation, Snowbird, Utha, 9-14 July, 1995.



Thursday, March 21, 1996

## Raman and Fluorescence in Tissues I

**BThC** 2:00 pm-4:05 pm  
Windsor Ballroom

Thomas Baer, *Presider*  
*Biometric Imaging*

## Raman and Fluorescence Spectroscopy for In Vivo Diagnosis of Pre-cancer

Rebecca Richards-Kortum  
The University of Texas at Austin  
Austin, TX 78712

The diagnosis of disease is more and more becoming a technical task. The clinician's goal is to assess the structural and functional changes in diseased tissue, infer the identity and stage of the disease, and predict the ultimate consequences to the organism as a whole, intervening with the proper treatment whenever possible. The diagnostic ordinance varies both for the suspected disease and with clinical specialty. Radiologists assess gross structural abnormalities utilizing variations in tissue or contrast agent absorption of x-rays. Endoscopists utilize visually apparent differences in reflectance of white light to identify malignant and pre-malignant tissues. These techniques rely predominantly on changes in tissue structure to identify diseased tissue. This structural information, although useful diagnostically, provides limited insight into the chemical and molecular etiology and pathogenesis of the disease, factors that are now appreciated to be important prognostically and in selecting appropriate therapy.

Pathology provides the most widely used clinical method of elucidating chemical information from diseased tissues. Traditional techniques of histology can be used to probe the microscopic structural alterations of diseased tissue. Using histochemical stains, many of the corresponding chemical alterations accompanying disease can be mapped on a microscopic scale. The chief disadvantage of these techniques is that they can only be applied *in vitro*, necessitating the removal of tissue. The requirement of biopsy limits the utility of this approach; it implies that, using histologic techniques, only small areas of tissue, accessible either to biopsy forceps, or needles, can be sampled. A more useful technique would combine the advantages of pathologic and radiologic methods, allowing for real time imaging of tissue *in vivo* to extract diagnostically relevant structural and histochemical information. Magnetic resonance spectroscopic imaging has the potential to provide chemical and structural images from the living patient; however there are several technical barriers to overcome before this technique is a clinical reality. Quantitative optical spectroscopic imaging is a new technique in the field of medical diagnosis which may ultimately provide these features at a lower cost and level of technology compared to that of MR spectroscopy.

Optical spectroscopy has long been an important tool in analytic chemistry [1]. The emergence of fiber optic technology has enabled the development of remote sensing and monitoring systems based on optical spectroscopy and over the last ten years, many reports have appeared suggesting the clinical potential of real time, non-invasive, quantitative, tissue diagnosis via optical spectroscopy [2-6]. Optical techniques have shown promise for automated recognition of disease in a range of organ sites in both intact tissues for diagnostic purposes [2-4] and in exfoliated cells for screening purposes [5, 6]. Various spectroscopic techniques have been applied to tissues to elucidate chemical information in the same manner as for traditional dilute solutions. Ultra-violet

and visible absorption and fluorescence spectroscopies of tissue have been studied to provide information about electronic energy level transitions; common endogenous chromophores which absorb and/or emit in this region include structural proteins, aromatic amino acids, cofactors NADH and FAD, and hemoglobin. These techniques are typically quite sensitive to small concentrations (nM- $\mu$ M) of chromophores, but because the range of naturally occurring chromophores is somewhat limited, much effort has gone into developing exogenous probes which either concentrate in diseased tissues or are sensitive to differences in the chemical environment present in diseased tissue [3]. Vibrational techniques, including IR absorption and Raman spectroscopies [4], have also been investigated recently. Here, the range of naturally occurring chromophores is broader and spectral fingerprint regions are well characterized; however, sensitivity to small concentrations (<mM) is difficult to achieve.

Although methods of recording tissue spectra clinically have been described, interpreting this information to yield meaningful structural and chemical information is the subject of much study [7]. If a tissue is thin enough compared to the penetration depth of the light, it can be treated as a dilute solution. However, most tissues are turbid, and spectra recorded from the surface can be regarded as a weighted superposition of signal generated by many thin, dilute layers. The contribution of each layer is determined by the attenuation of excitation light prior to reaching the layer and the attenuation of the return signal. This is further complicated by the layered geometry of most tissues, where individual layers have different optical properties. The effects of gross structure on tissue optics are already studied qualitatively by clinicians when tissue is examined under white light reflectance. Changes in scattering (which can be caused in pre-cancerous and cancerous tissue by an increased nuclear to cytoplasmic ratio) and absorption (which can be caused by increased hemoglobin resulting from the accompanying angiogenesis of pre-cancer and cancer) are observed visually. Tissue spectroscopy affords the opportunity to sort these out quantitatively, and determine changes in concentration of various chromophores, provided that accurate tissue optics models can be derived.

Even with current methods of analyzing this complex spectroscopic data, many groups have demonstrated in limited clinical trials that optical techniques can surpass current methods of disease detection. We have shown in trials of over 200 patients, that fluorescence spectroscopy can be used to identify precancer of the cervix with a similar false negative rate and a substantially lower false positive rate as compared to expert gynecologic oncologists [1]. Sevicik et al have shown that the significant effects of tissue optics can be deconvolved to give accurate fluorescence lifetimes of both endogenous and exogenous chromophores which are sensitive to the tissue micro-environment [3]. Feld and co-workers demonstrated that Raman spectra could be measured from fluorescent tissues in reasonable time periods, paving the way for potential clinical use of this important technology [4]. Palcic's group has shown that nuclear texture features can predict the progression and regression of precancerous lesions in breast, cervix, lung and possibly other tissues [5]. Evidence of these malignancy associated changes has also been found by Wong [6], who has measured IR spectra of exfoliated, unstained cervical cells.

This body of work demonstrates the potential for improving diagnostic medicine using quantitative optical techniques. I believe that the field is at a critical juncture, and as bioengineers, we have the unique opportunity to determine how these techniques can best improve clinical medicine and influence whether they will be accepted by the medical community. In order to best answer these questions, I believe the field must place priority on conducting moderate size clinical trials with standardized endpoints. Furthermore, as engineers, we must participate in economic analyses that determine the most cost-effective method to implement this technology. Finally, in order to determine the ultimate clinical utility, we must more fully understand the connections between tissue spectroscopy, gross and microscopic structure, chemical composition and neoplastic potential. Only then can we predict the most appropriate optical technique for a given clinical application, understand the limitations of optical diagnosis, and relate optical measurements to prognosis, selection and monitoring of therapy.

### References:

1. Campbell ID, Dwek RA; Biological Spectroscopy, The Benjamin Cummings Publishing Co, Menlo Park, CA, 1984.
2. Ramanujam N, Follen Mitchell M, Mahadevan A, Thomsen S, Richards-Kortum R, In Vivo Diagnosis of Cervical Intraepithelial Neoplasia Using 337 nm Laser Induced Fluorescence, PNAS, 91:10193, 1994.
3. Hutchinson CL, Lakowicz JR, Sevick-Muraca EM; Fluorescence lifetime-based sensing in tissues: a computational study, Biophysical Journal, 68(4):1574-82, 1995.
4. Manoharan R, Baraga JJ, Feld MS, Rava RP: Quantitative Histochemical Analysis of Human Artery Using Raman Spectroscopy, J Photochem Photobiol B, 16:211-23, 1992.
5. Palcic B: Nuclear Texture: Can it Be Used as a Surrogate Endpoint Biomarker?, J Cell Biochem S, 19:40-6, 1994.
6. Wong P, Wong R, Caputo TA, Godwin TA, Rigas B: Infrared spectroscopy of exfoliated human cervical cells: evidence of extensive structural changes during carcinogenesis, Proc Natl Acad Sci, 88:10988-92, 1991.
7. Richards-Kortum RR, Role of Laser Induced Fluorescence Spectroscopy in Diagnostic Medicine, in Welch AJ, Van Gemert M, eds, Optical-Thermal Response of Laser Irradiated Tissue, in press, 1994.

## Raman Measurements of Concentrations in Scattering Media

Jeffery S. Reynolds, Fred P. LaPlant\*, Charles A. Thompson,  
Kevin J. Webb, and Dor Ben-Amotz\*

School of Electrical and Computer Engineering

\*Department of Chemistry

Purdue University

West Lafayette, IN 47907

Contact: Kevin Webb, Email: [webb@ecn.purdue.edu](mailto:webb@ecn.purdue.edu)

Phone: (317) 494-3373 Fax: (317) 494-2706

Recent advances in optical and electronic technology, including holographic filters, cooled CCD detector arrays, compact lasers, and computer software, have opened many new applications for Raman spectroscopy. Others have demonstrated the use of Raman spectroscopy to differentiate between benign and malignant tissue and to do qualitative analysis of tissue composition.<sup>1,2</sup> We reported the use of Raman spectroscopy to detect the presence of a small diamond source in a highly scattering medium with 0.25 and 0.50% suspensions of Intralipid in water.<sup>3</sup> We also used the Raman detected signal of the diamond to localize single and multiple diamond sources in the scattering medium.<sup>4</sup>

Presently, we are attempting to quantify the concentration of liquids dispersed in scattering media using Raman spectroscopy. Understanding the effect of scatter on the measured Raman spectrum is important for possible future biomedical and remote sensing applications where local scattering conditions are unavoidable. The Raman interaction normally involves a change in the optical wavelength of only a few tens of nanometers with visible and near infrared excitation. To understand how the Raman spectrum is affected by the scatter, we add small concentrations of acetonitrile ( $\text{CH}_3\text{CN}$ ) to highly scattering solutions of Intralipid in water to simulate spectroscopy in biological samples.

The experimental arrangement that we use is shown in Figure 1. The micro-Raman system uses an Olympus BH-2 microscope to focus the excitation (normally 514 nm Argon-ion laser line) and collect the scattered light from a sample. The Raman scattered light is separated from the elastically scattered light by a holographic beam splitter and notch filter. The signal is then coupled to the spectrometer, which consists of a ISA HR320 single monochromator and a Princeton Instruments 0.26 in x 1.0 inch liquid nitrogen cooled CCD array. The spectrum recorded by the CCD is downloaded to a personal computer where it can be processed. As configured for this experiment, the spectrometer has a 600 groove/mm grating and a 75  $\mu\text{m}$  entrance slit, yielding a resolution of about  $\pm 0.3 \text{ cm}^{-1}$ .

In free space the depth of field of the microscope is approximately 500  $\mu\text{m}$ . However, in a highly scattering medium, light is not collected from around the focus point. Instead, any light which scatters into the imaging cone of the microscope objective is collected. A typical spectrum for a 5% mixture of acetonitrile in a water/Intralipid scattering medium is shown in Figure 2. This spectrum was taken with the microscope free air focus lowered 4 mm into the medium. Of course, the medium is highly scattering so no real focus is formed.

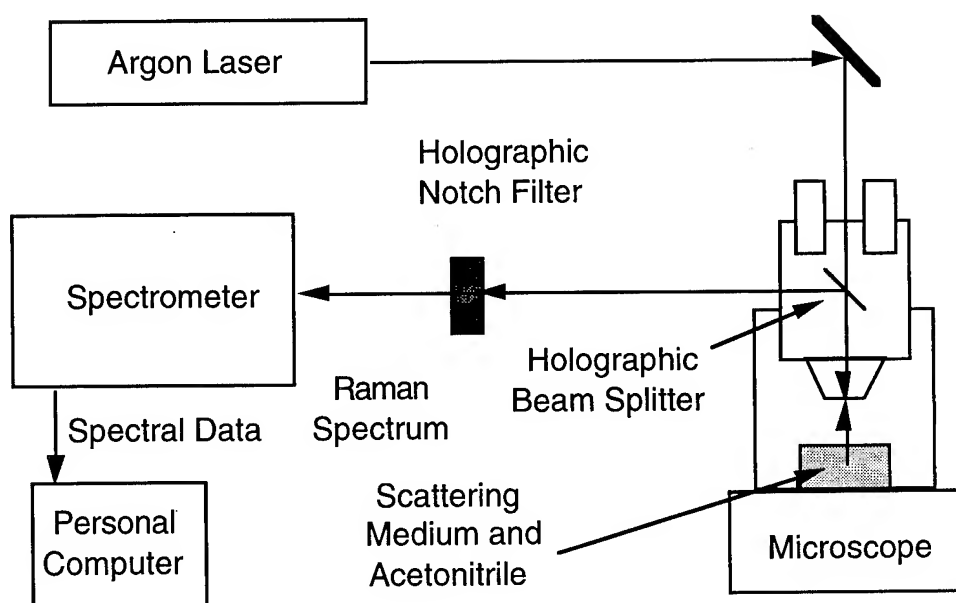


Figure 1. Experimental apparatus used to study Raman spectrum of acetonitrile dispersed in a scattering medium.

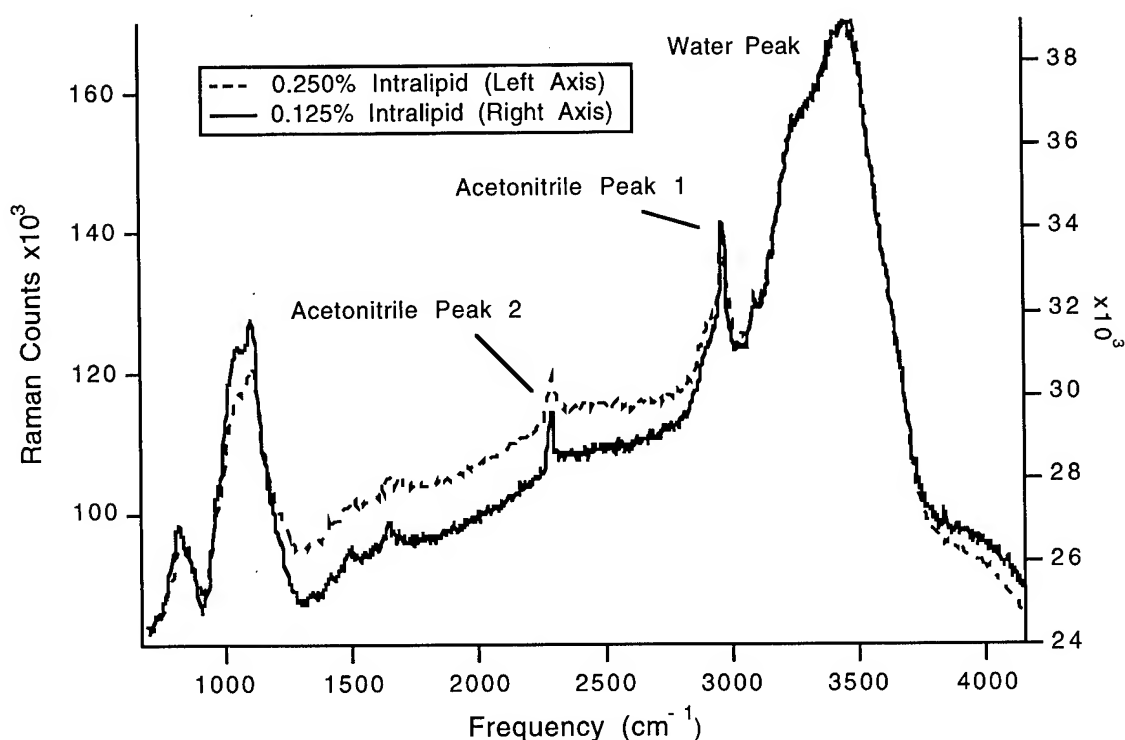


Figure 2. Raman spectrum of acetonitrile in 0.25% and 0.125% volume concentration of Intralipid in water.

If a careful measurement of the water Raman peak near  $3600\text{ cm}^{-1}$  is made and compared to the area of an acetonitrile peak height relative to the local background, the concentration of the acetonitrile relative to water can be found. As long as the scatter and absorption of the scattering medium at the two Raman shifted wavelengths is roughly the same, this measurement can be made independent of the scatter involved. Since the Raman shifted wavelengths are only a few



tens of nanometers from each other, this is probably a good assumption. A calibration curve using a careful background subtraction and relative peak height for water and peak area for acetonitrile is shown in Figure 3. Here the linear fit to experimental measurements of acetonitrile peak area relative to water peak height shows that the experimental values fall within 0.1% volume of the line of best fit.

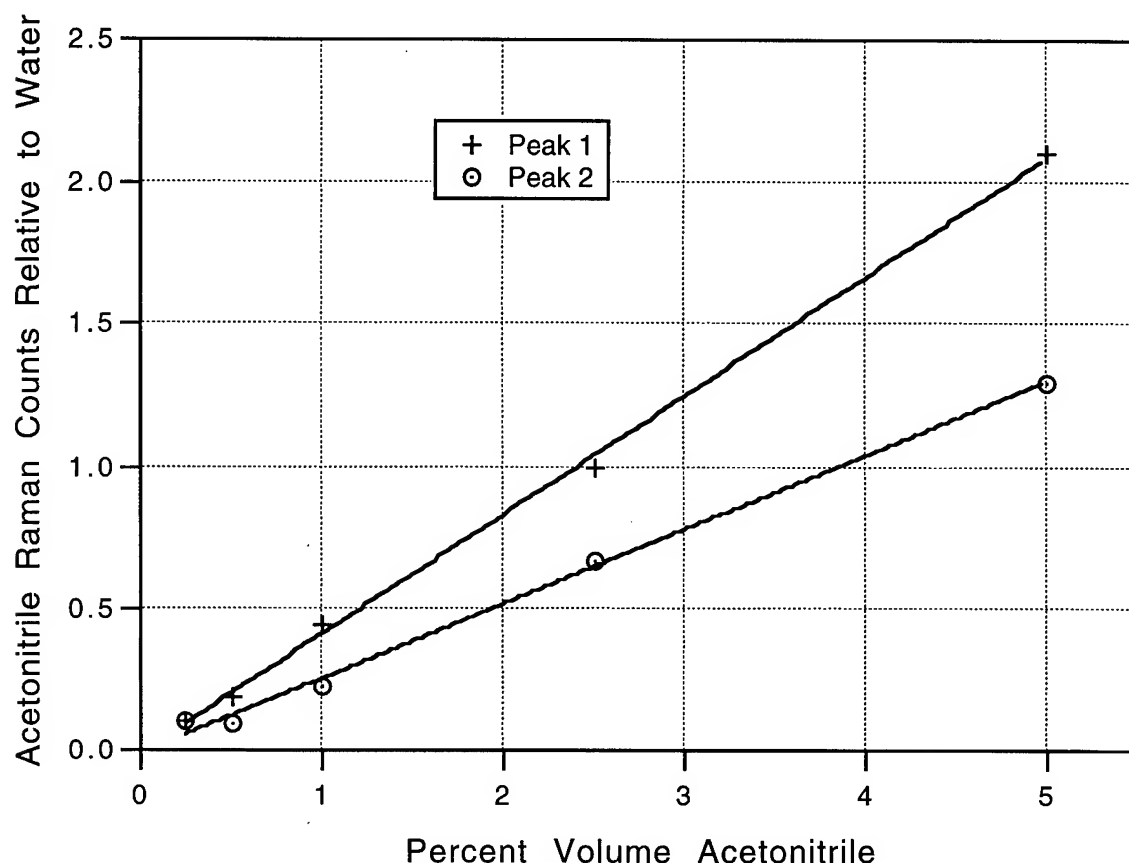


Figure 3. Calibration curve for various concentrations of acetonitrile in 1/4% scattering medium at a focus depth of 4.0 mm into the highly scattering medium.

1. R. Alfano, C. Liu, L. Sha, H. Zhu, D. Akins, J. Cleary, R. Prudente, and E. Cellmer, "Human breast tissues studied by IR Fourier transform Raman Spectroscopy," *Lasers Life Sci.*, vol. 4, pp. 23-28, 1991.
2. J. Baraga, M. Feld, and R. Rava, "In situ optical histochemistry of human artery using near infrared Fourier transform Raman spectroscopy," *Proc. Natl. Acad. Sci. USA*, vol. 89, pp. 3473-3477, 1992.
3. C. Thompson, J. Reynolds, F. LaPlant, D. Ben-Amotz, and K. Webb, "Raman spectroscopic studies of diamond in Intralipid," *Optics Letters*, vol. 20, no. 10, pp. 1195-97, 1995.
4. C. Thompson, F. LaPlant, J. Reynolds, D. Ben-Amotz, and K. Webb, "Detection of heterogeneities within scattering medium using Raman spectroscopy," *Proc. SPIE Optical Engineering Midwest 95*, vol. 2622, pp. 400-404, 1995.
5. F. LaPlant and D. Ben-Amotz, "Design and construction of a microscope-based Raman system," *Rev. Sci. Instrum.*, vol. 66, no. 6, 1995.

## **Raman Histopathology and the Plotkin Diamond**

Michael Feld  
Massachusetts Institute of Technology

The use of Raman spectroscopy to provide quantitative biological diagnostic information will be discussed.

## Fluorescence spectroscopy and imaging in random media

Christina L. Hutchinson, Tamara L. Troy, and Eva M. Sevick-Muraca

School of Chemical Engineering  
Purdue University

West Lafayette, IN 47907-1283

Phone: (317) 496-2739

Fax: (317) 494-0805

### Introduction

Recently, fluorescent and phosphorescent dyes have been developed whose lifetimes are sensitive to changes in the local environment, such as pH,  $pO_2$ ,  $Ca^{++}$ , glucose, and other metabolites.<sup>1-3</sup> From lifetime,  $\tau$ , the concentration of fluorescence-quenching metabolites can be found from the appropriate relationships describing quench kinetics. The lifetime of these dyes can be readily measured in a dilute, non-scattering solutions using the following frequency-domain measurements for phase-shift,  $\theta$ , and modulation,  $M$ :

$$\theta = \tan^{-1}(\omega\tau) \quad (1a)$$

$$M = \frac{1}{\sqrt{1+(\omega\tau)^2}} \quad (1b)$$

made at modulation frequency,  $\omega^*$ . However, when the medium is highly scattering, measurement of lifetime is complicated due to the additional time delay associated with photon migration.

Previously, we conducted finite element computations which describe the light propagation of the excitation and fluorescent light in a highly scattering medium in order to determine the location from which the fluorescent signals originate<sup>4</sup>. For a dye uniformly distributed in a scattering medium and activated by a pulsed excitation source at the surface, we illustrated that the depth from which a re-emitted fluorescent signal originates will be reduced as the lifetime increases. This phenomena occurs because the excitation fluence attenuates with distance away from the source, so the generation of an activated dye will be

greatest just beneath the source. At greater depths the excitation pulse is significantly attenuated. Therefore, the generation of activated dye is also reduced. For a long-lived dye, this means that the generated fluorescent light at the surface will predominate over that generated from deep within the tissue. This trend was also shown using a Green's function approach which describes the probability of fluorescence generation and photon propagation<sup>5</sup>. These results imply that dyes which have a long lifetime ( $> 50$  ns), may provide erroneous results when used as an optical contrast agent for biomedical optical imaging.

### Theory of short-lived excitation and fluorescence in scattering media

As a consequence of our work, we recognize that short-lived fluorescent dyes are required in order to probe deeply within scattering media. In order to investigate tissue fluorescence spectroscopy, we examined the probabilities for excitation and emission photon propagation and fluorescent generation. First, the probability for finding an excitation photon density wave launched at  $r_s$ , modulated at frequency,  $\omega$ , and located at position  $r$  is given by  $\Phi_x(r_s-r, \omega)$ . Second, the probability for fluorescent photon generation by a fluorophore located at position  $r$  is given by:

$$\begin{aligned} P(\omega) &= \int_0^\infty \frac{\alpha[C(r)]}{\tau} e^{-t/\tau} e^{-i\omega t} dt \\ &= \alpha[C(r)] \frac{1}{1+i\omega\tau} \end{aligned} \quad (2)$$

Finally, the probability that the fluorescent photon density wave modulated at frequency  $\omega$ , generated at position  $r$ , and detected at  $r_d$  is given by  $\Phi_m(r_d-r, \omega)$ . The probabilities  $\Phi_x(r_s-r, \omega)$  and  $\Phi_m(r_d-r, \omega)$  are given by the Green's function to the AC component of the diffusion equations in which multiple light scattering is assumed<sup>6</sup>. Otherwise, the probabilities are

\* Herein we assume single exponential decay kinetics of dyes with the provision that multi-exponential decays can also be considered.

described by an alternate model for non-diffuse light propagation. Regardless of the model, the fluorescent photon density wave modulated at frequency  $\omega$  detected at the surface is simply the product of these three probabilities, integrated over the entire volume:

$$P(\omega) = \frac{1}{1 + i\omega\tau} \oint_V \Phi_x(\omega, \mathbf{r}_s - \mathbf{r}) \Phi_m(\omega, \mathbf{r} - \mathbf{r}_d) d^3\mathbf{r} \quad (3)$$

Traditionally, fluorescence lifetime measurements are reported relative, or referenced, to the *incident* excitation light. However, if the above expression for detected (or re-emitted) fluorescence (superscript s) is referenced to the re-emitted signal of a second, "reference" fluorophore (superscript r):

$$\frac{P^s(\omega)}{P^r(\omega)} = \frac{\frac{1}{1 + i\omega\tau^s} \oint_V \Phi_x^s(\omega, \mathbf{r}_s - \mathbf{r}) \Phi_m^s(\omega, \mathbf{r} - \mathbf{r}_d) d^3\mathbf{r}}{\frac{1}{1 + i\omega\tau^r} \oint_V \Phi_x^r(\omega, \mathbf{r}_s - \mathbf{r}) \Phi_m^r(\omega, \mathbf{r} - \mathbf{r}_d) d^3\mathbf{r}} \quad (4)$$

and if the probabilities for photon migration of the excitation and emission light are assumed to be equal (i.e.  $\Phi_m^r = \Phi_m^s$ ), then the referenced signal is only a function of modulation frequency and lifetime of the two fluorophores. Noting that the "referenced" phase-shift will be the arc tangent of the ratio of imaginary to real components of  $P^s(\omega)/P^r(\omega)$  and that the amplitude modulation is the modulus of the complex number, then the expressions of phase-shift and amplitude demodulation relative to a reference fluorophore can be obtained:

$$\theta^s(\omega) - \theta^r(\omega) = \tan^{-1}(\omega\tau^s) - \tan^{-1}(\omega\tau^r) \quad (5a)$$

$$\frac{M^s(\omega)}{M^r(\omega)} = \frac{\sqrt{1 + (\omega\tau^r)^2}}{\sqrt{1 + (\omega\tau^s)^2}} \quad (5b)$$

Similarly, if the detected (or re-emitted) fluorescence (subscript m) is referenced relative to the re-emitted excitation light (subscript x), then when  $\Phi_x = \Phi_m$ , the phase shift and amplitude demodulation are given by<sup>7</sup>:

$$\theta_m(\omega) - \theta_x(\omega) = \tan^{-1}(\omega\tau) \quad (6a)$$

$$\frac{M_m(\omega)}{M_x(\omega)} = \frac{1}{\sqrt{1 + (\omega\tau)^2}} \quad (6b)$$

### Experimental measurements of $\theta$ and $M$

In order to verify the Green's functions results on lifetime determination in random media, frequency-domain measurements were conducted on micromolar solutions of 3,3'-Diethylthiatricarbocyanine iodide (DTTCI) and IR-125 in ethanol and 0.528 mm monodisperse polystyrene beads. Experimental measurements of phase-shift and amplitude demodulation of re-emitted fluorescent light were conducted at modulation frequencies between 4 and 240 MHz using a Ti:Sapphire laser (Spectra Physics, CA) at 780 nm. The laser was pulsed at a repetition rate of 4 MHz. Average powers were approximately 10 mW. A glass slide served as a beam splitter providing <1% reflection which was collected into a 1000 micron fiber optic and passed to the referencing PMT. The unreflected pulse train was focused onto the sample which was held in a 10 x 10 x 40 mm glass cuvette. The re-emitted light was collected at a 90° angle from the incident source using another fiber and was passed to the sample PMT. An 830 nm interference filter was used to make frequency-domain measurements at the emission wavelengths. The PMTs were heterodyned at a cross correlation frequency of 100 Hz using commercial electronics package and data acquisition modules (ISS, Champaign, IL).

### Results and Discussion

Figure 1a shows the phase-shift and amplitude demodulation of DTTCI and IR-125 in a dilute solution of ethanol as a function of modulation frequency. The following fluorescent lifetimes were determined by fitting the data to the standard equation for phase-shift (Equation (1a)): DTTCI, 1.17 ns; and IR-125, 0.58 ns. Reported literature values for DTTCI and IR-125 are 1.12 ns and 0.57 ns, respectively for excitation at 780 and emission at > 780 nm<sup>8</sup>. As expected, the values of lifetime obtained from experimental measurements in dilute, non-scattering solutions match those found in the literature for dilute solutions.

In order to verify the proposed referencing technique, experimental measurements were conducted for DTTCI and IR-125 in scattering solutions of polystyrene beads in ethanol. Figure 1b shows the phase-shift and amplitude demodulation of the dye DTTCI referenced to the dye IR-125 when the

scattering coefficient of both dyes was approximately  $10 \text{ cm}^{-1}$  (shown as open and closed squares). Scattering coefficients were computed from Mie scattering theory<sup>9</sup>. The lines represent the curve fits to the phase-shift using Equation (5a). The lifetimes match that of the dilute solutions (DTTCI, 1.17 ns and IR-125, 0.58 ns), therefore the referencing technique is valid for the fluorescent dyes used herein.

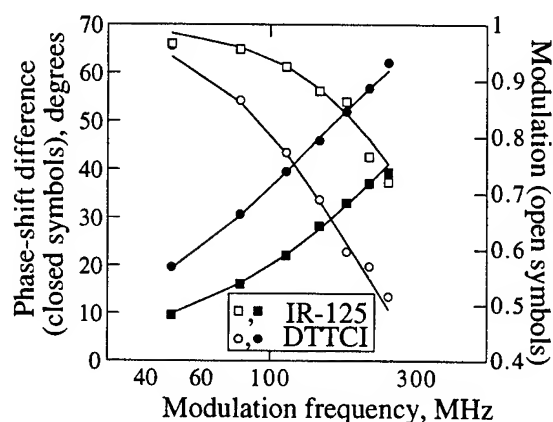


**FIGURE 1:** Frequency-domain measurement of  $\theta$  and  $M$  in a dilute, non-scattering solution of ethanol. The calculated lifetime for DTTCI was 1.17 ns and IR-125 was 0.58 ns.

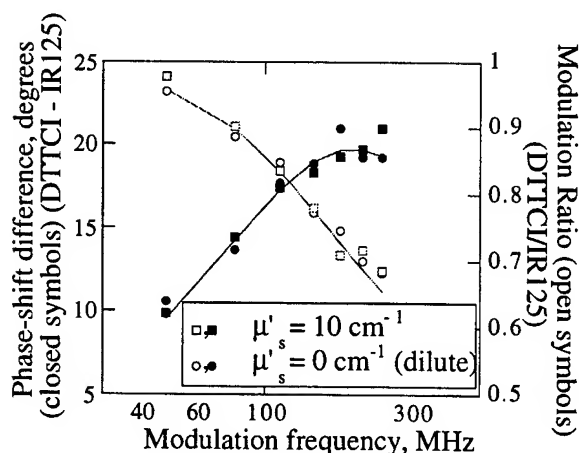


**FIGURE 2:** Frequency-domain measurement of  $\theta$  and  $M$  of DTTCI in a scattering solution, referenced to IR-125 in an identical scattering solution (squares). Also plotted is DTTCI referenced to IR-125 when the dye is present in a dilute solution (circles). The calculated lifetimes are DTTCI, 1.17 ns and IR-125, 0.58 ns.

In addition, recently we have shown that upon referencing re-emitted fluorescent signals with re-emitted excitation light, our approach works without the need for a second reference fluorescent dye<sup>7</sup>.

## Conclusions

Currently, researchers are using phosphorescent dyes for biomedical optical imaging. However, these long-lived dyes may not be probing beyond a few millimeters of tissue. This work shows that when the emission photons of two fluorescent dyes migrate similarly, then their lifetimes can be deconvolved from the times associated with photon migration. Our work shows that a second reference dye with known and constant lifetime is needed for fluorescence lifetime spectroscopy in tissues as it is needed in traditional lifetime spectroscopy in non-scattering solutions. The potentials to reference to re-emitted excitation light instead of the incident excitation light may eliminate the need for the second "reference" dye.

## Acknowledgments

This work was supported in part by the Whitaker Foundation and the National Science Foundation Young Investigator Award.

## References

- <sup>1</sup>Lakowicz, J.R., and H. Szmacinski, *Sensors and Actuators B*, **11**: 133-143, 1993.
- <sup>2</sup>Bacon, J.R., and J.N. Demas, *Anal. Chem.*, **59**: 2780-2785, 1987.
- <sup>3</sup>Wilson, D.F., *Oxygen Transport in Tissues XIV*, Plenum Press, New York, 1992.
- <sup>4</sup>Sevick-Muraca, E., Suddeath, L., and C.Burch, *SPIE*, **2137**: 673-683, 1994.
- <sup>5</sup>Sevick-Muraca, E., and C. Burch, *Opt. Lett.*, **19**: 1928-1930.
- <sup>6</sup>Boas, D.A., O'Leary, M.A., Chance, B., and A.G. Yodh, *Proc. Natl. Acad. Sci. USA*, **91**: 4887-4891, 1994.
- <sup>7</sup>Hutchinson, C.L., Troy, T.L., and E. M. Sevick-Muraca, *Appl. Optics*, in press.
- <sup>8</sup>Soper, S.A., and B. L. Legendre, *Appl. Spectro.*, **48**: 400-405, 1994.
- <sup>9</sup>Bohren, C.F., and D.R. Huffman, *Absorption and Scattering of Light By Small Particles*, John Wiley and Sons, New York, 1983.



Thursday, March 21, 1996

## Raman and Fluorescence in Tissues II

**BThD** 4:30 pm-5:50 pm  
Windsor Ballroom

Thomas Baer, *Presider*  
*Biometric Imaging*

## Diffusive Fluorescent Waves in Homogeneous and Heterogeneous Turbid Media: Analytic Solutions and Sensitivity Analysis

X. D. Li<sup>†\*</sup>, M. A. O'Leary<sup>†\*</sup>, D. A. Boas<sup>†\*</sup>, B. Chance<sup>\*</sup> and A. G. Yodh<sup>†</sup>

<sup>†</sup>Department of Physics, <sup>\*</sup>Department of Biochemistry and Biophysics

University of Pennsylvania, Philadelphia, PA 19104

Tel: (215)898-6354 FAX: (215)898-2010

Recently fluorescent contrast agents have been considered as a means to enhance the specificity and sensitivity in tumor detection [1-7]. Lifetime-based quantitations of different biological parameters have been proposed by several investigators, e.g., tissue oxygenation  $pO_2$  [8], pH value [9] and intracellular calcium concentration  $[Ca^{2+}]$  [10], etc. Substantial effort has been devoted to formulate the forward problem of fluorescent light in turbid media, including numerical studies by Sevick-Muraca and co-workers [11] as well as one and three dimensional mathematical studies of *homogeneous* systems by other investigators [12,13,2].

In this paper, we present exact analytic solutions for fluorescent diffusive waves in **homogeneous** turbid media containing a uniform distribution of fluorophores, and in **heterogeneous** media embedded with spherical objects. Most generally the inhomogeneity has fluorophore concentration, lifetime and optical properties that differ from those of the background. This simulates situations wherein fluorophores preferentially accumulate in tumors and may have environmentally sensitive lifetimes. Analytic solutions are limited to specific geometries and object shapes. In addition to being exact to all orders, one of the advantages of analytic solutions is the high computational speed, e.g., for 100 source-detector pairs in an infinite heterogeneous medium, the computation of fluorescent diffusive wave takes about 4 seconds of CPU time on Sun Sparc10 workstation. This enables one to investigate a large range of parameters relatively quickly. We will show that analytic solutions enable us to employ simple fitting procedures to obtain fluorophore concentration and lifetime in homogeneous media. In addition, the solutions in heterogeneous media are applied to expose signal-to-noise requirements for practical situations and the relative sensitivity of absorption and fluorescence of fluorophores. Numerical studies verify the accuracy of analytic solutions in other geometries such as semi-infinite homogeneous media.

Consider first an infinite homogeneous turbid medium with a spatially uniform distribution of fluorophores. The fluorophore is excited by an *excitation* diffuse photon density wave (DPDW) which is created by an intensity-modulated point light source at  $\mathbf{r}_s$ . When the excited fluorophore decays, it acts as a secondary source for the fluorescent diffuse photon density wave (FDPDW). The total FDPDW is found by integrating the fluorophore contribution at  $\mathbf{r}_1$  over all the space, i.e.

$$\begin{aligned} \phi_{0f}(\mathbf{r}, \mathbf{r}_s) &= \int \frac{vM_0 \exp(ik|\mathbf{r}_1 - \mathbf{r}_s|)}{D} \frac{\varepsilon N_t}{1 - i\omega\tau} \frac{v}{D_f} \frac{\exp(ik_f|\mathbf{r} - \mathbf{r}_1|)}{4\pi|\mathbf{r} - \mathbf{r}_1|} d\mathbf{r}_1 \\ &= \frac{v^2 M_0}{DD_f} \frac{\varepsilon N_t}{1 - i\omega\tau} \frac{1}{k^2 - k_f^2} \left[ \frac{\exp(ik|\mathbf{r} - \mathbf{r}_s|)}{4\pi|\mathbf{r} - \mathbf{r}_s|} - \frac{\exp(ik_f|\mathbf{r} - \mathbf{r}_s|)}{4\pi|\mathbf{r} - \mathbf{r}_s|} \right]. \end{aligned} \quad (1)$$

Here  $M_0$  is the excitation source strength.  $k$  is the wavenumber at excitation wavelength  $\lambda_{ex}$  and  $k^2 = (-v\mu_a + i\omega)/D$ .  $D = v/3\mu'_s$  is the photon diffusion coefficient and  $\omega = 2\pi f$  where  $f$  is the modulation frequency. In the presence of fluorophores, the *total* absorption coefficient is the sum of  $\mu_a^c$  due to the *chromophore* and  $\varepsilon N_t$  due to the *fluorophore*, i.e.,  $\mu_a = \mu_a^c + \varepsilon N_t$ .  $N_t$  is the concentration of fluorophore and  $\varepsilon$  is the fluorophore extinction coefficient.  $\tau$  is the fluorophore lifetime.  $k_f$  is the wavenumber and  $D_f$  is photon diffusion coefficient at fluorescence wavelength  $\lambda_{fl}$ . This result differs from the result in reference [2] in that the optical properties at  $\lambda_{ex}$  ( $\mu_a^c$ ,  $\mu'_s$ ) and the optical properties at  $\lambda_{fl}$  ( $\mu_{af}^c$ ,  $\mu'_{sf}$ ) need not be the same.

For an infinite homogeneous medium, one way to measure the fluorophore concentration and lifetime is to measure the FDPDW at multiple frequencies. The experimental data can then be fitted to the analytic solution (Eq.(1)) to get the concentration and lifetime. Fig.(1) shows the theoretical FDPDW data as well as simulated data with 5% amplitude and 5° phase random noise at multiple frequencies 0 - 500 MHz with 50 MHz step. Fitting the noisy data to Eq.(1), we find that the fitted concentration and lifetime are  $N^{fit} = (0.1003 \pm 0.0017) \mu M$  and  $\tau^{fit} = (1.005 \pm 0.016) ns$  while the real concentration and lifetime are  $N = 0.1 \mu M$  and  $\tau = 1.0 ns$ .

The situation for an infinite heterogeneous medium embedded with a spherical object is mathematically more complicated [14]. But the basic idea is the same as for the homogeneous case. We will not write down the complete solutions [14] here, instead we will focus on applications based on analytic solutions, e.g.,



the required fluorophore concentration contrast and lifetime variation to detect an spherical object, and the choice of either absorption or the fluorescence measurement for a given fluorophore.

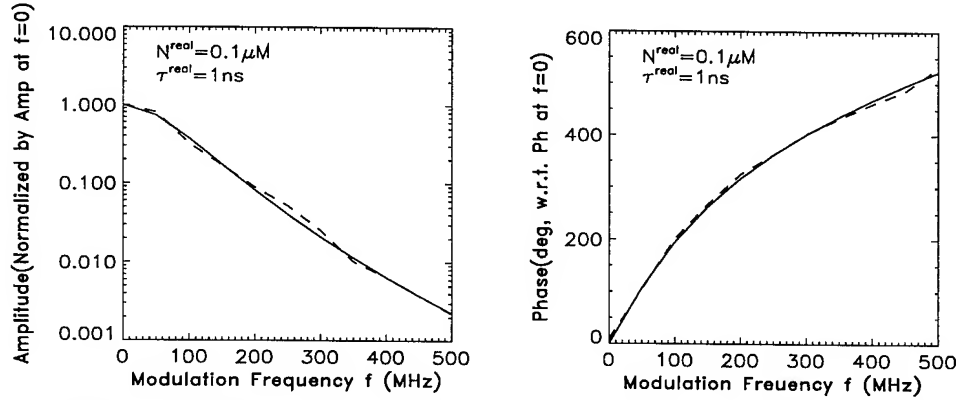


FIG. 1. (a) Amplitude normalized by the amplitude of DC component. (b) Phase shift with respect to DC component. Solid lines are the theoretical amplitude and phase while the dashed lines are the noisy amplitude (5% noise) and phase (5° noise). The source-detector separation is 6 cm and the optical properties ( $\mu_{a1}^c$ ,  $\mu_{s1}^c$ ,  $\mu_{a1f}^c$  and  $\mu_{s1f}^c$ ) are given in Table I. The fitted results are  $N^{fit} = (0.1003 \pm 0.0017) \mu M$  and  $\tau^{fit} = (1.005 \pm 0.016) ns$ .

The variations of fluorophore distribution and lifetime in normal and tumor tissues may give enhanced sensitivity and specificity for tumor detection. Using the analytic solutions, we calculate the amplitude and phase of FDPDW for an infinite heterogeneous system containing a spherical object. Fig.(2) shows the contour plots of the spatially dependent normalized amplitude  $|\phi_{hetero}^{fl}/\phi_{of}|$  and phase difference between  $\phi_{hetero}^{fl}$  and  $\phi_{of}$  in a potentially realistic situation, where  $\phi_{hetero}^{fl}$  [14] and  $\phi_{of}$  (Eq.(1)) are the analytic solution for an infinite heterogeneous and homogeneous system, respectively. We see that 0.5° phase and 1% amplitude measurement precision is sufficient for detection of a 0.6 cm radius object on these length scales (e.g., within ~ 4 cm of the object).

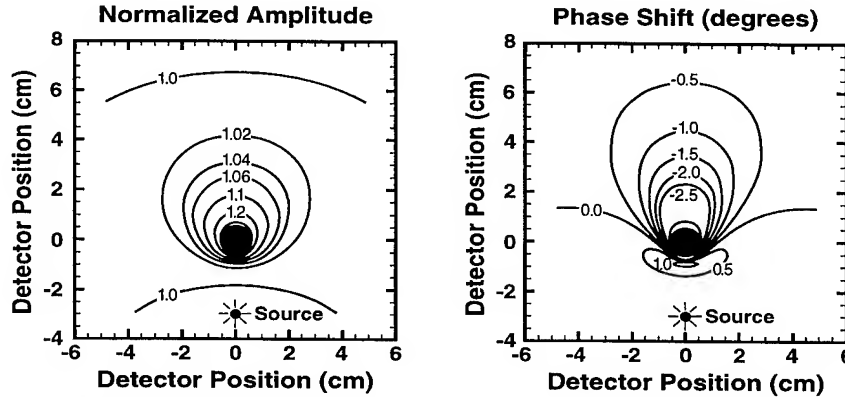


FIG. 2. (a) Contours of the normalized amplitude ( $|\phi_{hetero}^{fl}/\phi_{of}|$ ). (b) Contours of the phase difference between  $\phi_{hetero}^{fl}$  and  $\phi_{of}$ . A 0.6 cm radius object is at the origin and the source is 3 cm away from the object. A detector scans in the source-object plane. The lifetimes of the fluorophore outside ( $\tau_1$ ) and inside ( $\tau_2$ ) the sphere are assumed to be equal (1 ns), and the concentration contrast *Inside/Outside* ( $N_2/N_1$ ) is assumed to be 5. The optical properties and the modulation frequency are given in Table I.

For a heterogeneous medium, we find that ~ 5-fold fluorophore concentration contrast  $N_2/N_1$  and lifetime variation of a factor  $0.2 \leq \tau_2/\tau_1 \leq 1.8$  is sufficient to generate a differential signal above the 0.5° phase and 1% amplitude measurement precision, enabling the detection a 0.5 cm radius object between the source and detector with  $r_{sd} = 6$  cm. Comparing the FDPDW with the excitation DPDW, we find that for smaller fluorophore absorption cross-sections, e.g.,  $\epsilon \leq 6 \times 10^4 cm^{-1} M^{-1}$ , FDPDW gives a better sensitivity, while the excitation DPDW gives a better sensitivity for bigger fluorophore absorption cross-sections, e.g.,  $\epsilon \leq 6 \times 10^4 cm^{-1} M^{-1}$ . We will discuss these basic trends further.

Finally for a semi-infinite homogeneous system, we have found that we can take the solution in an infinite

homogeneous system for a source at  $\mathbf{r}_s$ , the solution for an image source at  $\mathbf{r}_s$ , superpose these two solutions and obtain quite accurate results by confirmation with numerical calculations. The resultant FDPDW for a semi-infinite homogeneous system  $\phi_{0f}^{si}$  is

$$\phi_{0f}^{si}(\mathbf{r}, \mathbf{r}_s) = \phi_{0f}(\mathbf{r}, \mathbf{r}_s) - \phi_{0f}(\mathbf{r}, \mathbf{r}_s), \quad (2)$$

where  $\mathbf{r}_s$  is the position of real source and the  $\mathbf{r}_s$  is the position of image source with respect to the extrapolated zero boundary.  $\phi_{0f}(\mathbf{r}, \mathbf{r}_s)$  and  $\phi_{0f}(\mathbf{r}, \mathbf{r}_s)$  are of the form of Eq.(1).

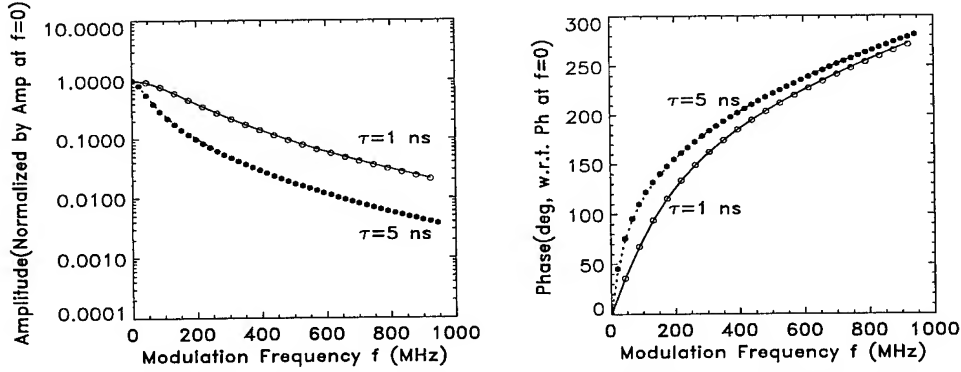


FIG. 3. (a) Normalized amplitude (by the amplitude at  $f = 0$ ). (b) Phase shift (with respect to the phase at  $f = 0$ ). Solid line ( $\tau = 1$  ns) and dashed line ( $\tau = 5$  ns) are the amplitude calculated using Eq.(2). Open circle ( $\tau = 1$  ns) and filled circle ( $\tau = 5$  ns) are the amplitude calculated using finite difference method.

Numerical calculations of FDPDW at different modulation frequencies ( $f$ ) using a finite difference algorithm have been carried out to verify the solution for a semi-infinite homogeneous system (Eq.(2)) for two lifetimes (1 ns and 5 ns). The fluorophore concentration is assumed to be  $N = 0.1 \mu M$ . The source and detector are placed on the surface of the medium with 2 cm separation and the optical properties ( $\mu_{a1}$ ,  $\mu'_{s1}$ ,  $\mu_{a1f}$ ,  $\mu'_{s1f}$ ,  $\epsilon$ ) are given in Table I. Results are shown in Fig.(3) where we plot out the theoretical amplitude and phase calculated by using Eq.(2) and the amplitude and phase calculated using the finite difference method. We find that the analytic solution of FDPDW for a semi-infinite homogeneous system (Eq.(2)) agrees with the finite differencing results, e.g., the amplitude difference is within  $\sim 3\%$  and the phase difference is within  $\sim 1^\circ$ , up to 800 MHz.

TABLE I. Chromophore Optical Properties (in units of  $cm^{-1}$ ) at  $\lambda_{ex}$  and  $\lambda_{fl}$  and Other Parameters (subscript 1-background or homogeneous medium; subscript 2-inside the object

$\mu_{a1}^c$	$\mu'_{s1}$	$\mu_{a2}^c$	$\mu'_{s2}$	$\mu_{a1f}^c$	$\mu'_{s1f}$	$\mu_{a2f}^c$	$\mu'_{s2f}$	$\epsilon(cm^{-1}M^{-1})$	$f(MHz)$	$r_{sd}(cm)$
0.02	8.0	0.04	10.0	0.025	8.0	0.05	10.0	$6 \times 10^4$	200	6

- [1] E. M. Sevick-Muraca and C. L. Burch, Optics Letters, Vol.19, No.23, 1928-1930(1994).
- [2] M. S. Patterson and B. W. Pogue, Applied Optics, Vol.33, No.10, 1963-1974(1994).
- [3] D. A. Boas, M. A. O'Leary, B. Chance and A. G. Yodh, Phys. Rev. E 47, R2999-R3002(1993).
- [4] M. A. O'Leary, D. A. Boas, B. Chance and A. G. Yodh, Journal of Luminescence, Vol.60-1, 281-286(1994).
- [5] J. Wu, Y. Wang, L. Perelman, I. Itzkan, R. R. Dasari and M. S. Feld, Optics Letters, Vol.20, No.5, 489-491(1995).
- [6] X. D. Li, B. Beauvoit, R. White, S. Nioka, B. Chance and A. G. Yodh, Optical Tomography, Photon Migration, and Spectroscopy of Tissue and Model Media: Theory, Human Studies, and Instrumentation, B. Chance and R. R. Alfano, Eds., SPIE Proceedings, Vol.2389, 789-797(1995).
- [7] S. B. Bambot, J. R. Lakowicz and G. Rao, Trends in Biotechnology, Vol.13, No.3, 106-115(1995).
- [8] W. L. Rumsey, J. M. Vanderkooi and D. F. Wilson, Science, Vol. 241, 1649-1651(1988).
- [9] H. Szmazinski and J. R. Lakowicz, Analytical Chemistry, Vol. 65, 1668-1674(1993).
- [10] J. R. Lakowicz, H. Szmazinski, K. Nowaczyk and M. L. Johnson, Cell Calcium, Vol. 13, 131-147(1992).
- [11] C. L. Hutchinson, J. R. Lakowicz and E. M. Sevick-Muraca, Biophysical Journal, Vol. 68, 1574-1582(1995).
- [12] B. J. Tromberg, S. Madsen, C. Chapman, L. O. Svaasand and R. C. Haskell, OSA Proceedings on Advances in Optical Imaging and Photon Migration, R. R. Alfano, Ed, Vol.21, 93-95(1994).
- [13] J. Wu, M. S. Feld and R. P. Rava, Applied Optics, Vol. 32, 3585-3595(1993).
- [14] X. D. Li, M. A. O'Leary, D. A. Boas, B. Chance and A. G. Yodh, accepted for publication, Applied Optics.

## Fluorescence Lifetime Imaging with Frequency-Domain Photon Migration Measurement

Dilip Y. Paithankar and Eva M. Sevick-Muraca

School of Chemical Engineering  
Purdue University  
West Lafayette, IN 47907  
Phone: (317) 496-2739  
Fax: (317) 494-0805  
email: paithan@ecn.purdue.edu

## Introduction

For effective cancer therapy, the oncologist needs information about the local metabolic state, for example, oxygen concentration in the suspected tumor tissue volume. There is a need for imaging techniques that not only provide detection of diseased tissue volumes but also provide additional metabolic information. A class of systemically administered optically active compounds, some of which are already used in photodynamic therapy, can be used as contrast agents to aid in obtaining crucial metabolic information. These compounds or drugs are fluorescent and have excitation and emission in the red and near-infrared spectral region. The lifetime of some of these dyes is strongly dependent on the local quenching environment. The lifetime ( $\tau$ ) dependence on the local metabolite concentration can follow the Stern-Volmer relationship

$$\frac{\tau}{\tau_0} = [1 + k\tau_0[O_2]]^{-1}$$

or other appropriate models describing fluorescence quench kinetics. Thus, a dye or compound whose lifetime is sensitive to the metabolite concentration can be administered to provide metabolic information. If a mapping of lifetime can be achieved, then it would provide metabolic imaging in tissue selectively dependent upon the dye employed. Development of such dyes is an active research area. In this presentation, we describe the algorithms associated with lifetime imaging in tissues.

Measurement of lifetime can be performed using either time- or frequency-domain techniques. Frequency-domain measurements are more robust and convenient and involve launching (into tissue) light whose intensity is sinusoidally modulated. The detected fluorescent light is phase shifted and amplitude demodulated with respect to the incident light. In non-scattering media, lifetime can be calculated as the inverse tangent of the phase lag. In scattering media with uniform optical properties, Hutchinson *et al.* determined that a referencing procedure is required (1). Herein, we describe the complex problem of determining the lifetime in a scattering, heterogeneous medium.

## Fluorescence Lifetime Imaging

The viability of photon migration imaging using re-emission characteristics of only excitation light has already been established by Pogue *et al.* (2), Yodh *et al.* (3), and Barbour *et al.* (4). Each describe a methodology to detect the presence of heterogeneities on basis of contrast due to the absorption coefficient ( $\mu_a$ ) and/or isotropic scattering coefficient ( $\mu'_s$ ) differences. In this section, we describe the computational aspects of image reconstruction based on contrast provided by fluorescence lifetime.

Similar to the work of Pogue *et al.*, our geometry consists of a circular phantom with four intensity modulated light sources as shown in Figure 1. The phase and modulation of the fluorescent light emanating from the object is detected by 20 detectors (relative to each of the sources) uniformly distributed on the periphery of the surface of the phantom.

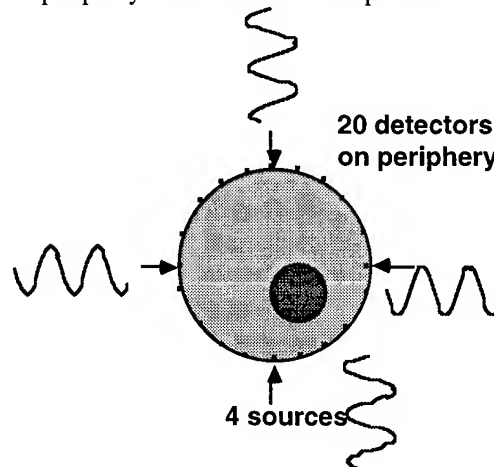


**Figure 1:** Schematic of tissue phantom with a hidden heterogeneity and arrangement of the multiple sources and multiple detectors on the surface.

Reconstruction is performed on a grid that is generated to facilitate numerical evaluation of fluorescent light transport in the object. The forward calculations are performed using a multigrid algorithm to solve the finite difference approximation to the diffusion equation for fluorescent light propagation. In our approach, the Newton-Raphson algorithm is

employed to update the values of lifetime at each grid point of the image, the eventual goal being minimization of the differences between the experimental data and the calculated detector response. This iterative scheme is similar to the one proposed by Yorkey *et al.* (5) for electrical impedance tomography.

#### The forward problem

The spatial and temporal transport of light in tissues or multiply scattered media can be accurately described by the diffusion approximation to the radiative transport equation. The excitation fluence  $\Phi_x(r, \omega)$  and emission fluence  $\Phi_f(r, \omega)$  in the frequency-domain can be predicted at any location  $r$  within the phantom by the diffusion equations (1) and (2) respectively.

$$\nabla \cdot [D_x(r) \nabla \Phi_x(r, \omega)] - \quad (1)$$

$$[\mu_{ax}(r) + i\omega / c_n] \Phi_x(r, \omega) + S_x(r_s, \omega) = 0$$

$$\nabla \cdot [D_f(r) \nabla \Phi_f(r, \omega)] - \quad (2)$$

$$[\mu_{af}(r) + i\omega / c_n] \Phi_f(r, \omega) + S_f(r, \omega) = 0$$

The source term for the excitation light  $S_x(r_s, \omega)$  occurs only at source location  $r_s$  and represents the sinusoidally modulated light at a frequency  $\omega$  where  $\omega$  is usually in the MHz range. The first term in both the equations represents the diffusive or "random-walk" transport of light where  $D$  is the optical diffusion coefficient

$$D = [3(\mu_a + \mu'_s)]^{-1} \quad (3)$$

Subscripts  $x$  and  $f$  denote excitation and fluorescence respectively. The velocity of light in tissue is  $c_n = c/n$  where  $n$  is the average index of refraction. The source term for the fluorescent light is dependent on the excitation light fluence  $\Phi_x(r, \omega)$  by:

$$S_f(r, \omega) = \eta \mu_{ax \rightarrow f} \Phi_x(r, \omega) \frac{1 - i\omega\tau(r)}{1 + \omega^2\tau(r)^2} \quad (4)$$

This term is the Fourier transform of the excitation fluence convoluted by the decay term  $(1/\tau)\exp(-t/\tau)$  in time domain for the fluorescent light. The quantum efficiency is given by  $\eta$  and the absorption coefficient at the excitation wavelength by the fluorophore is given by  $\mu_{ax \rightarrow f}$ .

#### Solution of the forward problem

Both equations (1) and (2) are linear elliptic equations that can be solved for the complex quantities  $\Phi_x(r, \omega)$  and  $\Phi_f(r, \omega)$ . We employ the method of finite differences in which we place a grid over the domain and obtain an approximation to the solution at each grid point. We use a multigrid solution procedure MUDPACK(6). In the solution of the equations, it is assumed that  $\Phi(r, \omega) = 0$  on the tissue surface which is known as the zero fluence boundary condition.

Solutions of equations (1) and (2) yield a

complex number for  $\Phi_f$  at each grid point. The AC intensity, also called the modulation, is given by the magnitude of this number, and the phase by the inverse tangent of the ratio of the imaginary to the real part.

#### Solution of the inverse problem

We begin our inverse calculations from a starting guess of a lifetime map. In the following equations, the modulation measurement is used to illustrate the image reconstruction algorithm and the extension that includes the phase measurement is straightforward. To execute the algorithm, we need the values of the elements of the Jacobian that contain the information about the sensitivity of the detector response to changes in lifetime at each grid point. The

elements of  $J(M, \tau)$ , given by  $j_{i,j} = \frac{\partial M_i}{\partial \tau_j}$  where  $i$  and  $j$

are the detector and grid point labels respectively, are calculated by solving the forward problem twice for each grid point with lifetime  $(\tau)$  and  $(\tau + \Delta\tau)$ . With this information, we can show:

$$\begin{aligned} [J(M, \tau)^T J(M, \tau) + \lambda I] [\Delta\tau] \approx \\ [J(M, \tau)^T (M_{obs} - M_{calc})] \end{aligned} \quad (5)$$

$[\Delta\tau]$  is the change suggested for  $[\tau]$  vector at each iteration.  $M_{obs}$  and  $M_{calc}$  are the observed and calculated modulation vectors at the detectors. We calculate the Jacobian at each iteration. Due to the ill-conditioned nature of the Jacobian matrix, a term  $\lambda I$ , as part of a Tikhonov regularization technique is added. The parameter  $\lambda$  is adjusted via a Marquardt-Levenberg type algorithm (7). Equation (5) is solved by standard numerical methods for simultaneous linear algebraic equations. In practice, the input to the image reconstruction is data of phase-shift and amplitude modulation obtained experimentally. At each iteration, we evaluate the merit function  $\chi^2$  defined as:

$$\chi^2 = \frac{1}{N_d} \sum_{i=1}^{N_d} \left( \frac{M_{obs,i} - M_{calc,i}}{\sigma_M} \right)^2 \quad (6)$$

where  $N_d$  is the total number of detectors for all sources and  $\sigma_M$  is the typical standard deviation of noise. The goal is to minimize  $\chi^2$ .

#### Computational results:

The goal of fluorescence-lifetime imaging is to reconstruct maps of fluorescent lifetime within a tissue or other scattering medium. Pogue *et al.* (1), Yodh *et al.* (3), and Barbour *et al.* (4) have already demonstrated the use of this technique for imaging scattering and absorbing tissue volumes located within a phantom. Here we discuss some of our results obtained for hidden fluorescent objects in a two-dimensional geometry.

We start with a case where there are two hidden heterogeneities of diameter 15 mm each and lifetimes of 1 and 2 ns. The heterogeneities are located in a phantom of 100 mm diameter with background isotropic scattering coefficient of  $1 \text{ mm}^{-1}$  and background fluorescence lifetime of 100 ns. Both background and the hidden heterogeneities have the same value of  $\mu_{ax} \rightarrow f$  and thus the contrast is solely due to the lifetime difference. Frequency-domain measurements are made at a frequency of 150 MHz. The forward problem is solved and the phase and modulation data are obtained. Gaussian noise corresponding to the experimental uncertainty in measuring phase and modulation is added and this data is provided as input into the inverse algorithm.

Figure 2 shows the convergence of the average lifetime in the hidden objects as a function of number of iterations for a starting guess of 0.2 ns.

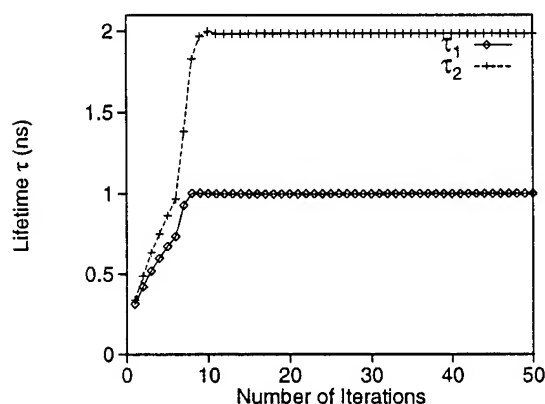


**Figure 2:** Convergence of the individual average lifetimes in the two hidden objects plotted versus number of iterations.

Figure 3 shows the lifetime map in a three-dimensional mesh graph. The actual tissue phantom geometry is circular but is shown as a square to facilitate illustration. These results show excellent agreement between the reconstructed image and the starting model for our simulated test data.

### Conclusions

We have shown that it is possible to perform inverse image reconstruction of lifetime maps in tissues. This has profound impact on optical detection and diagnosis techniques in medicine and science in the future.

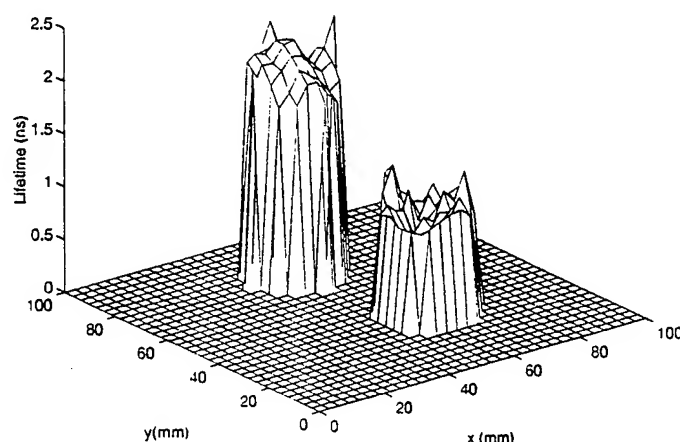


**Figure 3:** Three-dimensional mesh graph showing lifetime at each of the grid points. The background fluorescence lifetime is shown as zero for allowing the reader to discern the lifetimes in the heterogeneities.

### Acknowledgments

We gratefully acknowledge the assistance from Brian Pogue with the solutions to the forward and inverse problems for the excitation light. This work is supported in part by NIH (K04CA68374 and CA61413).

### References

- (1) Hutchinson C.L., Troy, T.L., and Seveck-Muraca, E.M., "Fluorescence-Lifetime Determination in Tissues or other Scattering Media from Measurement of Excitation and Emission Kinetics", *Applied Optics* (in press).
- (2) Pogue B.W., Patterson, M.S., Jiang, H., and Paulsen, K.D., "Initial assessment of a simple system for frequency domain diffuse optical tomography", to appear in *Physics in Medicine and Biology* (1995).
- (3) Boas, D.A., O'Leary, M.A., Chance, B., and Yodh, A.G., *Proc. Natl. Acad. Sci. USA*, **91**, 4887 (1994).
- (4) Barbour, R.L., Graber, H.L., Wang, Y., Chang, J.-H., and Aronson, R., *SPIE series*, **IS11**, 87(1993).
- (5) Yorkey, T.J., Webster, J.G., Tompkins, W.J., *IEEE Trans. Biomed. Eng.*, **34**, 843 (1987).
- (6) Adams, J.C., *Appl. Math. Comp.*, **34**, 133 (1989).
- (7) Press, W.H., Teukolsky, S.A., Vetterling, W.T., and Flannery, B.P., "Numerical Recipes: The Art of Scientific Computing", Cambridge University Press, New York, 1992.

## Concentration and Lifetime Images of Fluorescent Turbid Media

M. A. O'Leary<sup>\*†</sup>, D. A. Boas<sup>\*†</sup>, X. D. Li<sup>\*†</sup>, B. Chance<sup>†</sup>, and A. G. Yodh<sup>\*</sup>

<sup>\*</sup>Department of Physics, <sup>†</sup>Department of Biochemistry and Biophysics,  
University of Pennsylvania, Philadelphia, PA 19104  
phone: (215) 898-4387 fax: (215) 898-2010

The lifetime and number density of fluorophores in human tissue can potentially provide information about tissue oxygenation, pH, and glucose [1]. Tissue fluorescence measurements are generally made using fluorophores at or near the surface [2]; only recently have investigators begun to develop the methods needed to extract the fluorophore lifetime information from deep within heterogeneous turbid media [3-7]. Thus far, diffuse fluorescence in deep tissues has been primarily explored as a means of tumor detection by locating the center of fluorescing objects [8-10]. This approach relies on the fact that the fluorophore will preferentially accumulate in tumors in comparison to background tissues [12]. In this paper we demonstrate a method whereby one can simultaneously derive a spatial map of the concentration and lifetime of heterogeneous fluorophore distributions, using variations in the amplitude and phase of fluorescent diffuse photon density waves.

The propagation of photons through a highly scattering media with low absorption is well described by the diffusion equation [11]. Within the diffusion approximation, if fluorophores with lifetime  $\tau$  are embedded within a turbid medium, the fluorescent photon density,  $U_{fl}$ , measured at a detector position  $\mathbf{r}_d$  (for a source at the origin) is [13]

$$U_{fl}(\mathbf{r}_d, \omega, k^{\lambda_1}, k^{\lambda_2}) = \int d^3r U(\mathbf{r}, k^{\lambda_1}) \frac{\eta(\mathbf{r})}{1 - i\omega\tau(\mathbf{r})} \frac{v}{D^{\lambda_2}} G(\mathbf{r}_d - \mathbf{r}, k^{\lambda_2}). \quad (1)$$

The wavenumber  $k^{\lambda_1}$  ( $k^{\lambda_2}$ ) depends on the optical properties of the medium at the excitation (fluorescent) wavelength  $\lambda_1$  ( $\lambda_2$ ). Eq. 1 has three pieces,  $U(\mathbf{r}, k^{\lambda_1})$  represents the excitation wave to the fluorophore at  $\mathbf{r}$ ,  $\eta(\mathbf{r})/(1 - i\omega\tau(\mathbf{r}))$  represents the demodulation and phase shift due to the strength and lifetime of the fluorophore, and  $vG(\mathbf{r}_d - \mathbf{r}, k^{\lambda_2})/D^{\lambda_2}$  represents the demodulation and phase shift due to passage of the reradiated wave from  $\mathbf{r}$  to the detector at  $\mathbf{r}_d$  [9].  $\eta$  is the product of the fluorophore absorption coefficient and fluorescence quantum yield. One typically makes simplifying approximations for  $U$  and  $G$  in order to perturbatively solve (1) in heterogeneous media. In particular,  $U$  is replaced by  $U_o$ , the incident, unperturbed excitation wave in the homogeneous background media and  $G$  is treated similarly as an unperturbed fluorescent diffusive wave. In principle  $U_o$  and  $G$  may be updated to include the effects of heterogeneities. The model also assumes that there are no saturation or photon quenching effects.

The fluorescence model in eq. 1 is of the same form as the first order perturbation model for a scattering medium with inhomogeneous absorption [14]. Thus it should be feasible to generate images for  $\eta(\mathbf{r})$  and  $\tau(\mathbf{r})$  using standard imaging algorithms. (The reconstruction differs from the pure absorption case in that the reconstructed quantity is now complex, and is a function of the modulation frequency). We demonstrate this idea in the present paper using simulated data.

In this work, computer generated data are obtained from exact solutions to eq. 1 for the case of a fluorescent sphere in a uniform background [15]. Using forward amplitude and phase data from this solution (with added 1% amplitude and 0.1° phase noise), we have reconstructed images of  $\eta$  and  $\tau$ . The measurement geometry and simulation details are described in fig. 1a. In the first set of reconstructions all fluorophores are located in the object and there is no background fluorescence. In fig. 1b and d we demonstrate a reconstruction proportional to the fluorophore concentration with source modulation frequencies of 50 and 150 MHz respectively.

In the course of implementing these reconstructions we found that some isolated voxels had unphysically high values for both  $\eta$  and  $\tau$ . However, these voxels do not contribute significantly to the total signal since the quantity  $\eta/\omega\tau$  is comparable to or smaller than that of the neighboring voxels. As part of our image analysis, we identified these voxels and replaced  $\eta$  and  $\tau$  with the nearest neighbor averages. The object size was determined by including any voxel with fluorophore concentration of at least 50% of the maximum fluorophore concentration. The lifetime reported was the average lifetime of these voxels. figs. 2c,e (squares) exhibit good agreement between the average reconstructed value of the lifetime and its known value. Generally, we found that the lifetime reconstructions are more accurate at low source modulation frequencies where the occurrence of these spurious voxels is less frequent, and the intrinsic phase shift due to the lifetime of the fluorophore ( $\phi = \tan^{-1}(\omega\tau)$ ) is far from its saturation value ( $\pi/2$ ).

The image quality is improved if some *a priori* information is given. For example, if the fluorophore distribution is known, then we may focus solely on the lifetime inversion. Possible ways of determining the fluorophore density distribution include using the excitation wave at a high modulation frequency, or use of the zero modulation frequency fluorescence data. The results of the lifetime only reconstruction are shown in fig. 1c,e (circles).

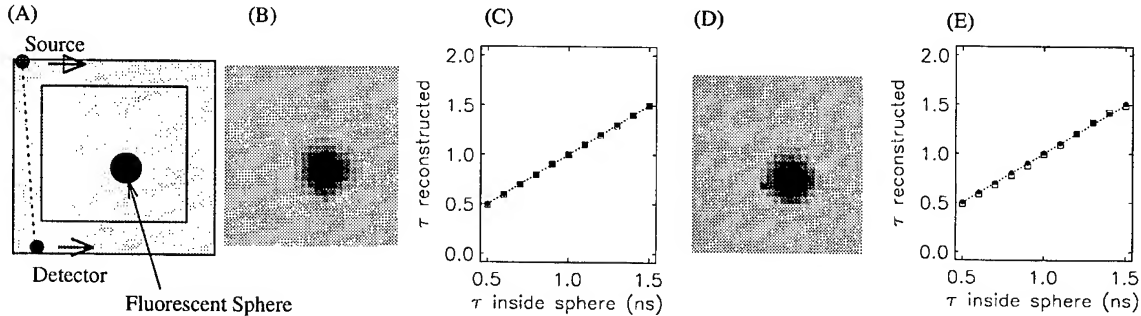


FIG. 1. (A) The scanning geometry consists of a source and detector scanning every 0.2 cm around the four sides of a 7.0 cm x 7.0 cm square in an infinite medium. The reconstruction area is a slab of area 5.0 cm x 5.0 cm and height 1.0 cm. The optical properties of the media are:  $\mu'_s = 10 \text{ cm}^{-1}$  everywhere,  $\mu_a$  (chromophore) =  $0.03 \text{ cm}^{-1}$  everywhere for both the excitation and the emission wavelength, and  $\mu_a$  (fluorophore - inside the sphere) =  $0.02 \text{ cm}^{-1}$  at the excitation wavelength, and  $0.01 \text{ cm}^{-1}$  at the emission wavelength. The source modulation frequency is 50 MHz. (B) The reconstruction of the fluorophore concentration for the system described in part A. The lifetime inside the 1.0 cm diameter sphere is 0.6 ns. The grey scale ranges from  $0 \text{ cm}^{-1}$  (white) to  $0.007 \text{ cm}^{-1}$  (black). 2500 SIRT iterations were performed with a constraint on both concentration ( $0.0 \leq \eta \leq 0.1 \text{ cm}^{-1}$ ) and lifetime ( $0 \leq \tau \leq 10 \text{ ns}$ ). (C) Using this setup, the actual lifetime of the fluorophore is varied from 0.5 ns to 1.5 ns, and the average reconstructed lifetime is calculated. The squares are derived from a reconstruction of both fluorophore concentration and lifetime and the circles are derived from the lifetime reconstruction only. Panels (D) and (E) are the same as (B) and (C) except the source modulation frequency has been increased to  $f = 150 \text{ MHz}$ . The greyscale in panel (D) ranges from  $0 \text{ cm}^{-1}$  (white) to  $0.009 \text{ cm}^{-1}$  (black).

In typical clinical situations, there will be a fluorophore throughout the system. In this case we separate the contributions from inside and outside the heterogeneous region, i.e.

$$U_{fl}(\mathbf{r}_s, \mathbf{r}_d, \omega, k^{\lambda 1}, k^{\lambda 2}) = \int_{\text{all space}} d^3r U_o(\mathbf{r} - \mathbf{r}_s, k^{\lambda 1}) \frac{\eta_o}{1 - i\omega\tau_o} \frac{v}{D^{\lambda 2}} G(\mathbf{r}_d - \mathbf{r}, k^{\lambda 2}) + \int_{\text{heterogeneity}} d^3r U_o(\mathbf{r} - \mathbf{r}_s, k^{\lambda 1}) \left[ \frac{\eta(\mathbf{r})}{1 - i\omega\tau(\mathbf{r})} - \frac{\eta_o}{1 - i\omega\tau_o} \right] \frac{v}{D^{\lambda 2}} G(\mathbf{r}_d - \mathbf{r}, k^{\lambda 2}). \quad (2)$$

Here  $\eta_o$  and  $\tau_o$  are the fluorescence properties outside the heterogeneity and  $\eta$  and  $\tau$  are the fluorescence properties inside the heterogeneity. Hereafter we will refer to the first term on the right hand side of eq. 2 as  $U_{bg}$ . If the object contrast is high, i.e.  $\eta(\mathbf{r})/(1 - i\omega\tau(\mathbf{r})) \gg \eta_o/(1 - i\omega\tau_o)$ , then the fluorescent signal due to the heterogeneity,  $\Delta U_{fl} = U_{fl} - U_{bg}$ , is given by

$$\Delta U_{fl}(\mathbf{r}_s, \mathbf{r}_d, \omega, k^{\lambda 1}, k^{\lambda 2}) = \int d^3r U_o(\mathbf{r}, k^{\lambda 1}) \frac{v\eta(\mathbf{r})}{1 - i\omega\tau(\mathbf{r})} \frac{v}{D^{\lambda 2}} G(\mathbf{r}_d - \mathbf{r}, k^{\lambda 2}). \quad (3)$$

Eq. (3) may be used to generate an image of  $\eta(\mathbf{r})$  and  $\tau(\mathbf{r})$  under these circumstances. To accomplish this subtraction, one may use analytic solutions for  $U_{bg}$  [15]. However this method requires knowledge of the background lifetime and concentration, which may not be possible in clinical situations. Another option is to eliminate the background signal by subtracting two measurements having the same source-detector separation, as shown in fig. 2a. In these *difference* measurements, the background (homogeneous) fluorescent contribution will cancel, and only the inhomogeneous part will remain. Note that in these images the fluorescent properties of the *heterogeneities* are reconstructed; no information about the background fluorescence is derived. This method has been employed successfully in absorption reconstructions to reduce the importance of accurate knowledge of the background optical properties [14].

In this work, computer generated data are obtained from exact solutions to eq. 1 for the case of a fluorescent sphere in a uniform background [15]. Using forward amplitude and phase data from this solution

(with added 1% amplitude and  $0.1^\circ$  phase noise), we have reconstructed images of  $\eta$  and  $\tau$ . Fig. 2a depicts the scanning geometry used for a system with fluorophore both inside and outside of the sphere (radius = 0.75 cm). Images of concentration heterogeneities are shown in fig. 2b and d using source modulation frequencies of 50 and 150 MHz respectively. The average reconstructed lifetime calculated over the area of the sphere is plotted in fig. 2c,e for a series of reconstructions for objects with different lifetimes inside the sphere.

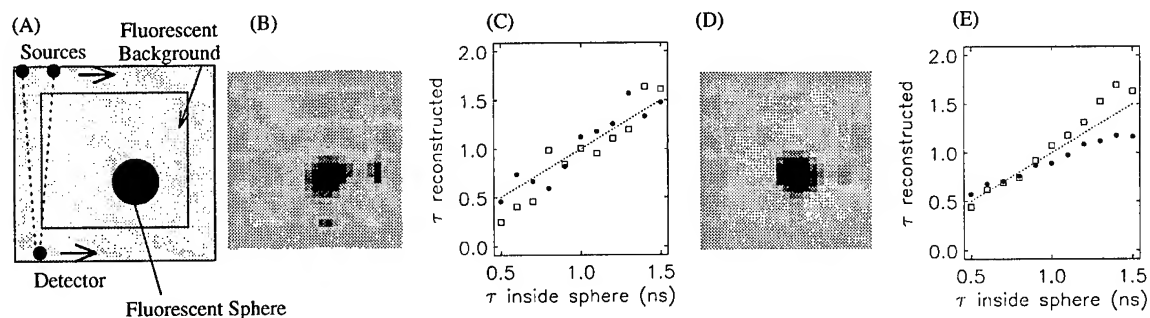


FIG. 2. (A) The scanning geometry for a system with background fluorophore.  $\mu_a$  of the background fluorophore =  $0.001 \text{ cm}^{-1}$  at the excitation wavelength, and  $0.0005 \text{ cm}^{-1}$  at the emission wavelength and the lifetime is 1.0 ns. The setup is the same as in fig. 1, part (A) with the addition of the background fluorophore and a second source 0.6 cm from the first. (B) The reconstruction of the heterogeneous fluorophore distribution for the system described in part A. The lifetime inside the 1.5 cm diameter sphere is 0.6 ns. The grey scale ranges from  $0 \text{ cm}^{-1}$  (white) to  $0.017 \text{ cm}^{-1}$  (black). 2500 SIRT iterations were performed with a constraint on both concentration ( $0.0 \leq \eta \leq 0.1 \text{ cm}^{-1}$ ) and lifetime ( $0 \leq \tau \leq 10 \text{ ns}$ ). (C) The average reconstructed lifetime for a series of reconstructions using the setup in part (A). The squares are derived from a reconstruction of both fluorophore concentration and lifetime. The circles are derived from the lifetime reconstruction only. Panels (D) and (E) are the same as (B) and (C) except the source modulation frequency has been increased to  $f = 150 \text{ MHz}$ . The greyscale in panel (D) ranges from  $0 \text{ cm}^{-1}$  (white) to  $0.020 \text{ cm}^{-1}$  (black).

We have presented and demonstrated an algorithm by which the heterogeneous fluorophore distribution and lifetime in a turbid medium may be obtained from tomographic measurements of near infra-red diffusing photon distributions. The solution for finite systems may be obtained by applying the appropriate boundary conditions. Such solutions are readily available for a variety of geometries [16].

- [1] S. B. Bambot, J. R. Lakowitz and G. Rao, Trends in Biotechnology, **13**(3), p 106 (1993).
- [2] D. W. Piston, M. S. Kirby, H. P. Cheng, W. J. Lederer, W. W. Webb, Applied Optics **33**(4) p 662 (1994).
- [3] E. M. Sevick-Muraca, C. L. Burch, Optics Letters **19**(23) p 1928 (1994). See also C. L. Hutchinson, T. L. Troy, and E. M. Sevick-Muraca *Proceedings of Optical Tomography, Photon Migration, and Spectroscopy of Tissues and Model Media: Theory, Human Studies, and Instrumentation*, B. Chance and R. R. Alfano ed, Proc. SPIE 2389, p 274 (1995).
- [4] M. S. Patterson, B. W. Pogue, Applied Optics **33**(10), p 1963 (1994).
- [5] B. J. Tromberg, S. Madsen, C. Chapman, L. O. Svaasand, R. C. Haskell, OSA Procs. on Advances in Optical Imaging and Photon Migration, R. R. Alfano ed., Optical Society of America, Washington DC, **21**, p 93 (1994).
- [6] A. J. Durkin, S. Jaikumar, N. Ramanujam, and R. Richards-Kortum, Applied Optics, **33**(3), p 414 (1994).
- [7] J. Wu, M. S. Feld and R. P. Rave, Applied Optics, **32**(19), p 3585 (1993).
- [8] A. Knüttel, J. M. Schmitt, R. Barnes and J. R. Knutson, Rev. Sci. Instrum. **64**(3), p 638 (1993).
- [9] M. A. O'Leary, D. A. Boas, B. Chance and A. G. Yodh, Journal of Luminescence, **60-61**, p 281 (1994), D.A. Boas, M.A. O'Leary, B. Chance, A.G. Yodh, Phys. Rev. E **47**, p R2999 (1993).
- [10] J. Wu, Y. Wang, L. Perelman, I. Itzkan, R. R. Desari and M. S. Feld, Optics Letters, **20**(5), p 489 (1995).
- [11] M. S. Patterson, B. Chance, B. C. Wilson, Applied Optics, **28**(12), p 2331 (1989).
- [12] X. D. Li, B. Beauvoit, R. White, S. Nioka, B. Chance, A. G. Yodh, *Proceedings of Optical Tomography, Photon Migration, and Spectroscopy of Tissues and Model Media: Theory, Human Studies, and Instrumentation*, B. Chance and R. R. Alfano ed, Proc. SPIE 2389, p 789 (1995).
- [13] Eq. 1 is the fourier transform of the time-domain equation presented by Sevick-Muraca *et al.* [3], and has been presented in a similar form by Patterson *et al.* [4]. Also see [5,9].
- [14] M. A. O'Leary, D. A. Boas, B. Chance, and A. G. Yodh, Optics Letters, **20**(5), p 426 (1995)
- [15] X. D. Li, M. A. O'Leary, D. A. Boas, B. Chance and A. G. Yodh, *accepted for publication, Applied Optics*.
- [16] S. R. Arridge, M. Cope, D. T. Delpy, Phys. Med. Biol. **37**(7) (1992).



Friday, March 22, 1996

## Dyes and Reporters in *In Vivo* I

**BFA** 8:30 am-10:35 am  
Windsor Ballroom

Eva Sevick-Muraca, *Presider*  
*Purdue University*

## Dye-Oligonucleotide Conformational Structures Studied by Satellite Holes

Ta-Chau Chang and Chien-Chih Chiang

Institute of Atomic and Molecular Sciences, Academia Sinica  
P.O. Box 23-166, Taipei, 10764, Taiwan  
Telephone: 8862-3668231, Fax: 8862-3620200  
e-mail: tcchang@po.iam.s.sinica.edu.tw

Here we illustrate that the satellite holes (SH) in the nonphotochemical hole burned (NPHB) spectra provide a new powerful method to investigate the interaction and conformational structure of dye-oligonucleotide complexes. The main theme of this work is the demonstration of the importance of SH for monitoring the chromophore-oligonucleotide interaction since the hole frequency, the width, and the structure of SHs (vibronic zero-phonon holes) are sensitive to microscopic perturbations of the localized interaction. The advantage of the NPHB than other spectroscopic methods is that the hole produced is persistent, which can serve as probe for monitoring the local interaction. In this work, we have performed the NPHB of a 4,4-difluoro-5-(4-phenyl-1,3-butadienyl)-4-bora-3a,4a-diaza-s-indacene-3-propionic acid, succinimidyl ester (BODIPY) molecule chemically bound to the oligonucleotide with two bases of guanosine deoxyribonucleotide followed by eight bases of thymidine deoxyribonucleotide (BODIPY-d(G<sub>2</sub>T<sub>8</sub>)). In the sample preparation of BODIPY-d(G<sub>2</sub>T<sub>8</sub>), two major eluents are collected at retention time of 24 min (BODIPY-d(G<sub>2</sub>T<sub>8</sub>)-A) and 35 min (BODIPY-d(G<sub>2</sub>T<sub>8</sub>)-B) in HPLC purification. The absorption of oligonucleotide at 260 nm and that of BODIPY at 590 nm are observed for both eluents. Figures 1a-1b show the hole burned spectra of BODIPY-d(G<sub>2</sub>T<sub>8</sub>)-A at  $\lambda_B$  = 580 nm and 560 nm by using pulse energies of  $\sim 2 \mu\text{J}$  and  $\sim 5 \mu\text{J}$  and the burning time of 5 min and 10 min, respectively. It is found that both spectra are very similar to the spectra of BODIPY-d(T<sub>10</sub>) [1]. Figures 1c-1d show the hole burned spectra of BODIPY-d(G<sub>2</sub>T<sub>8</sub>)-B at  $\lambda_B$  = 588 nm and 560 nm by using pulse energies of  $\sim 2 \mu\text{J}$  and  $\sim 5 \mu\text{J}$  and the burning time of 5 min and 20 min, respectively. However, these spectra are similar to the spectra of free BODIPY [2]. Different spectral features of these two eluents suggest that the BODIPY can interact with the oligonucleotides in more than one manner.

The BODIPY molecule contains a BF<sub>2</sub> functional group, the strong electronegativity of the F atom allows it to form an intermolecular hydrogen bond with PVOH and an intramolecular hydrogen bond with oligonucleotide. The intense SH at 424 cm<sup>-1</sup> is previously assigned to the bending vibration of the B-F bond [2]. In addition, the disappearance of the 1135 cm<sup>-1</sup> SH and the occurrence of the 1095 cm<sup>-1</sup> and 1050 cm<sup>-1</sup> SHs suggest that the 1135 cm<sup>-1</sup> SH corresponds to the stretching frequency of the BF mode [1]. The hole broadening of the BF bending mode shown in figure 1a and the line shifting of the BF stretching mode in figure 1b are attributed to the formation of an intramolecular hydrogen bond between BODIPY and oligonucleotide. The similarity of other SHs reveals that not all vibrational modes of BODIPY are perturbed by intramolecular hydrogen bond effect, but primarily those modes are associated with the formation of intramolecular

hydrogen bond. Hence, this work establishes that the spectral features of SHs can be used to investigate the hydrogen bond effect in the dye-DNA complexes.

Similar hole burned spectra of BODIPY-d(G<sub>2</sub>T<sub>8</sub>)-B and free BODIPY imply that the BODIPY molecule sits outside the oligonucleotide [3]. However, the presence of intramolecular hydrogen bond in BODIPY-d(G<sub>2</sub>T<sub>8</sub>)-A indicates that a loop is formed between the BODIPY and oligonucleotide. The BODIPY molecule does not sit outside the oligonucleotide. This conjecture may be supported by the different retention time in HPLC, which a longer retention time is taken for a hydrophobic compound than a hydrophilic compound. The mobility of BODIPY-d(G<sub>2</sub>T<sub>8</sub>)-A is better than that of BODIPY-d(G<sub>2</sub>T<sub>8</sub>)-B in HPLC because the BODIPY molecule is hydrophobic and it sits outside the oligonucleotide of BODIPY-d(G<sub>2</sub>T<sub>8</sub>)-B. Our results indicate that the spectral features of satellite holes can be used to identify various conformational structures formed during the sample preparation. The formation of intramolecular hydrogen bonding is essential in determining the dye-oligonucleotide conformation structures. In addition, quantitative measurement of these conformational components can be measured from the HPLC spectra.

#### Reference:

1. Chang, T.-C.; Chiang, C. C.; Wang J. H.; Cheng, J. Y.; Cheng, Y. R.; Chen, H. S.; Peck, K. submitted to *J. Phys. Chem.* 1995.
2. Chiang, C. C.; Wang, J. H.; Cheng, J. Y.; Chang, T.-C. *Chem. Phys. Lett.* **1995**, 239, 95.
3. Chang, T.-C.; Chiang, C. C.; Chou, S. H.; Peck, K. *J. Phys. Chem.* **1995**, 99, 6620.

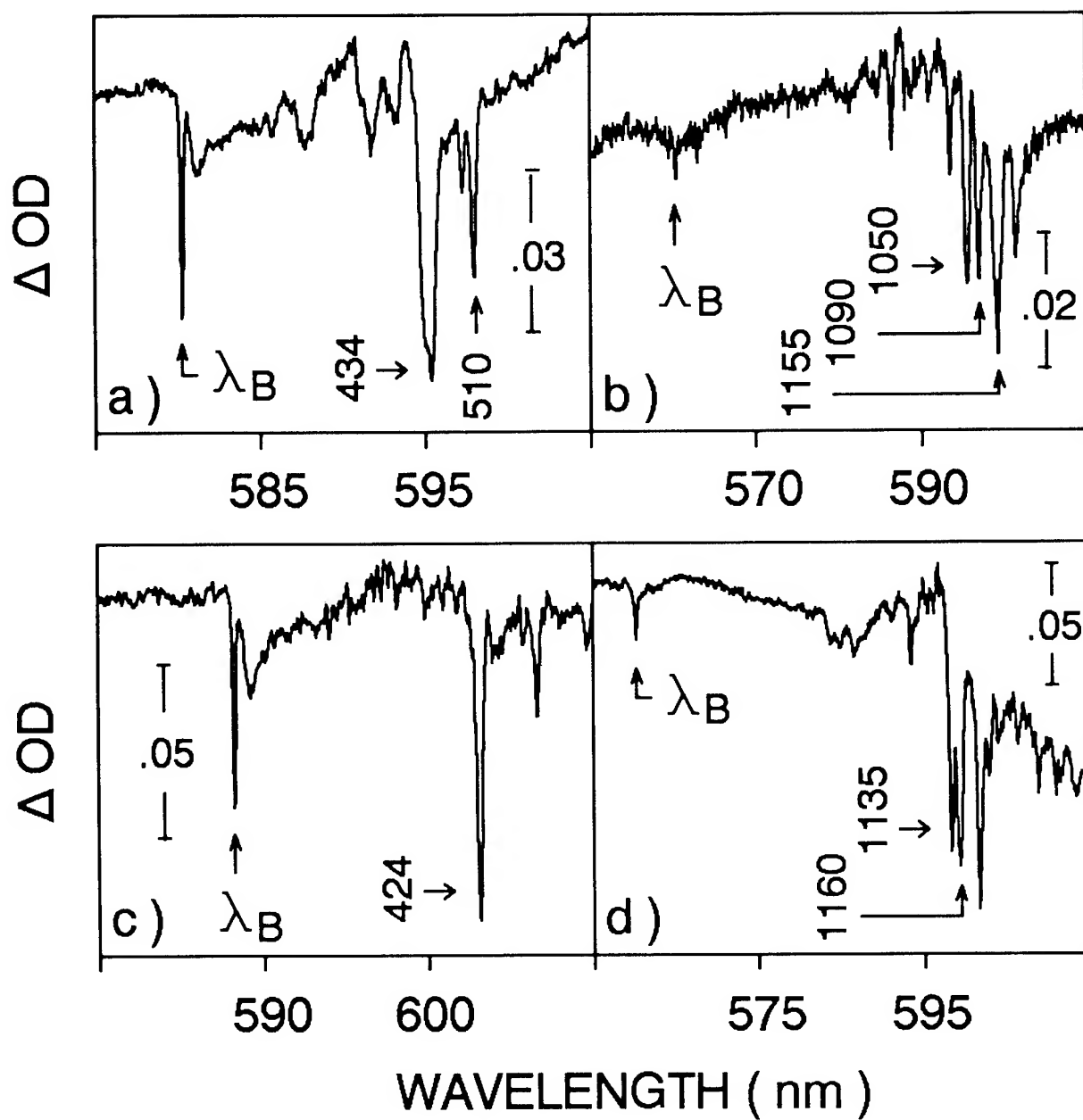


Figure 1. Hole burned spectra of BODIPY-d(G 2T<sub>8</sub>)-A at  $\lambda_B$ : a) 582 nm and b) 560 nm. Hole burned spectra of BODIPY-d(G 2T<sub>8</sub>)-B at  $\lambda_B$ : c) 588 nm and d) 560 nm. Several satellite holes are labeled with excited state vibrational frequencies.

## Photonic Monitoring of Infectious Disease and Gene Regulation

Christopher H. Contag  
Stanford University

**I. Overview:** Noninvasive assays for monitoring the progression of infectious agents and other biological processes, such as transcriptional regulation, in the living intact animal are needed to advance our understanding of host-pathogen interactions and gene regulation. Key molecules in these processes may not possess distinguishing features that allow them to be monitored from an external vantage point, and therefore analyses have been limited to *ex vivo* assays conducted in the absence of contextual influences of the intact animal. Reporter genes that encode proteins with unique characteristics are used widely to label biological processes. Successful use of light to monitor biological processes *in vivo* suggested that an optical method for evaluating of infectious disease processes and gene regulation in living mammals may be possible.

Transmission of light through opaque tissues *in vivo* has been used for noninvasive optical imaging and spectroscopy in animals and humans (1-4). Furthermore localization of photons, from bioluminescent molecules, transmitted through plant tissue has been used to quantitatively monitor gene expression (10, 12, 13). Similarly macroscopic (8) and microscopic (7) imaging of luciferase expression in mammalian cells in culture has been used to assay promoter activity. External imaging of an internal light source through a scattering medium (such as mammalian tissue) has not been previously described, however, it seemed likely that an intracellular bioluminescent source could have sufficient intensity to penetrate animal tissues provided that this endogenous light has a wavelength between 500 and 1500 nm. At these wavelengths tissue is relatively non-absorbing.

We determined that photons from luciferase penetrate animal tissue to an extent that photons emitted from internal organs can be externally monitored. We have used bioluminescent proteins to confer bioluminescence as a distinguishing characteristic of bacterial pathogens and of a viral transcriptional promoter. Bioluminescent light from originating from inside living mice was used to monitor disease progression in susceptible and resistant strains of mice, and the activity of the viral transcriptional promoter in transgenic animals.

**II. Infectious Disease:** The route that a pathogen takes in the infection of a living organism is influenced by both the features of the pathogen and of the host and therefore may best be studied in the context of the host. Infection of mice with *Salmonella typhimurium* is a well characterized animal model of infectious disease and was therefore, selected as the model with which to initially develop this bioluminescent technology. A wide variety of *Salmonella* strains that differ in their pathogenic potential in mice that have been characterized (16). In the present study, the phenotype of three *Salmonella* strains, with respect to adherence and entry, were confirmed in a modified cell culture assay, and subsequently evaluated in infected mice. These included the wildtype strain named SL1344 which is invasive in culture and virulent in mice (6), a less-invasive mutant of SL1344, named BJ66, with altered virulence in mice (9), and a low-virulence LT2 strain named LB5000 (16). These strains of *Salmonella* were selected to represent a broad range of virulence in susceptible strains of mice.

Bacterial luciferases are heterodimeric mixed-function oxidases that emit photons during the energetic catalysis of substrate and appeared to be a suitable source of bioluminescence for localizing pathogens in living hosts. Two genes encoding the heterodimeric luciferase from the soil bacterium *Photobacterium luminescens* (also called *Xenorhabdus luminescens*) are located on an operon along with genes that encode enzymes for biosynthesis of the fatty aldehyde, decanal, the substrate for bacterial luciferases ((5, 11, 19). A characterized plasmid encoding the entire *lux* operon from *P. luminescens* confers on *E. coli* the ability to emit photons at a wavelength of 486 nm in aerobic environments (5). Optimal bioluminescence for these transformed *E. coli* occurs at 37° C (17, 19), in contrast to the low temperature optima of luciferases from eukaryotic and other prokaryotic bioluminescent organisms (5). The luciferase from *P. luminescens* also demonstrates high thermal stability as compared to other bacterial luciferases (17). Thus, this luciferase appeared to be ideally suited for studying biological events in mammalian systems, and was used in the analysis of *Salmonella* infection of mice.

Susceptible BALB/c mice inoculated with three bioluminescent *Salmonella* strains, and resistant, BALB/c x 129, mice inoculated with the bioluminescent wild-type strain were evaluated by external monitoring of transmitted photons. We demonstrated that bioluminescent light generated within a pathogen can be transmitted through the tissue of an animal infected with that pathogen, thus allowing localization of the bacteria to specific body sites. In this manner, a progressive course of infection was distinguished from persistent or abortive infections, and efficacy of antibiotic treatment was noninvasively monitored in real time. The distribution of bioluminescence suggested that the cecum may be a site of *Salmonella* infection at which the critical events resulting systemic infection may occur.

The method that we describe facilitates understanding infectious processes through learning the tempo of the disease course and the spatial distribution of pathogens in living animals. Knowing the temporal and spatial distribution of pathogens and the affects of anti-infective agents on these distributions will greatly enhance our ability to intervene in disease processes. This study opens a window into the biology of infectious disease that will shed light on how bacteria, viruses and fungi overtake their host.

### III. Gene regulation

a. General: The use of reporter genes in transgenic animals has contributed greatly to our understanding of how genes are expressed *in vivo*. However, the reporter systems currently employed require *ex vivo* assays limited to post mortem analyses. We have adapted our method of localizing expression of bioluminescent reporter genes in living mice to the study of gene regulation for real-time analyses in living animals. Regulation of gene transcription is mediated by complex interactions among positive and negative regulatory elements that are ultimately directed by the environment of the cell. Studies of gene regulation in mammalian cells are often performed on cells from culture in the absence of contextual influences of the entire organism. A greater understanding of how specific promoters respond to stimuli associated with the development of the organism or to insult due to infection would be gained through analysis of promoter activity in living organisms over time. Using this approach, localization of active promoters can be temporally assessed in the context of the living intact animal, with the potential for analyses under both pathogenic and normal conditions or during the course of development.

Luciferase from firefly has been most widely used in promoter fusion studies, and in fact transgenic mice engineered with promoter-luciferase fusions have been reported (14, 15). In studies involving these animals the luciferase assay was performed on cell lysates from biopsy tissues. We selected the transcriptional promoter of HIV-1 (long terminal repeat, LTR, of the virus) for our initial studies due to its known expression in the skin when present in cells of transgenic mice. In these transgenic animals the HIV-1 LTR is placed in front of the firefly luciferase gene (14). The LTR is inducible with a variety of chemical and physical treatments, including topical application of dimethyl sulfoxide (DMSO) (15) thus, the HIV-1 promoter provides a genetic light switch in murine cells. In human T cells the expression from the LTR is dependent on a viral protein, Tat, and as such in human cells expressing the LTR-luciferase construct infected cells glow and the uninfected cells do not. We have assayed HIV-1 replication in cells in culture using the expression of Tat from the live virus to activate luciferase expression. A similar cell line has previously been used in single cell analysis (18).

The transition from labeled bacterial cells and cells in cultures to expression of luciferase genes in mammalian cells and *in vivo* detection required analysis of a eucaryotic luciferase *in vivo* and exogenous delivery of the substrate luciferin (the substrate for the bacterial luciferase is synthesized within the bacterial cells and therefore, did not need to be supplied exogenously). We have induced the expression of luciferase in transgenic mice using a topical treatment of DMSO, and delivered luciferin either systemically or topically. Our results indicated that luciferase expressed from the transgene present in skin cells of mice can be detected using an intensified CCD camera (Hamamatsu Corp., Japan). Regional activation of the LTR-luciferase construct was apparent. Photon emission from cells in the liver was also detected in mice given luciferin systemically. The two modes of luciferin delivery and the fact that photons originating from cells deep inside the animal indicate that tissue-specific promoters of many types expressed in a variety of different tissues may be studied in small laboratory animals using this approach.

IV. Discussion: Our approach opens a window through which gene regulation and progression of infectious diseases can be viewed *in vivo*, thus illuminating temporal and spatial distribution of these

biological processes. These studies demonstrate that real time noninvasive analyses of pathogenic events, pharmacologic monitoring and assessment of promoter activity can be performed *in vivo*.

**Acknowledgments:** We thank Hamamatsu Corporation for the use of their intensified CCD camera that was used to obtain much of the data in this report.

1. Benaron, D., and D. K. Stevenson. 1993. Optical time-of-flight and absorbance imaging in biological media. *Science*. **259**:1463-1466.
2. Benaron, D. A., G. Muller, and B. Chance. 1993. A medical perspective at the threshold of clinical optical tomography., p. 3-9. *In* G. Muller and B. Chance and R. Alfano and e. al. (ed.), *Medical Optical Tomography: Functional Imaging and Monitoring*. SPIE Press, Bellingham, WA USA.
3. Benaron, D. A., and K. D. Stevenson. 1994. Resolution of near-infrared time-of-flight brain oxygenation imaging. *Adv. Exp. Med. Biol.* **361**:609-617.
4. Benaron, D. A., J. P. Van Houten, W. F. Cheong, E. L. Kermit, K. R. A., and D. K. Stevenson. 1995. Early clinical results of time-of-flight optical tomography in a neonatal intensive care unit. *SPIE*. **2389**:In press.
5. Frackman, S., M. Anhalt, and K. H. Neelson. 1990. Cloning, organization, and expression of the bioluminescence genes of *Xenorhabdus luminescens*. *Journal of Bacteriology*. **172**:5767-5773.
6. Hoiseth, S. K., and B. A. D. Stocker. 1981. Aromatic-dependent *Salmonella typhimurium* are non-virulent and effective as live vaccines. *Nature*. **291**:238-239.
7. Hooper, C. E., R. E. Ansorge, H. M. Browne, and P. Tomkins. 1990. CCD imaging of luciferase gene expression in single mammalian cells. *J Biolumin Chemilumin.* **5**:123-30.
8. Israel, S., and a. Honigman. 1991. A bioluminescence assay for gene expression by continuously growing mammalian cells: application for detection of human immunodeficiency virus type-1 (HIV-1). *Gene*. **104**:139-145.
9. Jones, B. D., N. Ghorri, and S. Falkow. 1994. *Salmonella typhimurium* initiates murine infection by penetrating and destroying the specialized epithelial M cells of the Peyer's patches [see comments]. *J Exp Med*. **180**:15-23.
10. Kay, S. A. 1993. Shedding light on clock controlled cab gene transcription in higher plants. *Semin Cell Biol.* **4**:81-6.
11. Meighen, E. 1993. Bacterial bioluminescence: organization, regulation, and application of the lux genes. *FASEB J*. **7**:1016-22.
12. Millar, A. J., I. A. Carré, C. A. Strayer, N.-H. Chua, and S. A. Kay. 1995. Circadian clock mutants in *Arabidopsis* Identified by luciferase imaging. *Science*. **267**:1161-1163.
13. Millar, A. J., S. R. Short, N. H. Chua, and S. A. Kay. 1992. A novel circadian phenotype based on firefly luciferase expression in transgenic plants. *Plant Cell*. **4**:1075-87.
14. Morrey, J. D., S. M. Bourn, T. D. Bunch, M. K. Jackson, R. W. Sidwell, L. R. Barrows, R. A. Daynes, and C. A. Rosen. 1991. In vivo activation of human immunodeficiency virus type 1 long terminal repeat by UV type A (UV-A) light plus psoralen and UV-B light in the skin of transgenic mice. *J Virol*. **65**:5045-51.
15. Morrey, J. D., S. M. Bourn, T. D. Bunch, R. W. Sidwell, and C. A. Rosen. 1992. HIV-1 LTR activation model: evaluation of various agents in skin of transgenic mice. *J Acquir Immune Defic Syndr*. **5**:1195-203.
16. Sanderson, K. E., and B. A. D. Stocker. 1987. *Salmonella typhimurium* strains used in genetic analysis, p. 1220-1224. *In* F. C. e. i. c. Neidhardt and J. L. Ingraham and K. B. Low and B. Magasanik and M. Schaechter and E. Umberger (ed.), *Escherichia coli* and *Salmonella typhimurium*. Cellular and Molecular Biology, vol. 2. American Society of Microbiology, Washington DC.
17. Szittner, R., and E. Meighen. 1990. Nucleotide sequence, expression and properties of luciferase coded by lux genes from terrestrial bacterium. *Journal of Biological Chemistry*. **265**:16581-16587.
18. White, M. R. H., M. Masuko, L. Amet, G. Elliott, M. Braddock, A. Kingsman, and S. Kingsman. 1995. Real-time analysis of the transcriptional regulation of HIV and hCMV promoters in single mammalian cells. *J. Cell Sci*. **108**:441-455.
19. Xi, L., K. W. Cho, and S. C. Tu. 1991. Cloning and nucleotide sequences of lux genes and characterization of luciferase of *Xenorhabdus luminescens* from a human wound. *Journal of Bacteriology*. **173**:1399-1405.

**Phosphorescence probes for measurement of O<sub>2</sub> and NO in tissues.** Jane M. Vanderkooi,  
Department of Biochemistry & Biophysics, School of Medicine, University of Pennsylvania,  
Philadelphia PA

When molecules absorb light, they become more reactive. The reactivity of excited state molecules, relative to the ground state molecules, is the basis of the use of photoactivated molecules as sensors for the paramagnetic molecules, O<sub>2</sub> and NO. The concentration of these physiological diatoms can be determined by their effect in increasing the rates of the transition from the excited state to the ground state of probe molecules. The longer the probe lifetime, the greater the chance for contact between the sensor and sensed molecules. This means that long-lived phosphorescence will be sensitive to O<sub>2</sub> and NO at low concentrations, while shorter-lived fluorescence will be less sensitive. Extrinsic probes added to tissue or cells allow one to make an image of the oxygen distribution. We are also examining the use of molecules that are intrinsic to the cell as use in oxygen sensor, and recent results will be presented.



**Upconverting Reporters for Immunodiagnostics:  
Applications in Immunohistochemistry and Surgical Imaging**

Gregory W. Faris, William H. Wright, David A. Zarling, and Luke V. Schneider  
Science and Technology Group  
SRI International  
333 Ravenswood Avenue  
Menlo Park, CA 94025  
(415) 859-4131  
FAX (415) 859-6196  
FARIS@MPLVAX.SRI.COM

We are exploring the use of a novel type of ultrasensitive upconverting reporter for a variety of applications, including immunohistochemistry and surgical imaging. This class of reporter consists of rare earth elements in an inorganic crystalline particle. These phosphors are unusual in that they exhibit upconversion. That is, they can convert light from low energy (infrared) to high energy (e.g., visible). This is the opposite of conventional fluorescent and phosphorescent materials such as dyes. Because upconversion is very uncommon in nature, autofluorescence background is essentially nonexistent for measurements with upconverters.

Upconverting phosphors can be excited very efficiently using cw near infrared diode lasers. This distinguishes these materials from two-photon-excited dyes that require very high light intensities. At moderate cw laser intensities, upconversion efficiencies of over 5% can be obtained. The high efficiency and low background allows the performance of extremely sensitive tests using the upconverters. We have demonstrated that upconverting phosphors provide sufficient sensitivity to allow detection of a single 0.3 phosphor particle against a background from biological material.

The use of laser diode excitation offers a number of additional advantages for the upconverters. Laser diodes are relatively inexpensive, power efficient, and compact, allowing for small and inexpensive instrumentation. The upconverting phosphors are excited with light at 960 or 1500 nm and emit in distinct narrow bands between 400 and 800 nm. The use of near infrared light exhibits low tissue damage compared to visible or ultraviolet excitation sources. Near infrared light shorter than 1300 nm can penetrate tissue more effectively than shorter wavelengths.

Because the phosphors emit in narrow distinct bands they are well suited to multi-analyte tests with very little overlap. The energy transfer process involved in the upconversion process

allows excitation of several phosphors emitting at different wavelengths with a single laser. We believe that these phosphors have essentially infinite shelf life, no toxicity, and are unaffected by environmental conditions such as pH, temperature, enzymatic reactions, or solvent effects. The phosphors are immune to photobleaching.

The beneficial properties of the upconverting phosphors will allow their use in many application areas. These include *in vitro* diagnostics (immunoassays and DNA probes), photodynamic therapy, immunohistology, and surgical imaging.

A key step in using the upconverting phosphors is the covalent binding to representative probes. To covalently bind the inorganic phosphor to probes such as antibodies, we have used coating techniques. We have successfully silanized upconverting phosphors and covalently bound them to avidin. These avidin-linked phosphor particles have been used in both immuno- and nucleic-acid assays.

An immunodiagnostic cell surface antigen assay was performed to detect the presence of human lymphoblastoid cells using the phosphor reporters. Streptavidin coated phosphors were used to detect the presence of a secondary antibody against a mouse IgG1 monoclonal antibody to  $\beta_2$ -microglobulin antigen on the surface of the lymphoblastoid cells. Separation of the bound phosphors to the cells was performed using magnetic beads coated with another secondary antibody against the mouse IgG1 bound to the cell surface. Single cell detection was observed using a photomultiplier tube in a scanning laser microscope modified for infrared excitation of the phosphor reporters.

Nucleic acids can also be detected with the phosphor reporters. Plasmid DNA labeled with biotin and digoxigenin was incubated with a mouse IgG1 anti-digoxigenin antibody. Detection of the labeled DNA was performed using streptavidin coated phosphors. Separation of bound phosphor to the DNA strand from unbound phosphor was performed using anti-mouse IgG1 antibody coated magnetic beads. Measurements in a fluorimeter modified for infrared laser diode excitation, controlling for non-specific binding of the phosphor labels, demonstrate detection well above background levels.

Imaging with upconverting phosphors was performed using the human  $\beta_2$ -microglobulin cell surface assay described above with individual lymphoblastoid cells. Imaging was performed using a Zeiss CLSM-10 confocal microscope that was modified to accept infrared scanning optics and a 960 nm infrared laser diode. Because of the lack of biologically-induced background during scanning with the infrared laser, separate visible and infrared illuminated images were taken. On a visible/infrared composite image individual phosphor particles can be clearly seen attached to the cell surfaces.

Friday, March 22, 1996

## Dyes and Reporters *In Vivo* II

**BFB** 11:00 am-12:20 pm  
Windsor Ballroom

Eva Sevick-Muraca, *Presider*  
*Purdue University*

## Laser Spectroscopy in Tissue Characterisation

Katarina Svanberg<sup>1</sup>, Claes af Klinteberg<sup>2</sup>, Annika Nilsson<sup>2</sup>,  
Ingrid Wang<sup>1</sup>, Stefan Andersson-Engels<sup>2</sup>, and Sune Svanberg<sup>2</sup>

<sup>1</sup>Department of Oncology, Lund University Hospital, S-221 85 Lund, Sweden

<sup>2</sup>Department of Physics, Lund Institute of Technology, P.O. Box 118, S-221 00 Lund, Sweden

### Introduction

Laser-induced fluorescence (LIF) can be used for non-invasive spectroscopic identification of biological tissue and is of special interest in early tumour detection. The basis for this "optical biopsy" method is the interaction of the laser light with tissue chromophores, such as tryptophan, collagen, elastin, NADH,  $\beta$ -carotene and haemoglobin. The UV-excited fluorescence that arises from the native chromophores, the autofluorescence, has a broad distribution, peaking at about 490 nm with a lower intensity in tumour compared to normal tissue. The tumour detection potential is enhanced with exogenously administered tumour marking agents, such as different Haematoporphyrin derivatives. Recently, the haem precursor  $\delta$ -amino levulinic acid (ALA) administered topically, orally or intravenously was introduced for the induction of Protoporphyrin IX (PpIX) tissue sensitisation [1-3]. Time-integrated laser-induced fluorescence measurements utilising a point monitoring fluorosensor and a multi-colour fluorescence imaging system were performed *in vivo* in patients with various malignant tumours. The autofluorescence as well as the PpIX-related fluorescence signals were monitored and dimensionless tumour demarcation functions were calculated for different human malignant tumours, such as tumours in the urinary bladder, in the head and neck region and in the skin.

### Fluorescence equipment

A fibre-based mobile clinical fluorosensor was used for the point-monitoring measurements, in which the full spectral information was collected. The equipment is described in detail in Ref. 4. Conventional biopsy sampling was performed and a correlation between the spectral shape and the histopathology was performed. A multi-colour fluorescence imaging system was utilised for the investigation of larger tissue areas. The system is described in Ref. 5. Examples from point-monitoring measurements as well as tissue fluorescence imaging will be given in some clinical specialities.

### Non-melanoma malignant skin tumours

Topical application of ALA on non-melanoma malignant skin tumours, such as basal cell carcinoma was utilised in photodynamic therapy [1,3]. By monitoring the PpIX-related fluorescence the tumour borders might be demarcated more precisely than only by visual judgement. It is well known that several recurrences occur in the border zone of the tumour. One example recorded from a basal cell carcinoma is shown in Fig. 1. The tumour area and the surrounding skin was topically applied with 20% ALA cream 6 hours *prior* to the point-monitoring measurements. As seen in Fig. 1a the autofluorescence peaking at about 490 nm is decreasing in the tumour area. The PpIX-related signal with a dual-peaked emission at about 635 and 700 nm is clearly seen within the tumour area and the border zone. The same tumour scan was recorded after the laser irradiation with a total light dose delivery of 60 J/cm<sup>2</sup>. As illustrated in the figure the PpIX-related fluorescence signal is decreased after the treatment which is due to a photo-induced bleaching. The bleaching monitoring might be useful in the planning of the treatment procedure. A computer processed image superimposed on a normal video recording of a basal cell carcinoma is shown in Fig. 1b.

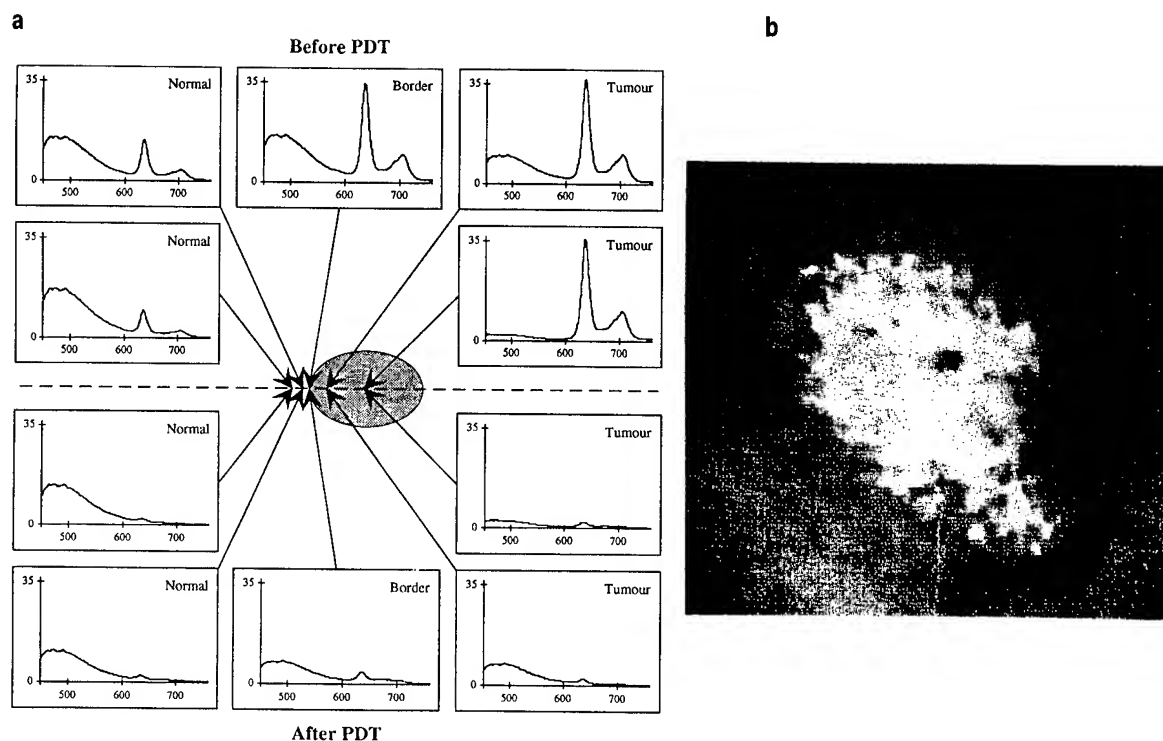


**Figure 1. a)** A point-monitoring fluorescence scan through a basal cell carcinoma (BBC) and surrounding normal skin in a patient. The whole area had been topically applied with a 20% ALA cream 6 hours before the investigation. The PpIX-related fluorescence, peaking at about 635 and 700 nm, shows a high intensity within the tumour area and the border zone. A photo-induced PpIX bleaching is recorded after the laser treatment. The autofluorescence peaking at about 490 nm shows higher intensity in the normal skin as compared to the tumour. **b)** A multi-colour fluorescence image of a BBC treated with ALA. The area fulfilling the "tumour demarcation criterion" with a high ratio  $I(635 \text{ nm})/I(490 \text{ nm})$  is seen overlaying the normal video image.

### Urinary bladder tumours

Some malignant tumours in the urinary bladder are very aggressive and invade the underlying tissue. There are indications that these aggressive tumours are developed from the shallow carcinoma *in situ* lesions. Therefore, these lesions are of special interest from a diagnostic point of view, since they may be hard to discover and instead visually judged as areas of inflammation only. In a series of clinical studies, local application of ALA was used and the PpIX-related fluorescence was studied [5] as well as combined with the autofluorescence for tumour demarcation [6]. Spectra recorded in an *in vivo* scan are shown in Fig. 2. The evaluated ratios are also given for the corresponding points.

### Discussion

All medical diagnostic procedures have as the ultimate aim to reveal the correct diagnosis. Most commonly tissue sampling is performed for histopathological confirmation of the disease. However, some organs are sensitive and might be disfigured by multiple biopsy procedures. In other locations, the area to investigate is large and a randomised procedure is performed according to a standard "map" for each organ. Thus, in many clinical situations the optical characterisation of tumour tissue has the great advantage of being non-invasive and providing real-time information on the status of the tissue. By developing the LIF techniques as guiding tools for the biopsy sampling the precision in the procedure might be enhanced. With the point monitoring the full spectral characterisation is obtained and the relevant wavelengths for different tumour types can be determined to be used for the imaging monitoring of larger tissue areas.

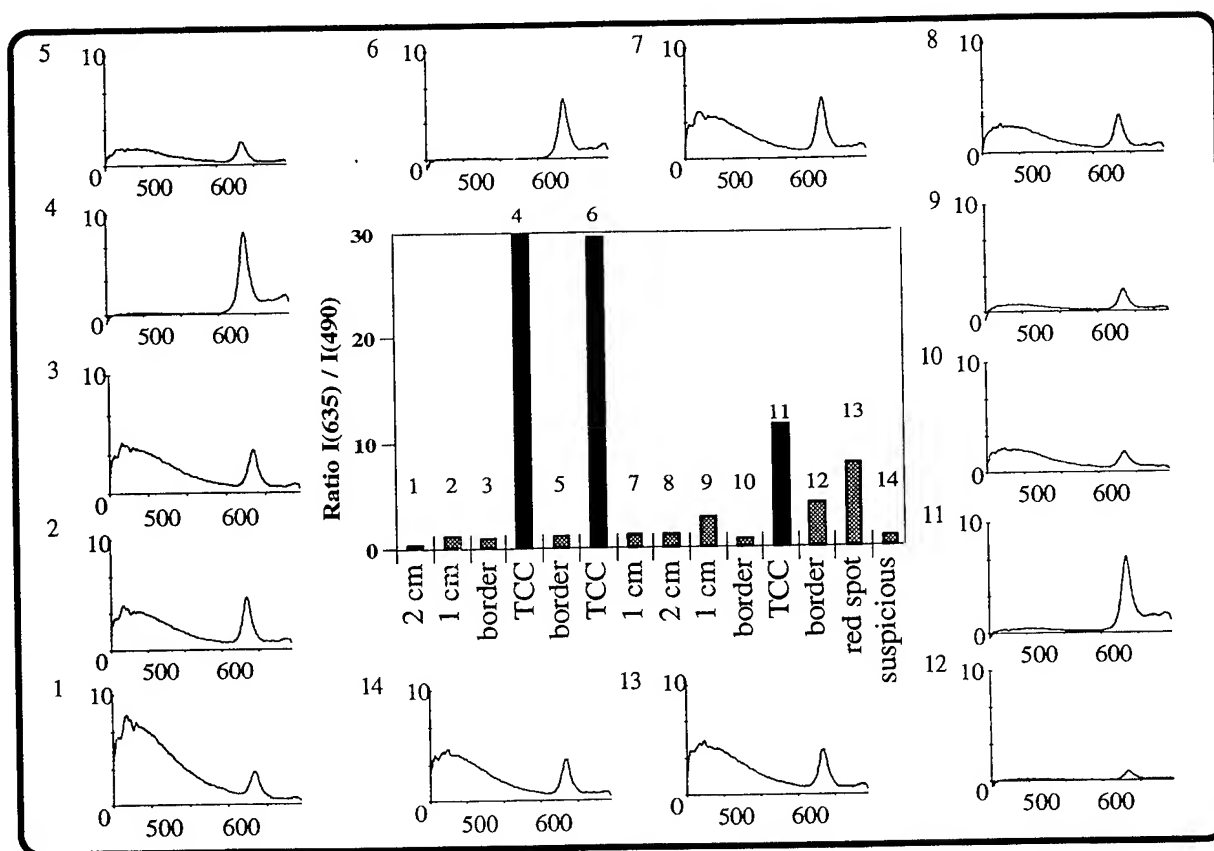


**Figure 2.** Fluorescence spectra and the corresponding histogram of the intensity ratio  $I(635\text{nm})/I(490\text{ nm})$  recorded in a patient with transitional cell carcinoma lesions in the bladder. A solution of 1% ALA was instilled 4 hours prior to the investigation. The excitation wavelength was 405 nm. (See Ref. 6).

### References

1. J.C. Kennedy, R.H. Pottier, Photodynamic therapy with endogenous protoporphyrin IX: Basic principles and present clinical status. *J. Photochem. Photobiol.*, **6**, 143-48 (1990).
2. C.S. Loh, A.J. MacRobert, J. Bedwell, J. Regula, N. Krasner, S.G. Bown, Oral versus intravenous administration of 5-amino levulinic acid for photodynamic therapy. *British J. Cancer*, **68**, 41-51 (1992).
3. K. Svanberg, T. Andersson, D. Killander, I. Wang, U. Stenram, S. Andersson-Engels, R. Berg, J. Johansson, S. Svanberg, Photodynamic therapy of non-melanoma malignant tumours of the skin using topical  $\delta$ -amino levulinic acid sensitisation and laser irradiation. *British J. Dermatol.*, **130**, 743-751 (1994).
4. S. Andersson-Engels, Å. Elner, J. Johansson, S.-E. Karlsson, L.G. Salford, L.-G. Strömblad, K. Svanberg, S. Svanberg, Clinical recordings of laser-induced fluorescence spectra for evaluation of tumour demarcation feasibility in selected clinical specialities. *Laser Med. Sci.*, **6**, 415-24 (1991).
5. K. Svanberg, I. Wang, S. Colleen, I. Idvall, C. Ingvar, R. Lundgren, R. Rydell, D. Jocham, A. Knipper, S. Thomas, H. Diddens, S.G. Bown, G. Gregory, S. Montán, I. Jonsson, Multi-colour fluorescence imaging of malignant tumours-Initial experience, To be published
5. M. Kriegmayr, R. Baumgartner, R. Knüchel, H. Stepp, F. Hofstädter, A. Hofstetter, Detection of early bladder cancer by 5-aminolevulinic acid induced porphyrin fluorescence, *J. Urology* (in press).
6. I. Rokahr, S. Andersson-Engels, S. Svanberg, M.A. D'Hallewin, L. Baert, I. Wang, K. Svanberg, Optical detection of human urinary ladder carcinoma utilising tissue autofluorescence and protoporphyrin IX-induced fluorescence following low-dose ALA instillation, *Proceeding BiOS '95, Barcelona, Sept. 9-13, 1995*.

**Spectroscopic Characterization and Biodistribution of Tissue Site-  
Selective Polyazacyclic Terbium Chelates.**

Darryl J. Bornhop, Darren S. Hubbard and Michel P. Houlne

Department of Chemistry and Biochemistry

Texas Tech University

Box 41061

Lubbock, Texas 79409-1061

Tel: (806) 742-3142

Fax: (806) 742-1289

e-mail: qzdjb@ttacs.ttu.edu

e-mail: qzlab@ttacs.ttu.edu

## INTRODUCTION

To perform early stage diagnostic imaging in tissue matrices, solute site-selectivity is critical. Recently, several new lanthanide based chelates have been synthesized and characterized for use as biomarkers which show tissue selectivity under the appropriate chemical conditions.<sup>1</sup> By modifying the external structural moieties or charge carriers, tissue site-selectivity can be tuned. In the work presented here, we show that similar tissue selectivity can be achieved for chelates of Terbium (Tb) and that these chelates have superior spectral properties for fluorescence imaging.

These Tb(III) complexes are ideally suited for biological analysis since they absorb light in the UV (255 - 270 nm) and emit light in the visible region (550 nm). Radiative emission in the visible region is far from the native autofluorescence of most biological matrices excited with UV light leading to an inherent S/N ratio advantage.

Quantitative investigations reported here include the spectroscopic evaluation of the Terbium chelates and the demonstration that a very simple optical train permits resolution and analysis of individual cells. This instrument, combined with the unique chemical selectivity and spectral specificity of the chelates of Terbium (III), can be employed for imaging specific tissue sites in tumors.

## EXPERIMENTAL

Resolution tests were performed by back-illumination of a USAF target with white light. The image was collected by a rod lens and focused onto a commercial grade CCD by a 10X microscope objective. The image from the CCD can be played onto a high-resolution monitor or grabbed by a Matrox frame-grabber for subsequent analysis. Tissue samples were excited by UV light (255 - 270 nm) and the emitted light was collected by the optical train, with a 550 nm excitation filter placed between the microscope objective and the CCD, (figure 1.) The terbium compounds, as well as tissue perfused with the three Tb<sup>3+</sup> compounds, were acquired from our corporate collaborators.

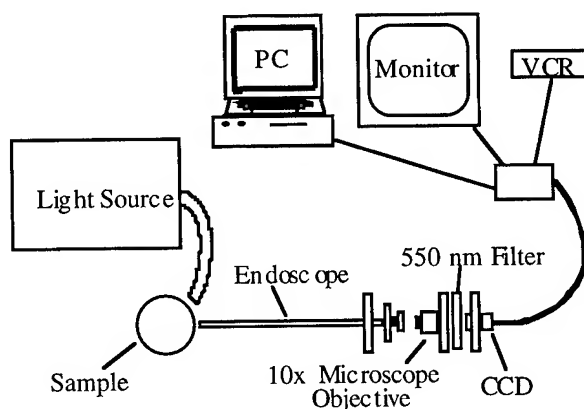


**Figure 1. Instrument block diagram**



## RESULTS AND DISCUSSION

Using a rod-lens endoscope system, 181 Line pairs/mm could be resolved on the USAF target. This corresponds to 2.76  $\mu\text{m}$  and is significantly smaller than most cells. Fluorescent species such as fluorescein were imaged and the detection limit was calculated to be 25 pmol.

Fluorescence for aqueous solutions of the Terbium complexes occurs in the visible at about 550 nm. These spectra were nearly identical for all three terbium compounds studied and is minimally perturbed by introduction onto a matrix. This spectroscopic phenomena of an exceedingly large Stokes shift is indicative of metal-ion fluorescence of lanthanide chelates.<sup>2</sup> The blue-green emission of these chelates is observed even when the species are bound or entrained into a tissue matrix.

Fluorescent images of the Terbium doped tissues were compared to biodistribution studies, using radio-tracer techniques exhibiting excellent correlation.

We have demonstrated that a new class of lanthanide chelates can be excited at 270 nm to produce a red shifted blue-green fluorescence at 550 nm, that the quantum yields are significant, that they exhibit tissue site-selectivity and that these molecules can be used as tissue selective markers for fluorescence imaging.

Future modifications of the instrument could enhance the imaging capability of the instrument by increasing resolution and limit of detection. One major obstacle is the use of band-pass filters (20 nm FWHM) which allow only 25 % of the light to pass. Future efforts will focus on overlapping high-throughput, colored glass filters to increase the number of photons playing onto the detector. This, combined with using a higher-grade CCD, should provide significant improvements in the limit of detection and resolution of the system.

A long term goal of our research is to further tune the chemistry and instrumentation so that minimally invasive methods based on endoscopic imaging and non-toxic lanthanide chelate fluorescence probes (as site directed markers) can be used in early warning disease diagnosis. The demonstrated characteristics such as the large Stokes shift, large quantum yield and the tissue selectivity make these compounds excellent candidates for the planned work.

## REFERENCES

1. W. Kim, G. Kiefer, F. Maton, K. McMillan, R. Muller and A. Sherry, Relaxometry, luminescence measurement, electrophoresis and animal biodistribution of lanthanide (III) complexes of some polyazamacrocyclic acetates containing pyridine, *Inorganic Chemistry*, **34**, 2233, (1995).
2. J-M Devoiselle, V. Maunory, S. Mordon, and D. Coustaut, Measurement of in-vivo tumorous/normal tissue pH by localized spectroscopy using a fluorescent marker, *Optical Engineering*, **32**(2), 239, (1993).

## Non-invasive Technique for the Diagnosis of Diseased Salivary Glands in situ

Gannot I<sup>1</sup>, Gandjbakhche AH<sup>2</sup>, Gannot G<sup>3</sup>, Fox PC<sup>3</sup>, Koch H<sup>4</sup> and Bonner RF<sup>4</sup>

1. Electro-optics Branch, CDRH, Food and Drug Administration, Rockville, MD 20857.  
Tel.: (301)-594-3442, Fax: (301)-443-2208, E-mail: israel@eob.cderh.fda.gov

2. Physical Sciences Laboratories DCRT, National Institutes of Health, Bethesda, Maryland 20892

Tel.: (301)-496-1335, Fax: (301)-402-4544, E-Mail: amir@helix.nih.gov

3. Clinical Investigations and Patient Care Branch, National Institute of Dental Research, National Institutes of Health, Bethesda, Maryland 20892

Tel.: (301)-496-60557, Fax: (301)-402-1228, E-Mail: gannot@yoda.nidr.nih.gov, pfox@yoda.nidr.nih.gov

4. Biomedical Optics, BEIP, National Institute of Health, Bethesda, MD 20892

Tel.: (301)-496-63606, Fax: (301)-496-3608, E-Mail: bonner@helix.nih.gov

### Abstract:

Fuoresceinated antibodies which specifically bind to infiltrating lymphocytes in minor salivary glands are imaged in order to provide monitoring of the progression of Sjögren's syndrome.

### Introduction:

Sjögren's syndrome (SS) [1] is an auto-immune disorder primarily affecting peri- or post menopausal women (over 90% of the cases). It is estimated there are more than 1 million persons with SS in the United States. The major symptoms [2] (dry eyes and dry mouth due to decreased tear and saliva secretion) are the result of progressive immune-mediated dysfunction of the lacrimal and salivary glands. Currently diagnosis [3] is made by measurements of stimulated and unstimulated saliva flow, salivary scintigraphy, sialography, and excisional biopsies of the minor salivary glands in the lower lip.

This latter exam [4], though considered the best criterion for diagnosis, involves a surgical procedure under local anesthesia followed by post operative discomfort (swelling, pain) and frequently a temporary loss of sensation of the lower lip biopsy site. Additionally, biopsy inherently is subject to sampling errors while requiring the preparation of histopathological slides which is time consuming, complicated and expensive and needs the skills of several persons (dentist, pathologist, laboratory technician). Thus, there is a clear need for a noninvasive diagnostic procedure [5] which reflects the underlying gland pathology and has good specificity. A quantitative noninvasive assay would also allow repetition of the test to monitor disease progression and the results of treatments. In general, such quantitative imaging techniques may be applied to many other diseases for which specific in situ fluorescent markers are developed.

Our goal is to quantitatively label infiltrating lymphocytes within the salivary glands with specific fluoresceinated antibodies [6]. By applying inverse methods [7] to images obtained with a special laser scanning system we propose to determine the 3-D distribution of the fluorescence within the tissue. The primary objective of this research is to find a specific molecular probe or a specific spectral feature of the fluorescence of a less specific probe that will correlate with the presence of the disease and the degree of

its progression.

### Results:

The quantitation of fluorophore concentration within the tissue from images of the surface requires measuring the optical properties of the tissue, determining the intensities of the surface image for sources as a function of depth and transverse distance, and obtaining sufficient image information to predict 3D distribution fluorophores within the tissue. As a laser scans the tissue surface a series of images will be obtained (one for each surface point irradiated). From these images we expect to utilize an inverse method based on analytical photon migration models in order to compute the 3D concentration distribution of the fluorophore.

Initially, we have measured the optical properties of the oral mucosa of the lower lip in human subjects *in vivo*. A series of holes in an opaque disk held a collecting optical fiber at a large number of radial separations from a fixed central illuminating fiber (633nm). The output of the illuminating fiber and the collecting fiber was measured at each position and then compared with identical measurements on a Delrin standard of known optical properties. The graphs of the intensity of the reflected beam as a function of the distance from the impinging laser beam are shown in Fig.1.

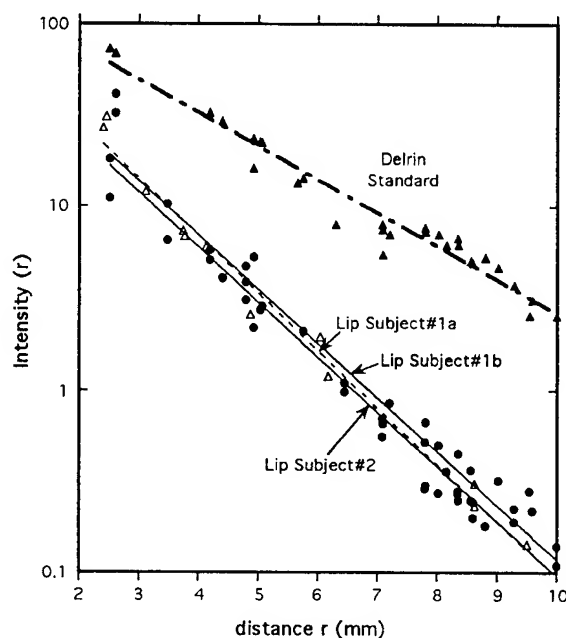


Figure 1. Optical measurements of  $I(r)$  from human lip *in vivo* and delrin reference standard.

From these measurements, we estimate the  $\mu_a = 0.1 \text{ mm}^{-1}$  and  $\mu_s = 0.7 \text{ mm}^{-1}$  for the human lip *in vivo* at 633nm. These values were then inserted in our Random Walk Theory models of depth sensitivity to generate depth sensitivity maps. An example is shown in Fig.2.

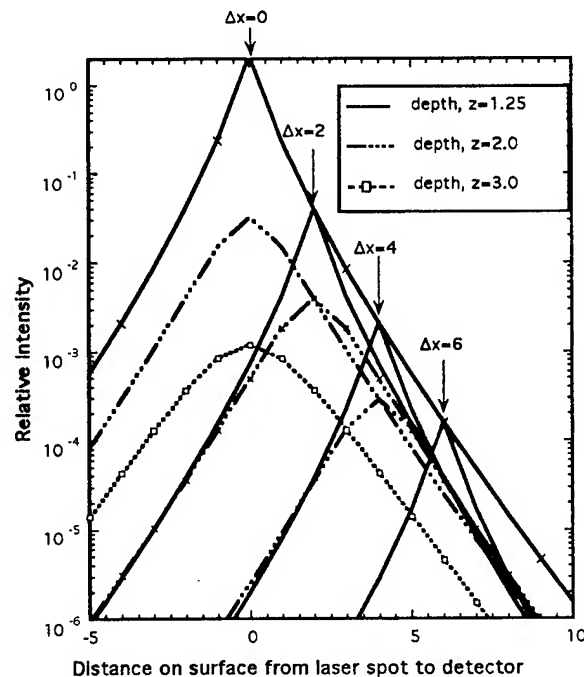


Fig. 2 Depth sensitivity maps for 3 test cases of embedded optical probes.

Summary:

Employing the above results we shall perform simulation experiments by embedding the chosen optical probe fluorescein in the Delrin, in distances similar to the minor salivary glands which exist in the lower lip about 1-3 mm under the surface.

References:

1. K. J. Bloch, W. W. Buchanan, M.J. Wohl, J.J. Bunim, "Sjögren's syndrome", *Medicine*, 44 (3), 187-405, 1965.
2. Robert I. Fox, Editor, "Sjögren syndrome", *Rheumatic disease clinic of North America*, August 1992.
3. J. S. Greenspan, T. E. Daniels, N. Talal, R. A. Sylvester, "The histopathology of Sjogren's syndrome in labial salivary gland biopsies", *Oral Surg.* Feb. 1974, vol 37, no. 2, 217-229.
4. T. E. Daniels, "Labial salivary gland biopsy in Sjogren's syndrome", *Arthritis and Rheumatism* vol. 27 no. 2, 147-156, Feb. 1984.
5. Nishioka NS., "Laser induced fluorescence spectroscopy", *Gastrointest Endosc Clin N Amer* 1994, Apr, 4(2):313-326.
6. G. Gannot and P.C. Fox, "Development of Non-Invasive method for the diagnosis of Sjögren's syndrome in the Minor Salivary Glands", *Internal Communication*, NIH/NIDR, 1995.
7. Gandjbakhche AH, Bonner RF., Nossal R, and Weiss GH, "Absorptivity Contrast in Transillumination Imaging of Tissue Abnormalities, *Applied Optics*, 1995, In press.

- af Klinteberg, Claes — BFB1  
 Alfano, R. R. — BThA13  
 Almenrader, N. — BThA5  
 Anderson, Eric — BWB2  
 Andersson-Engels, Stefan — BFB1  
 Araki, Ryuichiro — BThA15  
 Arnold, Mark A. — BWA1
- Baer, Thomas — BWC3, BThC, BThD  
 Bamber, J. C. — BThA6  
 Barbieri, Beniamino — BWB4  
 Barbour, Randall L. — BThA23  
 Ben-Amotz, Dor — BThC2  
 Benaron, David — BWA, BWB  
 Bevilacqua, Frederic — BFA, BFB  
 Bigio, Irving J. — BWC, BWD, BThB2, BThB4  
 Boas, D. A. — BWA5, BThD1, BThD3  
 Bocker, D. — BWA3  
 Bonner, R. F. — BFB3  
 Bornhop, Darryl J. — BThA11, BFB2  
 Boyer, James — BThB2  
 Bruulsema, J. T. — BWA3
- Campbell, Arlene — BWA4  
 Canto, Marcia I. — BWC2  
 Celmer, E. J. — BThA13  
 Cerussi, Albert — BWB3, BWB4, BThA14  
 Chance, B. — BWA5, BWB4, BThA18, BThB1, BThD1, BThD3  
 Chang, Jenghwa — BThA23  
 Chang, Richard K. — BWD2  
 Chang, Ta-Chau — BFA1  
 Chen, Gang — BWD2  
 Chiang, Chien-Chih — BFA1  
 Contag, Christopher H. — BFA2  
 Cope, M. — BWB5, BThA25  
 Coquoz, Olivier — BWB2  
 Crawford, D. C. — BThA6
- De Blasi, R. A. — BThA5  
 Deka, C. — BWD1  
 Delpy, D. T. — BWB5, BThA25  
 Dietz, Louis J. — BWC3  
 Dunn, Andrew — BWD3
- Eda, Hideo — BThA24  
 Essenpreis, M. — BWA3  
 Eversole, J. D. — BThA16
- Fantini, Sergio — BWB3, BWB4, BThA14  
 Faris, Gregory W. — BFA4  
 Farrell, T. J. — BWA3  
 Feld, Michael S. — BThC3  
 Fernandez, Gilbert L. — BWD2  
 Ferrari, Marco — BThA3, BThA4, BThA5  
 Foster, T. H. — BWA2
- Fox, P. C. — BFB3  
 Franceschini, Maria Angela — BWB3, BWB4, BThA14
- Gandjbakhche, A. H. — BFB3  
 Gannot, G. — BFB3  
 Gannot, I. — BFB3  
 George, John S. — BThA8  
 Graber, Harry — BThA23  
 Gratton, Enrico — BWB3, BWB4, BThA14  
 Gries, F. A. — BWA3  
 Gupta, P. K. — BThA12
- Hall, Jeffrey W. — BThA4  
 Haskell, Richard C. — BWB2  
 Hayward, J. E. — BWA3  
 Heinemann, L. — BWA3  
 Herman, B. — BWC1  
 Hielscher, Andreas H. — BThA8, BThB3, BThB4  
 Hill, Steven C. — BWD2  
 Houlne, Michael P. — BThA11, BFB2  
 Hubbard, Darren S. — BThA11, BFB2  
 Hull, E. L. — BWA2  
 Hutchinson, Christina L. — BThA19, BThC4
- Itabashi, Akira — BThA15  
 Iwamoto, Shin-itchi — BThA24  
 Izatt, Joseph A. — BWC2
- Jacques, Steven L. — BWB1, BThA17  
 Johnson, Tamara M. — BThB2  
 Jones, G. M. — BWD1
- Kaplan, A. E. — BThA7  
 Katz, A. — BThA13  
 Khurgin, J. B. — BThA7  
 Kim, Beop-Min — BWB1  
 Kimura, Mika — BThB1  
 Koch, H. — BFB3  
 Kohl, M. — BWB5  
 Koschinsky, T. — BWA3
- Lacey, JoAnne — BThB2  
 LaPlant, Fred P. — BThC2  
 Lawrence, S. — BWB5  
 Lehnert, B. E. — BWD1  
 Lehnert, N. M. — BWD1  
 Li, X. D. — BThD1, BThD3  
 Lin, S. — BThA17  
 Liu, Hanli — BThA18, BThB1
- MacKenzie, Hugh A. — BWA4  
 Maier, John — BWB3, BThA14  
 Majumder, S. K. — BThA12  
 Masters, Barry R. — BThA2  
 Matcher, Steve J. — BThA4, BThA25  
 Mayo, Michael W. — BWD2

Meglinsky, I. V. — BWA5  
Melloch, M. R. — AMC4  
Mortimer, P. S. — BThA6  
Motamedi, Massoud — BWB1  
Mourant, Judith R. — BThA8, BThB2, BThB3, BThB4

Nachman, Paul — BWD2  
Nahid, K. — BThA25  
Nathel, Howard — BThB  
Nelson-Larry, Lena — BThA19  
Nichols, M. G. — BWA2  
Niessner, R. — BThA1  
Nilsson, Annika — BFB1

O'Brien, P. — BWB5  
O'Leary, M. A. — BThA18, BThD1, BThD3  
Obeidat, A. T. — BThA7  
Oikawa, Yukio — BThA24  
Orskov, H. — BWA3  
Ostermeyer, Martin — BWB1

Page, David L. — BThA20  
Paithankar, Dilip Y. — BThD2  
Patterson, M. S. — BWA3  
Pinnick, Ronald G. — BWD2  
Pinto, J. F. — BThA16  
Pizzi, Assunta — BThA3  
Proskurin, Sergei G. — BThA15

Quaresima, Valentina — BThA3, BThA4

Rae, Peter W. H. — BWA4  
Rastegar, Sohi — BWB1  
Rava, Richard P. — BThA9, BThA10  
Reynolds, Jeffery S. — BThC2  
Richards-Kortum, Rebecca — BWD3, BThC1  
Rosen-Zvi, Michal — BThA21

Sandahl-Christiansen, J. — BWA3  
Schmidt, David M. — BThA8  
Schneider, Luke V. — BFA4  
Seaver, M. — BThA16  
Sevick-Muraca, Eva M. — BThA19, BThA20, BThC4,  
BThD2, BFA, BFB  
Sfareni, Romina — BThA3, BThA4  
Sivak, Michael V. — BWC2

Sklar, L. A. — BWD1  
Smithpeter, Colin — BWD3  
Spanner, G. — BThA1  
Steinkamp, J. A. — BWD1  
Stern, David — BThA9, BThA10  
Stern, M. D. — BThA7  
Svaasand, Lars O. — BWB2  
Svanberg, Katarina — BFB1  
Svanberg, Sune — BFB1

Taitelbaum, Haim — BThA21  
Takada, Michinosuke — BThA24  
Takahashi, Yukari — BThA15  
Takeuchi, Akira — BThA15  
Thompson, Charles A. — BThC2  
Tittel, Frank — BThA17  
Tromberg, Bruce J. — BWB2  
Troy, Tamara L. — BThA19, BThA20, BThC4  
Trulson, Mark O. — BThA9, BThA10  
Tsuchiya, Yutaka — BThA22  
Tsunazawa, Yoshio — BThA24

Uppal, A. — BThA12  
Urakami, Tsuneyuki — BThA22

Vanderkooi, Jane M. — BFA3

Wallace, V. P. — BThA6  
Walton, Ian D. — BThA9, BThA10  
Wang, Hsing-Wen — BWC2  
Wang, Ingrid — BFB1  
Wang, L. H. — BThA17  
Watson, R. — BWB5  
Webb, Kevin J. — BThC2  
Welch, A. J. — BWD3  
Willis, Joseph — BWC2  
Wright, William H. — BFA4

Yamada, Yukio — BThA15  
Yang, Y. — BThA13  
Yang, Yunsong — BThA18  
Yodh, A. G. — BWA5, BThD1, BThD3

Zarling, David A. — BFA4  
Zhang, Yutao — BThB1  
Zurawska-Szczepaniak, M. — BThA13

**BIOMEDICAL OPTICAL SPECTROSCOPY  
AND DIAGNOSTICS  
TECHNICAL PROGRAM COMMITTEE**

David Benaron, *Stanford University, General Chair*

Eva Sevick-Muraca, *Purdue University, Program Chair*

Thomas Baer, *Biometric Imaging*

Irving Bigio, *Los Alamos National Laboratory*

Britton Chance, *University of Pennsylvania*

Michael Feld, *Massachusetts Institute of Technology*

Howard Nathal, *Lawrence Livermore National Laboratory*

Rebecca Richards-Kortum, *University of Texas at Austin*

Ries Robinson, *University of New Mexico*

Katarina Svanberg, *Lund Institute of Technology, Sweden*

Bruce Tromberg, *Beckman Laser Institute and Medical Clinic*

Alan Waggoner, *Biological Detection Systems*